UNIVERSITÉ DE SHERBROOKE
Faculté de génie
Département de génie civil et de génie du bâtiment

Étude expérimentale de la micro-fracturation dans les roches et les interfaces roche-mortier sous chargement de traction directe et indirecte

Experimental study of micro-fracturing in rock and rock-mortar interfaces under direct and indirect tensile loading

Thèse de doctorat
Spécialité: génie civil

Ghasem SHAMS

Jury: Patrice RIVARD (directeur)
Jury 1: Jean-François NOËL
Jury 2: Nicholas VLACHOPOULOS
Rapporteur : Mathieu NUTH

Sherbrooke (Québec) Canada January 2023

This thesis is dedicated to

Mahsa (Jina) Amini

and all the brave women of Iran

Freedom will be yours.

RÉSUMÉ

L'initiation et la propagation de fractures à grande échelle peuvent entraîner une défaillance catastrophique de nombreuses structures de génie civil, minier et pétrolier. Il a été reconnu que les fractures macroscopiques sont produites par l'initiation, la propagation et la coalescence de nombreuses microfissures dans une région localisée autour de micro-défauts préexistants appelée zone de processus de fracture (ZPF). D'autre part, les matériaux rocheux étant plus faibles en traction qu'en compression et en cisaillement, le développement des mécanismes de ZPF et de microfissuration sous chargement en traction est d'un intérêt primordial. Les risques naturels tels que les coups de roche et les glissements de terrain sont liés à la nucléation et à la croissance de fissures de traction dans les roches. La résistance à la traction et la fracturation en traction sont tout aussi importantes dans le contrôle des structures en béton de roche. Par exemple, la résistance à la traction existant dans l'interface barrage-fondation résiste au moment de renversement dans la zone du pied du barrage en raison des forces agissantes du réservoir. En outre, dans certaines applications, l'étendue de la ZPF et les caractéristiques de rugosité des fractures créées sont d'une importance critique. Par exemple, en fracturation hydraulique, la ZPF et la rugosité de fracture sont les deux concepts qui décrivent la complexité et la connectivité de la roche réservoir fracturée. Par conséquent, le développement de la ZPF ou du nouveau réseau de fractures dans les roches a non seulement un impact sur leurs propriétés mécaniques (par exemple, la résistance), mais également sur leurs caractéristiques hydrauliques (par exemple, la perméabilité).

À ce jour, des recherches approfondies ont été menées sur la résistance et les propriétés de fracturation des roches intactes et des interfaces roche-béton sous des charges de compression et de cisaillement. Cependant, les processus et mécanismes de microfissuration et la relation entre la micro- et la macro-fracturation dans les interfaces roche et roche-béton sous chargement de traction n'ont pas encore été bien étudiés. Par conséquent, cette thèse étudie les processus de microfissuration et les mécanismes de micro-fracturation dans les spécimens de roche et de mortier rocheux sous des charges de traction directes et indirectes (brésiliennes). En particulier, il vise à (1) identifier et décrire la micromécanique de l'endommagement et l'évolution de la zone de processus de rupture dans le granite sous chargement de traction indirecte (brésilienne), (2) déterminer l'effet de deux taux de chargement sur les micro- et macro- et -comportement à la fracturation et résistance sous charge de traction indirecte (brésilienne), (3) caractériser la rugosité de la rupture de surface d'éprouvettes de granit sous charge de traction indirecte (brésilienne) et directe, (4) identifier et décrire la micromécanique de l'endommagement sous charge de traction directe dans une tentative d'expliquer la différence entre les valeurs de résistance obtenues à partir d'essais de traction directs et indirects (brésiliens), et (5) identifier et décrire la micromécanique des dommages à l'interface granit-mortier soumis à des charges de traction directes et indirectes (brésiliennes). À cette fin, des techniques d'émission acoustique (EA) et de corrélation d'images numériques (CIN) ont été utilisées pour surveiller les processus de fracturation dans des spécimens à l'échelle du laboratoire de granit intact et de mortier de granit testés sous une charge de traction directe et brésilienne.

Les spécimens comprenaient (1) des spécimens de disques cylindriques d'un diamètre de 75 mm et d'une épaisseur de 37,5 mm pour les essais brésiliens et (2) des spécimens prismatiques rectangulaires de dimensions 100 × 37 × 30 mm pour les essais de tension directe.

Nos résultats ont montré une cohérence entre les ZPF obtenus à partir des données EA et CIN pour tous les spécimens testés ; cependant, EA a fourni une zone de traitement légèrement plus grande. Les résultats de l'EA ont indiqué que la microfissuration dans la ZPF pourrait s'amorcer sous la traction, le cisaillement ou une combinaison des deux mécanismes pour les spécimens testés sous des charges de traction directes et brésiliennes. Il a également été démontré que la réduction du taux de charge dans les essais brésiliens (1) réduisait la résistance à la traction et (2) augmentait l'étendue de la ZPF, ce qui signifie que la résistance à la traction et la ZPF sont significativement affectées par le taux de charge de traction.

De plus, les résultats ont montré que la résistance à la traction directe des éprouvettes est inférieure à leur résistance à la traction indirecte, avec un rapport de résistance à la traction directe/indirecte de 66 % pour les éprouvettes de granit-mortier et de 70 % pour les éprouvettes de granit intact. Cela indique que ce rapport pour les spécimens de mortier de roche reste dans la même gamme que pour les roches intactes, au moins pour les matériaux testés et dans le cadre de la configuration expérimentale utilisée dans cette recherche. À ce jour, la relation entre les résistances à la traction directe et brésilienne des spécimens de mortier de roche n'a pas été rapportée dans la littérature.

L'inversion du tenseur des moments des formes d'onde EA et les données du champ de déformation CIN ont montré que les fractures macroscopiques générées, qui sont classiquement considérées comme des fractures de traction, étaient composées de mécanismes de fissuration en traction, en cisaillement et en compression à l'échelle microscopique. Cela était vrai pour les échantillons intacts et bi-matériaux testés sous des charges de traction directes et indirectes (brésiliennes). Cependant, différents mécanismes de microfissuration ont des contributions (proportions) différentes à la formation des macro-fractures finales. Comme pour les échantillons de granit intact, la macro-fracture ultime dite de traction était majoritairement composée de microfissures de cisaillement dans les essais brésiliens et de microfissures de traction dans les essais de traction directe. De même, il a été observé qu'un nombre significatif de microfissures de cisaillement se sont produites dans les spécimens de mortier de granit soumis à l'essai brésilien.

Au contraire, les microfissures de cisaillement ont joué un rôle minime dans la formation des macro-fractures finales dans les échantillons de granit-mortier sous tension directe. Les microfissures de cisaillement ont une résistance plus élevée que les microfissures de traction et nécessitent une énergie plus élevée pour se rompre. Ainsi, la contribution plus élevée des microfissures de cisaillement (avec une résistance plus élevée) à la formation de la macro-fracture ultime dans les spécimens brésiliens (tant intacts que granit-mortier) explique pourquoi la résistance à la traction des spécimens obtenue à partir de l'essai brésilien est supérieure à celle obtenue du test de tension directe.

En outre, il a été observé que les mécanismes de microfissuration dans tous les spécimens testés pourraient être influencés de manière critique par (1) l'état de contrainte de compression dans le test brésilien en raison de son champ de contrainte biaxial et (2) le type de matériau. La réduction du confinement et le changement de type de matériau (granit à grain coulé en mortier à grain fin) diminuent la contribution des microfissures de cisaillement lors du processus de fracturation des éprouvettes, entraînant une résistance à la traction globale plus faible. L'effet du type de matériau sur les mécanismes de microfissuration a été observé pour les essais de traction directs et brésiliens. De plus, il a été montré que le taux de chargement influence de manière significative les mécanismes de microfissuration dans les disques de granit sous la condition de chargement brésilienne.

Il a également été observé que la rugosité de surface des fractures macroscopiques générées dans les spécimens intacts augmente avec (a) la réduction du taux de chargement et (b) l'augmentation de la taille des grains. De plus, les fractures macroscopiques ultimes ont montré une rugosité plus faible avec des surfaces plus plates dans les spécimens de mortier de roche testés sous tension indirecte (brésilienne) que ceux testés sous tension directe.

En général, il a été clairement observé que différents mécanismes de microfissuration (c'est-à-dire différentes contributions des microfissures de cisaillement, de traction et de compression) (1) expliquent la différence entre les résistances à la traction directe et brésilienne des matériaux testés et (2) déterminent la rugosité de surface des a produit des macro-fractures sous des tests directs et brésiliens.

Dans les projets d'ingénierie des roches, en raison des difficultés de préparation des échantillons et d'exécution des tests dans les tests de traction directe, la résistance à la traction des matériaux de type roche est principalement mesurée indirectement par le test brésilien. En raison de la présence de microfissures de cisaillement dans les spécimens testés sous chargement brésilien, la résistance brésilienne obtenue surestime la résistance à la traction directe des matériaux pour les spécimens intacts et de granit-mortier. On pense que le test de traction directe fournit des valeurs représentant la véritable résistance à la traction des matériaux. Mais la résistance à la traction obtenue à partir d'un essai de traction directe est invariablement appliquée dans les projets d'ingénierie avec des gradients de contrainte. D'autre part, le matériau du disque dans un essai brésilien subit à la fois des gradients de contrainte et des champs de contrainte biaxiale, représentant mieux l'état de contrainte dans une masse rocheuse lorsqu'une rupture de traction se produit in situ. Par conséquent, la question est de savoir comment déterminer la résistance à la traction des matériaux fragiles. Plus précisément, quelle configuration d'essai doit être considérée comme fournissant la véritable mesure de la résistance à la traction?

Mots-clés: zone de processus de fracture (ZPF), corrélation d'images numériques, émission acoustique, inversion du tenseur des moments, mécanismes de microfissuration, rugosité de fracture, résistance à la traction, béton- roche,

ABSTRACT

Fracture initiation and propagation at a large scale may cause catastrophic failure of many civil, mining, and petroleum engineering structures. It has been recognized that macroscopic fractures are produced by the initiation, propagation, and coalescence of many microcracks in a localized region around pre-existing micro-flaws called the fracture process zone (FPZ). On the other hand, as the rock materials are weaker in tension than in compression and shear, the development of FPZ and microcracking mechanisms under tensile loading are of primary interest. Natural hazards such as rock bursts and rockslides are related to the nucleation and growth of tensile cracks in rocks. Tensile strength and tensile fracturing are equally important in controlling rock-concrete structures. For instance, the tensile strength existing in the dam-foundation interface resists the overturning moment at the toe zone of the dam due to the acting forces of the reservoir. Besides, in some applications, both the extend of the FPZ, and the roughness characteristics of the created fractures are of critical importance. For instance, in hydraulic fracturing, the FPZ and fracture roughness are the two concepts that describe the complexity and the connectivity of the fractured reservoir rock. Therefore, the development of the FPZ or new fracture network in rocks not only impacts their mechanical properties (e.g., strength) but also affects their hydraulic characteristics (e.g., permeability).

To date, extensive research has been carried out on the strength and fracturing properties of both intact rocks and rock-concrete interfaces under compression and shear loads. However, the microcracking processes and mechanisms and the relationship between micro- and macro-fracturing in rock and rock-concrete interfaces under tensile loading have not been well studied yet. Therefore, this thesis investigates the microcracking processes and micro-fracturing mechanisms in rock and rock-mortar specimens under direct and indirect (Brazilian) tensile loadings. In particular, it aims to (1) identify and describe the micromechanics of damage and the evolution of the fracture process zone in granite under indirect (Brazilian) tensile loading, (2) determine the effect of two loading rates on granite's micro- and macro-fracturing behaviour and strength under indirect (Brazilian) tensile loading, (3) characterize the roughness of the surface failure of granite specimens in indirect (Brazilian) and direct tensile loading, (4) identify and describe the micromechanics of damage in direct tensile loadings in an attempt to explain the difference between strength values obtained from direct and indirect (Brazilian) tensile tests, and (5) identify and describe the micromechanics of damage at granite-mortar interface subjected to both direct and indirect (Brazilian) tensile loadings. To this end, acoustic emission (AE) and digital image correlation (DIC) techniques were employed to monitor the fracturing processes in laboratory-scale specimens of intact granite and granite-mortar tested under direct and Brazilian tensile loading. Specimens included (1) cylindrical disc specimens with a diameter of 75 mm and a thickness of 37.5 mm for Brazilian tests and (2) rectangular prismatic specimens with dimensions of 100 × 37 × 30 mm for direct tension tests.

Our results showed consistency between the FPZs obtained from AE and DIC data for all tested specimens; however, AE provided a slightly larger process zone. AE results

indicated that the microcracking within the FPZ might initiate under tensile, shear, or a combination of both mechanisms for specimens tested under direct and Brazilian tensile loadings. It was also shown that reducing the loading rate in the Brazilian tests (1) reduced the tensile strength and (2) increased the extent of the FPZ, meaning that both tensile strength and the FPZ are significantly affected by the tensile loading rate.

In addition, the results showed that the direct tensile strength of the specimens is lower than their indirect tensile strength, with a direct/indirect tensile strength ratio of 66% for granite-mortar specimens and 70% for intact granite specimens. This indicates that this ratio for rock-mortar specimens remains in the same range as for intact rocks, at least for materials tested and under the experimental setup used in this research. To date, the relationship between direct and Brazilian tensile strengths of rock-mortar specimens has not been reported in the literature.

The moment tensor inversion of the AE waveforms and the DIC strain field data showed that the generated macroscopic fractures, which are conventionally regarded as tensile fractures, were composed of tensile, shear, and compressive cracking mechanisms at the microscale. This was true for both intact and bi-material specimens tested under direct and indirect (Brazilian) tensile loadings. However, different microcracking mechanisms had different contributions (proportions) to the formation of the final macro-fractures. As for intact granite specimens, the ultimate so-called tensile macro-fracture was predominantly composed of shear microcracks in Brazilian tests and of tensile microcracks in the direct tension tests. Similarly, it was observed that a significant number of shear microcracks occurred in the granite-mortar specimens subjected to the Brazilian test.

On the contrary, shear microcracks played a minimal role in the formation of the final macro-fractures in granite-mortar specimens under direct tension. Shear microcracks have higher strength than tensile microcracks and require higher energy to break. Thus, the higher contribution of shear microcracks (with a higher strength) to the formation of the ultimate macro-fracture in Brazilian specimens (both intact and granite-mortar) explains why specimens' tensile strength obtained from the Brazilian test is higher than that obtained from direct tension test.

Furthermore, it was observed that the microcracking mechanisms in all tested specimens might critically be influenced by (1) the compressive stress state in the Brazilian test due to its biaxial stress field and (2) the material type. Reducing the confinement and changing the material type (coursed-grain granite to fine-grained mortar) decreases the contribution of shear microcracks during the specimens' fracturing process, leading to a lower overall tensile strength. The effect of material type on microcracking mechanisms was seen for both direct and Brazilian tensile tests. In addition, it was shown that the loading rate significantly influences the microcracking mechanisms in granite discs under the Brazilian loading condition.

It was also observed that the surface roughness of the generated macroscopic fractures in intact specimens increases with (a) reducing the loading rate and (b) increasing the grain

size. In addition, the ultimate macroscopic fractures showed lower roughness with flatter surfaces in rock-mortar specimens tested under indirect (Brazilian) tension than those tested under direct tension.

In general, it was clearly observed that different microcracking mechanisms (i.e., different contributions of shear, tensile, and compressive microcracks) (1) explain the difference between direct and Brazilian tensile strengths of tested materials and (2) determine the surface roughness of the produced macro-fractures under direct and Brazilian tests.

In rock engineering projects, due to the difficulties in sample preparation and test execution in direct tensile tests, the tensile strength of rock-like materials is mostly measured indirectly by the Brazilian test. Because of the presence of shear microcracks in specimens tested under Brazilian loading, the obtained Brazilian strength overestimates the direct tensile strength of materials for both intact and granite-mortar specimens. It is believed that the direct tensile test provides values representing the true tensile strength of materials. But the tensile strength obtained from a direct tensile test is invariably applied in engineering projects with stress gradients. On the other hand, the disc material in a Brazilian test undergoes both stress gradients and biaxial stress fields, better representing the stress state in a rock mass when a tensile failure occurs in situ. Therefore, the question is how to determine the tensile strength of brittle materials. More precisely, which test configuration should be regarded as providing the true measure of the tensile strength?

Keywords: Fracture process zone, Digital image correlation, Acoustic emission, Moment tensor inversion, Microcracking mechanisms, Fracture roughness, Tensile Strength, Rock-concrete

PUBLICATIONS

During the research work at the University of Sherbrooke, the candidate has participated in the following publications:

Journal Papers:

1. **G. Shams**, P. Rivard, O. Moradian, (2022). '*Tensile strength and failure behaviour of rock-concrete interfaces: Direct and indirect measurements*.' Journal of Rock Mechanics and Geotechnical Engineering. October 2022, accepted with revision.
2. **G. Shams**, P. Rivard, O. Moradian, (2022b). '*Micro-scale Fracturing Mechanisms in Rocks During Tensile Failure*.' Rock Mechanics and Rock Engineering. July 2022, accepted (under press).
3. **G. Shams**, P. Rivard, O. Moradian, (2022c). '*Observation of fracture process zone and produced fracture surface roughness in granite under Brazilian splitting tests.*' Theoretical and Applied Fracture Mechanics. June 2022, published.

Refereed Conferences Publications:

1. **G. Shams**, P. Rivard, O. Moradian, (2022). '*Effects of roughness on the strength and fracturing processes in Mortar-Granite interface under tensile loading.*' In: The 75th Canadian Geotechnical Society (CGS), GeoCalgary 2022 Conference.
2. **G. Shams**, P. Rivard, O. Moradian, (2022). '*Microscale investigation of strength and failure behaviour of rock-concrete interfaces under tensile loading.*' In: The 56th US Rock Mechanics/Geomechanics Symposium held in Santa Fe, New Mexico, USA.

Posters:

1. **G. Shams**, P. Rivard, O. Moradian, (2022). '*Studying the strength and fracturing properties of rock-concrete interfaces under tensile loading at the microscale.*' In: The 22nd Canadian Rock Mechanics Symposium, RockEng22 Symposium.
2. M. Belhaj, P. Rivard, **G. Shams**, O. Moradian, (2022). '*Reconstructing roughness of rock discontinuities by geostatistical procedure.*' In: The 22nd Canadian Rock Mechanics Symposium, RockEng22 Symposium.

ACKNOWLEDGMENTS

First and foremost, I am extremely grateful to my supervisor, Prof. Patrice Rivard, for his invaluable advice, continuous support, and inspiration during my Ph.D. study. Beyond being a professional professor, Patrice has been a true friend to me over the past years. A friend who has always inspired me to become a better person inside and out. Thank you, my Prof! You know I appreciate you in so many ways.

I also sincerely thank Dr. Omid Moradian for all his precious advice and constructive guidance through my studies. His knowledge and continued availability for numerous and intense discussions are greatly appreciated.

Acknowledgments are also given to the examination committee, Prof. Nicholas Vlachopoulos, Dr. Jean-François Noël, Prof. Mathieu Nuth, and Prof. Rolland Leduc who took their precious time to assess my thesis and provide constructive advice, suggestions, and comments.

I would also like to acknowledge the financial contributions of the Natural Sciences and Research Council of Canada (NSERC) and Fonds de Recherche du Québec Nature et technologies (FRQNT). I am also very grateful to NVIDIA for providing a free Graphics processing unit (GPU) and Correlated Solutions, Inc. for providing a free license for VIC-2D DIC software.

Many thanks go to Mr. Danick Charbonneau and Mr. Jean-Christophe Lacasse, technicians at the Rock Mechanics Laboratory of the University of Sherbrooke, for their valuable cooperation. I also thank Mr. Alex Loignon for his support in setting up the DIC system.

I owe great thanks to my family, especially my mother, for her unlimited, unceasing, and loving support. The immense love and support of my incredible wife, Elaheh Oliaii, has been significant to completing this thesis.

TABLE OF CONTENTS

RÉSUMÉ i
ABSTRACT v
PUBLICATIONS ix
ACKNOWLEDGMENTS xi
TABLE OF CONTENTS xiii
LIST OF FIGURES xvii
LIST OF TABLES xxiv

CHAPTER 1: INTRODUCTION 1
1.1. Problem Statement 1
1.1. Tensile Strength of Rocks and Rock-like Materials 5
1.1.1. Direct Tensile Test 5
1.1.2. Indirect Tension Test 7
1.2. Scientific Gaps 10
1.3. Hypotheses 10
1.4. Objectives 11
1.5. Thesis Contributions 11
1.6. Thesis Outline 12

CHAPTER 2: EXPERIMENTAL PROGRAM 15
2.1. Experimental Approach 15
2.1.1. Materials and Specimen Preparation 16
2.1.2. Experimental System and Testing Methodology 19

CHAPTER 3: OBSERVATION OF FRACTURE PROCESS ZONE AND PRODUCED FRACTURE SURFACE ROUGHNESS IN GRANITE UNDER BRAZILIAN SPLITTING TESTS 30
Résumé 31
Abstract 32
3.1. Introduction 32
3.2. Methodology 34
3.2.1. Materials and Specimen Preparation 34

3.2.2. Experimental System and Testing Methodology 35
3.3. Experimental Results 38
3.3.1. Tensile Strength and Behaviour 38
3.3.2. Temporal Evolution of Damage 40
3.3.3. Observation of Fracturing Processes 41
3.4. Discussion 58
3.4.1. Acoustic vs. Visual Observation of Fracturing Processes 58
3.4.2. Effects of Time-dependent Loading on FPZ and Fracture Roughness 60
3.5. Conclusions 61

CHAPTER 4: MICRO-SCALE FRACTURING MECHANISMS IN ROCKS DURING TENSILE FAILURE 64

Résumé 65
Abstract 65
4.1. Introduction 66
4.2. Experiments 70
4.2.1. Materials and Specimen Preparation 70
4.2.2. Experimental Setup 71
4.3. Results 74
4.3.1. Direct vs. Indirect Tensile Strength 74
4.3.2. Acoustic Observation of Tensile Fracturing 76
4.3.3. Visual Observation of Tensile Fracturing 84
4.4. Discussion 89
4.4.1. Macro- and Micro-scale Fracturing 89
4.4.2. Implication to Field Applications 92
.4.5 Conclusions 93

CHAPTER 5: TENSILE STRENGTH AND FAILURE BEHAVIOUR OF ROCK-MORTAR INTERFACES: DIRECT AND INDIRECT MEASUREMENTS 96

Résumé 97
Abstract 97
5.1. Introduction 98
5.2. Materials, Specimens, and Experimental Procedure 100
5.2.1. Materials and Specimen Preparation 100

5.2.2. Experimental System and Testing Methodology 101
5.3. Experimental Results 105
5.3.1. Tensile Strength 105
.5.3.2 Acoustic (AE) and Visual (DIC) Observations of Fracturing Processes .. 106
5.3.3. AE Microcracking Source Mechanisms 111
5.3.4. Fracture Surface Roughness Characterization 114
5.4. Discussion 117
5.4.1. Tensile behavior of RM specimens under direct vs. Brazilian tensile tests 117
5.4.2. Limitations and future studies 119
5.5. Conclusions 120

CHAPTER 6: CONCLUSIONS, LIMITATIONS, AND RECOMMENDATIONS 123

6.1. Conclusions (Français) 123
6.2. Conclusions (English) 126
6.3. Research Limitations 128
6.4. Recommendations 129

APPENDICES 132

APPENDIX 1: Roughness measurement procedure 132
APPENDIX 2: Analysis of variability and reproducibility of results 136
APPENDIX 3: All tested samples and their corresponding data 151

REFERENCES 200

LIST OF FIGURES

Fig. 1.1 The relationship between BTS and DTS for granite found in the literature..... 3
Fig. 1.2 The relationship between BTS and DTS for different rock types (from Perras and Diederichs (2014) [22])..... 3
Fig. 1.3 Loading configurations in direct tension test a) split grips for dog-bone shaped specimens, b) glued end caps for cylindrical specimens, c) biaxial extension, and d) compression to tension load converter. A is the area, and LVDT denotes Linear Variable Differential Transformer for measuring the displacement..... 6
Fig. 1.4 Typical loading configurations for Brazilian test, a) curved loading jaws [92], b) flat loading platens [116], c) steel loading arcs [117], d) flat loading platens with small diameter cylinders [118], e) ISRM suggested device with a cushion [119], f) ASTM suggested method with a cushion [104], and g) flatten Brazilian disc [120]. R_d and R_j are the radius of the specimen and the jaws, respectively. 8
Fig. 1.5 Loading configuration in the Brazilian test 10
Fig. 2.1. An overview of the employed experimental approach in the current study 15
Fig. 2.2. Overview of the prepared samples for this study 16
Fig. 2.3. (a) specimen types and shapes and (b) specimen preparation procedure 18
Fig. 2.4 (a) Servo-controlled material testing system (MTS) equipment used for implementing Brazilian tests and (b) INSTRON 4482 dual-column Universal Testing machine for implementing direct tensile test 19
Fig. 2.5 Photograph of MISTRAS μ-SAMOS acoustic emission equipment..... 21
Fig. 2.6 Imaging system setup for the 2D DIC method 25
Fig. 2.7 Schematic diagram of (a) reference subset in the undeformed image, (b) the corresponding deformed subset in a deformed image, and in-plane displacements (u, v) and deformation of the subset. 26
Fig. 2.8. A granite-mortar specimen with three strain gauges installed over its back surface. 28
Fig. 3.1. (a) Schematic view of standard Brazilian jaws, (b) AE sensor positioning on the specimen, (c) The arrival time determined using the AIC function, AIC values in red, and the AE waveform in black. The time corresponding to the minimum of the AIC function yields the arrival time, as depicted in the inset. 37
Fig. 3.2. Load-displacement curves for all tested Brazilian discs up to the peak loads. The inset shows the Brazilian tensile strength of specimens. Specimens GI-1 to GI-3 have been tested with a loading rate of 1 μm/sec (high-loading rate), and Specimens GII-1 to GII-3 have been tested with a loading rate of 0.1 μm/sec (low-loading rate). The higher the loading rate, the higher the tensile strength. 39
Fig. 3.3. Macroscopic failure pattern of (a) GI-1 representing the group 1 specimens with a loading rate of 1 μm/sec (high-loading rate) and (b) GII-1 representing the group 2 specimens with a loading rate of 0.1 μm/sec (low-loading rate) in Brazilian tests. The blue lines represent the macro fracture path at the failure in the corresponding load-displacement curves shown in Fig. 3.2. 40

Fig. 3.4. Load-displacement curve with AE hits, cumulative hits, and cumulative energy for (a) specimen GI-1 with a loading rate of 1 μm/sec (high-loading rate) and (b) specimen GII-1 with a loading rate of 0.1 μm/sec (low-loading rate). F_p denotes the failure load. Four loading stages exist for both specimens, and the microcracking process initiates from the third stage. 41
Fig. 3.5. Spatiotemporal evolution of the AE events within the specimen GI-1 with a loading rate of 1 μm/sec (high-loading rate) at monitoring points (a) point A, (b) point B, (c) point C, and (d) point D. The size and the color of circles represent the magnitude of the events. AEs appear from the beginning of the third stage and are almost evenly distributed throughout the vertical diameter of the specimen. That is, microcracks occurred throughout the vertical diameter of GI-1. 43
Fig. 3.6. Spatiotemporal evolution of the AE events within the specimen GII-1 with a loading rate of 0.1 μm/sec (low-loading rate) at monitoring points (a) point A, (b) point B, (c) point C, and (d) point D. The size and the color of circles represent the magnitude of the events. AEs appear from the beginning of the third stage and are mostly distributed in the middle part of the specimen along the loading diameter. That is, microcracks are mostly concentrated in the middle of GII-1. 44
Fig. 3.7. Spatial distribution of AE events at failure load detected by a minimum of 6 sensors decomposed into different focal mechanisms for specimens tested under a loading rate of 1 μm/sec (high-loading rate): GI-1 (upper panel) and GI-2 (lower panel). The color codes represent the average focal amplitude (A_0) of AEs. The leftmost column indicates all detected AE events, while the other three columns show the distribution of tensile, compressive, and shear AE sources. 45
Fig. 3.8. Spatial distribution of AE events at failure load detected by a minimum of 6 sensors and AE focal mechanisms for specimens tested under a loading rate of 0.1 μm/sec (low-loading rate): GII-1 (upper panel) and GII-2 (lower panel). The color codes represent the average focal amplitude (A_0) of AEs. The leftmost column indicates all detected AE events, while the other three columns show the distribution of tensile, compressive, and shear AE sources. 46
Fig. 3.9. Horizontal plastic strain field immediately prior to failure (point D in Fig. 3.4) for (a) specimen GI-1 with a loading rate of 1 μm/sec (high-loading rate) and (b) specimen GII-1 with a loading rate of 0.1 μm/sec (low-loading rate), and scatter plot of AE distributions colored by density for (c) specimen GI-1 and (d) specimen GII-1 (darker shades of red indicate higher concentrations of AE events). 49
Fig. 3.10. Horizontal plastic strain (εxxp) development in the ROI during the loading process for specimen GI-1 (high-loading rate). The plastic strain begins to appear at the beginning of the third stage and mostly accumulates in a narrow strip along the loading direction. 50
Fig. 3.11. Horizontal plastic strain (εxxp) development in the ROI during the loading process for specimen GII-1 (low-loading rate). The plastic strain begins to appear at the beginning of the third stage and accumulates in the broader area (compared to GI-1 in Fig. 3.10) along the loading direction. 51

Fig. 3.12. (a) the location of the monitoring points in the ROI for GI-1 with a loading rate of 1 μm/sec (high-loading rate), and the evolution of the total horizontal strain (b) and the horizontal plastic strain component (c) at monitoring points. A comparison between (b) and (c) shows that GI-1 underwent elastic deformation in the second loading stage, and plastic deformation begins to accumulate from the beginning of the third stage. The accumulation rate of plastic strain increased dramatically in the last loading stage, which lasted a very short time. 53
Fig. 3.13. (a) the location of the monitoring points in the ROI for GII-1 with a loading rate of 0.1 μm/sec (low-loading rate), and the evolution of the total horizontal strain (b) and the horizontal plastic strain component (c) at monitoring points. A comparison between (b) and (c) shows that GII-1 underwent elastic deformation in the second loading stage, and plastic deformation begins to accumulate from the beginning of the third stage. The accumulation rate of plastic strain increased dramatically in the last loading stage, which lasted a very short time. 54
Fig. 3.14. The 3D surface of the macroscopic fractures for (a) GI-1 with a loading rate of 1 μm/sec (high-loading rate) and (b) GII-1 with a loading rate of 0.1 μm/sec (low-loading rate). The lower the loading rate (GII-1), the higher the surface roughness of the main fracture. 55
Fig. 3.15. Histogram of absolute asperity height over the fracture surface for (a) GI-1 with a loading rate of 1 μm/sec (high-loading rate) and (b) GII-1 with a loading rate of 0.1 μm/sec (low-loading rate). The colors represent various percentiles of height distribution. The insets are the histogram of the complete height distribution of asperities; positive and negative numbers indicate picks and valleys, respectively. The lower the loading rate (GII-1), the higher the surface roughness of the main fracture. 56
Fig. 3.16. Roughness parameters (a) D1d, (b) Ra, (c) Rp, (d) Rq, (e) Z2s, and (f) SF of the macroscopic fractures for GI-1 with loading rate of 1 μm/sec (high-loading rate) and GII-1 with loading rate of 0.1 μm/sec (low-loading rate). The blue and red arrows in each subplot indicate the average values of the corresponding roughness parameters for the first and second groups of specimens. The lower the loading rate (GII-1), the higher the surface roughness of the main fracture. 56
Fig. 3.17. Average power spectrum (red line) of the fracture surface of (a) GI-1 with a loading rate of 1 μm/sec (high-loading rate) and (b) GII-1 with a loading rate of 0.1 μm/sec (low-loading rate). Each gray line represents the power spectra of a 2D profile extracted from the corresponding fracture surfaces. 57
Fig. 3.18. Contour plot (left plots) of AE events and the fracture surface plots (right plots) for (a) GI-1 with loading rate of 1 μm/sec (high-loading rate) and (b) GII-1 with loading rate of 0.1 μm/sec (low-loading rate). The color bar at the bottom is associated with the fracture surface plots. The size of the circles shows the relative amplitude of the AEs superimposed over the fracture surface plots. There seems to be no clear correlation between the spatial distribution of AEs and the surface roughness of the main fractures. 58
Fig. 4.1 Schematic view of (a) a disc specimen mounted on standard Brazilian jaws and (b) a prismatic specimen glued to loading platens. Locations of AE sensors for (c) Brazilian specimens and (d) specimens tested under direct tension. 71

Fig. 4.2 Load-displacement curves for (a) Brazilian specimens, (b) specimens under direct tensile loading, and (c) the direct and Brazilian tensile strength of granite from literature: (A) Mellor and Hawkes [63], (B) Ramana and Sarma [65], (C) Alehossein and Boland [61], (D) Liu et al. [10], (E) Perras and Diederichs [22], (F1, and F2) Cacciari and Futai [62], (G) Qi et al. [64], (H) Efe et al. [31], and (I) this study. The blue and red dashed lines represent the average values of Brazilian and direct tensile strengths..... 75
Fig. 4.3 Continuous AE waveform recorded during fracturing process for (a) B1 and (b) D1. The plots show the waveform for (i) the entire loading time, (ii) 25 seconds before the failure load, (iii) 2 seconds before the failure load, and (iv) a representative waveform at the failure point. 76
Fig. 4.4 AE events amplitude, cumulative AE events, and loads of the specimens (a) B1, (b) B2, (c) D1, and (d) D2 throughout the loading process. 78
Fig. 4.5 Spatial distribution of AE events at failure load detected by a minimum of 6 sensors and AE focal mechanisms for B1 (upper panel) and B2 (lower panel). Shear cracking mechanism is predominant in specimens tested under Brazilian loading..... 80
Fig. 4.6 Spatial distribution of AE events at failure load detected by a minimum of 6 sensors and AE focal mechanisms for D1 (upper panel) and D2 (lower panel). The tensile cracking mechanism is predominant in specimens tested under direct tensile loading. However, shear microcracks' contribution to the formation of the macro fracture is still significant. 81
Fig. 4.7 Cumulative histogram of the temporal distribution of AE events of different focal mechanisms for (a) B1, (b) B2, (c) D1, and (d) D2 during the loading process. The crack initiation is almost equally composed of tensile and shear cracking mechanisms for both Brazilian and direct tensile loadings. However, from the middle of the second loading stage, microcracks become predominantly shear for Brazilian loading and tensile for direct tensile loading. 82
Fig. 4.8 Spatial distribution of AE events at failure load detected by a minimum of 6 sensors and AE focal mechanisms for mortar specimens tested under Brazilian (upper panel) and direct tensile (lower panel) loading. Reducing the grain size increased the contribution of tensile microcracks in the Brazilian specimen (compare 60% in Fig. 4.8b with 25% and 20% in Fig. 4.5b and f). Removing the confinement factor further increased the contribution of tensile microcracks in specimens tested under direct tension (compare 100% in Fig. 4.8f with 47% and 63% in Fig. 4.6b and f). 83
Fig. 4.9 Plastic strain field at failure (upper panel) and AE density plot at failure (lower panel) for (a) B1, (b) B2, (c) D1, and (d) D2. Darker shades of red indicate higher concentrations of AE events in AE density plots. Overall, the zones of the highest strain concentration (upper panel) coincide well with the zones of the highest AE density (lower panel). However, the AE-based process zones (lower panel) are slightly larger than the DIC-based process zones. 86
Fig. 4.10 Histograms of total extensile strain distribution in the ROI at different loading stages: εxx (horizontal strain) for (a) B1 and (b) B2, and εyy (vertical strain) for (c) D1 and (d) D2. Positive (+) and negative (−) strains represent tension and compression, respectively. The loading stages 1, 2, and 3 for each specimen are shown in Fig. 4.4. With

the applied load, the heterogeneity in the tensile strain field (zones of tensile strain concentration) progressively developed in both Brazilian and direct tensile specimens, as reflected by the wider and shorter histograms in stages 2 and 3. 87
Fig. 4.11 Histograms of shear strain (εxy) distribution in the ROI at different loading stages for (a) B1, (b) B2, (c) D1, and (d) D2. The loading stages 1, 2, and 3 for each specimen are shown in Fig. 4.4. With the applied load, the heterogeneity in the shear strain field (zones of shear strain concentration) progressively developed in B1 and B2, as reflected by the wider and shorter histograms in the stages 2 and 3 in Fig. 4.11a and b. However, there is no significant change in the spread of the shear strain histogram for D1 and D2, suggesting that shear microcracking may not have played an essential role in the fracturing process of specimens D1 and D2. 88
Fig. 4.12 A simplified representation of the load configuration and the induced normal and shear stresses at grain scale for (a) Brazilian and (b) direct tensile loading. Applied external load induces compressive and tensile normal stresses over grain boundaries in Brazilian and direct tensile loading, respectively (Adapted from Nicksiar and Martin [243] and Qi et al. [64]). 90
Fig. 4.13 Surface roughness geometry of the created macroscopic fractured after specimen failure for Brazilian specimens (a) B1, (b) B2, (c) MB (Brazilian mortar disc), and specimens tested under the direct tensile loading (d) D1, (e) D2, and (f) MD (mortar specimen subjected to the direct tension), and (h) average Z2 value of the created fracture in x and y directions for all specimens. The rougher surfaces suggest that there would be some shear sliding along the walls of two semi-samples when they are splitting apart under the action of the tensile load. 91
Fig. 4.14 Direct tensile test on materials with coarse and fine grain sizes. A 2D roughness profile for (a) granite (coarse grain material) and (b) mortar (fine grain material). Due to the larger grain size in granite, the induced tensile damage is accompanied by some shear sliding along the grain boundaries. For mortar, shear sliding is basically absent. 92
Fig. 5.1 Specimens' dimensions, the location of AE sensors, and the speckle pattern created over the front face of specimens for (a) the Brazilian test and (b) the direct tension test. 102
Fig. 5.2 Load-axial displacement of (a) B and (b) D specimens. The insets show the tensile strength values. 106
Fig. 5.3 Instantaneous hits, cumulative hits, and load against the normalized time $(t/t_{max})*100$ for (a) B1 and (b) B2. 106
Fig. 5.4 (a)-(e) AE and DIC results for B1 corresponding to points P1 to P5 (shown in Fig. 5.3a). Upper panel: Full-field major principal strain (ε_1) obtained by DIC, and lower panel: Spatial distribution of AE events; the blue line represents the observed macroscopic fracture path, and (f) the specimen's failure patter and its interfacial failure morphology. The AEs are also projected over the interface in (f), and the black lines indicate the mortar remaining on the granite's surface. 108
Fig. 5.5 Instantaneous hits, cumulative hits, and load vs. the percentage of the normalized time $(t/t_{max})*100$ for (a) D1 and (b) D2. 110

Fig. 5.6 (a)-(d) AE and DIC results for D1 corresponding to points P1 to P4 (shown in Fig. 5.5a). Upper panel: Full-field major principal strain (ε_1) obtained by DIC, and lower panel: spatial distribution of AE events; the blue line represents the observed macroscopic fracture path, and (e) the specimen's failure patter and its interfacial failure morphology. The AEs are also projected over the interface in (e), and the black lines indicate the mortar remaining on the granite's surface. 111
Fig. 5.7 Spatial distribution of AE events at failure and AE focal mechanisms for B1. (a) AE events with at least 6 P-wave arrivals, (b) tensile microcracks, (c) compressive microcracks, and (d) shear microcracks. The color bar corresponds to the average focal amplitude (A_0) of AEs (Eq. 5.2), where the unit of the amplitude is V. Granite is on the right side of the disc and mortar is on the left. 113
Fig. 5.8 Spatial distribution of AE events at failure and AE focal mechanisms for D1. (a) AE events with at least 6 P-wave arrivals, (b) tensile microcracks, (c) compressive microcracks, and (d) shear microcracks. The color bar corresponds to the average focal amplitude (A0) of AEs (Eq. 5.2), where the unit of the amplitude is V. 114
Fig. 5.9 Interface's surface roughness geometry of generated macro fracture for (a) B1: mortar, (b) B1: granite, (c) D1: mortar, and (d) D1: granite. 115
Fig. 5.10 Histogram of absolute asperity height over the fracture surface for (a) B1 and (b) D1. The minimum, maximum, mean, and standard deviation of asperity heights, as well as the Z2 values, are given in (a) and (b). Average power spectrum (red line) of the fracture surface of (c) B1 and (d) D1. Each blue line represents the power spectra of a 2D profile extracted from the corresponding fracture surfaces. The Hurst exponent (H) and fractal dimension (D) values are also indicated in (c) and (d). All roughness parameters and plots suggest that the fracture surface was rougher in the specimen subjected to direct tension than that subject to the Brazilian tensile test. 116
Fig. 5.11 Stress states at typical failure modes of rocks [2], [44]. In the Brazilian specimen, normal compressive stress acts over the surface of the microcracks due to the applied compressive load, meaning that these microcracks may be produced under the confined tension failure mode (i.e., the blue circle). In contrast, microcracks in the specimen under direct tension are predominantly produced in the uniaxial tension failure mode (i.e., the red circle). Microcracks that fail in confined tension (Brazilian) have a greater shear strength than those that fail in uniaxial tension resulting in a higher overall tensile strength. 119

LIST OF TABLES

Table 3.1. Mechanical and physical properties of Stanstead granite 35
Table 4.1. Mechanical and physical properties of Stanstead granite ... **Erreur ! Signet non défini.**
Table 5.1 Mechanical and physical properties of Stanstead granite and mortar 103

CHAPTER 1: INTRODUCTION

INTRODUCTION

1.1. Problem Statement

Crystalline rocks contain numerous micro-defects, such as intra-crystalline cracks (cleavage) and grain boundaries [1]. Under various types of applied external loads, microcracks nucleate and propagate in rocks in a localized region around pre-existing micro-flaws called the fracture process zone (FPZ) [2]–[9]. The development of the FPZ or new fracture network in rocks not only impacts their mechanical properties (e.g., strength) but also affects their hydraulic characteristics (e.g., permeability) [10].

As discussed in many relevant studies, the initiation, propagation, and coalescence of cracks in FPZ at the microscopic scale cause the formation of macroscopic fractures, leading to rock failure [11]–[15] [2], [4], [16]–[20]. Failures of large-scale geotechnical, mining, or civil engineering structures cause substantial safety hazards, material damage, and postponement or even cessation of civil and mining services [21]. Numerous researchers have noted that many of such large-scale macroscopic failure processes are controlled by the tensile capacity of rocks [22]–[27]. The tensile strength of rocks is often less than the shear strength and much lower than the compressive strength, reflecting the critical role of tensile strength in planning, design, and analysis of engineering practice involving rocks [22], [24], [25]. For instance, the tensile strength of rocks controls the failure of rocks and rock masses in underground excavations such as mining roofs and galleries [28]–[30]. It is an indispensable property in rock fracturing, crushing, tunnel boring, drilling, and blasting [29], [31]–[34]. Tensile strength is also one of the most important parameters for hydraulic fracturing design, as it governs the stability of boreholes and determines the minimum borehole pressures for the hydraulic fracturing process [35]–[37].

Furthermore, the growth and coalescence of microcracks in the PFZ may lead to the formation of conduits for fluid migration in rock, which could positively or negatively impact different rock engineering applications. For example, in the geological disposal of radioactive waste projects, the created fracture network (or FPZ) may provide a pathway for the leakage of radioactive wastes through surrounding rocks, negatively affecting the project's safety [38]. On the other hand, in hydraulic fracturing for shale gas or geothermal energy extraction, the main goal is to increase the hydraulic permeability of rocks by

producing a fracture network [39]–[41]. Therefore, a larger FPZ can reflect a more successful hydraulic fracturing design.

In general, there are three basic loading modes defined in rock fracture mechanics, including tensile mode (Mode I), sliding or in-plane shear mode (Mode II), and tearing or anti-plane shear mode (Mode III) [42], [43]. The stress state at cracks/flaws tip in geomaterials may be a combination of shear, compression, and tension, causing cracks to propagate under tensile, shear, or a combination of tensile and shear mechanisms. This is especially true in rocks [43]–[45]. Moreover, because rock materials are weak in tension and strong in compression and shear, the microcracking processes and mechanisms under Mode I loading are of primary interest in rocks [22], [25], [42].

Therefore, obtaining a reliable measure of strength and fracturing process in rocks under tensile loading is essential in different fields such as geotechnical engineering (e.g., designing rock slopes and underground excavations) [46], mining (e.g., rock blasting and fragmentation) [11], and hydraulic fracturing [12], [47].

The development of the PFZ and its effect on rock behaviour has been extensively investigated [2], [45], [48]–[54]. Most of the previous studies, however, approached the fracturing behaviour of rocks under compression [55]–[57] and shear loading [58], [59]. Comparatively, fewer data on rock strength and fracturing behaviour under tensile loading is available. In fact, the mechanisms governing nucleation and growth of FPZ are still not well understood. In particular, the literature has not fully addressed mechanisms and the spatiotemporal evolution of microcracks in the process zone under tensile loading.

In addition to the created FPZ (fracture network), the fracture surface roughness of the produced macro-fractures affects the fluid flow in the fractured rocks [60]. However, the relationship between the fracture processes zone, fracture roughness, and the microdamage evolution mechanism under tensile loading is not still evaluated in the literature.

In general, the mechanical behaviour of rock materials under tensile loading is assessed using two testing methods: 1) direct and 2) indirect tensile tests (e.g., the Brazilian test). These methods are further explained in Section 1.1.1.

Many researchers have stated that the tensile strength of rocks obtained from the Brazilian test overestimates their true tensile strength, which is determined by the direct tension test [10], [22], [31], [61]–[65]. Fig. 1.1 illustrates the relationship between the direct tensile strength (DTS) and the Brazilian tensile strength (BTS) of granite in the literature. On average, the DTS of granite is 83% of its BTS. In addition, based on a comprehensive literature review, Perras and Diederichs (2014) [22] reported that the average ratio of BTS/DTS for metamorphic, igneous, and sedimentary rocks is 0.9, 0.8, and 0.7, respectively (Fig. 1.2).

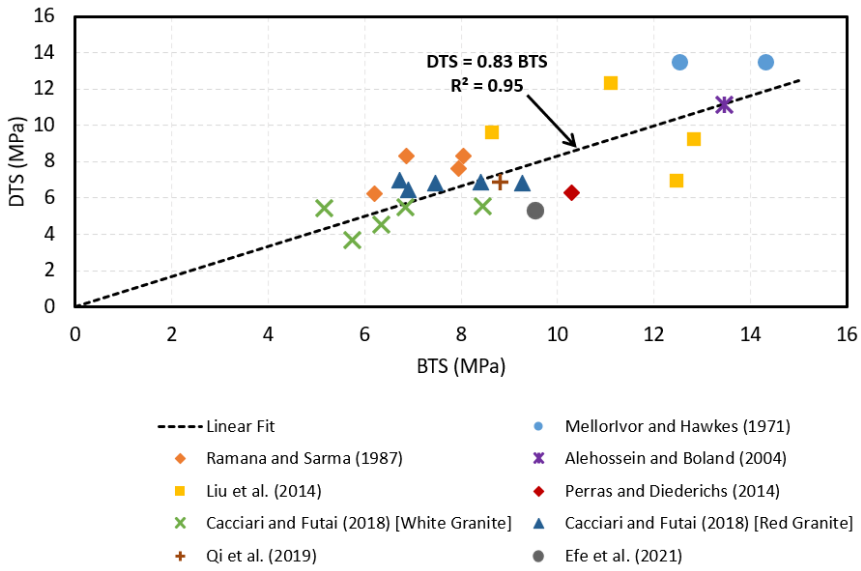

Fig. 1.1 The relationship between BTS and DTS for granite found in the literature.

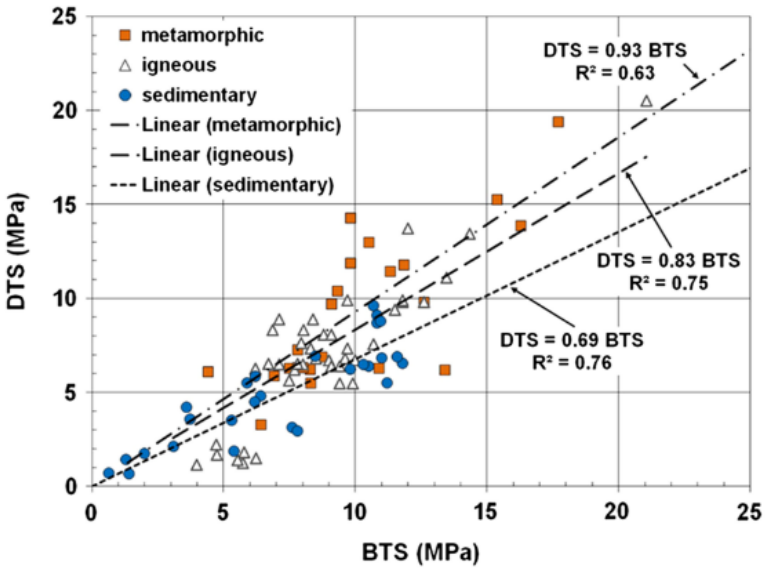

Fig. 1.2 The relationship between BTS and DTS for different rock types (from Perras and Diederichs (2014) [22]).

The difference between the BTS and DTS of rocks has been attributed to different stress states in direct and Brazilian tensile loadings [66] and the effect of pre-existing micro flaws in rocks [64], [67]. While these findings may explain the macroscale response of rocks under tensile loadings, the fundamental explanation of rocks' behaviour subjected to tensile loading is still missing. Notably, previous studies have not explained this discrepancy from

a microscopic point of view, as macroscopic failure/strength of rocks depends on microscopic damage.

Tensile strength and tensile fracturing behaviour are also critical parameters controlling failure processes of rock-concrete (RC) structures [22], [24], [25]. For instance, the tensile strength existing in the dam-foundation interface resists the overturning moment at the toe zone of the dam due to the acting forces of the reservoir [68], [69]. In addition, the tensile failure at the rock-shotcrete interface is the source of instabilities and the failure mode for the shotcrete, which, in turn, can influence the overall structure stability [70]–[73]. Furthermore, the tensile strength and behaviour at the cement-caprock interface are crucial factors controlling leakage in wells in the oil and gas industry [74], [75]. Therefore, to provide a safe design of elements incorporating RC interfaces, obtaining a reliable understanding of the tensile behaviour of such bi-material interfaces and its impact on the fracturing process of the whole structure is essential.

During the last decades, numerous studies have investigated the mechanical behaviour of RC interfaces under compression [76], [77] and shear loading [58], [78]–[82]. However, very few studies have focused on the tensile interaction mechanism and tensile strength of the RC interfaces.

The literature review outlines that the failure properties and the BTS of RC specimens subjected to the Brazilian loading are controlled by various parameters, including the interface roughness, interface inclination angle, rock type, and concrete properties [70], [71], [76], [83]–[85].

Some studies have reported that the BTS of bi-material specimens increases with the interface's roughness [70], [71], [83], [85]. According to Zhu et al. [70] and Qiu et al. [85], increasing the interface's roughness increases the contact area and the interlocking effect (anchorage) between rock and concrete along the interface, contributing to an increase in the BTS of RC Brazilian discs. Luo et al. [83] observed that the BTS of the RC interface is governed by a combined contribution of adhesion loss and cohesion loss. The adhesion loss occurs when rock and concrete semi-samples are detached exactly along their interface without any failure in the interface asperities. While in cohesion loss, failure occurs at the asperities root either in the concrete or the rock.

The BTS of RC interfaces is also affected by the properties of the rock and the concrete constituents. Chang et al. [71], Selçuk and Aşma [76], and Zhu et al. [70] showed that the increase of the concrete strength increases the BTS of bi-material discs. According to Selçuk and Aşma [76] and Zhu et al. [70], the concrete constituents and the degree of hydration of the cement produce different adhesion between rock and concrete that affect the BTS of specimens. Moreover, the mechanical properties of rocks seem to have a negligible effect on the BTS of bi-material specimens [70], [85]. On the contrary, the interface adhesive strength is affected by the physical properties of rocks, ex., the porosity. For instance, concrete adheres much more to sandstone than granite and marble, resulting

in a higher adhesion between sandstone and concrete, thereby, a higher BTS of RC interface [70].

The effect of the interface on the DTS of RC specimens has rarely been studied. Bauret and Rivard [86] studied the effect of interface roughness on the DTS of bi-material cylindrical specimens composed of high-strength mortar – low-strength mortar. Their results indicated that bond strength increases with roughness. A few researchers have simply reported the DTS of RC specimens without examining the effect of different parameters on the DTS [69], [72], [77], [80], [87]. An important conclusion is that the RC interface has a smaller, yet considerable, DTS compared to intact rock and concrete [69], [80]. In some cases, RC interfaces yielded a DTS at the same level as the intact concrete [87].

Son [72] studied the adhesion strength at the granite-concrete interface using direct and indirect tensile tests. Their experiments resulted in an average DTS of 0.95 MPa and an average BTS of 2.35 MPa, with a DTS/BTS ratio of 0.4. Therefore, they reported that the RC interface's adhesion (tensile) strength is a highly test-method-dependent parameter.

The few existing studies on the tensile behaviour of RC interfaces are primarily aimed at evaluating the macroscopic fracture characteristics of RC materials. To the best of the author's knowledge, no study has investigated the microcracking mechanisms of RC interfaces under direct and Brazilian tensile loading and their effect on the macro fracturing behaviour and tensile strength. Besides, while the relationship between DTS and BTS of "intact" rocks has been investigated to some extent, the research on the relationship between the direct and indirect tensile strength of RC interfaces and their tensile fracturing behaviour remains lacking, especially at the microscopic scale.

1.1. Tensile Strength of Rocks and Rock-like Materials

1.1.1. Direct Tensile Test

The direct tension test provides the most reliable and representative results of the tensile strength of materials [88], [89]. As Perras and Diederichs (2014) [22] reported in their recent review paper, the most common test configurations of the direct tension test include a) split grips for dog-bone-shaped specimens, b) glued end caps for cylindrical specimens, c) biaxial extension and, d) compression to tension load converter (Fig. 1.3).

The dog-bone shape specimens are usually tested by grips, which pull the lips of the specimen apart at a constant rate of elongation (Fig. 1.3a). In a valid direct tensile test, the fractures should occur at the centre of the specimen. However, in the dog-bone shape tensile test, the grips may induce non-real stress concentrations at the ends of the specimen near the grips. The highly concentrated stress may cause plastic deformation of the gripped portion of the sample, causing an improper measurement of the tensile strength [22], [90].

To reduce the stress concentration, the direct tensile test can be implemented by directly gluing the loading caps of the same diameter to the specimen (Fig. 1.3b) [22], [33], [91].

This method is the standardized procedure for the direct tension test suggested by the International Society for Rock Mechanics (ISRM) [92].

In both tests mentioned above, the direct tensile strength (DTS) is measured by dividing the maximum applied load by the initial cross-sectional area of the central part of the specimens.

A pervasive problem with the tensile test methods of fixed grips (Fig. 1.3a) and glued caps (Fig. 1.3b) is that the specimen may fail in torsion, not in tension, yielding invalid results. A solution to this problem is using the biaxial extension apparatus (Fig. 1.3c), in which the specimen is kept in the centre of the loading frame during the test [22].

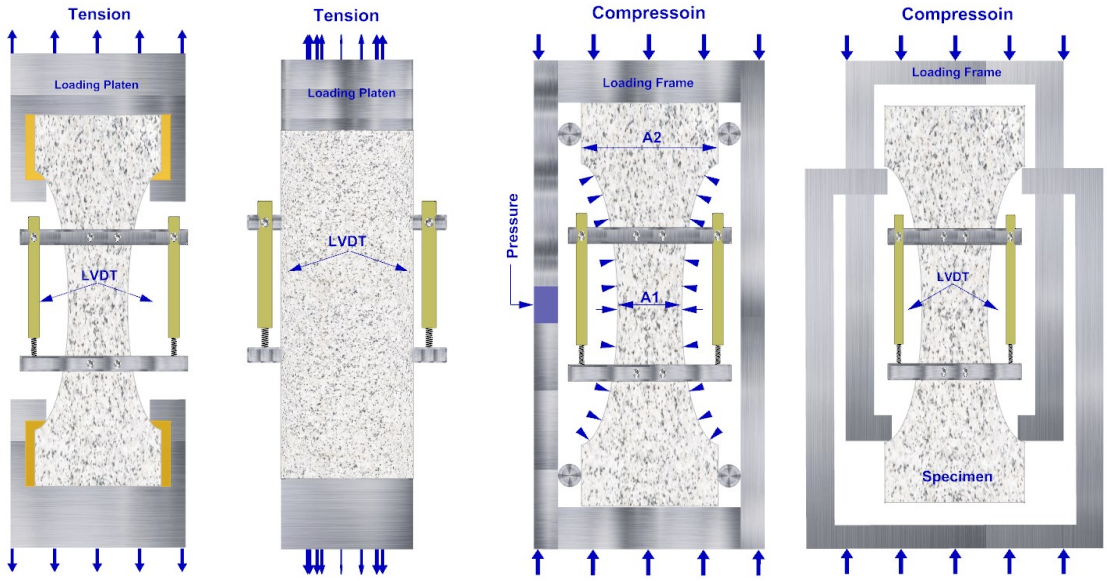

Fig. 1.3 Loading configurations in direct tension test a) split grips for dog-bone shaped specimens, b) glued end caps for cylindrical specimens, c) biaxial extension, and d) compression to tension load converter. A is the area, and LVDT denotes Linear Variable Differential Transformer for measuring the displacement.

The biaxial extension test is conducted in a conventional triaxial cell. The main difference between the biaxial extension test and the conventional triaxial compression test is that, in the latter, the major compressive principal stress is axial, and the confinement stress is the minor principal stress. In contrast, axial stress is the least compressive principal stress in the former. With this arrangement, the axial extension induced by the compressive confinement stress on the curved portion of the specimen (blue arrows in Fig. 1.3c) results in a tensile failure [22], [90]. Then, the direct tensile strength (DTS) can be calculated using Eq. 1.1;

$$\sigma_t = \frac{F}{A_1} - \frac{P(A_2 - A_1)}{A_1} \quad \text{Eq. 1.1}$$

Where F is the axial load at failure, P is the confining pressure, and A_1 and A_2 are the cross-sectional diameters at the centre and the head of the dog-bone shape specimen [22]. Without axial load, the biaxial extent test turns into a uniaxial tensile test [22], [91].

Finally, the load converter device developed by Gorski (1993) [93] and modified by Sippakorn (2010) [35] can be used to measure the tensile strength of rock-like materials (Fig. 1.3d). In this device, the applied compressive load is converted into a tensile load that extends a dog-bone-shaped specimen [22], [35], [93]. In this method, the tensile strength is computed as the ratio between the failure force and the area of the specimen's cross-section at its central part. For more details about the direct tensile test techniques, the reader can refer to [22], [33], [35], [88], [91], [93], [94].

1.1.2. Indirect Tension Test

Although the direct tensile test results in the most valid tensile strength of rock-like materials, there are difficulties with the sample preparation, especially for the dog-bone-shape samples and for weak rocks, and with implementing the complicated test setup [22], [33], [67], [95]. In addition, laboratories often do not have access to such loading devices [22]. Due to these drawbacks, researchers have developed several indirect methods as an alternative to the direct tensile test for determining the tensile strength of materials. Among the various indirect methods, only a few provide a reliable estimate of the true material tensile strength. These methods include the bending test, the Brazilian test (BT), the ring test (RT), and the hydraulic extension test (HE) [22], [33], [66], [96], [97]. Among them, the Brazilian test is the most widely used method to measure the indirect tensile strength of rock materials.

1.1.2.1. Brazilian Splitting Test

The Brazilian test is the most desirable alternative to the direct tensile test. This test was first introduced independently by Carneiro (1943) [98] and Akazawa (1943) [99] for use in testing concrete [22], [66], [100]. Sixteen years later, Berenbaum and Brodie (1959) [101] applied the Brazilian test for rock samples for the first time [22]. Since its advent, the Brazilian test has extensively been used in numerical, analytical, and experimental investigations of the tensile strength and the failure properties of brittle materials [22], [26], [33], [66], [67], [71], [76], [85], [96], [97], [102]–[115].

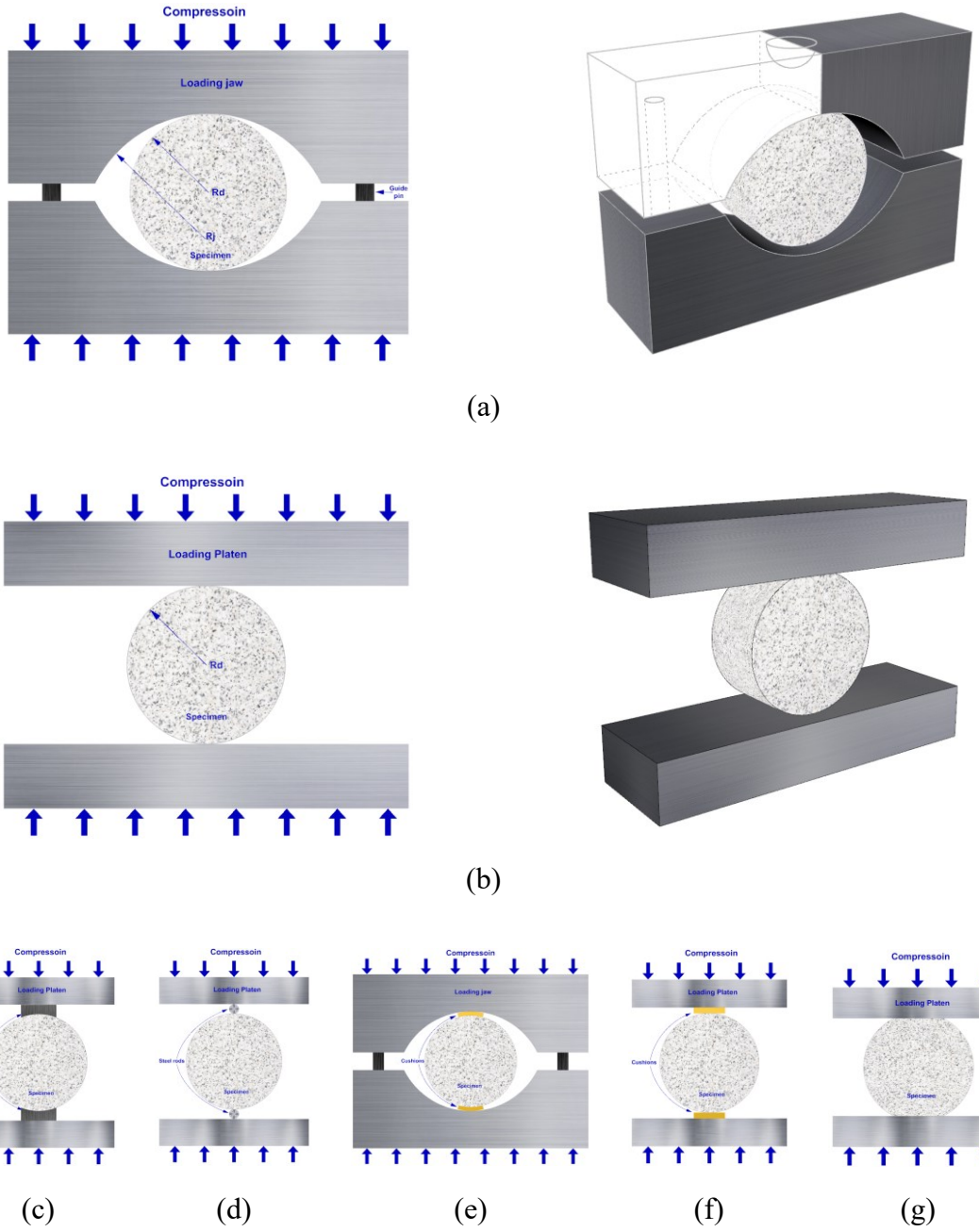

Fig. 1.4 Typical loading configurations for Brazilian test, a) curved loading jaws [92], b) flat loading platens [116], c) steel loading arcs [117], d) flat loading platens with small diameter cylinders [118], e) ISRM suggested device with a cushion [119], f) ASTM suggested method with a cushion [104], and g) flatten Brazilian disc [120]. R_d and R_j are the radius of the specimen and the jaws, respectively.

In the Brazilian test, a compressive load is applied along the diameter of a thin disc-shaped specimen, which induces local tensile stress in the transverse direction of the applied load.

Scholars have often used two major loading configurations for the Brazilian test: curved loading jaws [103], [121]–[123] and planar loading platens [103], [114], [121], [124]. The curved loading jaws with the ratio of the disc's radius R_d to that of the jaws R_j equal to 0.67, i.e., $R_j = 1.5R_d$ (Fig. 1.4a) corresponds to the standard loading arrangement adopted by ISRM (1978) [92]. Fig. 1.4c. depicts a special case of the curved jaws, so-called loading arcs, in which $R_j = R_d$ [66], [97], [117]. The flat loading platens (Fig. 1.4b) is the procedure standardized by ASTM (2016) [116]. A different form of the flat-loading platens is displayed in Fig. 1.4d., in which small metallic cylinders are placed between the disc and the platens [66], [118]. A common use of the curved and flat platens is shown in Fig. 1.4e and 1.4f, respectively, in which a soft material cushion is inserted between the specimen and the loading device to reduce the local stress concentration [104], [119]. The flattened Brazilian disc (Fig. 1.4g) is another special loading configuration of the Brazilian test, in which the compressive load is applied over two equal-width parallel planes in the sample [120], [125].

Both ISRM [92] and ASTM [116] standards have suggested Eq. 1.2 for calculating the Brazilian (indirect) tensile strength (BTS) of disc specimens:

$$\sigma_t = \frac{F_f}{\pi R t} \qquad \text{Eq. 1.2}$$

Where σ_t is the BTS (MPa), F_f is the applied load at failure (N), and R and t are the radius and the thickness of the specimen (mm), respectively. Although the Brazilian test is popular for its simplicity in specimen preparation and test procedure, Mellor and Hawkes (1971) [63] pointed out that this test produces failure in a biaxial, rather than a uniaxial, stress field; hence, the Brazilian test results may not represent the true tensile strength of specimens. In this regard, ISRM (1978) explains that: "*the justification for the test is based on the experimental fact that most rocks in biaxial stress fields fail in tension at their uniaxial tensile strength when one principal stress is tensile, and the other finite principal stress is compressive with a magnitude not exceeding three times that of the tensile principal stress*" [92].

The Brazilian test has several fundamental assumptions; violating any may cause the test to provide invalid results [63], [126], [127]. It is assumed that:

- Specimen material is homogenous, isotropic, and pre-peak linearly elastic;
- Applied compressive load is radial that is uniformly distributed over a certain angular width (usually, $\alpha \leq 15^o$) [63] at both ends of the loading diameter (Fig. 1.5);
- Compression induces tensile stresses perpendicular to the diametral loading direction, which is almost constant over a region about the centre [63] (Fig. 1.5);
- Tensile fractures initiate from the centre of the disc, where the maximum induced tensile stress occurs and propagates along the loading diameter [102], [117], [128];
- Maximum tensile stress along the loading line at failure is regarded as the Brazilian (indirect) tensile strength [63].

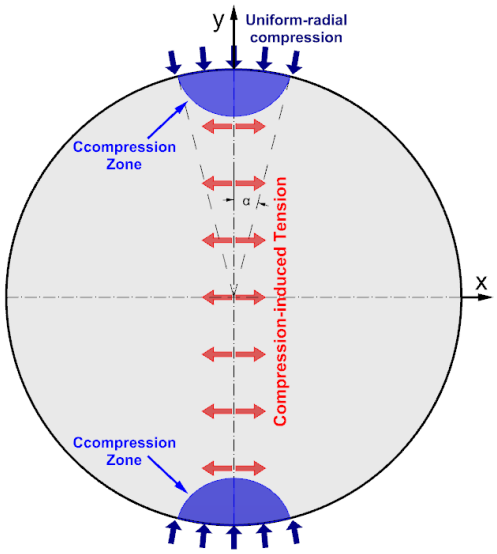

Fig. 1.5 Loading configuration in the Brazilian test

1.2. Scientific Gaps

In summary, the following scientific gaps were identified from the literature review (cited in Section 1.1 and CHAPTERS 3 to 5):

1. The mechanisms and the spatiotemporal evolution of microcracks in the process zone under tensile loading are still unclear and warrant further study.

2. The cause of the difference between micro- and macro- fracturing in rocks is not well understood yet.

3. The relationship between the FPZ, fracture roughness, and the microdamage evolution mechanism under tensile loading has rarely been investigated.

4. The literature has not addressed microcracking processes and mechanisms in rock-concrete interfaces.

1.3. Hypotheses

The thesis hypotheses are as follows:

1. The macroscopic failure/strength of crystalline rocks depends on the microscopic damage.

2. The loading rate affects granite's micro-fracturing mechanics, which governs the strength under tensile loading.

3. The roughness of the failure surfaces depends on the microcracking mechanisms associated with specific tensile loading conditions (rate and test set-up).

4. The micro-fracturing mechanics differ between indirect (Brazilian) and direct tensile loadings. It explains the difference between direct and indirect tensile strength values for intact and bi-material specimens.

5. The interface of bi-materials (granite-mortar) affects the distribution and mechanisms of microcracks.

1.4. Objectives

As explained above, there is still a lack of understanding of the fracturing properties in rock and rock-mortar materials under tensile loading, particularly at the microscale. Therefore, to validate the thesis hypotheses and to fill the abovementioned scientific gaps, the global objective of this research project is defined as follows:

Investigate the micro-fracturing processes and microcracking mechanisms in granite and granite-mortar specimens under direct and indirect (Brazilian) tensile loadings to further understand the parameters affecting the tensile strength and the macro-failure of such materials.

The following points summarize the specific objectives of this research:

1. Identify and describe the micromechanics of damage and the evolution of the fracture process zone in granite under indirect tensile loading.

2. Determine the effect of two loading rates on granite's micro- and macro-fracturing behaviour and strength under indirect tensile loading.

3. Characterize the roughness of the surface failure of granite specimens under two loading rates in indirect and direct tensile loads.

4. Identify and describe the micromechanics of damage in direct tensile loadings in an attempt to explain the difference between strength values obtained from direct and indirect tensile.

5. Identify and describe the micromechanics of damage at the granite-mortar interface subjected to tensile loading.

1.5. Thesis Contributions

This research stands out for its experimental nature in studying the rock and rock-like materials' fracturing and strength properties under tensile loading and delivering a better understanding of its behaviour through laboratory testing.

The originality of this study and contributions that are made through the completion of this thesis can be summarized as follows:

The Brazilian test has been the most frequently used experimental method for measuring the tensile strength of rock. Researchers have mainly studied the tensile behaviour of rocks macroscopically. The mechanisms governing the initiation and evolution of FPZ in specimens subjected to the Brazilian loading at the microscale are not fully understood yet. This thesis applied a combined AE-DIC technique to examine the micro-damage, microcracking mechanism, and evolution of the process zone in specimens under Brazilian loading.

This study investigated the effect of the loading rate on the characteristics of the fracture surface roughness produced by tensile failure of Brazilian discs. It argued how the complexity of a fracture is affected by the loading rate and grain size.

Many studies have revealed that the tensile strength of rock obtained from the Brazilian tensile test exceeds that obtained from the direct tensile test. Some researchers have attributed this difference to (1) the different loading configurations and (2) different cracking mechanisms at macro and micro scales in these testing methods. However, previous studies have failed to address (1) why and how cracking mechanisms differ at micro and macro scales and (2) how loading conditions affect micro-cracking processes during tensile failure. In this study, the Moment tensor inversion of AE events and DIC strain fields were simultaneously used to answer these questions. It was shown that the material type (coursed-grain granite vs. fine-grained mortar) and confinement stress (due to the biaxial stress field in the Brazilian test) govern the microcracking mechanisms, thereby the tensile strength of tested specimens.

The literature has shown that the direct tensile strength of intact rocks falls in the range of 70 to 90% of their Brazilian tensile strength. This relationship between the direct and indirect tensile strength of rock-mortar specimens has not been addressed yet. Moreover, the characteristics of microcracking mechanisms of rock-mortar interfaces and their effect on the tensile strength of such bi-materials have not been dealt with in depth. In this study, these knowledge gaps were further investigated. The tensile strength and fracturing behaviour of rock-mortar specimens under direct and indirect tensile loadings were evaluated by synthesizing the load-displacement measurements, AE, and AIC observations. It was attempted to determine how and why RC interfaces' tensile strength differs when subjected to direct and indirect tensile loadings.

1.6. Thesis Outline

This thesis is structured as a paper-based thesis consisting of five chapters and three appendices outlined below. A complete list of references is presented at the end of the thesis.

CHAPTER 1 introduces the topics to be discussed in this thesis and includes context, research objectives, originality of thesis, research methodology, and thesis outline.

CHAPTER 2 details the experimental program employed in this study, including materials, sample preparation, and experimental setup.

CHAPTER 3 examines the microcracking processes and the evolution of fracture process zone (FPZ) in granite under indirect (Brazilian) tensile loading at two different loading rates. Digital image correlation (DIC) and acoustic emission (AE) monitoring techniques were used for this purpose. In addition, the surfaced roughness characteristics of the generated macro fractures in Brazilian disc specimens under tensile loading are studied in this chapter. Furthermore, the potential link between the asperity height distribution over the produced fracture surfaces and the location and magnitude of the radiated acoustic emission (AE) events is discussed. This chapter has been published in "*Theoretical and Applied Fracture Mechanics*" and is entitled "*Observation of fracture process zone and produced fracture surface roughness in granite under Brazilian splitting tests*."

CHAPTER 4 takes an in-depth look at the microcracking processes and mechanisms within intact granite specimens under both direct and indirect (Brazilian) tensile loadings through AE and DIC techniques. The factors controlling the microcracking mechanisms in granite under direct and indirect tension are investigated to determine why cracking mechanisms differ at micro and macro scales (as reported in the literature). Also, the contribution of different microcracking mechanisms to the formation of the ultimate macro fracture, hence, to the overall tensile strength of granite specimens under direct and Brazilian tests, is discussed. This chapter was submitted as a revised version to "*Rock Mechanics and Rock Engineering journal*" on December 17, 2022, and is entitled "*Micro-scale fracturing mechanisms in rocks during tensile failure*."

CHAPTER 5 investigates the failure mechanisms and tensile strength of granite-mortar interfaces under direct and indirect (Brazilian) tensile loadings using AE and DIC techniques. This chapter attempts to determine how the tensile strength of rock-mortar interfaces obtained from the direct tensile test differs from that obtained from the Brazilian test. The effect of microcracking mechanisms on (1) the direct and indirect tensile strength of rock-mortar interfaces and (2) the surface roughness characteristics of the produced macro fracture in specimens under direct and indirect tensile loadings is discussed. This chapter was submitted as a paper to "*Journal of Rock Mechanics and Geotechnical Engineering*" on October 30, 2022, and is entitled "*Tensile strength and failure behaviour of rock-concrete interfaces: Direct and indirect measurements*."

CHAPTER 6 presents a general discussion of the key findings and a summary of conclusions and contributions made through this research.

APPENDIX 1 briefly indicates the procedure for computing the different roughness parameters used to characterize the fracture surface roughness.

APPENDIX 2 summarizes the experimental results obtained for all tested specimens. Through bar charts, this chapter studies the variability/repeatability of the tensile strength (direct and indirect), microcracking (AE) mechanisms, and roughness characteristics of the final macro-fractures among each group of conducted experiments in this research.

APPENDIX 3 provides detailed experimental results and photos of all tested specimens in this study.

It should be noted throughout this study that **microcracks** are defined as cracks that are not visible to the naked eye. Microcracks are usually studied using thin sections under a microscope, such as scanning electron microscopy (SEM). On the contrary, **macrocracks** are cracks that are visible to the naked eye. The initiation, growth, and coalescence of many microcracks form macrocracks.

CHAPTER 2: EXPERIMENTAL PROGRAM

2.1. Experimental Approach

The general experimental approach used in this research study includes (Fig. 2.1):

a) Two testing methods: (1) Brazilian and (2) direct tensile tests;
b) Two fracturing monitoring techniques: (1) acoustic emission (AE) and (2) digital image correlation (DIC);
c) Two materials categories: (1) granite and (2) mortar;
d) Two specimen shapes: (1) circular discs (for Brazilian tests) and (2) rectangular prismatic (for direct tensile tests);
e) Two specimen types: (1) intact mortar and intact granite and (2) granite-mortar bi-materials.

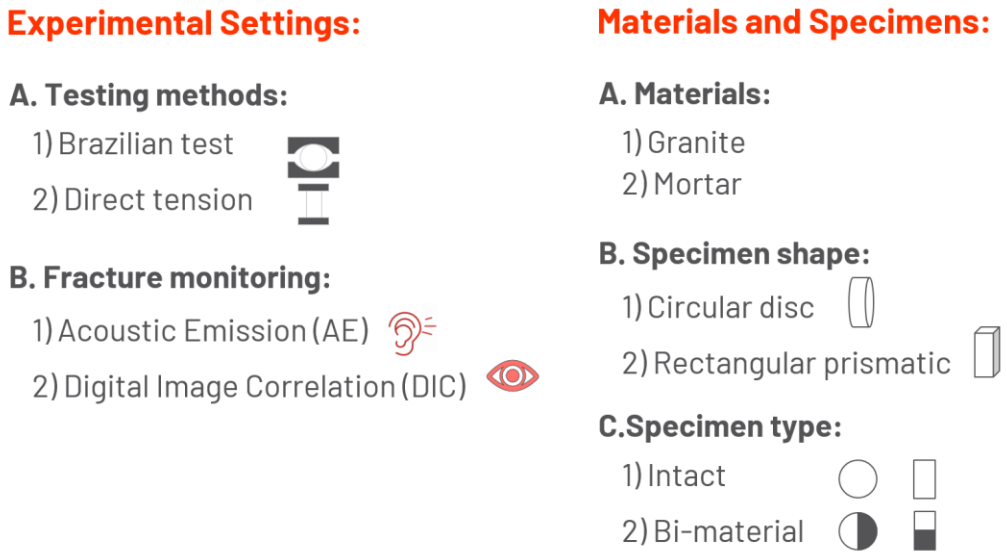

Fig. 2.1. An overview of the employed experimental approach in the current study

Over 100 specimens were tested in this research study. About 45% of them were used to develop the different tests, as for calibrating the tests. Fig. 2.2 shows an overview of prepared samples. Appendices 2 and 3 provide the results of the specimens for all different groups of tested specimens. Only specimens with valid results are provided. This includes the results of the following:

a) Five intact granite discs tested under the Brazilian test with a loading rate of 1 µm/s (associated with CHAPTER 3)
b) Six intact granite discs tested under the Brazilian test with a loading rate of 0.1 µm/s (associated with CHAPTER 3)

c) Seven intact mortar discs tested under the Brazilian test with a loading rate of 0.1 µm/s (associated with CHAPTER 4)
d) Six intact granite discs tested under the Brazilian test with a loading rate of 0.1 µm/s (associated with CHAPTER 4);
e) Five intact rectangular mortar specimens tested under direct tension with a loading rate of 0.1 µm/s (associated with CHAPTER 4);
f) Four intact rectangular granite specimens tested under direct tension with a loading rate of 0.1 µm/s (associated with CHAPTER 4);
g) Six granite-mortar discs tested under Brazilian test with a loading rate of 0.1 µm/s (associated with CHAPTER 5);
h) Four rectangular granite-mortar specimens tested under direct tension test with a loading rate of 0.1 µm/s (associated with CHAPTER 5).

These 43 specimens out of all tested samples yielded valid results (i.e., load-displacement, AE, DIC, and roughness results).

Fig. 2.2. Overview of the prepared samples for this study

2.1.1. Materials and Specimen Preparation

As mentioned, two specimen categories were tested in this study, including 1) intact granite and intact mortar and 2) granite-mortar bi-material specimens Fig. 2.3a. The rock material was prepared from Stanstead granite, while bi-material specimens were composed of

Stanstead granite and mortar (composed of water and SikaGrout 212 at a ratio of 0.18). Stanstead granite was selected for the study because it is a well-studied rock with known mechanical and physical properties. It is a homogenous rock, which is an essential material property for this study.

Two groups of specimens were prepared for each category: (1) cylindrical disc specimens for testing under the Brazilian indirect tensile loading and (2) rectangular prismatic specimens for testing under direct tensile loading Fig. 2.3a. The diameter of Brazilian discs was approximately 75 mm, and their thickness varied between 30 mm to 37.5 mm. Rectangular prismatic specimens' height, width, and thickness were 100 mm, 37 mm, and 30 mm Fig. 2.3a. The interface of the granite-mortar specimens was parallel to the loading direction when subjected to the Brazilian test.

To prepare the intact granite specimen, cylindrical cores and cubic blocks were extracted from a granite panel. The cubes and cylinders were then cut into smaller rectangular prismatic and cylindrical disc specimens, respectively, as illustrated on the right side of Fig. 2.3b. To prepare the granite-mortar specimens, a granite panel with a saw-cut smooth surface was placed in a wooden mold, and mortar was poured onto the rock surface into the mold. A plastic sheet was used to cover the cast mortar for 48 hours, after which, once the mortar hardened, the granite-mortar block was kept in a wet room at room temperature for 28 days. Cylindrical cores and cubic blocks were extracted from the granite-mortar block, which then were cut into smaller rectangular prisms and cylindrical discs, as illustrated in the left side of Fig. 2.3b. To prepare intact mortar specimens (rectangular and disc specimens), the mortar was poured into cubic and cylindrical PVC molds. Similarly, a plastic sheet was used to cover the cast mortar for 48 hours, after which, once the mortar hardened, the mortar cylinders and cubes were kept in a wet room at room temperature for 28 days. Finally, rectangular prisms and cylindrical discs of intact mortar were prepared, as shown in Fig. 2.3b.

A direct tensile test is regarded as valid only if the failure occurs at the midpoint of the specimen [22]. Therefore, two 5 mm notches were cut on both sides of the intact mortar and intact granite specimens to achieve this Fig. 2.3a and 1.8b. The ends of all prismatic specimens were polished and glued onto the loading plates with a strong adhesive epoxy Fig. 2.3b. The International Society for Rock Mechanics (ISRM) recommendations were adopted for rock specimen preparation, including coring, cutting, grinding, and polishing [92], [129].

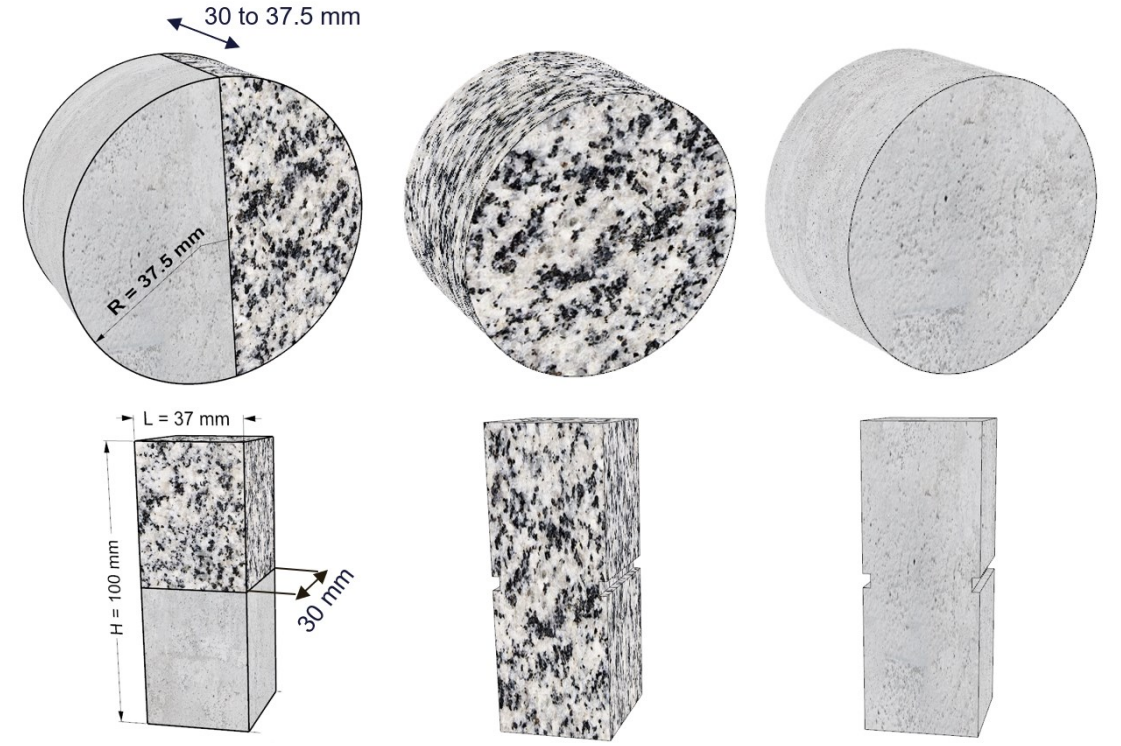

(a)

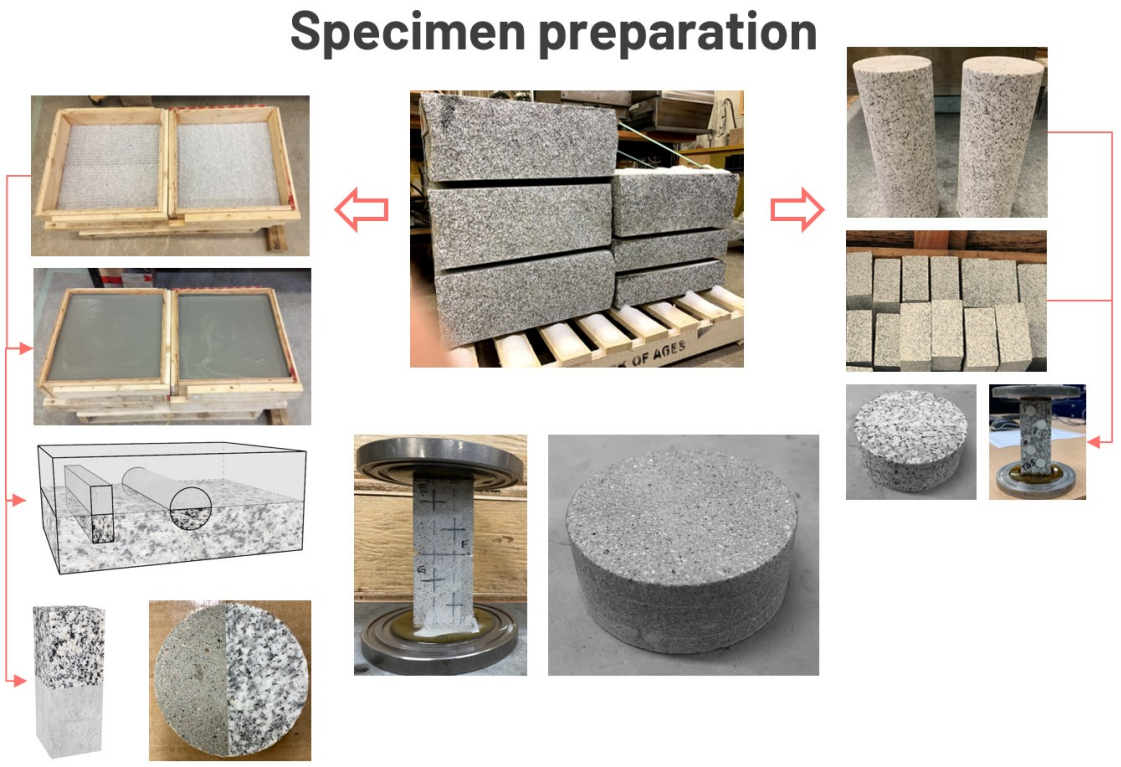

(b)

Fig. 2.3. (a) specimen types and shapes and (b) specimen preparation procedure

2.1.2. Experimental System and Testing Methodology

The experimental setup used in this study is detailed in CHAPTERS 3 to 5.

(a)

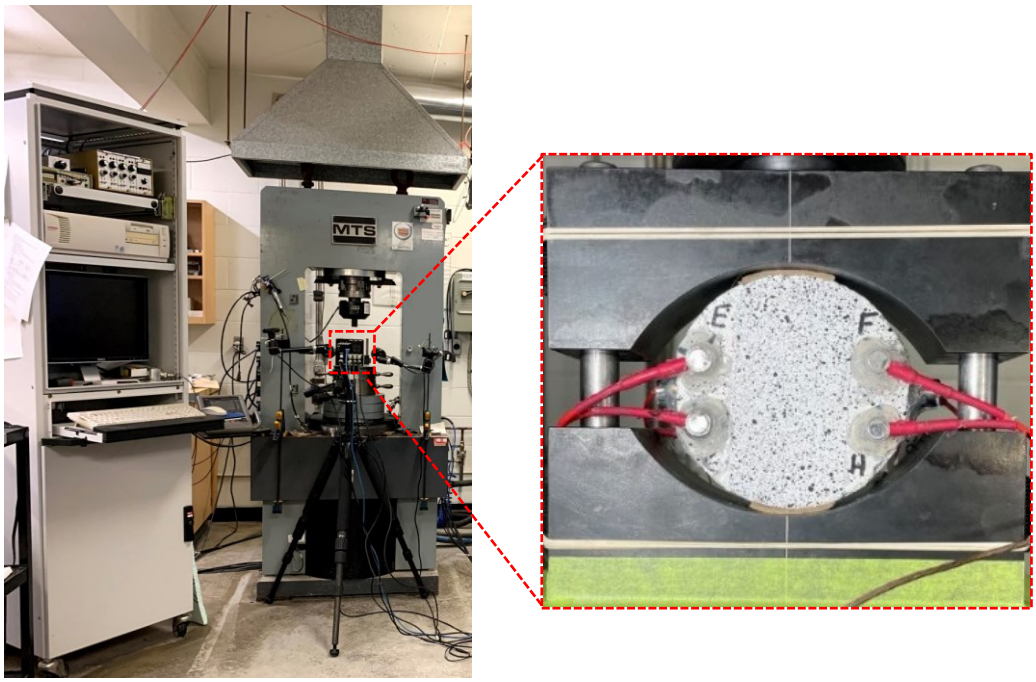

(b)

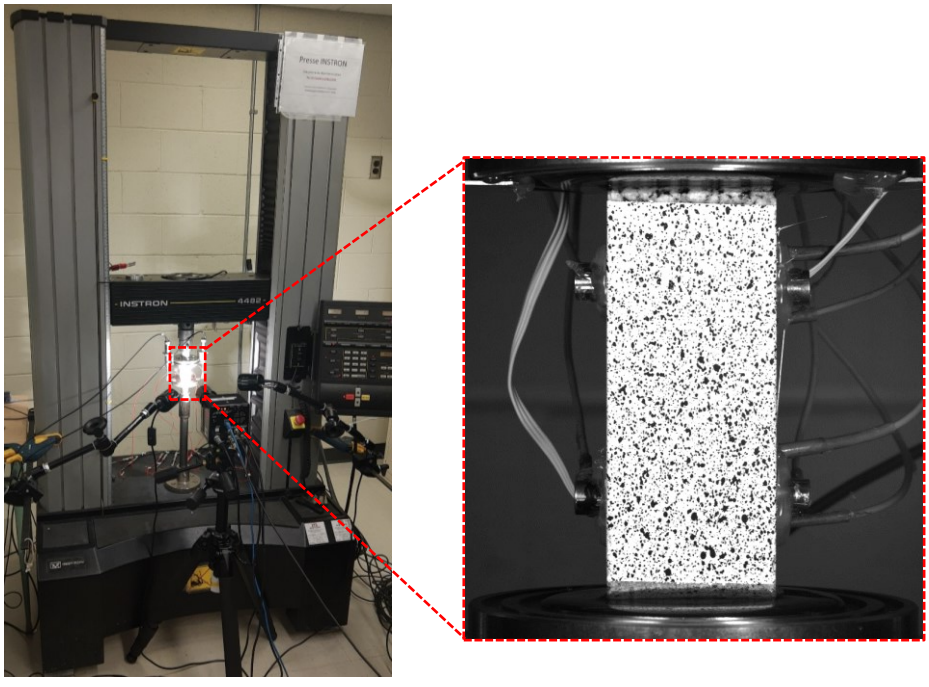

Fig. 2.4 (a) Servo-controlled material testing system (MTS) equipment used for implementing Brazilian tests and (b) INSTRON 4482 dual-column Universal Testing machine for implementing direct tensile test

2.1.2.1. Loading System

The Brazilian tests were performed in a servo-controlled material testing system (MTS) equipment (Fig. 2.4a), and the direct tensile tests were carried out with an INSTRON 4482 dual-column Universal Testing Machine (Fig. 2.4b). All experiments were conducted at the Laboratory of Rock Mechanics of the Université de Sherbrooke.

2.1.2.2. Acoustic Emission (AE) Monitoring

Acoustic emission (AE) is simply referred to phenomena/events through which transient elastic stress waves are internally generated by the rapid release of strain energy from localized sources in materials [130], [131]. The stress waves can originate within a material due to externally applied stress or some other unstable situation, such as a phase transition on a micro-scale. Or on a larger scale, such as earthquakes, a shifting mine slope, and rock bursts in mines [130], [132]. Depending on the material, the actual source of emissions could be deformation, crack initiation and propagation (e.g., in rocks/metals), crack opening and closure, interparticle slip and failure (e.g., in soils), and fiber breakage (e.g., in composites) [131]–[133]. Therefore, AEs are predominantly damage-related phenomena. Accordingly, AE monitoring involves detecting, recording, and analyzing the released strain energy (cracks) during their propagation in materials/structures to identify crack initiation and propagation, damage localization, cracking mechanisms, and failure prediction in different materials/structures [131], [133]–[135]. Due to this unique feature, the AE technique has widely been applied in research endeavors of rocks [58], [59], [135], [136], composite materials [137], [138], and metals [139], [140], and in industries such as monitoring of pressure vessels [141], hydro testing of storage tanks [137], and piping systems [142]. In geotechnics and geomechanics, in particular, the AE method has been employed to investigate basic deformation, fracture process, and failure mechanisms in geological materials such as rocks and concrete under various loading conditions, including rock burst problems in mines [132], [143], [144], uniaxial compression [46], [55], [59], [135], [145]–[147], triaxial compression [148], [149], direct shear [59], [150], and direct and indirect (Brazilian) tensile tests [10], [27], [59], [122]. The AE technique can also be applied to study structures composed of two or more materials, such as RC interfaces. Nevertheless, studies on the AE characteristics of such bi-materials remain limited. In bi-material specimens, AE signals can originate from either material or at their interface. Therefore, the AE sources can be associated with, among others, matrix microcracks, inter-grain movements, mortar/aggregate debonding in concrete, growth of a pre-existing crack, and/or slip/debonding movements along the bi-material interface.

In this study, the AE events were recorded using MISTRAS μ-SAMOS acoustic emission equipment to monitor the spatiotemporal distribution of cracks during the failure process of specimens (Fig. 2.5). For details on the AE setup and AE sensors, please refer to CHAPTERS 3 to 5.

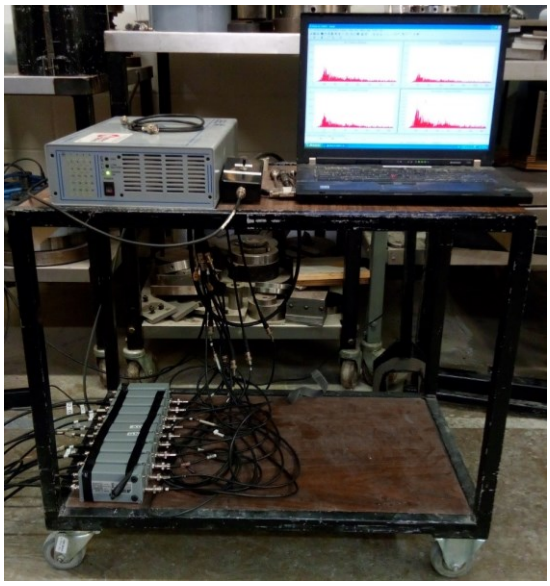

Fig. 2.5 Photograph of MISTRAS μ-SAMOS acoustic emission equipment

The AE source localization was done by picking up the arrival time of the P-waves using the Akaike information criterion (AIC) [134], [151]. A constant P-wave velocity field model, optimized using the "fmincon" function in MATLAB, was applied to locate AE sources for a minimum distance error of 3 mm. We followed the procedure developed in Li et al. [47] for source localization and moment tensor inversion of the AE events. It should be noted that the source localization procedure requires that each event trigger a minimum of four observation points (AE sensors) to determine the four unknowns, including the event origin coordinates (x, y, z) and the event time (t). Therefore, the minimum 4-sensor criterion was applied in this study to locate the AE events. In addition, to gain a better insight into the cracking process at the microscale during the whole loading process, the AE source mechanism was also analyzed using the moment tensor inversion method [47]. To increase the accuracy of the analyses, the source localization was performed for a minimum of six AE sensors when AE source mechanisms were investigated using the moment tensor inversion (MTI).

According to Ohtsu (1991) [152] and Ohno and Ohtsu (2010) [134], AE waves generated by dynamic-crack (dislocation) motions inside a solid are mathematically expressed by the moment tensor M_{pq} as,

$$u_k(x,t) = G_{kp,q}(x,y,t)\, M_{pq} * S(t) \qquad \text{Eq. 2.1}$$

Where $u_k(x,t)$ is the displacement at crack location x, $G_{kp,q}$ is the spatial derivative of Green's function, which describes the response of the medium from the source to the sensor, the symbol $*$ means the convolution integral, and S(t) represents the source-time function.

In this study, the SiGMA (Simplified Green's functions for Moment tensor Analysis) procedure was employed to perform the moment tensor inversion analysis developed by [153], [154]. The moment tensor inversion analysis aims to 1) identify cracking mechanisms, including shear, tensile, or mixed mode cracks, and 2) determine the crack orientation during the crack evolution process. The arrival time (P1) and the first motion amplitude of the detected AE signals (P2) are input parameters of SiGMA analysis. The SiGMA code consists of two steps: 1) AE source location procedure and 2) moment tensor analysis of AE source. In SiGMA procedure, the arrival time of the P waves (P1), automatically detected using the Akaike information criterion (AIC), is used to determine the AE source locations. The AE sources are localized from the arrival time differences t_i between two monitoring (sensor) locations x_i and x_{i+1}, by solving the following equations,

$$R_i - R_{i+1} = |x_i - y| - |x_{i+1} - y| = v_p t_i \qquad \text{Eq. 2.2}$$

Where R_i denotes the distance between the ith sensor and the AE source y, and v_p is the P-wave velocity of the material.

The amplitude of the first motion is given by,

$$A(x) = C_s \frac{Ref(t,r)}{R} r_p r_q \mathbf{M}_{pq} \qquad \text{Eq. 2.3}$$

Where A(x) represents the first motion amplitude (P_2) at the observation point x, C_s is the calibration coefficient of the sensor sensitivity and material constants, Ref (t, r) is the reflection coefficient, M_{pq} is the moment tensor, R is the distance between the source y and the observation point x, for which the direction vector is given by r.

By substitution of the first motion amplitude P2 collected from each sensor into the right hand of Eq. 2.3, a series of algebraic equations on unknown moment tensor components M_{pq} is obtained as,

$$A(x) = C_s \frac{Ref(t,r)}{R} [r_1\ r_2\ r_3] \begin{bmatrix} m_{11}\ m_{12}\ m_{13} \\ m_{12}\ m_{22}\ m_{23} \\ m_{13}\ m_{23}\ m_{33} \end{bmatrix} \begin{bmatrix} r_1 \\ r_2 \\ r_3 \end{bmatrix} \qquad \text{Eq. 2.4}$$

Where m_{ii} are the moment tensor components that physically represent the kinematics of the AE source (i.e., the rack motion), each component represents one of the nine double-couples acting at the source. The diagonal elements represent tensile or compressional couples, and the off-diagonal elements represent the shear couples.

To solve Eq. 2.4, all necessary parameters are known except for moment tensor components. Note that the parameters distance R and its direction vector r are determined from the AE source location procedure. Hence, the source location analysis is inevitable to determine moment tensor components.

The moment tensor is a symmetric tensor of the 2nd rank; thus, it is made of only six unknown independent components (m_{11}, m_{22}, m_{33}, m_{12}, m_{13}, m_{23}). As a result, the

amplitudes of the first motion at more than six sensors are required to determine all components of the moment tensor [134].

After determining the moment tensor components, the moment tensor is transformed into three eigenvalues and three eigenvectors in the following way:

$$\mathbf{M}_{\mathrm{pq}} = M_1\boldsymbol{e_1}\boldsymbol{e_1} + M_1\boldsymbol{e_1}\boldsymbol{e_1} + M_3\boldsymbol{e_3}\boldsymbol{e_3} \quad \text{Eq. 2.5}$$

Where $M_1 \geq M_2 \geq M_3$ are the maximum, intermediate and minimum eigenvalues, respectively, and $\boldsymbol{e_1}, \boldsymbol{e_2}$, and $\boldsymbol{e_3}$ are three eigenvectors. Eigenvalues and three eigenvectors are used to classify the crack type and determine crack orientation. The eigenvectors and eigenvalues represent the principal strain axes and their magnitudes [134]. The moment tensor is diagonalized and further restructured to form double-couple (DC), compensated linear vector dipole (CLVD), and isotropic (ISO) components as follows:

$$\mathbf{M}_{\mathrm{pq}} = \mathbf{M}_{\mathrm{ISO}} + \mathbf{M}_{\mathrm{DC}} + \mathbf{M}_{\mathrm{CLVD}} = M_{\mathrm{ISO}}\mathbf{E}_{\mathrm{ISO}} + M_{\mathrm{DC}}\mathbf{E}_{\mathrm{DC}} + M_{\mathrm{CLVD}}\mathbf{E}_{\mathrm{CLVD}} \quad \text{Eq. 2.6}$$

Where $\mathbf{E}_{\mathrm{ISO}}$, $\mathbf{E}_{\mathrm{DC}}$, and $\mathbf{E}_{\mathrm{CLVD}}$ are the ISO, DC, and CLVD base tensors, and M_{ISO}, M_{DC}, and M_{CLVD} are the ISO, DC, and CLVD coordinates in the 3-D source-type space, defined as follows:

$$\begin{aligned} M_{\mathrm{ISO}} &= \tfrac{1}{3}(M_1 + M_2 + M_3), \\ M_{DC} &= \tfrac{1}{2}(M_1 - M_3 - |M_1 + M_3 - 2M_2|), \\ M_{CLVD} &= \tfrac{2}{3}(M_1 + M_3 - 2M_2) \end{aligned} \quad \text{Eq. 2.7}$$

After computing the values of M_{ISO}, M_{DC}, and M_{CLVD}, AE events are classified as shear ($|M_{\mathrm{ISO}}| < 15\%$), compaction ($M_{\mathrm{ISO}} \leq -15\%$ and $M_{\mathrm{CLVD}} \leq 15\%$), and tensile ($M_{\mathrm{ISO}} \geq 15\%$ and $M_{\mathrm{CLVD}} \geq -15\%$) events [155].

Moreover, three eigenvectors $\boldsymbol{e_1}, \boldsymbol{e_2}$, and $\boldsymbol{e_3}$ computed from the eigenvalue analysis of the moment tensor can be used to identify the crack orientation. The crack orientation is represented by two vectors: the crack-motion vector l and the normal vector n to the crack surface. The eigenvectors are expressed by the two vectors l and n as,

$$\begin{aligned} \boldsymbol{e_1} &= l + n \\ \boldsymbol{e_2} &= l \times n \\ \boldsymbol{e_3} &= l - n \end{aligned} \quad \text{Eq. 2.8}$$

Where $\times$ stands for the vector product. While the two vectors l and n are parallel for tensile cracks (Mode I), they are usually perpendicular for shear cracks (Mode II and III).

It should be noted that the source localization procedure requires a minimum of four observation points (sensors) to determine the four unknowns, including the source coordinates (x, y, z) and the event time (t). However, as explained before, the moment tensor consists of six unknown independent elements meaning that more than six waveforms for each AE source have to be recorded. Therefore, in this study, the source localization was also performed for a minimum of six AE sensors.

Although an AE monitoring technique provides a tool for real-time inspection of AE activities at micro-, macro-, and mega-scale, it does not determine the size of generated defects [131], [133]. Therefore, a complementary inspection method, such as the digital image correlation (DIC) technique, is usually needed to establish a more accurate picture of the failure process and fracture size in materials under various loading conditions.

2.1.2.3. Image Acquisition and Digital Image Correlation Technique

During the tests, the entire failure process of specimens was recorded by capturing images using a Basler acA2440-75um camera along with a Scheinder Xenoplan 1.9/35-0901 CM120 BK 15 compact lens with a resolution of 5 (2448 × 2048) megapixel at one frame per second. Two LED lights were used to maintain stable and constant lighting of the observed specimen's surface, hence minimizing DIC post-possessing errors (Fig. 2.6).

After image acquisition, the digital image correlation (DIC) technique was applied to analyze the captured images during the experiments to measure displacements and strains at the surface of specimens for extracting fracture damage parameters during the failure process.

To investigate the deformation process and failure mechanisms in quasi-brittle materials (concrete, rock, and masonry), various experimental methods have been used, including particle image velocimetry method, laser measurement, Moiré method, X-ray CT method, Caustics method, Photoelasticity method, and Digital Image Correlation (DIC) [156]. Among these methods, the DIC, as a simple-to-implement, accurate, cost-effective, and non-destructive non-contact optical method, has been employed for measuring real-time displacement and full-field strain fields on the surface of materials [157]–[160].

The DIC technique was first proposed and employed by Peters and Ranson (1982) [161] and Chu et al. (1985) [162], and it has since been widely used, among other fields, in geotechnical investigations. These include analyzing the fracturing process and strain measurements in geomaterials under both quasi-static loading [52], [163]–[165] and dynamic loading [166]–[168]. The DIC has also been used in experimental studies on deformation behaviour and cracking mechanisms of geomaterials in various testing methods such as the Brazilian test [110], [159], [169], the uniaxial compression [46], [56], [57], biaxial compression [52], triaxial compression [170], [171], uniaxial tension [172], [173], and bending test [174]–[176]. All these studies have pronounced the strong capability of the DIC technique in capturing the location and the time of the crack initiation and in tracing the fracture propagation during the entire failure process.

In general, the DIC is implemented in three consecutive steps: (a) preparing the specimen and imaging system, (b) capturing and storing images of the specimen surface continuously at different stages of deformation, and (c) processing the captured images to determine displacement/strain fields [157], [177].

DIC's imaging system comprises one (2D DIC) or two (3D DIC) cameras connected to an image acquisition unit. Fig. 2.6 illuminates a typical imaging system setup for the 2D DIC method to capture the images of the fracturing process in the Brazilian disk test. As shown in Fig. 2.6., for 2D DIC, a camera is mounted on a tripod and placed at a given distance from the surface of the object of interest. An external light source, usually an LED light source, is also used to provide an appropriate lighting condition. Detailed recommendations for selecting lenses and employing suitable cameras for specific experiments, imaging system configuration, etc., are provided by Sutton et al. (2009) [157].

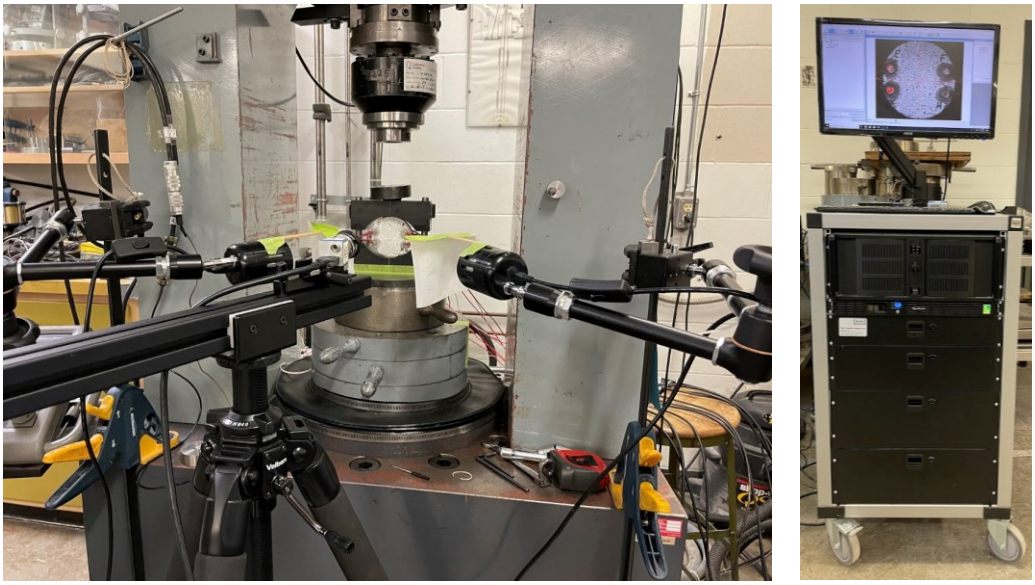

Fig. 2.6 Imaging system setup for the 2D DIC method

To increase the DIC technique's accuracy, the specimen's surface has to be covered with a speckle pattern to eliminate surface uniqueness issues [157]. The speckle pattern is usually created by spraying black and/or white paints over the surface of the specimen (Fig. 2.4). For DIC to work effectively, the specular markers must be distributed randomly and show a range of contrast and intensity levels. The details of the procedure of making speckle patterns are described by CorelatedSolutions [178].

DIC works by comparing a series of digital images captured from the specimen's surface at different stages of deformation. Displacement calculation begins with defining the calculation area (i.e., region of interest, ROI) in the first image or the reference image (ex., the blue region in Fig. 2.7). The ROI is then further divided into equally spaced virtual grids or subsets composed of a group of pixels (ex., the red and blue grids in Fig. 2.7a).

Through tracking and matching the same pixel points between an undeformed image (i.e., the reference image) and a deformed image, as depicted in Fig. 2.7b, the surface displacements in horizontal (u) and vertical (v) directions and strain is calculated by applying a correlation algorithm [157].

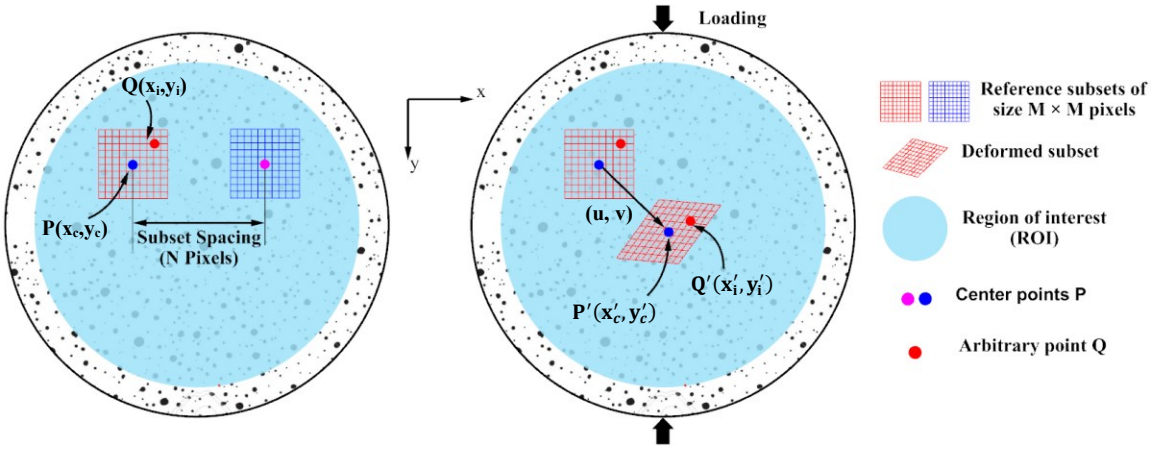

(a) Undeformed image (before loading) (b) Deformed image (after loading)

Fig. 2.7 Schematic diagram of (a) reference subset in the undeformed image, (b) the corresponding deformed subset in a deformed image, and in-plane displacements (u, v) and deformation of the subset.

To calculate the displacements of a given point P, a reference square subset of (M × M) pixels centered at point P (x_c, y_c) in the reference image (Fig. 2.7a) is selected and used to track its corresponding location in subsequent deformed images. In fact, the average greyscale pattern intensity is calculated for each subset on the reference image and then compared with that of the corresponding subset on the deformed image. A cross-correlation criterion is used to assess the similarity between the reference subset and the deformed subset. Eq. 2.9 is one of the most commonly used cross-correlation criteria [177].

$$ZNCC = \frac{\sum_{i=-M}^{M}\sum_{j=-M}^{M}[f(x_i,y_i)-f_m]\times[g(x_i',y_i')-g_m]}{\sqrt{\sum_{i=-M}^{M}\sum_{j=-M}^{M}[f(x_i,y_i)-f_m]^2}\sqrt{\sum_{i=-M}^{M}\sum_{j=-M}^{M}[g(x_i',y_i')-g_m]^2}}, \quad \text{(a)}$$

$$f_m = \frac{1}{(2M+1)^2}\sum_{i=-M}^{M}\sum_{j=-M}^{M} f(x_i,y_i), \quad \text{(b)} \qquad \text{Eq. 2.9}$$

$$g_m = \frac{1}{(2M+1)^2}\sum_{i=-M}^{M}\sum_{j=-M}^{M} g(x_i',y_i') \quad \text{(c)}$$

Where ZNCC stands for Zero-normalized cross-correlation calculated for a subset of size M × M pixels, f_m and g_m are the average gray values of the corresponding subset in the

reference image and deformed image, respectively, $f(x_i, y_i)$ is the gray value (pixel intensity) at the pixel position (x_i, y_i) on the reference image, and $g(x_i', y_i')$ is the gray value at (x_i', y_i') on the reference image.

The matching procedure relies on maximizing the correlation coefficient (CC) and is completed when the maximum value of CC is detected. The deformed subset corresponding to the maximum value of CC is the subset that most closely matches the reference subset. Subsequently, as indicated in Fig. 2.7b, the difference between the coordinates of the centre points of the deformed subset and the reference subset yields the local displacement vector at the centre point P(x_c, y_c). The components of the displacement vector can then be used to map the coordinates of an arbitrary point $Q(x_i, y_i)$ in the reference subset to point $Q'(x_i', y_i')$ in the corresponding deformed subset (Fig. 2.7b). Eq. 2.10 presents the shape function for calculating the coordinates of the point $Q'(x_i', y_i')$ [157], [177]. More details of the DIC technique can be found in Sutton et al. (2009) [157].

$$x_i' = x_i + u + \frac{\partial u}{\partial x}(x_c - x_i) + \frac{\partial u}{\partial y}(y_c - y_i) \quad \text{(a)}$$

$$y_i' = y_i + v + \frac{\partial v}{\partial x}(x_c - x_i) + \frac{\partial v}{\partial y}(y_c - y_i) \quad \text{(b)} \qquad \text{Eq. 2.10}$$

Where (x_i', y_i') is the new coordinate of point Q in the deformed subset on the deformed image, u and v are displacement components at the centre point of the reference subset in the x and y directions, respectively, and $\frac{\partial u}{\partial x}$, $\frac{\partial u}{\partial y}$, $\frac{\partial v}{\partial x}$, $\frac{\partial v}{\partial y}$ are the first-order displacement gradients.

It should be noted that the accuracy of the DIC strain fields was verified by comparing them with the strain reading from the strain gauges installed on some specimens. Fig. 2.8 shows an example of strain gauges installed on the back surface of a granite-mortar specimen. To calibrate the DIC strain values, subset size and the subset spacing parameters were changed, by trial and error, so that the DIC strain values best match with the strain gauge readings. The detailed DIC calibration procedure can be found in Aliabadian et al. (2019) [169].

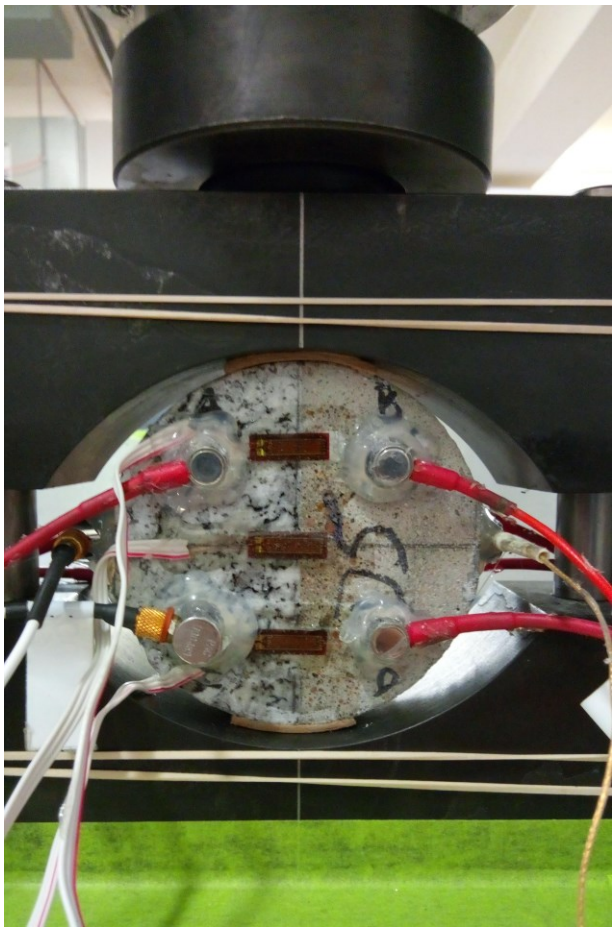

Fig. 2.8. A granite-mortar specimen with three strain gauges installed over its back surface.

CHAPTER 3: OBSERVATION OF FRACTURE PROCESS ZONE AND PRODUCED FRACTURE SURFACE ROUGHNESS IN GRANITE UNDER BRAZILIAN SPLITTING TESTS

OBSERVATION DE LA ZONE DE PROCESSUS DE FRACTURE ET DE LA RUGOSITÉ DE SURFACE DE FRACTURE PRODUITE DANS LE GRANITE SOUS LES ESSAIS BRÉSILIENS

Authors and Affiliation:

Ghasem Shams: Ph.D. Candidate, Civil Engineering and Building Engineering Department, Université de Sherbrooke, Sherbrooke, Québec, Canada.

Patrice Rivard: Professor, Candidate, Civil Engineering and Building Engineering Department, Université de Sherbrooke, Sherbrooke, Québec, Canada.

Omid Moradian: Lecturer, Department of Earth Sciences, Swiss Federal Institute of Technology (ETH), Zurich, Switzerland and Currently Research Associate Professor, Department of Civil and Environmental Engineering, Colorado School of Mines, Golden, Colorado, USA.

Journal Title and Paper Status:
Submitted to ***Theoretical and Applied Fracture Mechanics*, June 2022**. **Published**.

Contribution to the Thesis
This chapter investigates the cracking processes and development of the fracture process zone at the microscale in granite specimens subjected to Brazilian tensile loading. It discusses the fracturing mechanisms in Brazilian discs under two different loading rates and attempts to reveal the effect of microcracking mechanisms on the overall Brazilian tensile strength of granite discs. In addition, the effect of loading rate on the characteristics of the fracture surface roughness and complexity of produced fractures are discussed. Also, this chapter looks at the potential correlation between fracture surface roughness and the spatial distribution of AEs over the fracture surface.

This chapter is aimed to address the following specific objectives (see Section 1.4):

1. Identify and describe the micromechanics of damage and the evolution of the fracture process zone in granite under indirect tensile loading.
2. Determine the effect of two loading rates on granite's micro- and macro-fracturing behaviour and strength under indirect tensile loading.
3. Characterize the roughness of the surface failure of granite specimens under two loading rates in indirect tensile loads.

Résumé

Dans de nombreuses structures d'ingénierie des roches, la complexité du réseau de fractures et la rugosité des fractures générées sont extrêmement importantes pour comprendre la conductivité hydraulique de la masse rocheuse. Malgré des progrès significatifs, les mécanismes régissant la nucléation et la croissance de la zone de processus de fracture (FPZ) sont encore débattus. Le présent travail étudie les caractéristiques de la zone de processus de fracture et la rugosité de surface de la fracture produite dans le granit sous une charge de traction à deux taux de charge différents. Des techniques d'émission acoustique (EA) et de corrélation d'images numériques (CIN) ont été utilisées simultanément pour surveiller le développement de la FPZ dans des échantillons de disque de granite soumis à des essais brésiliens (Brazilian splitting tests). De plus, plusieurs paramètres de rugosité des fractures produites ont été mesurés, et on a essayé de lier les emplacements et les amplitudes des événements AE avec la distribution en hauteur de la surface de fracture. Nos résultats indiquent que le taux de chargement influence significativement l'étendue de la FPZ. La résistance à la traction des échantillons a également augmenté avec le taux de chargement. Les FPZ estimés à partir des données AE et DIC étaient en bon accord; cependant, le relevé d'EA a fourni une FPZ légèrement plus large pour tous les échantillons, quel que soit le taux de chargement. Il a été observé que la réduction du taux de chargement entraînait une plus grande FPZ et générait des fractures macroscopiques avec des caractéristiques de rugosité plus élevées. L'inversion du tenseur des moments des signaux AE a révélé que dans tous les échantillons testés, les fractures macroscopiques, qui sont classiquement considérées comme des fractures de traction, sont composées de trois principaux mécanismes de fissuration à l'échelle microscopique, notamment les sources de traction, de cisaillement et de compression. La distribution des mécanismes focaux a montré que les fissures pouvaient s'amorcer sous la traction, le cisaillement ou une combinaison des deux mécanismes. Les résultats de cette étude peuvent aider à mieux comprendre les processus de fracturation des roches sous charge de traction dans les roches granitiques pour des applications sur le terrain.

Abstract

In many rock engineering structures, the fracture network's complexity and the generated fractures' roughness are immensely important for understanding the hydraulic conductivity of the rock mass. Despite significant progress, the mechanisms governing nucleation and growth of fracture process zone (FPZ) are still debated. The present work investigates the characteristics of the FPZ and the surface roughness of the produced fracture in granite under tensile loading at two different loading rates. Acoustic emission (AE) and digital image correlation (DIC) techniques were simultaneously employed to monitor the development of the FPZ in disc specimens of granite subjected to Brazilian splitting tests. In addition, several roughness parameters of the produced fractures were measured, and it was tried to link the locations and the magnitudes of the AE events with the height distribution of the fracture surface. Our results indicated that the loading rate significantly influences the extent of the FPZ. The tensile strength of specimens also increased with the loading rate. The FPZ estimated from the AE and DIC data were in good agreement; however, AE provided a slightly wider process zone for all specimens, regardless of the loading rate. It was observed that reducing the loading rate led to a larger FPZ and generated macroscopic fractures with higher roughness characteristics. Moment tensor inversion of the AE signals revealed that in all tested specimens, macroscopic fractures, which are conventionally considered tensile fractures, are composed of three main cracking mechanisms at the microscale, including tensile, shear, and compressive sources. Focal mechanisms distribution showed that the cracks might initiate under tensile, shear, or a combination of both mechanisms. This study's findings can help in better understanding the rock fracturing processes under tensile loading in granitic rocks for field applications.

Keywords: Loading rate, Fracture process zone, Digital image correlation, Acoustic emission, Moment tensor inversion, Microcracking mechanisms, Fracture roughness

3.1. Introduction

Understanding the fracturing and cracking processes in rock is fundamental to many rock mechanics applications in civil, mining, and petroleum engineering. Previous studies on the fracturing process in geo-materials indicated that under various types of loads, microcracks nucleate and propagate in a localized region around pre-existing micro-flaws called the fracture process zone (FPZ). As the applied load increases, the propagation and coalescence of generated microcracks produce macroscopic fractures, leading to rock failure [11]–[15]. Various observation techniques have been employed to study the FPZ in concrete and rocks including computed tomography (CT) scan [179], holographic interferometry (HI) [180], electronic speckle pattern interferometry (ESPI) [181], scanning electron microscopy (SEM) [180], [182], acoustic emissions (AE) [10], [59], and digital image correlation (DIC) [52], [110]. The AE and DIC are the most frequently used techniques in monitoring the fracturing processes in rocks.

AEs are elastic stress waves generated by the rapid release of strain energy in quasi-brittle materials such as rock and concrete due to the crack initiation and propagation, crack

opening and closure, and interparticle slip and failure [45], [135], [183]. Accordingly, AE monitoring has been applied by many scholars to identify the FPZ [46], [55], the effect of specimen size and loading rate on the FPZ [48], [184], and the cracking process during hydraulic fracturing [185]. The AE characteristics of rocks have been mainly studied under uniaxial compression [46], [55], triaxial compression [146], [149], direct shear [58], [59], and direct and indirect tension [27], [59], [175], [186].

Eberhardt et al. [55] employed AE and strain gauge data to study the progressive cracking process in granite specimens under uniaxial compression. The authors found that the combined analysis of AE and strain gauge data provides a reliable method for determining the crack propagation stages, including crack initiation (σ_{ci}) and crack damage (σ_{cd}) stress thresholds in brittle rocks. Using parametric AE analysis, Moradian et al. [187] introduced a classification of cracking levels in granite specimens containing pre-existing flaws under uniaxial compression. They reported that the correlation of AE parameters with stress-strain measurements provides detailed information on different cracking levels in the granite fracturing process from micro- to macro-cracking.

Dai and Xia [188] evaluated the effect of loading rate on the tensile strength anisotropy of granite under static and dynamic loadings. Their results indicated that with the increase of the loading rate, the tensile strength of specimens increased, while the tensile strength anisotropy decreased. Chen et al. [189] employed the AE technique to monitor the effect of loading rate on the fracture behaviour of concrete specimens under TPB tests. Their results showed that the increase in loading rate increases the proportion of shear cracks in concrete and decreases the width of FPZ. Wang et al. [190] studied the effect of the loading rate on the mechanical and AE characteristics of fractured sandstones under uniaxial compression. They stated that the loading rate significantly controlled the mechanical and microfracturing processes in tested specimens.

In contrast to Chen et al. [189], Wang et al. [190] observed that with the increase in loading rate, the contribution of shear microcracks predominantly decreased. Li et al. [191] used DIC and AE techniques to investigate the effect of the loading rate on the FPZ of concrete subjected to TPB. They stated that the higher loading rates yielded higher tensile strength values and a narrower (smaller) FPZ. AE technique was also used by Backers et al. [184] to study the influence of loading rate on the development of the FPZ in sandstone under TPB. The authors applied clip-gage opening displacement (COD) rates ranging from 5×10^{-6} to 5×10^{-10} m/s and reported that both the crack density and the FPZ width remained constant in the range of applied loading rates. Ali et al. [48] applied the AE analysis to evaluate the size dependency of the FPZ in granite beams of different sizes in TPB tests. It was found that with an increase in specimen size, the length and width of the PFZ increase. Following a spatial AE location analysis, Yang et al. [146] concluded that AE can accurately identify the failure characteristics and the fracture mode of sandstone specimens under triaxial compression. Using the analysis of dominant frequency characteristics of AE signals, Wang et al. [27] reported that the difference between the direct and indirect

(Brazilian) tensile strength values of marble specimens results from the higher proportion of micro-shear failure in the Brazilian test.

DIC, as a simple-to-implement, accurate, and cost-effective method, has considerably been employed in studying the fracturing process and strain measurements in geo-materials under various testing methods such as uniaxial compression [46], [56], [57], biaxial compression [52], triaxial compression [170], and direct and indirect tension [110], [173], [175], [186]. Munoz et al. [57] used a combination of strain gauge measurements and the 3D DIC method to evaluate the deformation characteristics of sandstone under uniaxial compression. Their observations highlighted that while measuring large strains in the post-peak region is impossible with strain gauges (because of strain gauge damage caused by generated macrocracks), it can be easily measured with the DIC technique. Using a combined DIC and AE monitoring, Alam et al. [175] studied the cracking mechanisms and the FPZ in concrete beams during TPB tests. They reported that while DIC and AE effectively identify the extent of the FPZ, DIC is more successful in measuring crack length than AE. Tang et al. [173] employed the DIC method to examine the deformation behaviour and failure process of tuff specimens in compression–tension cycle tests. The authors stated that the DIC strain measurements not only identify the cracking evolution process but also accurately explain the effect of crack growth on the evolution of deformation moduli and energy dissipation in rocks.

While several studies have been conducted to understand the initiation and growth of the cracking processes under tensile [27], [56], [192], compression [55]–[57], and shear loading [58], [59], the mechanisms governing nucleation and growth of FPZ are still not well understood. Fracture processes zone and fracture roughness are the two concepts that describe the complexity and the connectivity of the fractured reservoir rock. Therefore, the objectives of this study are defined as follows: 1) determine the micromechanics of damage and the moment tensor inversion (MTI) of fracturing mechanisms (tensile, shear, and compressive) and their spatiotemporal evolution in the process zone for two different loading rates, 2) investigate the characteristics of the fracture surface roughness caused by two different loading rates and argued how the complexity of a fracture is affected by the loading rate and grain sizes, and 3) determine if there is any potential correlation between fracture surface roughness and the distribution of AEs over the fracture surface. For this purpose, the Brazilian test was adopted to apply tensile load to granite specimens under two different loading rates. Meanwhile, DIC and AE techniques were simultaneously used to monitor the cracking process in granite discs throughout the loading process.

3.2. Methodology

3.2.1. Materials and Specimen Preparation

The rock investigated here is the Stanstead granite (Eastern Township region, Quebec, Canada), which is mainly composed of quartz, mica (biotite), alkali feldspar (orthoclase), plagioclase (albite), and opaque minerals and is coarse-grained with an average grain size of 1.08 mm [193]. A total of 6 cylindrical disc specimens with a diameter of 75 mm and a thickness of 30 mm were prepared for the experiment, referred to as GI-1, GI-2, GI-3, GII-

1, GII-2, and GII-3. Besides, four cylindrical specimens with a height of 170 mm and a diameter of 75 mm were tested to determine the basic mechanical and physical properties of the Stanstead granite (Table 3.1). All rock specimen preparation, including coring, cutting, grinding, and polishing, was performed according to the International Society for Rock Mechanics (ISRM) recommendations [92], [129].

Table 3.1. Mechanical and physical properties of Stanstead granite

Parameter	No. of Samples	Min	Max	Mean	SD*
Uniaxial compressive strength (MPa)	4	136.8	138.0	137.0	0.61
Brazilian tensile strength (MPa)**	6	7.4	8.3	7.85	0.30
Modulus of elasticity (GPa)	3	49.9	51.1	50.6	0.62
Poisson's ratio	3	0.21	0.27	0.23	0.03
P-wave velocity (km/s)	4	4.07	4.17	4.12	0.02
Density (kg/m^3)	4	2636	2646	2643	4.85

* Standard deviation

** Obtained under a loading rate of 0.1 μm/s

3.2.2. Experimental System and Testing Methodology

3.2.2.1. Loading System

The Brazilian tests were performed using servo-controlled material testing system (MTS) equipment at the Laboratory of Rock Mechanics of Université de Sherbrooke. The load cell capacity was 225 KN. Two LVDT displacement transducers (Solartron Metrology, Model 925604 DCR15) were used to record the axial displacement along the loading direction. To ensure the quasi-static loading condition, the displacement loading mode was employed. To evaluate the effect of the loading rate on the tensile mechanical properties of the rock, two different loading rates were applied: 1) a loading rate of 1 μm/sec (high-loading rate) for the first group of specimens (GI-1, GI-2, GI-3); and 2) a loading rate of 0.1 μm/sec (low loading rate) for the second group of specimens (GII-1, GII-2, GII-3). It should be noted that these loading rates are lower than the ISRM recommended loading rate for measuring the indirect tensile strength of the rock: "*the load on the specimen shall be applied continuously at a constant rate such that failure in the weakest rocks occurs within 15-30 s"* [92]. Since the purpose of this study was to understand the fracturing processes, rather than reporting the tensile strength, lower loading rates with an average test duration of 31 and 290 minutes were selected for group I (GI) and group II (GII) specimens, respectively. In fact, crack initiation and propagation in brittle materials is a highly rapid process, and crack propagation speeds increase with loading rates [41]. High loading rates may lead to AE system saturation, causing many AE events to be missed. Therefore, to fully characterize the whole rock cracking process through AE and DIC, these two low-loading rates were chosen in this study.

The ISRM standard loading jaws were used (Fig. 3.1) [92]. In addition, two cardboard cushions with 2.5 mm thickness were inserted between jaws and specimens (Fig. 3.1) to avoid an excessive concentration of compressive stress at the jaws-specimen contact areas [22], [63], [66], [108]. This is because the compressive stress concentration may cause premature fracture initiation at the jaws-specimen contact vicinity, invalidating the Brazilian test results [63], [119], [194].

3.2.2.2. Acoustic Emission (AE) Monitoring

The AE signals were recorded using MISTRAS μ-SAMOS system to monitor the spatiotemporal distribution of cracks during the failure process of specimens. This device consists of two 8-channel AE data acquisition boards (PCI-8). Ten Nano-30 AE sensors with a frequency response over the range of 125-750 kHz with a resonant frequency of 300 kHz were attached to the surface of the granite disc to record AE signals. Four sensors were attached to the front surface, four to the back surface, and two to the sides of the specimens to capture the 3D distribution of events (Fig. 3.1b). The sides of the discs were slightly flattened to provide a better coupling between the sensors and the specimens. A circular double-sided adhesive tape (DSAT) was inserted between the sensors and the specimen to attach the sensors to the specimen's surface. Then, sensors were glued to the specimens with hot glue (Fig. 3.1b). The auto sensor test (AST) was implemented to verify the efficiency of sensor-specimen coupling [195].

PAC 2/3/4 preamplifiers were employed with a gain of 40 dB to amplify the low amplitude AE signal produced from AE sensors. Full-waveform AE data were recorded using a threshold value of 35 dB at a sampling frequency of 3 MHz, with a pre-trigger of 50 μs and a sample length of 4k. To calculate the AE parameters, the PDT (Peak Definition Time), HDT (Hit Definition Time), and HLT (Hit Lockout Time) parameters were set to 200, 800, and 350 μs, respectively. The maximum duration was 10 ms. The AE setup input parameters were selected according to Moradian and Li [196]. The location error was measured as ±2 mm.

The AE source localization was done by picking up the arrival time of the P-waves using the Akaike information criterion (AIC) [134]. In this method, the values of the AIC function are computed for the time series (signal), and the minima of the AIC correspond to the onset time of the AE signal, as shown in Fig. 3.1c [151]. A constant P-wave velocity field model was applied to locate AE sources for a minimum distance error of 3 mm and optimized using the "fmincon" function in MATLAB [40]. It should be noted that the source localization procedure requires that each event trigger a minimum of four observation points (AE sensors) to determine the four unknowns, including the event origin coordinates (x, y, z) and the event time (t). However, to increase the accuracy of the localized AE events, the source localization was performed for a minimum of six AE sensors.

3.2.2.3. Digital Image Correlation Technique

DIC works by comparing a series of digital images of a specimen surface at different stages of deformation. Displacement calculation begins with defining the calculation area (i.e., region of interest, ROI) on the first image, called the reference image. The ROI is, then, further divided into equally spaced virtual grids or subsets composed of a group of pixels. By tracking and matching the same pixel points between an undeformed image (i.e., the reference image) and a deformed image, surface displacements and strains are calculated using a correlation algorithm [157].

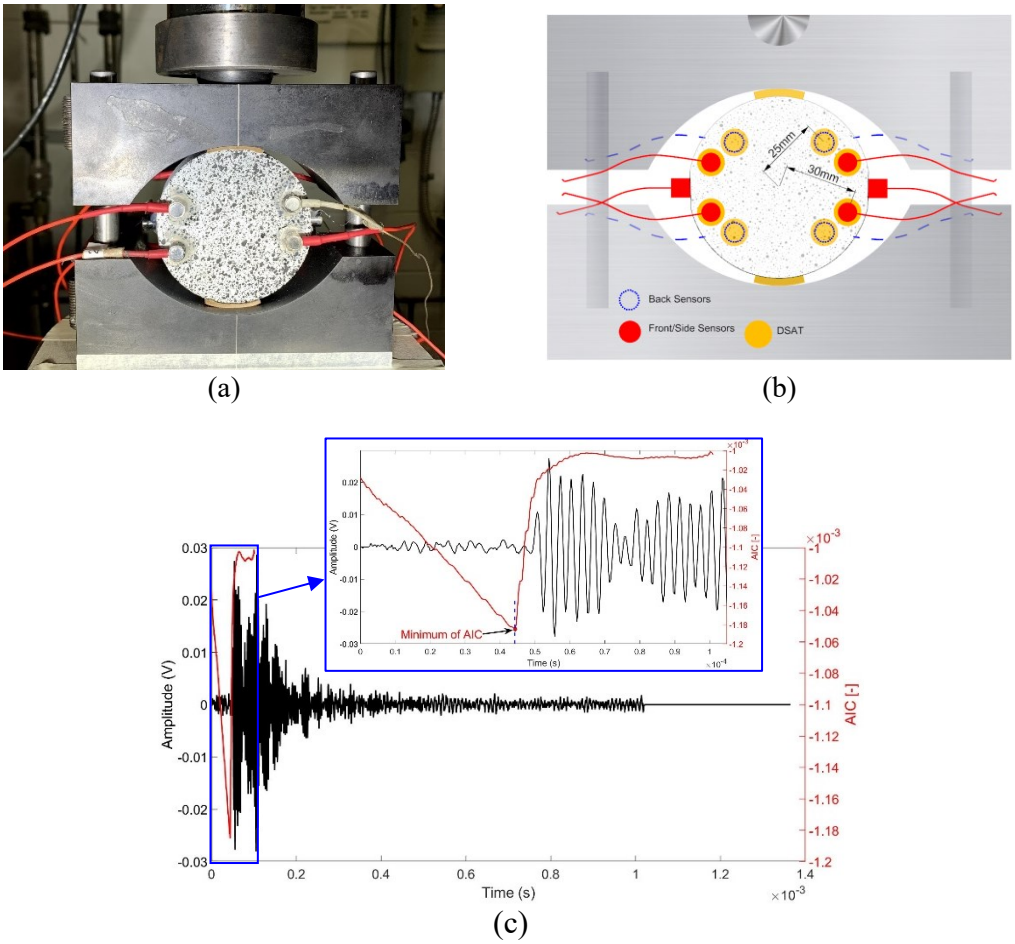

Fig. 3.1. (a) Schematic view of standard Brazilian jaws, (b) AE sensor positioning on the specimen, (c) The arrival time determined using the AIC function, AIC values in red, and the AE waveform in black. The time corresponding to the minimum of the AIC function yields the arrival time, as depicted in the inset.

The entire test duration was recorded by capturing images at 1 fps with a resolution of 2448 × 2048 pixels using a Basler acA2440-75um camera and a Scheinder Xenoplan 1.9/35-0901 CM120 BK 15 compact lens. Two LED lights were used to maintain stable and

constant lighting of the observed specimen's surface, hence minimizing digital image correlation (DIC) post-possessing errors. In addition, to eliminate surface uniqueness issues and increase the DIC technique's accuracy [46], a stochastic speckle pattern was generated by spraying black paints over the specimen's front surface (Fig. 3.1). The details of the procedure of making speckle patterns are described by CorelatedSolutions [178]. After the image acquisition, the DIC technique (using VIC-2D software [178]) was applied to measure and visualize full-field displacement and strain data at the surface of the granite specimens.

At the beginning of the experiments, the three systems, including loading, imaging, and AE monitoring, were synchronized to record experimental data simultaneously.

3.2.2.4. Fracture Roughness Analysis

To characterize the surface roughness of macroscopic fractures generated after loading the granite specimens, 3D coordinates defining the fracture surface were acquired using a high-accuracy profilometer 3D laser scanner (Kreon Zephyr© 25). The laser scanner device has a maximum resolution of 72 µm for the x and y-axes and 16 µm for the Z-axis. For detailed information on this device, readers are referred to previous research conducted at the Université de Sherbrooke [197], [198]. The roughness characterization process is explained in APPENDIX 1.

Various methods have been employed to characterize the surface roughness using statistical [199]–[202] and fractal approaches [203], [204]. These methods adopt 2D parameters based on analysis of 2D surface profiles or 3D parameters based on analysis of 3D fracture surfaces. Among commonly employed 2D parameters is the root mean square of the first deviation of the roughness profiles (Z2), structure function (SF), the arithmetical mean deviation roughness index (R_a), the roughness profile indexes (R_p), and the root mean square roughness index (R_q) [200]. In addition, $\theta^*_{max}/(C+1)$ proposed by Tatone and Grasselli [205] and Z2s (3D equivalent of Z2) proposed by Belem et al. [206] are among the 3D parameters. Furthermore, the fractal dimension (D) concept has been recently applied to describe rock fracture surfaces [203], [204], [207]. D parameter of a given fracture surface can be determined using 2D roughness profiles, called one-dimensional fractal dimension D_{1d}, or 3D roughness surfaces, called two-dimensional fractal dimension D_{2d} [207]. Higher values of the roughness parameters mentioned above indicate a rougher surface. Note that since the goal here is to determine the general trends in fracture roughness with loading rate, the roughness parameters were only calculated along the loading direction (i.e., Y^+ axis in Fig.A1. 1) for all specimens.

3.3. Experimental Results

3.3.1. Tensile Strength and Behaviour

Two loading rates were applied for two groups of specimens. The load-displacement curves of all specimens are illustrated in Fig. 3.2.

The inset in Fig. 3.2 indicates the indirect tensile strength of Brazilian specimens, which was determined following the ISRM recommendation [92] as follows:

$$\sigma_t = \frac{F_p}{\pi R t} \qquad \text{Eq. 3.1}$$

Where σ_t is the indirect (Brazilian) tensile strength (MPa), F_p is the applied load at failure (N), and R and t are the radius and the thickness of the specimen (mm), respectively.

Fig. 3.2 shows that with decreasing the loading rate from 1 µm/s to 0.1 µm/s, the average BTS decreased from 9.2 MPa for group 1 to 7.6 MPa for group 2, a decrease of 17%. These results agree with the well-established fact that rocks indicate increases in strength with the rise of the loading rate or strain rate [188], [208], [209].

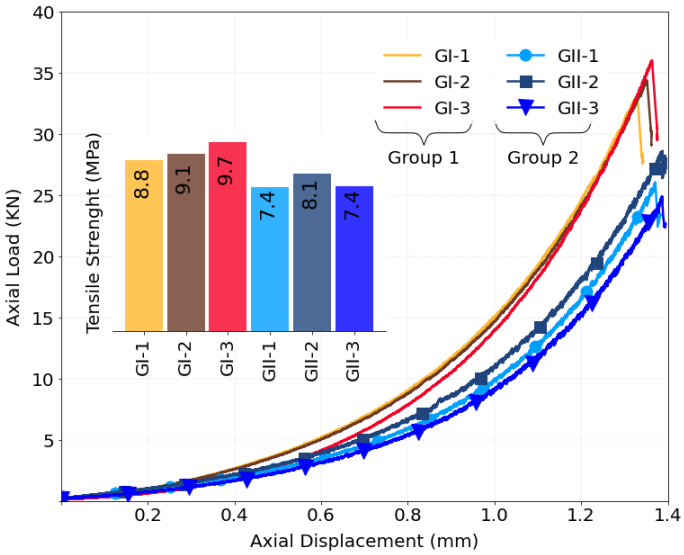

Fig. 3.2. Load-displacement curves for all tested Brazilian discs up to the peak loads. The inset shows the Brazilian tensile strength of specimens. Specimens GI-1 to GI-3 have been tested with a loading rate of 1 µm/sec (high-loading rate), and Specimens GII-1 to GII-3 have been tested with a loading rate of 0.1 µm/sec (low-loading rate). The higher the loading rate, the higher the tensile strength.

Fig. 3.3 represents typical macroscopic fracture patterns of GI-1 and GII-1. The blue lines represent the macroscopic fracture trace. After the experiments, the surface of generated macro fractures was scanned to analyze their surface roughness characteristics. At the failure load, all group 1 and group 2 specimens (e.g., GI-1 and GII-1in Fig. 3.3) failed along their vertical central line and formed a diametrical split.

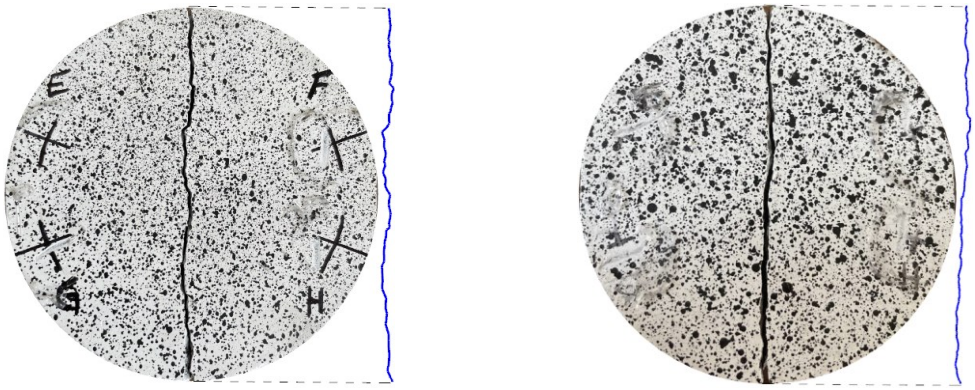

(a) GI-1 (b) GII-1

Fig. 3.3. Macroscopic failure pattern of (a) GI-1 representing the group 1 specimens with a loading rate of 1 µm/sec (high-loading rate) and (b) GII-1 representing the group 2 specimens with a loading rate of 0.1 µm/sec (low-loading rate) in Brazilian tests. The blue lines represent the macro fracture path at the failure in the corresponding load-displacement curves shown in Fig. 3.2.

3.3.2. Temporal Evolution of Damage

AE hits detected throughout the loading process correspond to newly generated microcracks in specimens [10], [46], [136]. Since the AE hits captured for different specimens (in each group) were similar, the AE data of GI-1 and GII-1, representing the group 1 and group 2 specimens, respectively, were chosen and further analyzed.

Fig. 3.4 illustrates the recorded AE hits, the cumulative AE hits, the cumulative AE energy, and the applied load curves recorded during the Brazilian tests for GI-1 and GII-1. The acoustic activity can be explained in four loading stages for both GI-1 and GII-1. At the first stage, no AE hits are recorded: it is the initial load transfer process at the specimen-loading jaws contact. The second stage is characterized by a minimal number of AE hits, where the corresponding cumulative AE energy remains remarkably low. These early AE activities mostly represent the closure of pre-existing microcracks in the granite specimens (minimal AE energy value). At the third stage, the accumulated hits number rises sharply, as pointed out by the local increase of the slope of the cumulative AE hits. This sharp increase in AE hits is accompanied by an increase in the cumulative AE energy indicating the initiation and growth of microcracks within the granite specimens. Finally, the last stage begins with a steeper AE accumulation rate, leading to an abrupt increase in the cumulative hits and energy corresponding to the final macroscopic failure. The AE hits closely represent the initiation and propagation of microcracks within materials, and the AE energy represents the magnitude of the microcracks. Therefore, both GI-1 and GII-1 underwent very little damage before the final failure, as reflected by the low level of the cumulative hits and cumulative energy (Fig. 3.4). This is the characteristic of brittle rocks, as the stored energy in them is released abruptly through the macroscopic failure. In fact, in granite specimens under tensile loading, the damage initiation and peak strength are nearly coincident [122].

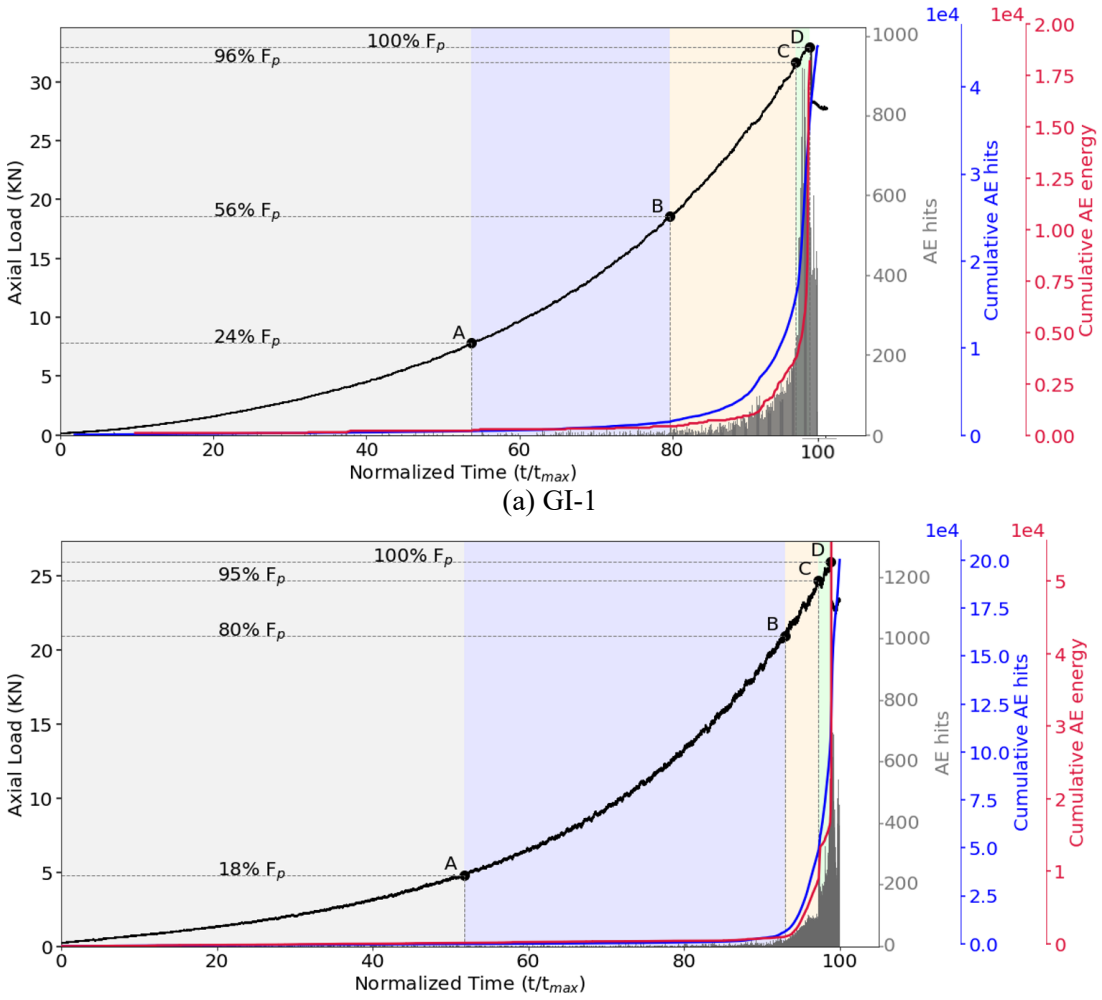

(a) GI-1

(b) GII-1

Fig. 3.4. Load-displacement curve with AE hits, cumulative hits, and cumulative energy for (a) specimen GI-1 with a loading rate of 1 μm/sec (high-loading rate) and (b) specimen GII-1 with a loading rate of 0.1 μm/sec (low-loading rate). F_p denotes the failure load. Four loading stages exist for both specimens, and the microcracking process initiates from the third stage.

3.3.3. Observation of Fracturing Processes

3.3.3.1. AE Monitoring of the Fracturing Processes

In total, 238 (GI-1) and 2245 (GII-1) AE events, detected by a minimum of six AE sensors, were located until the peak load. Fig. 3.5 and Fig. 3.6 illustrate the typical cracking process of granite specimens and the AE source distribution at four tracepoints (points A, B, C, and D shown on the load-displacement curves in Fig. 3.4a and b) for the high (GI-1) and the low (GII-1) loading rates, respectively. As indicated in Fig. 3.4, for both GI-1 and GII-1, the control points A, B, C, and D denote the end of the first, second, third, and fourth stages.

In addition, the size and color of the circles in Fig. 3.5 and Fig. 3.6 are scaled by the average focal amplitude (A_0) of the AEs, which indicates the source energy magnitude. Following Zang et al. [210], the amplitude of the AE events was calculated from the maximum amplitude of the AE signals using Eq. 3.2:

$$A_0 = \sqrt{\frac{1}{n}\sum_{i=1}^{n}\left(A_{max}^{i}\frac{r_i}{10}\right)^2} \qquad \text{Eq. 3.2}$$

Where n is the number of sensors receiving the same AE signal, A_{max}^{i} is the maximum signal amplitude received by the i^{th} sensor, and r_i (in mm) is the signal source distance to the i^{th} sensor. In Eq. 3.2, it is assumed that AE signals spread spherically, and the amplitude A_0 is computed on a reference sphere (radius 10 mm), with its origin at the signal source [210].

As observed from Fig. 3.5a and b, less than 3% of the total AE events occur before 56% of the peak load (point B). These very few AE sources can represent the closure of pre-existing microcracks within the specimen, meaning that the granite specimen can be assumed to be entirely elastic. The third stage spans from 56% (point B) to 96% (point C) of the failure load. Nearly 37% of the total AE events were captured in this stage until the control point C (Fig. 3.5c). The trend of the cumulative AE hits and energy curves (Fig. 3.4a) suggests that the granite specimen undergoes stable microcrack initiation and growth in this stage, as the released AE energy level remains very low. The fourth stage begins at 96% failure load and corresponds to an unstable fracture initiation and propagation. This can be confirmed by the dramatic rise in both AE hits and AE energy (Fig. 3.4a) and the fact that around 63% of the total AE signals were captured in this very short stage (Fig. 3.5d).

Similarly, only 1.3% of the total AE events occurred in GII-1 before the end of the second stage (point B), as shown in Fig. 3.6a and b. However, the second stage, in which the accumulated AE energy is negligible, covers a wider range of the applied load and continues up to 80% of the peak load, while this was 56% for GI-1 (Fig. 3.4a and b). This difference can imply that with decreasing loading rate, the generation of new microcracks may be delayed to higher values of the applied load. On the contrary, the third stage includes a narrower band of the applied load, which is 15% of the total load for GII-1 versus 40% for GI-1 (Fig. 3.4a and b). In the third stage, the initiation and the stable growth of microcracks are considerably accelerated, as evidenced by the accumulated AE hits and energy at this stage. Like GI-1, the third stage ends when 95% of the peak load is reached (point C), and 23% of the total AE events were detected in this stage, as displayed in Fig. 3.6c. Finally, like GI-1, the last stage starts after 95% of the final load. As shown in Fig. 3.6d, 77% of the total AE events occur in this stage, resulting mainly from unstable fracture growth and a sudden increase in both AE hits and AE energy rates. The accumulation of the AE events leads to macroscopic failure at the control point D.

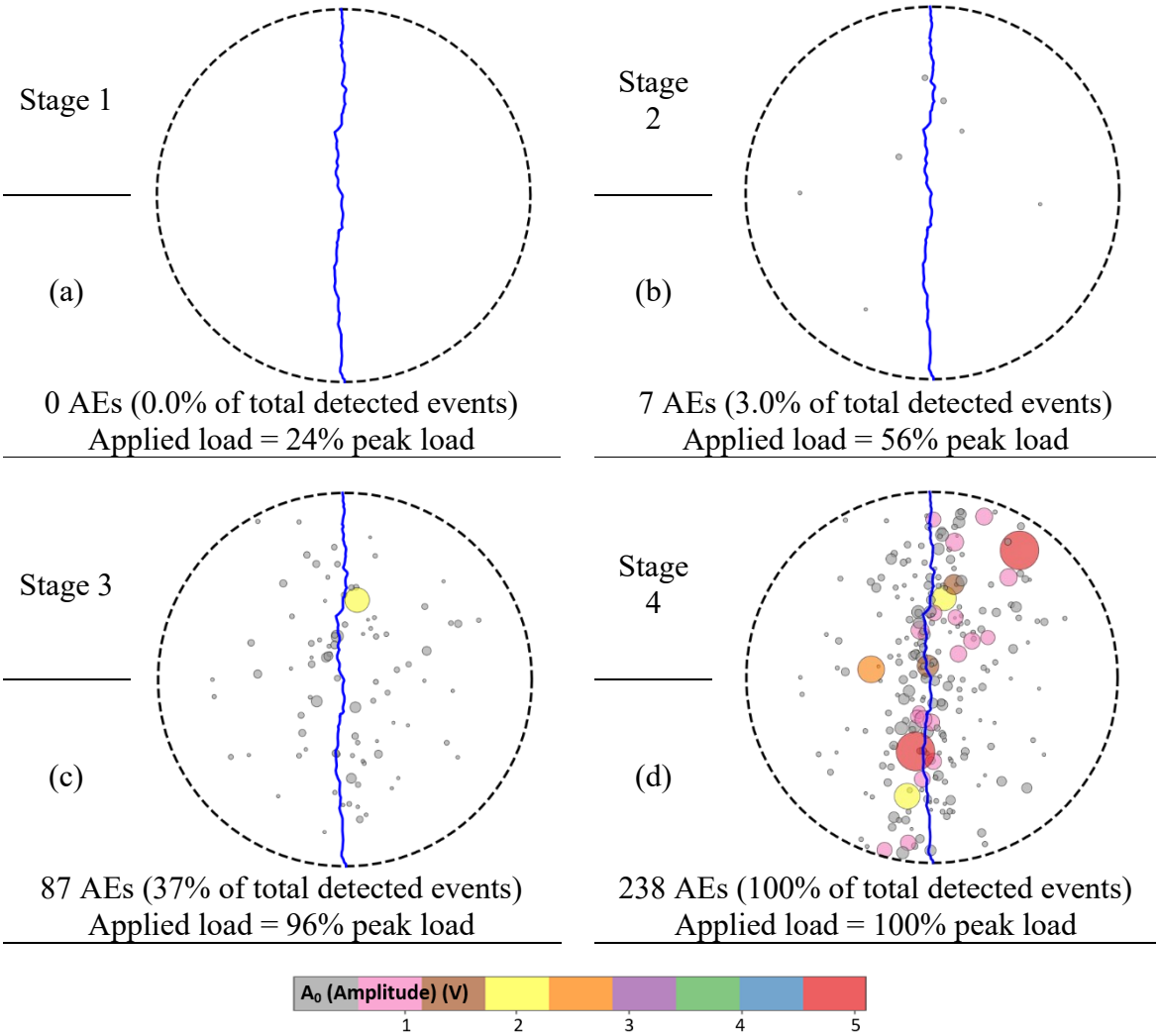

Fig. 3.5. Spatiotemporal evolution of the AE events within the specimen GI-1 with a loading rate of 1 μm/sec (high-loading rate) at monitoring points (a) point A, (b) point B, (c) point C, and (d) point D. The size and the color of circles represent the magnitude of the events. AEs appear from the beginning of the third stage and are almost evenly distributed throughout the vertical diameter of the specimen. That is, microcracks occurred throughout the vertical diameter of GI-1.

For GI-1, AEs distribute all along the diameter line, from the upper to the lower ends, of the specimen as soon as they begin to occur (Fig. 3.5). For GII-1, AEs mainly occur in the mid-diameter line of the specimen for all loading stages (Fig. 3.6). Furthermore, the comparison between Fig. 3.5 and Fig. 3.6 suggests that while the AE events are relatively widely spread within specimen GII-1, they are mainly located along the loading diameter in specimen GI-1. Even though the macroscopic fracture occurred along the loading direction for both specimens. This difference suggests that reducing the loading rate can result in a more complex fracture network and a greater process zone around the final macroscopic fracture. Moreover, in both cases, the density of microcracks and the

amplitude of AEs increase approaching the eventual macro fracture (Fig. 3.5 and Fig. 3.6). This is consistent with the findings of a previous study conducted on the fracture process zone in granite [50].

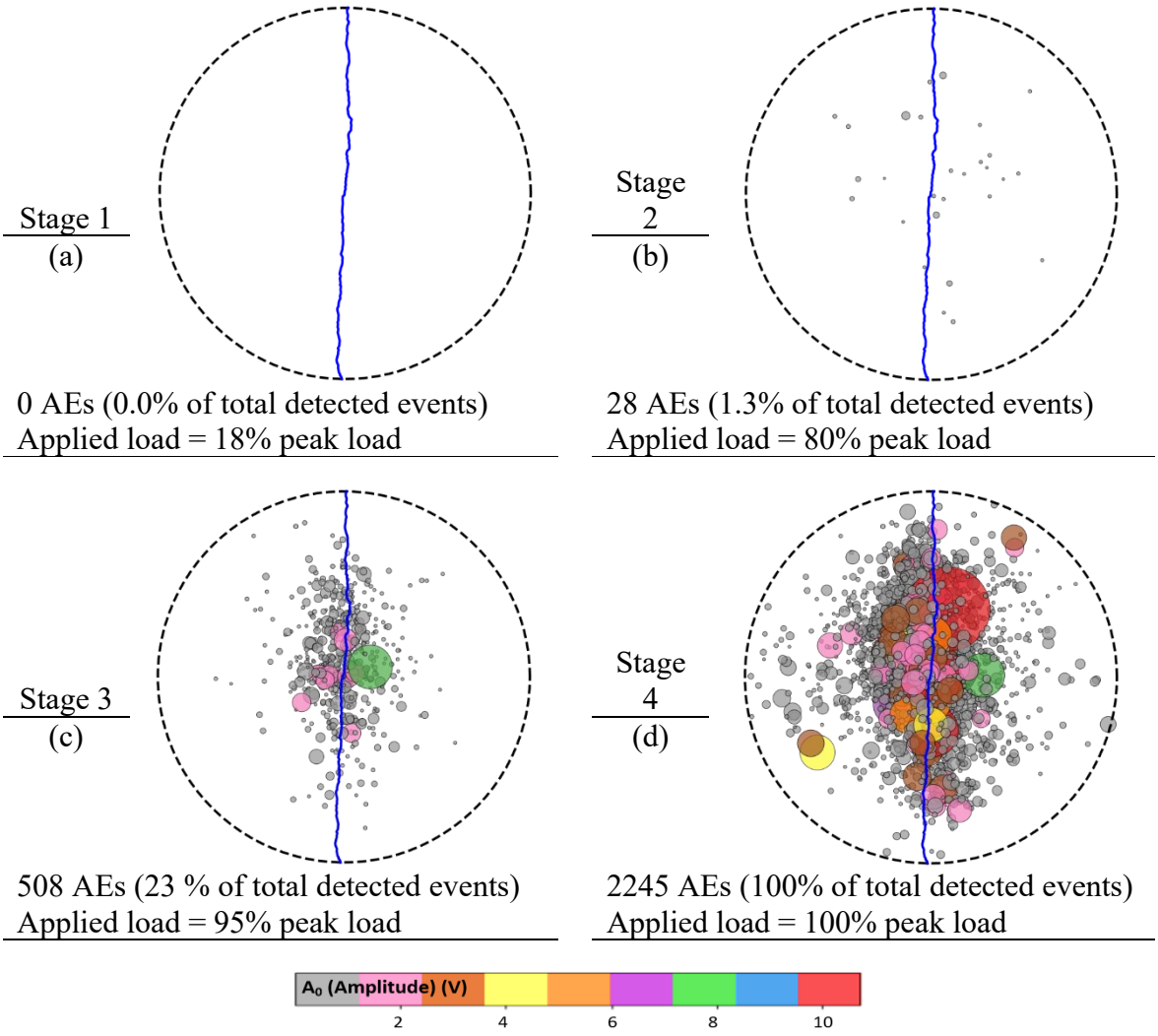

Fig. 3.6. Spatiotemporal evolution of the AE events within the specimen GII-1 with a loading rate of 0.1 µm/sec (low-loading rate) at monitoring points (a) point A, (b) point B, (c) point C, and (d) point D. The size and the color of circles represent the magnitude of the events. AEs appear from the beginning of the third stage and are mostly distributed in the middle part of the specimen along the loading diameter. That is, microcracks are mostly concentrated in the middle of GII-1.

3.3.3.2. Moment Tensor Inversion and Source Mechanisms

AE source mechanisms were determined from the moment tensor inversion (MTI) method, which yields a moment tensor that describes the force components acting at the source. The MTI was performed on events with six or more P-wave arrival detections following a 2D

implementation of the SiGMA (Simplified Green's functions for Moment tensor Analysis) procedure [134], [211]. We modified the procedure developed in [40] and used it in this study. The moment tensor obtained for each AE event was then decomposed into the isotropic (ISO), double-couple (DC), and compensated linear vector dipole (CLVD) components [211]. Finally, AEs were characterized as tensile (ISO ≥ 15% and CLVD ≥ -15%), compression (ISO ≤ -15% and CLVD ≤ 15%), or shear (|ISO| < 15%) [155].

Fig. 3.7 and Fig. 3.8 represent the spatial distribution of microcracks with different mechanisms at rock failure for GI-1 and GI-2 (group 1 specimens) and GII-1 and GII-2 (group 2 specimens). The leftmost column shows the AE events detected at failure, while the other three columns indicate the three microcrack mechanisms. The color codes represent the average focal amplitude (A_0) of the AEs. Note that the direction of line segments in the second columns of Fig. 3.7 and Fig. 3.8 (the tensile cracks) represents the direction of tensile crack propagation.

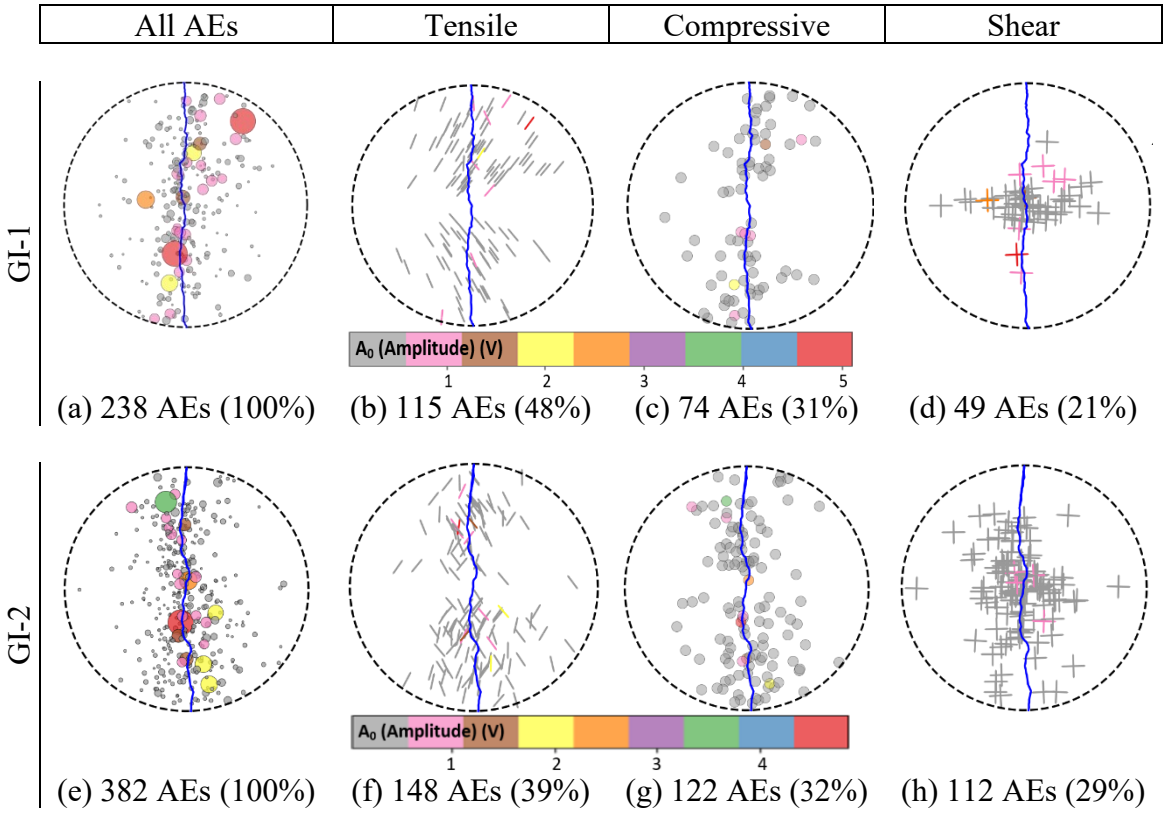

Fig. 3.7. Spatial distribution of AE events at failure load detected by a minimum of 6 sensors decomposed into different focal mechanisms for specimens tested under a loading rate of 1 µm/sec (high-loading rate): GI-1 (upper panel) and GI-2 (lower panel). The color codes represent the average focal amplitude (A_0) of AEs. The leftmost column indicates all detected AE events, while the other three columns show the distribution of tensile, compressive, and shear AE sources.

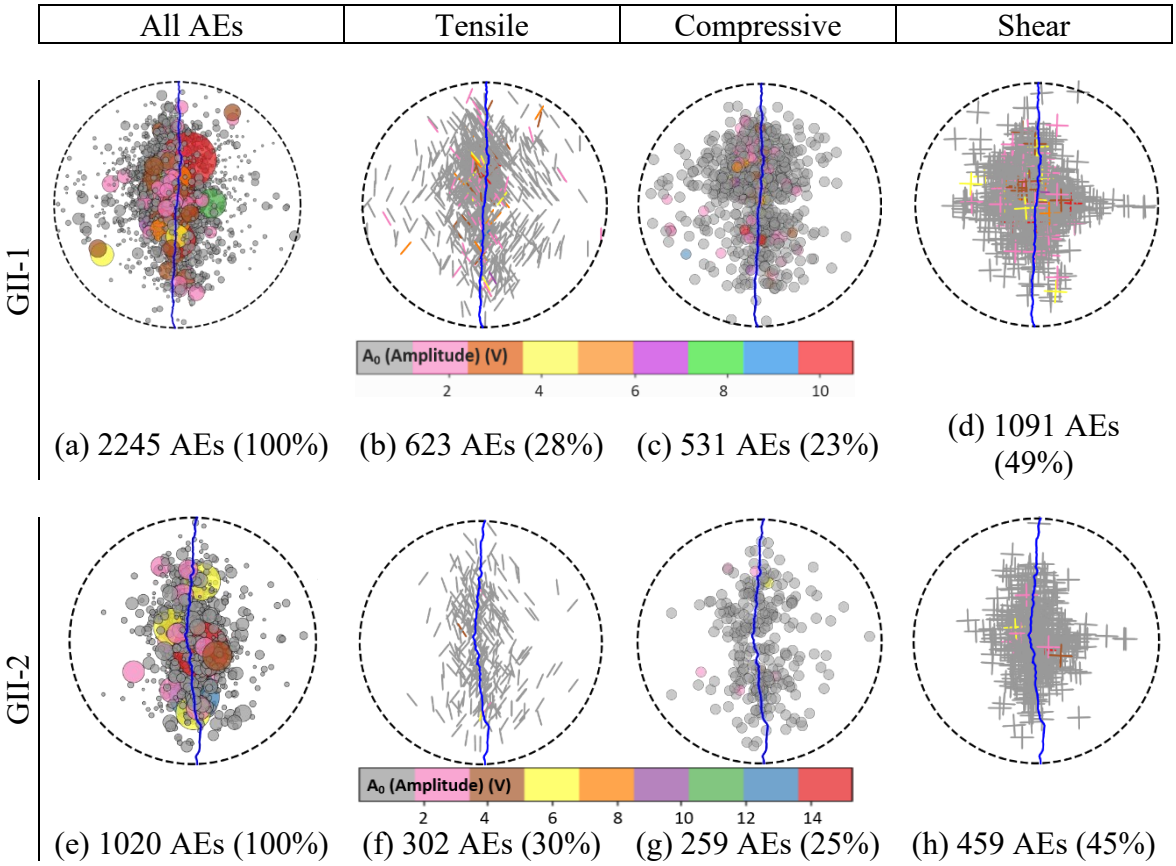

Fig. 3.8. Spatial distribution of AE events at failure load detected by a minimum of 6 sensors and AE focal mechanisms for specimens tested under a loading rate of 0.1 µm/sec (low-loading rate): GII-1 (upper panel) and GII-2 (lower panel). The color codes represent the average focal amplitude (A_0) of AEs. The leftmost column indicates all detected AE events, while the other three columns show the distribution of tensile, compressive, and shear AE sources.

In general, as seen in Fig. 3.7 and Fig. 3.8 and explained earlier, group 2 specimens (with a lower loading rate) underwent much more microcracks than those of group 1. In terms of AE activity and crack mechanisms, there is a strong consistency between specimens of the same group.

In Fig. 3.7, the number of AEs for both GI-1 and GI-2 is very close: 238 against 382. Tensile, compressive, and shear microcracks made up 48%, 31%, and 21% of all AE events for GI-1 (upper panel in Fig. 3.7). These numbers are 39%, 32%, and 29% for GI-2 (lower panel in Fig. 3.7). All three cracking mechanisms contributed to the formation of the macroscopic fracture. The tensile and compressive cracks are distributed all along the loading diameter. Shear events are relatively less scattered in the vertical direction and mainly concentrated in the middle third of specimens. In both cases (GI-1 and GI-2), tensile cracks orientated vertically to sub-vertically, which is, as expected, parallel to the applied axial compression. In both specimens, shear-type events are mostly concentrated in the

middle part of the discs, while tensile and compressive sources are distributed in the upper and lower halves of specimens. This is not in agreement with the linear elastic fracture mechanics (LEFM) theory hypothesizing that the applied compression over the Brazilian discs triggers tensile failure at the specimen's centre [66], [102]. There are two potential explanations for this discrepancy. First, the macroscopic fracture could originate from the centre under the tensile mechanism, where shear microcracks coincided. As a result, small-scale tensile cracks might have been masked by large-scale shear cracks. Second, the absence or the low number of tensile, compressive, and especially shear events might be because of the system saturation at the failure point, making them undetectable by AE sensors.

Compared with GI-1 and GI-2, the absolute number of all crack types increased with decreasing the loading rate for both GII-1 and GII-2 (Fig. 3.8). For GII-1, of 2245 detected AEs, 623 AEs tensile, 531 are compressive, and 1091 AEs are compressive and shear cracks. For GII-2, among the 1020 detected events, we found 302 tensile, 259 compressive, and 459 shear AEs. It was observed that all three cracking mechanisms contributed to the formation of the macroscopic fracture and are well distributed all along the loading diameter within the process zone. In particular, both specimens had many tensile events at the disc centre. That is, with decreasing the loading rate, a higher number of tensile sources accumulated at the disc centre leading to the initiation of macroscopic tensile failure from the centre, as the DIC results will confirm (e.g., Fig. 3.9b). In addition, the lower number of tensile and compressive AEs in the centre of the samples might be because of their low seismic energy making them undetectable by AE sensors. Compared with Fig. 3.7, the absolute number of all crack types has increased, while the percentage of tensile and shear events has decreased and increased, respectively. This reduction of the percentage of detected tensile cracks and the augmentation of the percentage of detected shear cracks under a lower loading rate could be because 1) low-energy tensile microcracks might not be detected by AE sensors, and 2) more shear microcracks can be detected as the system doesn't saturate.

The average tensile and shear source mechanisms for Group 1 specimens, i.e., GI-1 and GI-2, are 43% and 25%. These values for Group 2 specimens are 29% and 47%, respectively. As seen, the MTI results indicate that with decreasing the loading rate, the percentage of shear-type events increases, while that of tensile AEs reduces. This can be explained as follows. With decreasing the loading rate, much more microcracks occur within the process zone during the loading process (compare Fig. 3.7 and Fig. 3.8). The generated microcracks are composed of both tensile and shear types. However, due to the low loading rate, many tensile microcracks might happen under subcritical crack growth, and therefore their low seismic energy may not be detected by AE sensors. At the same time, most of the shear events are captured as they emit high seismic energy. Therefore, this results in a much higher percentage of shear AEs (relative to total detected events) than the percentage of tensile AEs.

For both loading rates, the compressive microcracks are detected on the upper and lower part of the specimens where we expected compressive load due to the essence of the Brazilian test. This is in accordance with previous studies such as [66], [126], [128], [194].

Fig. 3.7 and Fig. 3.8 indicate that the shear cracking mechanism is present at the disc centre for all tested specimens, regardless of the loading rate. This suggests that the fracturing process is composed of a combination of tensile and shear cracking, even in the Brazilian test in which a tensile-induced macroscopic failure is assumed. Therefore, the tensile strength of rock specimens obtained from the Brazilian test is controlled by both tensile and shear microcracking. This may explain why the Brazilian tensile strength of rocks exceeds that obtained from the direct tension test [22], [27], [66].

3.3.3.3. DIC Monitoring of the Fracturing Processes

The displacement and strain fields in the test specimens were obtained using the DIC technique. The DIC analysis was performed using the software VIC-2D, developed by Correlated Solutions, Inc [178]. The measurements were taken for a region of interest (ROI) covering the central part of specimens, as shown in Fig. 3.9a and b; this ROI involves the area where the final macroscopic fractures occurred. A subset size of 29 × 29 pixels was chosen to ensure a unique speckle pattern within each subset [157], [178]. Also, a step size of 7 pixels was picked between subset meshes to get independent and non-repetitive data points over the specimen surface [157], [178].

Fig. 3.9 shows representative examples of the contour plots of the horizontal plastic strain ($i.e.,\ \varepsilon_{xx}^{p}$) in the desired ROI immediately prior to failure (point D in Fig. 3.4) for experiments conducted under two different loading rates. The same legend scale is applied to both cases to better visualize the tensile strain developed across the specimens' surfaces and to determine the fracture process zone (FPZ) just before the occurrence of the final macroscopic fractures. The extremes of the legend scale were set to values that include the compression and the tension strains when the first visible fracture occurs.

It should be noted that the formation of microcracks (i.e., AE events) in granite, as a brittle rock, corresponds with plastic deformation [10]. Therefore, to compare the AE and the DIC results properly, it is necessary to compute the plastic strain component ($i.e.,\ \varepsilon_{xx}^{p}$) rather than the total tensile strain in the horizontal direction ($i.e.,\ \varepsilon_{xx}$). The total tensile strain is composed of the elastic and the plastic strain components. Therefore, the plastic strain component can be determined by subtracting the elastic strain component from the total strain. Here, the AE events detected during the rock deformation process are used to determine the elastic limit. As explained above, until point B in Fig. 3.4a and b, less than 3% of the total AE events were generated for both GI-1 and GII-1. Therefore, the maximum horizontal tensile strain at point B was assumed to be a reasonable estimation of the elastic limit. This limit was around 550 με (GI-1) and 950 με (GII-2).

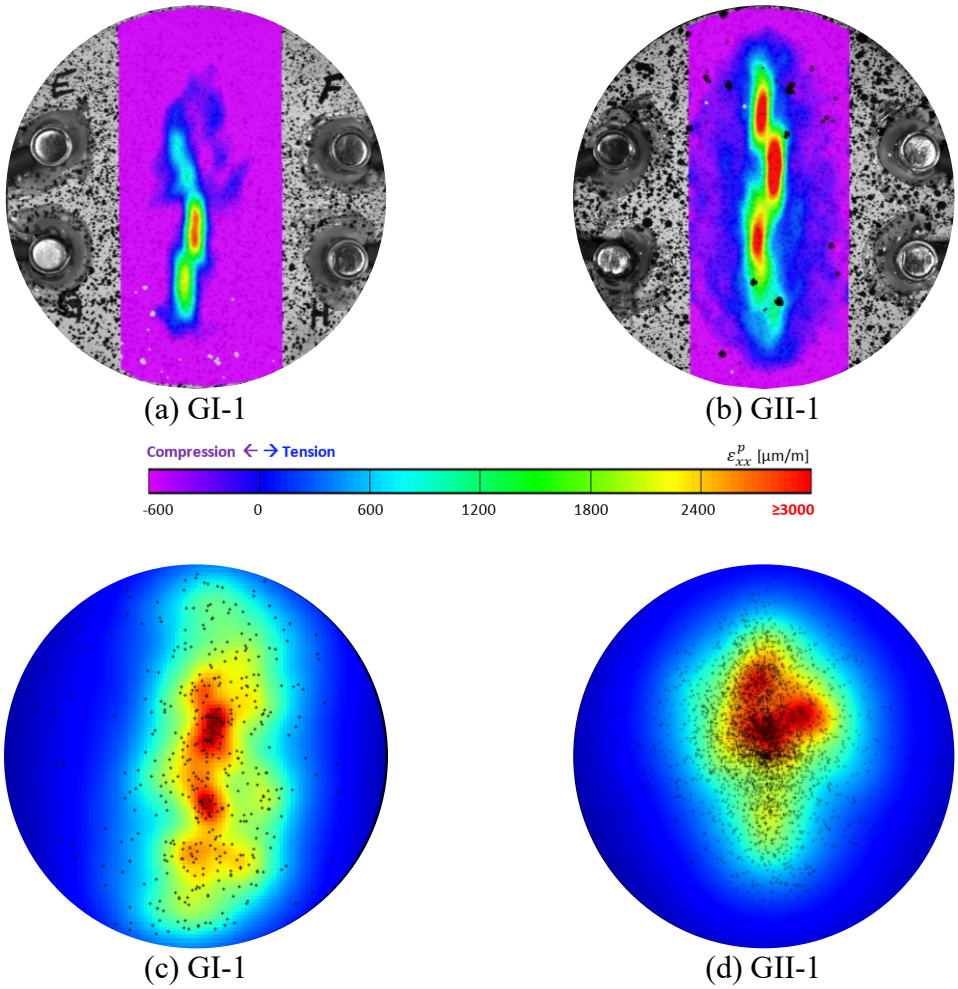

Fig. 3.9. Horizontal plastic strain field immediately prior to failure (point D in Fig. 3.4) for (a) specimen GI-1 with a loading rate of 1 µm/sec (high-loading rate) and (b) specimen GII-1 with a loading rate of 0.1 µm/sec (low-loading rate), and scatter plot of AE distributions colored by density for (c) specimen GI-1 and (d) specimen GII-1 (darker shades of red indicate higher concentrations of AE events).

A qualitative assessment of Fig. 3.9 reveals that the horizontal extension accumulated at the planar centre of the discs for both specimens. The maximum plastic tensile strains are seen at or near the centre point of specimens where the macroscopic fractures occurred. This confirms the validity of the obtained experimental results from the Brazilian tests [102], [117]. Moreover, the strain contours in Fig. 3.9a and b emphasize that even though the maximum tension concentration appears in a narrow strip along the loading direction for both specimen groups, the horizontal extent of the process zone is far wider for the specimen subjected to the lower load rate (i.e., GII-1) compared to that tested under the higher load rate (i.e., GI-1). That is, for lower loading rates, the induced tensile strain along the loading direction produces a wider process zone consisting of more microcracks, as can also be deduced from a comparison between Fig. 3.9, Fig. 3.5, and Fig. 3.6. This again

implies that reducing the loading rate can lead to a more complex process zone in brittle materials such as granite. The DIC process zone illustrated in Fig. 3.9a and b is consistent with the AE process zone exhibited in Fig. 3.5d and Fig. 3.6d, respectively. In addition, Fig. 3.9c and d show the scatter plot of the captured AEs colored by density for the specimens GI-1 and GII-1. It is observed that the extent of the DIC process zone (Fig. 3.9a and b) is in good agreement with the extent of the process zone from AE data (Fig. 3.9c and d) for both specimens.

Interestingly, the zones of the highest concentration of horizontal plastic strain coincided very well with zones of the highest spatial concentration of AEs. However, in both cases, the AE process zone is slightly extended beyond the DIC process zone. The reason for this discrepancy could be that AEs are triggered by microcracks occurring in the whole volume of the specimen, while DIC strain measurements are only related to the surface deformation of the specimen.

Fig. 3.10 and Fig. 3.11 show the contours of the horizontal plastic strains (ε_{xx}^{p}) at four monitoring points on the stress-strain curves for GI-1 (Fig. 3.4a) and GII-1 (Fig. 3.4b), respectively. In addition, the strain fields corresponding to the early stages of the loading process and immediately after the formation of the final macro fracture are shown.

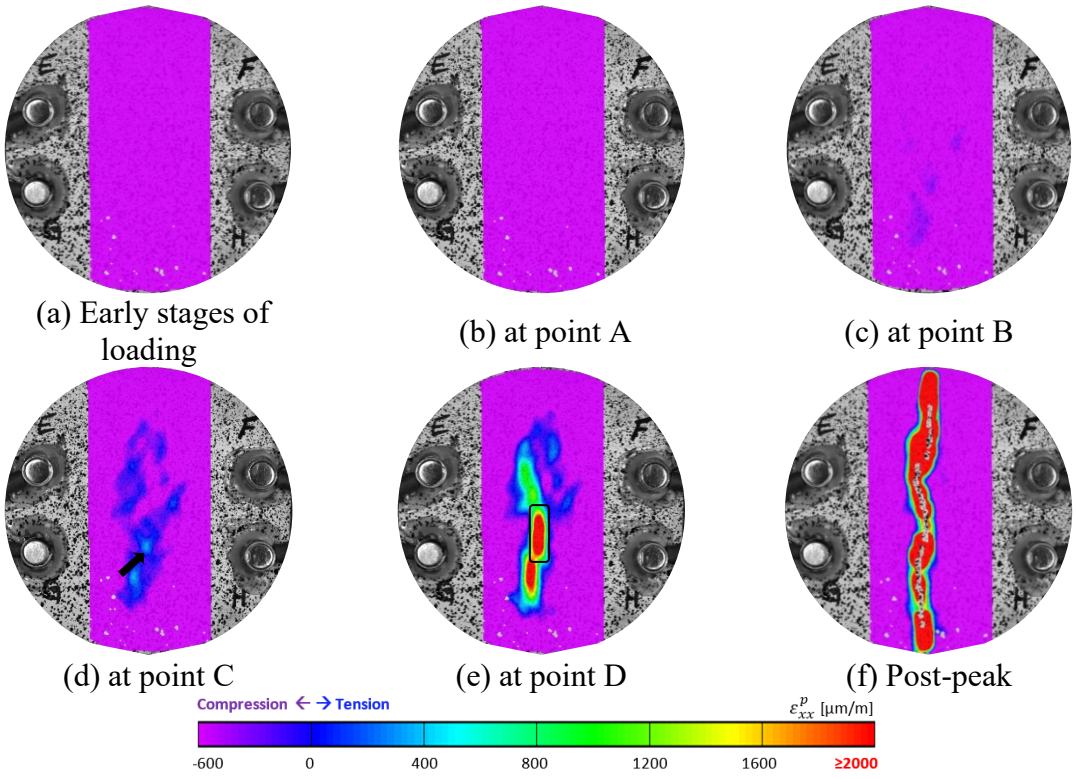

Fig. 3.10. Horizontal plastic strain (ε_{xx}^{p}) development in the ROI during the loading process for specimen GI-1 (high-loading rate). The plastic strain begins to appear at the beginning of the third stage and mostly accumulates in a narrow strip along the loading direction.

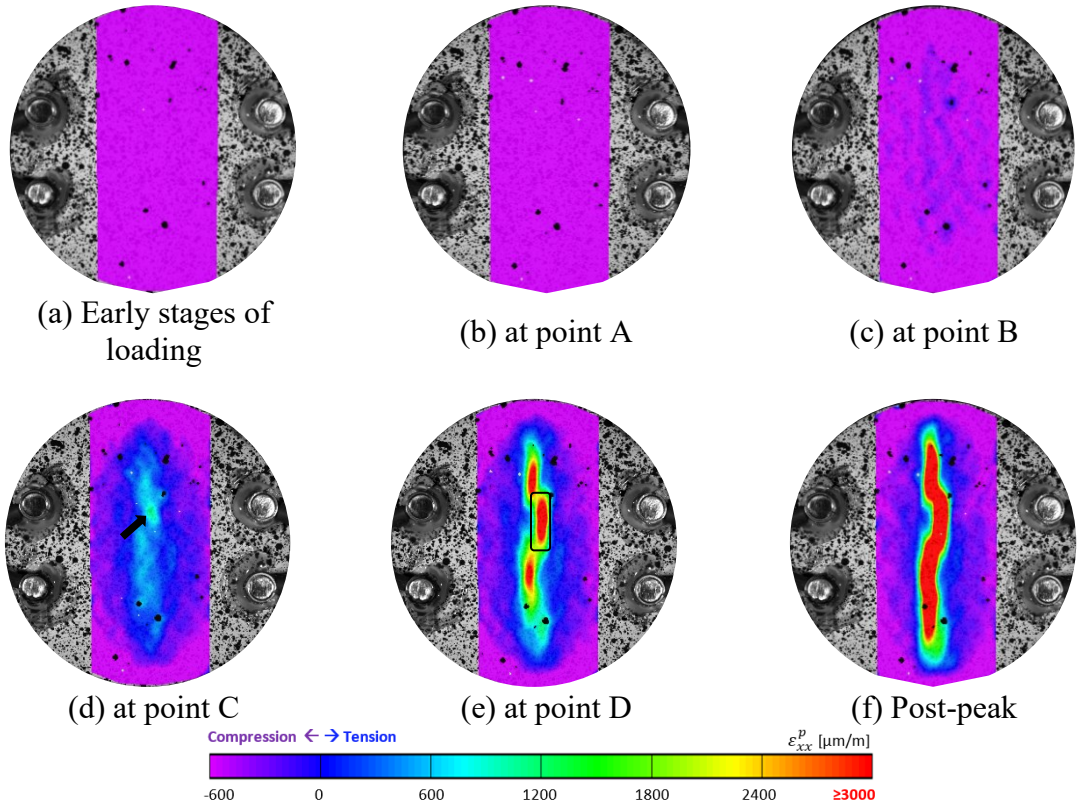

Fig. 3.11. Horizontal plastic strain (ε_{xx}^{p}) development in the ROI during the loading process for specimen GII-1 (low-loading rate). The plastic strain begins to appear at the beginning of the third stage and accumulates in the broader area (compared to GI-1 in Fig. 3.10) along the loading direction.

Since the first loading stage (up to point A) corresponds to the initial load transfer process at the specimen-loading jaws contact, not much strain was generated by the early loading levels as exhibited in Fig. 3.10a and b. Fig. 3.10c depicts the FPZ at the end of the second stage (point B in Fig. 3.4a). The contour plot indicates a negligible plastic strain at this stage. As shown by the trend of the cumulative hits and energy in Fig. 3.4a as well as the located AE sources in Fig. 3.5, with loading beyond point B, further plastic strain is accumulated in the specimen. When the applied load reaches 96% of the peak load (point C in Fig. 3.4a), a plastic strain concentration appears near the centre of the specimen along its vertical diameter (indicated by a black arrow in Fig. 3.10d). However, strain accumulation is not yet associated with the formation of any macro crack. Fig. 3.10e displays the strain field at the peak load, where the development of the FPZ is completed with the appearance of the first visible fracture. A black rectangle shows the location of the first macro crack in Fig. 3.10e. Note that two regions of dominant tensile strain are located in the contour plot of Fig. 3.10e, but the macroscopic fracture originated from the upper strain localization.

Furthermore, the maximum horizontal plastic strain (ε_{xx}^{p}) at the failure load was about 2200 με. Finally, Fig. 3.10f illustrates the FPZ immediately after the peak load. The macroscopic fracture initiated at the specimen's central part and then propagated along the loading direction toward the loading platens.

Similar explanations apply to the development of the DIC process zone for GII-1 (shown in Fig. 3.11), with two important differences. 1) in all loading stages, the DIC process zone for GII-1 is larger than that of GI-1 (Fig. 3.10 vs. Fig. 3.11). This difference in the extent of the process zones was earlier highlighted in Fig. 3.5 and Fig. 3.6. Fig. 3.10 and Fig. 3.11 illustrate the plastic strain components (ε_{xx}^{p}) in the horizontal direction, meaning that $\varepsilon_{xx}^{p} > 0$ reflects damage in the specimens. The purple color shows zero plastic strain (or compression, if any), and the colors from blue to red represent the tensile plastic strain (damage) in the sample. Therefore, the extent of the blue color on the purple background was supposed to indicate the size of the FPZ. 2) the maximum plastic tensile strain at failure for GII-1 was 3300 με, which is greater than that of GI-1 (color bars in Fig. 3.10 vs. Fig. 3.11). This difference can be because, under the lower loading rate (i.e., for GII-1), the applied load can better transfer through the specimen; thereby, the tensile microcracks take more time to develop, which leads to a higher horizontal extension in the specimens.

To further evaluate the location of the first macro crack, the horizontal strain variation in the process zone throughout the loading process was monitored at 32 points along the observed macro fracture path. Fig. 3.12a and Fig. 3.13a show the location of the monitoring points on GI-1 and GII-1. Fig. 3.12b and Fig. 3.13a depict the variation of the total horizontal tensile strain (ε_{xx}) in the trace points and the applied load curves for GI-1 and GII-1, respectively. No local strain is visible in the first loading stage for both specimens, and specimens can be regarded as entirely elastic. With increased applied load beyond point A, the horizontal extension occurs with a low accumulation rate throughout the second loading stage and almost equally in all monitoring points. After point B, the strain accumulation rate increases rapidly, reaching its maximum value at points 21 (GI-1) and 14 (GII-1). When the loading process enters the fourth stage, a dramatic transition from the process zone to the initiation of a macro crack at these points is evident.

To filter out the plastic strain formation during the process zone development, the value of the elastic strain component was subtracted from the apparent total strain in all monitoring points and replotted in a zoom-in box in Fig. 3.12c and Fig. 3.13c. As explained before, the elastic limit was assumed to reach when the first AE events were detected within the specimen (Fig. 3.5b and Fig. 3.6b), which is about 550 and 950 με for GI-1 and GII-1, respectively. These elastic limits were equivalent to about 20% of the total strain for both GI-1 and GII-1.

As highlighted by Fig. 3.12c and Fig. 3.13c, GI-1 and GII-1 undergo almost no plastic deformation before point B. The applied load in the third stage (i.e., from point B to C) results in the formation and accumulation of plastic deformation within the granite specimens. The plastic deformation is more concentrated in the lower half (GI-1) and the

upper half (GII-1) of the specimen close to the disc centre. As the load increases, the accumulation rate of plastic strain accelerates, and the last stage exhibits much more deformation accumulation than the third stage. Finally, points 21 (GI-1) and 14 (GII-1) underwent the most rapid plastic strain increase, representing the origin of the macroscopic fractures.

The trend of the plastic strain accumulation in the DIC process zone is strongly consistent with the AE events accumulation. For example, as shown in Fig. 3.5c and Fig. 3.6c., 37% (GI-1) and 23% (GII-1) of the total AE events that occurred during the third loading stage correlate well with the small amount of plastic deformation developed in this stage (Fig. 3.12c and Fig. 3.13c). Moreover, the majority of the AE events (63% and 77% for GI-1 and GII-1, Fig. 3.5d and Fig. 3.6d) in the AE process zone were detected in the last stage that is again confirmed by the fact that the majority of the plastic strain in the DIC process zone occurred during the fourth stage (Fig. 3.12c and Fig. 3.13c).

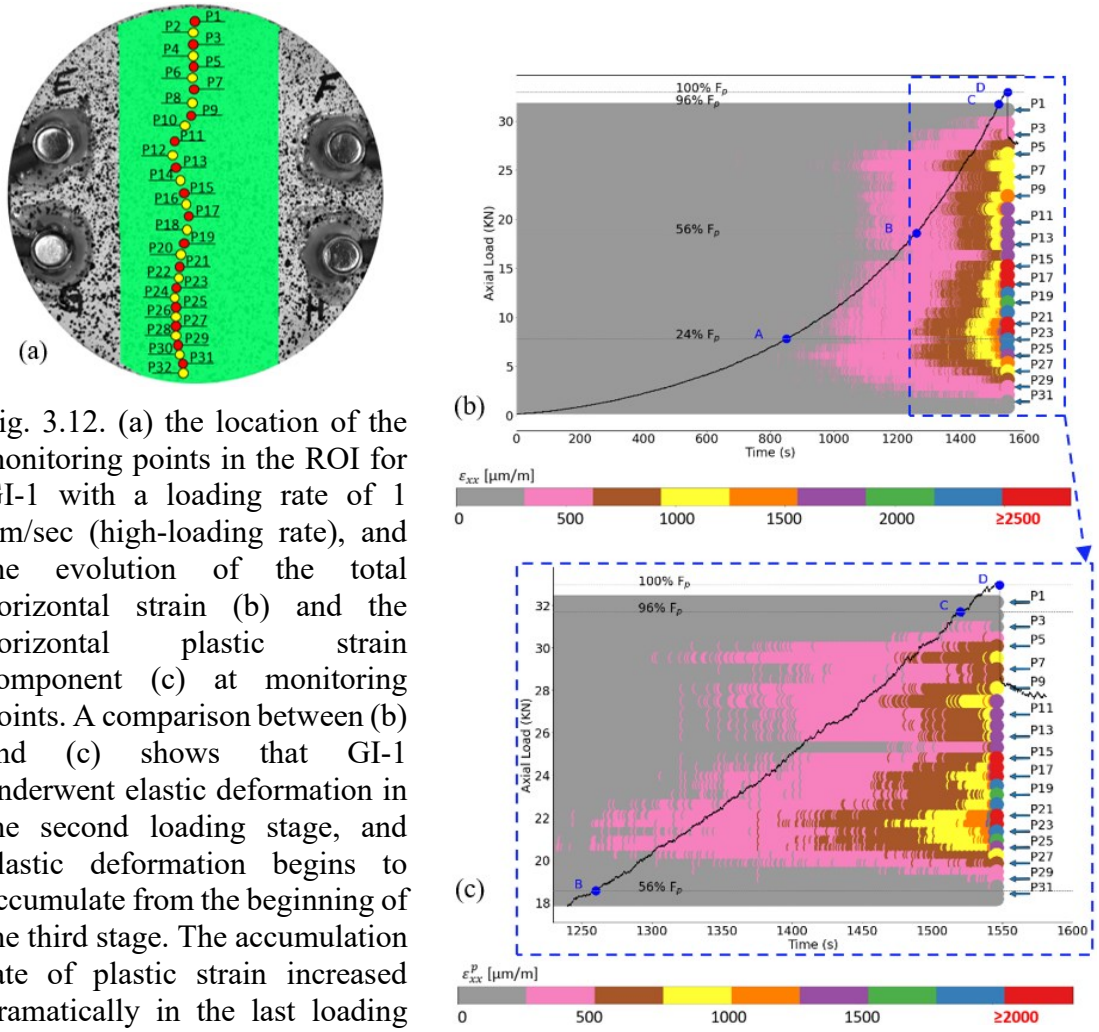

Fig. 3.12. (a) the location of the monitoring points in the ROI for GI-1 with a loading rate of 1 μm/sec (high-loading rate), and the evolution of the total horizontal strain (b) and the horizontal plastic strain component (c) at monitoring points. A comparison between (b) and (c) shows that GI-1 underwent elastic deformation in the second loading stage, and plastic deformation begins to accumulate from the beginning of the third stage. The accumulation rate of plastic strain increased dramatically in the last loading stage, which lasted a very short time.

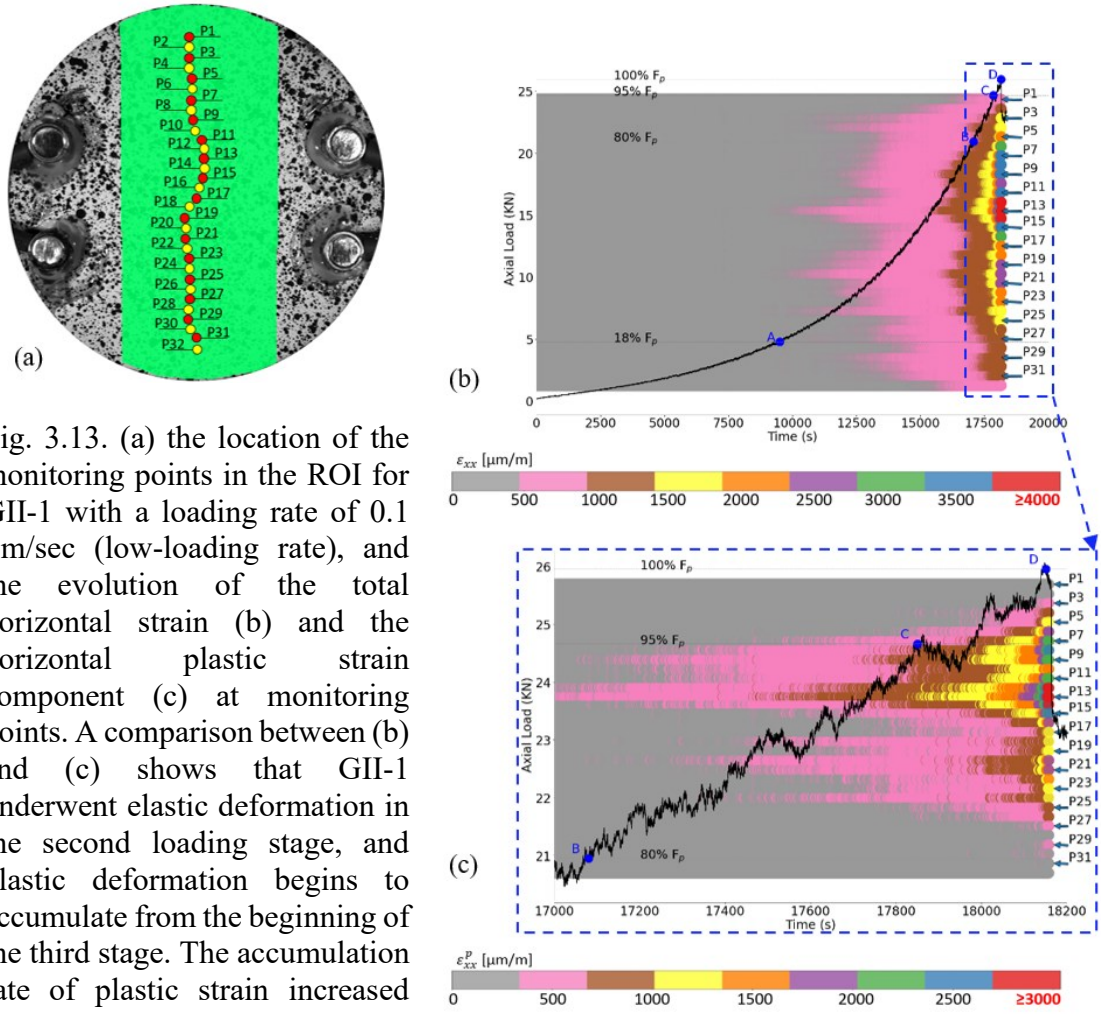

Fig. 3.13. (a) the location of the monitoring points in the ROI for GII-1 with a loading rate of 0.1 μm/sec (low-loading rate), and the evolution of the total horizontal strain (b) and the horizontal plastic strain component (c) at monitoring points. A comparison between (b) and (c) shows that GII-1 underwent elastic deformation in the second loading stage, and plastic deformation begins to accumulate from the beginning of the third stage. The accumulation rate of plastic strain increased dramatically in the last loading stage, which lasted a very short time.

3.3.3.4. Roughness Characterization of the Generated Macroscopic Fractures

To further evaluate the fracturing behaviour of tested granite specimens under two different loading rates, the roughness of the surface of the generated macrocracks was studied. The fracture surfaces were scanned, and a 3D cloud of points was acquired and processed, as explained in APPENDIX 1. The roughness parameters were then calculated for the processed 3D surfaces.

Fig. 3.14 illustrates the 3D geometry of the macroscopic fractures for the GI-1 and GII-1. Note that as both faces of each fracture were almost identical, only one of the faces is displayed.

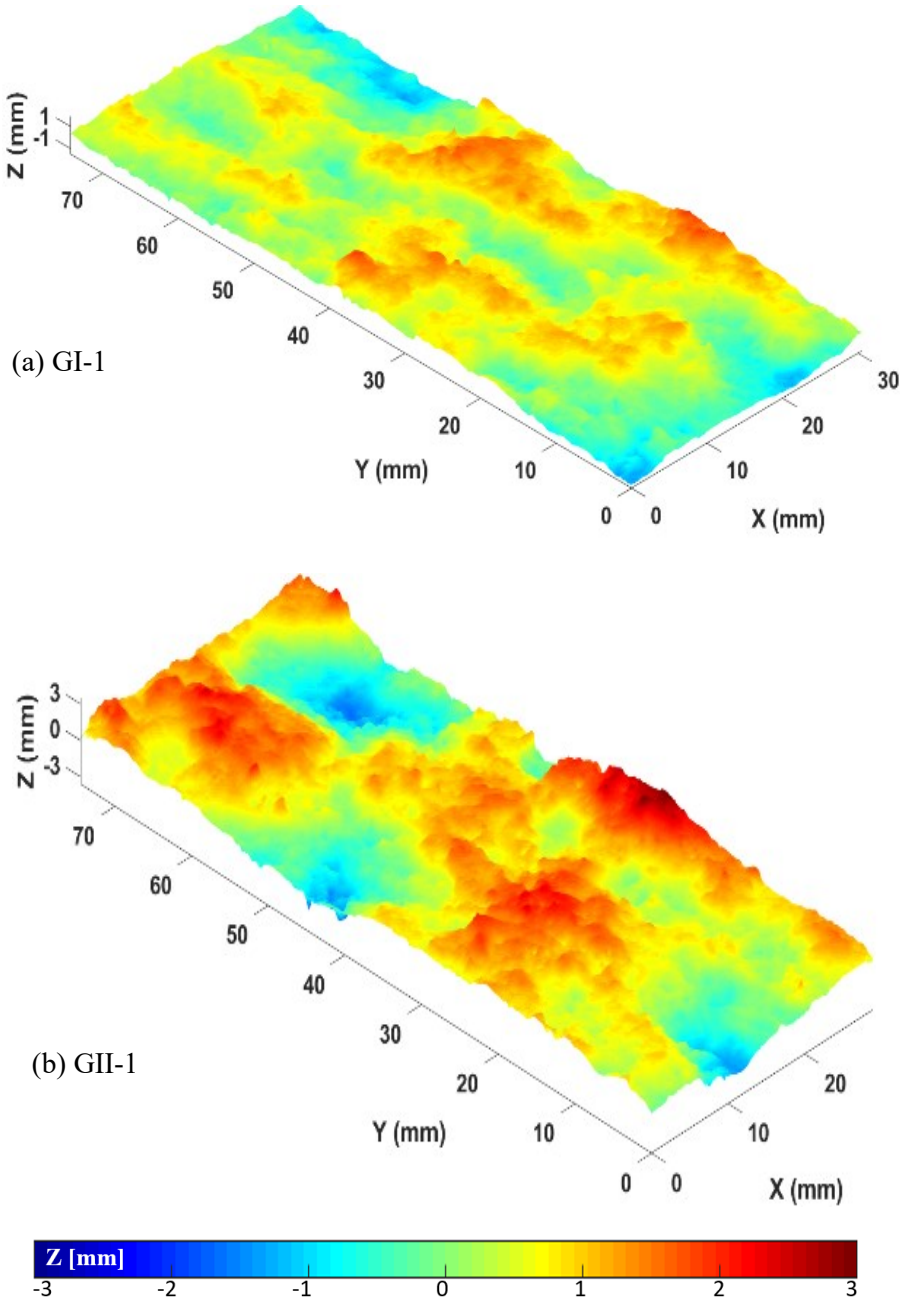

Fig. 3.14. The 3D surface of the macroscopic fractures for (a) GI-1 with a loading rate of 1 μm/sec (high-loading rate) and (b) GII-1 with a loading rate of 0.1 μm/sec (low-loading rate). The lower the loading rate (GII-1), the higher the surface roughness of the main fracture.

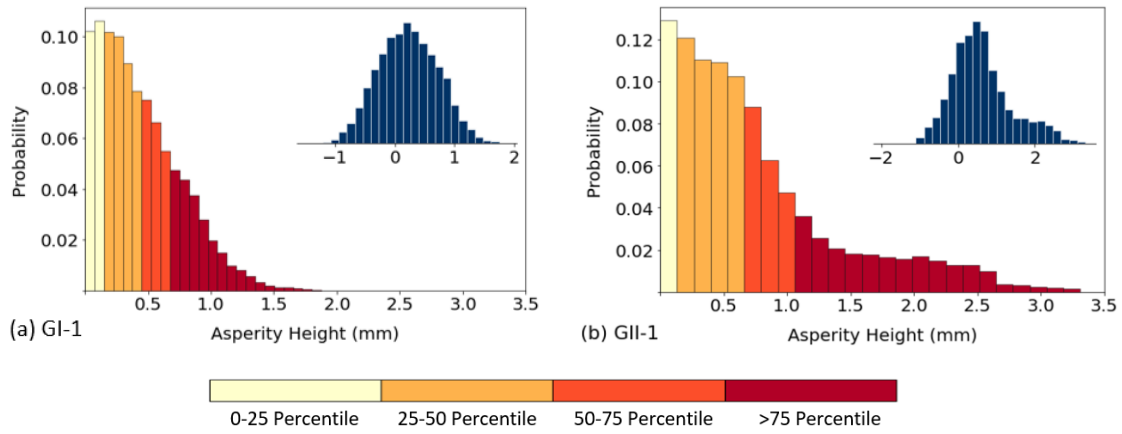

Fig. 3.15. Histogram of absolute asperity height over the fracture surface for (a) GI-1 with a loading rate of 1 μm/sec (high-loading rate) and (b) GII-1 with a loading rate of 0.1 μm/sec (low-loading rate). The colors represent various percentiles of height distribution. The insets are the histogram of the complete height distribution of asperities; positive and negative numbers indicate picks and valleys, respectively. The lower the loading rate (GII-1), the higher the surface roughness of the main fracture.

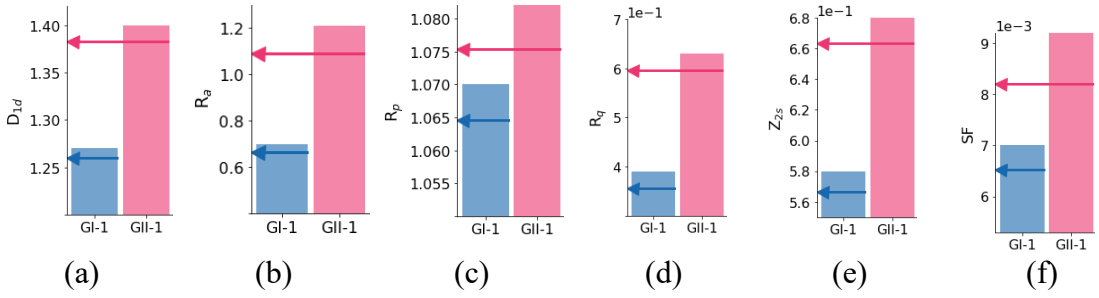

Fig. 3.16. Roughness parameters (a) D1d, (b) Ra, (c) Rp, (d) Rq, (e) Z2s, and (f) SF of the macroscopic fractures for GI-1 with loading rate of 1 μm/sec (high-loading rate) and GII-1 with loading rate of 0.1 μm/sec (low-loading rate). The blue and red arrows in each subplot indicate the average values of the corresponding roughness parameters for the first and second groups of specimens. The lower the loading rate (GII-1), the higher the surface roughness of the main fracture.

Compared with GI-1, the fracture surface of GII-1 is composed of a wider range of asperity heights, i.e., higher peaks and deeper valleys. This is better highlighted from the plot of the distribution of the absolute roughness height (Fig. 3.15). The insets illustrate the complete distribution of asperity height relative to the best-fit plane of the fracture surface. The color codes in Fig. 3.15 indicate the various percentile of the asperity heights. For GI-1, almost 40% of asperities have an absolute height higher than 0.5 mm, with a maximum value of 1.8 mm. While, for GII-1, nearly more than 60% of asperities have an absolute height higher than 0.5 mm, with a maximum value of 3.3 mm. This difference in surface roughness and asperity height distribution between GI-1 and GII-1 was similarly observed between all specimens from groups I and II. These observations imply that the surface of

the generated macrocracks in Brazilian discs under a lower loading rate (i.e., group 2) is rougher than those of specimens tested under a higher loading rate (i.e., group 1). This was confirmed by determining the roughness parameters, including SF, R_a, R_p, R_q, $Z2_s$, and D_{1d} for the fracture surfaces (Fig. 3.16). The roughness parameters were calculated according to the procedure given in APPENDIX 1. Fig. 3.16 compiles different measured roughness parameters derived from the fracture surface of GI-1 and GII-1 (in the direction of axial loading). The blue (group 1) and red (group 2) arrows represent the average values of roughness parameters. In all cases, the average values of roughness parameters derived from the data of the first group of specimens fall below those of the second group, confirming that the indirect tensile test under a lower loading rate led to macroscopic fractures with rougher surfaces.

As explained in APPENDIX 1, Hurst exponents for 2D roughness profiles were first computed to calculate the fractal dimension values D1d (Fig. 3.16a). Note that 2D profiles were extracted from the fracture surface along the loading direction. The Hurst exponent of the entire fracture surface was then obtained by stacking and averaging all 2D Fourier spectra. Upon determining the average Hurst exponent of the surfaces, their corresponding fractal dimension was calculated using Eq. A1. 7 [207], [212], [213]. Fig. 3.17 shows the typical average power spectra of the fracture surface of GI-1 and GII-1. The light gray graphs represent the spectra of individual roughness profiles extracted from the surfaces, the black lines are maximum and minimum limits, and the red graphs are the average power spectrum of the given fracture. The corresponding Hurst exponent is obtained as the slope of the linear fit to the red graph.

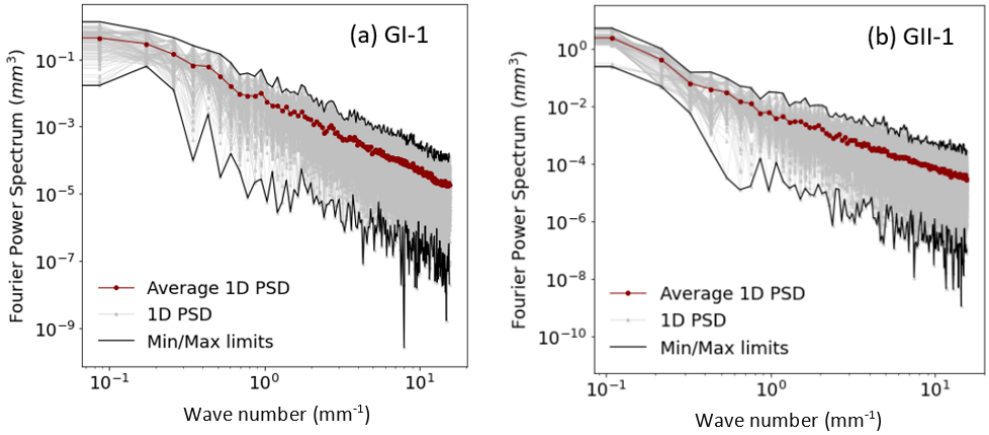

Fig. 3.17. Average power spectrum (red line) of the fracture surface of (a) GI-1 with a loading rate of 1 µm/sec (high-loading rate) and (b) GII-1 with a loading rate of 0.1 µm/sec (low-loading rate). Each gray line represents the power spectra of a 2D profile extracted from the corresponding fracture surfaces.

Further assessment of the AE data was performed to determine whether there is any potential correlation between the localized AE sources and the surface roughness of the generated macroscopic fractures. Two different plots are depicted for GI-1 and GII-1 in

Fig. 3.18. The AE contour plots (left plots) show the density of the AE sources distributed over the surface of the macro-fractures. Darker shades of red indicate a higher concentration of AE events, and darker shades of blue indicate lower AE activities. The fracture surface plots (right plots) also show the asperity height distribution over the produced macro fractures. The color of the fracture surface plots can be interpreted by the color bar at the bottom of Fig. 3.18. The scatter plot of AEs distribution is also superimposed over the fracture surface plots.

It has been shown by previous researchers such as Moradian et al. [58] and Goebel et al. [214] that there is a clear link between the location and the magnitude of AEs with the asperity height distribution of the joint surfaces during shear failure. However, we could not see such a correlation between the cloud of the AE events and the roughness of the produced fracture in our experiment, in which the fractures were created under tensile failure.

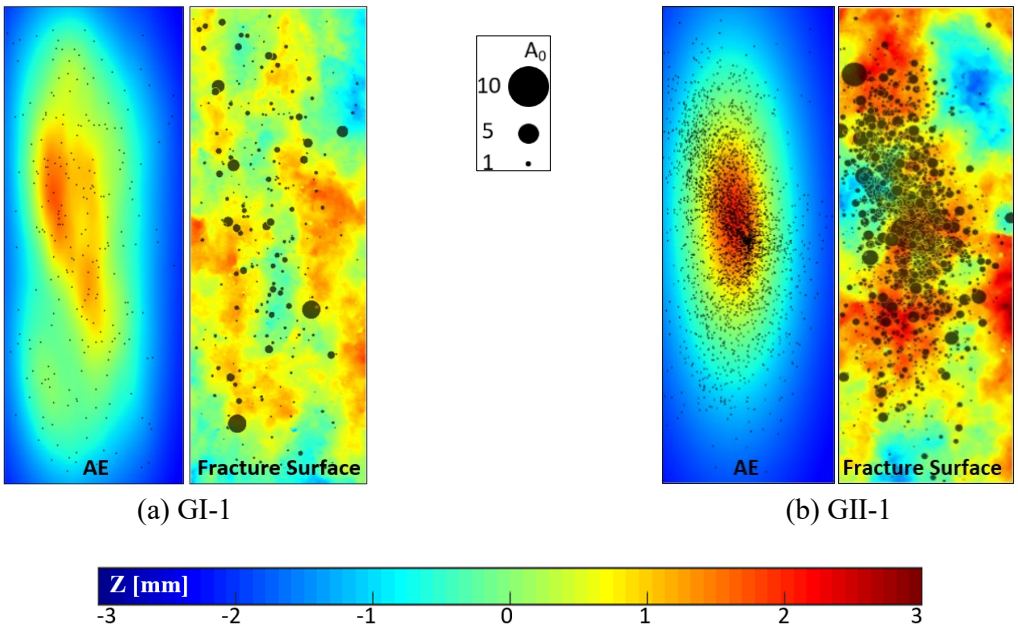

(a) GI-1 (b) GII-1

Fig. 3.18. Contour plot (left plots) of AE events and the fracture surface plots (right plots) for (a) GI-1 with loading rate of 1 µm/sec (high-loading rate) and (b) GII-1 with loading rate of 0.1 µm/sec (low-loading rate). The color bar at the bottom is associated with the fracture surface plots. The size of the circles shows the relative amplitude of the AEs superimposed over the fracture surface plots. There seems to be no clear correlation between the spatial distribution of AEs and the surface roughness of the main fractures.

3.4. Discussion

3.4.1. Acoustic vs. Visual Observation of Fracturing Processes

The results indicate a strong correlation between the progressive evolution of AE events (i.e., internal deformation) and the DIC strain localizations (i.e., extensional deformation ε_{xx}). However, AE points out a larger process zone than the DIC (Fig. 3.9). A similar

phenomenon was observed by Li and Einstein [186] and Alam et al. [175], who experimentally studied pre-notched beam specimens under bending tests. This was also highlighted by Arno and Christian [50], reporting that the width of the FPZ obtained from AE data and optical crack inspection was 9 and 2 times the grain size in granite, respectively. The larger AE process zone could be because the AE represents the cracking of the whole volume, while DIC only shows surface deformations. That is, even the slightest internal deformation (e.g., friction between grains) can be reflected in the form of AE events and extend the AE process zone, while DIC is not capable of capturing them. For example, in Fig. 3.5d and Fig. 3.6d, most AEs appearing far from the loading diameter have small magnitude values, which can represent very small volumetric deformations not appearing at the specimen's surface. In general, we can say that AE has a higher resolution in imaging the nucleation and growth of the FPZ.

Another reason for obtaining a larger FPZ from AE data might be related to the fact that AE events were localized using a constant P-wave velocity (V_p) field model. This model requires a pre-measured V_p of the propagation medium as input and takes it as the average wave velocity to determine the location of AEs. However, due to the heterogeneity of granite (different grain sizes, pre-existing cracks, etc.), the average V_p may be different from that of various locations inside the granite, meaning that the actual location of AEs (microcracks) is not necessarily in the predetermined V_p area [215]. In addition, AE events imply damage to the specimen. P-wave velocity decreases with increasing microfracturing degree [216], meaning that the assumption of a single constant V_p may result in notable AE location errors [215]. As a result, a 3D velocity model that considers the intrinsic and the stress-induced anisotropy of rocks is needed for localizing AE events more accurately.

Moment tensor inversion of the AE signals revealed that both tensile and shear microcracks grow during the fracturing processes. Tensile cracks were detected to initiate from the disc centre at a low rate. However, they may initiate away from the disc centre under a higher loading rate.

Comparing Figures Fig. 3.7 and Fig. 3.8 with Fig. 3.10 and Fig. 3.11, one can see that the location of tensile AEs in Fig. 3.7 and Fig. 3.8 differs a little from the zones of high tensile strain accumulation from DIC contour plots in Fig. 3.10 and Fig. 3.11. In addition to the issues discussed in Section 3.3.3.2, i.e., tensile cracks being masked with the shear cracks and AE system saturation at the failure point, this difference between AE and DIC observations, could be due to the fact that DIC captures the evolution of the macro-crack while AE captures the micro-cracks. Previous studies have shown that a tensile macro crack is not necessarily tensile on the micro-scale [41]. Furthermore, as mentioned, DIC only captures the evolution of cracking on the surface facing the camera, while AE captures the whole fracturing processes in the volume. Roughness observation of the produced fracture in Fig. 3.14 revealed that, while the fractures are almost planar in the fracture direction, they are tortuous and rough on the fracture surface. This tortuosity behaviour of the fracture can only be observed by AE and not DIC. All these could cause complex and different fracturing processes detected by AE and DIC.

3.4.2. Effects of Time-dependent Loading on FPZ and Fracture Roughness

Knowledge of the fracturing behaviour of rock under time-dependent loading is essential as it provides additional insight into designing rock engineering projects such as fractured reservoir rock. There are two main ways of applying time-dependent loading: a) gradually increasing load at different but constant deformation rates, and b) applying constant load for different time durations (i.e., the creep phenomena) [217]. In this work, the former case was studied. Our results showed that more microcracks (AEs) were triggered at a lower loading rate during the development of the FPZ (e.g., Fig. 3.6). In fact, for lower loading rates, there is enough time for the applied load to be more smoothly transferred to farther points within the specimen. This, in turn, means that there would be more time and space for microcracks to initiate and propagate inside the specimen, leading to the formation of a larger FPZ. It is therefore concluded that the extent of the FPZ is highly influenced by the loading rate, which is in accordance with other studies [189], [191]. However, Arno and Christian (2000) [50] observed the opposite, i.e., that higher loading rates might produce a wider process zone in granite. The possible reason behind this discrepancy could be different testing methods employed in our study and theirs. They evaluated the FPZ in granite under a special uniaxial compression test designed to induce a pre-defined shear rupture in specimens. Our experiments, as well as those of Li et al. [191] and Chen et al. [189], were performed to induce a pre-defined tensile failure in specimens. Therefore, it appears that the influence of the loading rate on the FPZ may itself depend on the fracturing mode (tensile, shear). However, further experiments are needed to validate this hypothesis.

Under time-dependent and sub-critical crack growth, microcracks, especially tensile cracks, initiate and propagate with low-radiated seismic energy. In such a case, a low triggering threshold, a good noise filtration strategy, and a high-resolution data acquisition system are needed to be able to pick up these low-magnitude signals. Otherwise, they may not be properly detected. This could be the reason for the smaller number of detected tensile events in the central part of specimens. This could also be the reason why in some AE studies, people have observed lower AE and smaller process zones under lower loading rates [184].

On the other hand, a high-loading rate may cause a catastrophic failure with critical fracturing processes, which can saturate the AE system causing data loss around the failure point. This is the reason for the smaller number of detected shear events under a higher loading rate, as they mostly happen in the later stage, close to the failure point. In general, under a higher loading rate, there is a chance of losing some shear events due to the system saturation at the failure point. Besides, there is a chance of losing some tensile events under a low loading rate due to the system's resolution. Considering these limitations, it is believed that a combination of AE and DIC can yield a better picture of the fracturing processes.

Under very high-loading rates, especially for brittle materials like ceramic with small grains, the fracturing processes become dynamic, and fragmentation and branching may

create a complex fracture network. However, this is not the case for semi-brittle materials like granite, in which large grains may blunt the fracture. Also, there is a difference in strength and elastic properties of grains with different mineralogy. For instance, quartz and biotite have very different mechanical and elastic properties. Therefore, crack deviation and grain boundary fracturing may happen more frequently, especially under lower loading rates. Under a lower loading rate, the accumulated stress is not high enough to break the grains, and therefore we expect more tortuous fractures and maybe a larger process zone due to crack deviation. The more tortuous fractures, the rougher the surface of the final macro-fracture, especially for the coarse-grained rocks. This could be the reason why the fracture surfaces of the second group specimens, under a lower loading rate, were rougher (Fig. 3.16).

3.5. Conclusions

The effect of the loading rate on the evolution of the FPZ and the surface roughness of the generated fractures was monitored in granite discs under the indirect tensile (Brazilian) loading. Load-displacement, acoustic emissions, and full-field surface deformations were recorded, analyzed, and compared to identify the fracturing behaviour and nucleation and growth of FPZ of granite specimens at various loading stages.

The tensile failure process of granite specimens up to the peak load is divided into four stages, as reflected in the load-displacement, cumulative AE hits, and cumulative AE energy curves. These included 1) initial load transfer, 2) closure of pre-existing microcracks, 3) initiation and growth of microcracks, and 4) coalescence of microcracks leading to the final macroscopic failure. This evolution is similar for both specimen groups, GI and GII, tested under different loading rates. However, according to the AE results, the FPZ was formed at a relatively earlier loading state under a higher loading rate; that is, the third stage begins earlier at a higher loading rate.

Moment tensor inversion was conducted on the AE signals to determine the temporal and spatial evolution of tensile, compressive, and shear microcracks during the fracturing processes. The results showed that the fracturing process was composed of all crack types in all cases regardless of the loading rate.

It is observed that the evolution and the extent of the PFZ determined by AE and DIC are well consistent, although the AE presents a slightly wider process zone. The results also revealed that decreasing the loading rate results in a more extended FPZ in granite specimens and produces macroscopic fractures with rougher surfaces. However, unlike the direct shear test on rock joints, we could not find any correlation between the location and the magnitude of AEs and the roughness of the produced main fractures under tensile failure.

Our results indicated that reducing the loading rate can produce a more extensive fracturing network that, in turn, can improve the hydraulic characteristics of the rock. On the other hand, the roughness of the fracture surface increases with decreasing the loading rate. This can significantly impact fracture fluid flow and transport processes in the rock. These

laboratory-scale experimental results shed light on understanding the fracturing processes under tensile loading in field applications such as enhanced geothermal systems (EGS) and shale-gas extraction projects, where the critical goal is to maximize the stimulated reservoir volume to enhance the production rate.

CHAPTER 4: MICRO-SCALE FRACTURING MECHANISMS IN ROCKS DURING TENSILE FAILURE

MÉCANISMES DE FRACTURATION À MICRO-ÉCHELLE DANS LES ROCHES LORS D'UNE RUPTURE DE TRACTION

Authors and Affiliation:

Ghasem Shams: Ph.D. Candidate, Civil Engineering and Building Engineering Department, Université de Sherbrooke, Sherbrooke, Québec, Canada.

Patrice Rivard: Professor, Candidate, Civil Engineering and Building Engineering Department, Université de Sherbrooke, Sherbrooke, Québec, Canada.

Omid Moradian: Lecturer, Department of Earth Sciences, Swiss Federal Institute of Technology (ETH), Zurich, Switzerland and Currently Research Associate Professor, Department of Civil and Environmental Engineering, Colorado School of Mines, Golden, Colorado, USA.

Journal Title and Paper Status:
Submitted to ***Rock Mechanics and Rock Engineering*, July 2022, accepted (under press)**.

Contribution to the Thesis

In the previous chapter, it was shown that the macroscopic fractures generated within Brazilian discs (which are conventionally considered tensile fractures) were composed of different proportions of tensile, shear, and compressive cracks at the microscale. In addition, it was discussed that grain size could influence the fracturing process and cracking mechanisms at the micro-scale within rock specimens. This can, itself, affect the obtained tensile strength and the roughness of the produced macro-fractures. This chapter aims to determine why cracking mechanisms differ at micro and macro scales. It discusses how microcracking mechanisms change when the loading conditions change from direct

to indirect (Brazilian) tensile loading and how these changes affect the tensile strength of intact rocks obtained from direct and indirect tensile tests. Furthermore, the effect of the grain size on the microcracking mechanisms, thus, on the tensile strength of intact rocks, is discussed.

This chapter is aimed to address the following specific objectives (see Section 1.4):

1. Characterize the roughness of the surface failure of granite specimens under two loading rates in indirect and direct tensile loads.
2. Identify and describe the micromechanics of damage in direct tensile loadings in an attempt to explain the difference between strength values obtained from direct and indirect tensile.

Résumé

Comprendre les mécanismes de fracturation de la roche à la fois à macro et à micro-échelle est important pour une conception appropriée des applications d'ingénierie des roches. Cependant, on ne comprend toujours pas pourquoi les mécanismes de fracturation à macro et à micro-échelle diffèrent. Dans cette étude, des techniques d'émission acoustique (AE) et de corrélation d'images numériques (DIC) ont été utilisées pour suivre les processus de microfissuration dans des échantillons de granite soumis à des charges de traction indirectes (brésiliennes) et directes. L'inversion du tenseur des moments des signaux AE et les données du champ de déformation DIC ont révélé que la fracture macroscopique de traction ultime était principalement composée de microfissures de cisaillement dans les essais brésiliens et de microfissures de traction dans les essais de tension directe. Les différentes contributions des microfissures de cisaillement et de traction à la formation de la fracture macroscopique expliquent la différence entre les résistances à la traction directe et indirecte. Nos résultats ont montré que la contrainte de confinement dans l'essai brésilien due à son champ de contrainte biaxial et la taille des grains sont les deux facteurs critiques affectant les mécanismes de microfissuration dans le granite à gros grains testé. La caractérisation de la surface des fractures macroscopiques générées et les résultats d'une série d'essais de traction complémentaires effectués sur des échantillons de mortier à grains fins suggèrent que la réduction du confinement et de la taille des grains diminue la contribution des microfissures de cisaillement. Les résultats de cette étude peuvent être utilisés dans des applications telles que la fracturation hydraulique pour le gaz de schiste (shale gas) ou l'extraction d'énergie géothermique, où la connaissance de l'emplacement et des mécanismes de fissuration est essentielle pour améliorer la productivité du réservoir et réduire le risque de sismicité.

Abstract

Understanding the fracturing mechanisms of rock on both macro- and micro-scale is important for properly designing rock engineering applications. However, there is still a lack of understanding of why macro and micro-scale fracturing mechanisms differ. In this study, acoustic emission (AE) and digital image correlation (DIC) techniques were

employed to track the microcracking processes in granite specimens subjected to indirect (Brazilian) and direct tensile loadings. The moment tensor inversion of the AE waveforms and the DIC strain field data revealed that the ultimate so-called *tensile* macro-fracture was predominantly composed of shear microcracks in Brazilian tests and tensile microcracks in the direct tension tests. The different contributions of shear and tensile microcracks to the formation of the macro-fracture explain the difference between direct and indirect tensile strengths. Our results showed that the compressive stress in the Brazilian test due to its biaxial stress field and the grain size are the two critical factors affecting the microcracking mechanisms in the tested coarse-grained granite. Characterizing the surface of the generated macro-fractures and the results of a series of complementary tensile tests performed on fine-grained mortar specimens suggested that reducing the compressive stress and grain size decreases the contribution of shear microcracks. The results of this study can be used in rock fracture applications in granitic rocks such as hydraulic fracturing for geothermal energy extraction, where the knowledge of the cracking location and mechanisms is critical for enhancing the reservoir's productivity.

Keywords: Microcracking. Acoustic Emission. Digital Image Correlation. Cracking Mechanisms. Tensile Strength. Moment Tensor Inversion

List of Symbols

σ_{Bt}	Brazilian tensile strength
σ_{Dt}	Direct tensile strength
F_p	Applied external load at failure
D	Brazilian disc diameter
T	Brazilian disc thickness
A	Nominal cross-sectional area of prismatic specimens
A_0	Average focal amplitude of acoustic emissions
A_i	Maximum signal amplitude received by the i^{th} sensor
r_i	Signal source distance to the i^{th} sensor
n	Number of sensors receiving the same AE signal
ε^e	Elastic strain component
ε^p	Plastic strain component
ε^t	Total strain

4.1. Introduction

Crystalline rocks contain numerous micro-defects, such as intra-crystalline cracks (cleavage) and grain boundaries [1]. According to Griffith's tensile theory [24], once the rock is loaded, these pre-existing defects could be the location of high tensile stress concentration, where new microcracks may nucleate, propagate, and coalesce, leading to eventual macroscopic failure of rock structures [2]–[9], [136], [186], [218]–[220]. A detailed understanding of the failure mechanism of rocks is essential in different fields such as geotechnical engineering (e.g., designing rock slopes and underground excavations)

[46], [220], mining (e.g., rock blasting and fragmentation) [11], seismology [214], [221], and hydraulic fracturing [12], [47].

Numerous researchers have studied the failure processes in rocks and rock-like materials at the macroscale and reported that two major crack types, i.e., tensile and shear, are created when specimens are subjected to compression or tension [3], [7], [8], [44], [46], [124], [221]–[223]. Cheng and Wong [221] studied the microcracking characteristics of macroscopic tensile and shear fractures observed in marble specimens containing en-echelon flaws subjected to uniaxial compressive loading. Their study showed that there are distinct differences between macro-tensile and macro-shear fractures at the microscale. For example, the authors stated that the damage zone around a tensile fracture mainly comprised grain boundary microcracks. However, in addition to grain boundary microcracks, transgranular microcracks, and grain spallings were also prevalent in the damage zone of observed shear fractures. Many studies have investigated the cracking processes and the crack types at the microscale using different direct and indirect experimental observations to obtain a more detailed insight into the failure mechanism in rocks. Among the most important techniques are digital image correlation (DIC) [45], [186], [224], [225], acoustic emission (AE) [19], [27], [45], [186], [187], [218], [224], optical microscope (OM) [11], [221], and scanning electron microscope (SEM) [6], [11], [53], [54].

In general, there are three basic loading modes defined in rock fracture mechanics, including tensile mode (Mode I), sliding or in-plane shear mode (Mode II), and tearing or anti-plane shear mode (Mode III) [43]. The stress state at cracks/flaws tip in geomaterials may be a combination of shear, compression, and tension, causing cracks to propagate under tensile, shear, or a combination of tensile and shear mechanisms. This is especially true in rocks [43]–[45]. Moreover, because rock materials are weak in tension and strong in compression and shear, the microcracking processes and mechanisms under Mode I loading are of primary interest in rocks [22], [25], [42].

Wong and Einstein [53] employed the environmental scanning electron microscope (ESEM) and SEM imaging techniques to examine the microscopic cracking processes and crack mechanisms in marble specimens with two pre-existing flaws under uniaxial compression. The authors reported that the formation of macroscopic cracks is associated with developing macroscopic white patches on the specimen surface, which consist of microcracking zones (process zones) with mainly tensile microcracks. Zhao et al. [54] performed real-time SEM observations of microcracking development in marble specimens with a pre-existing slot under uniaxial compression. As per cracking mechanisms, the authors reported that the observed microcracks were mostly tensile, with very few shear microcracks. Similarly, based on the SEM examination of granite specimens tested under triaxial compression, Tapponnier and Brace [6] reported that fracturing was mainly associated with the formation of tensile cracks, with a scarcity of shear cracks.

Sun and Wu [19] used AE to investigate the crack mechanisms in sandstone under the Brazilian test. They reported that the cracking process in Brazilian specimens is predominantly composed of tensile microcracks, while shear microcracks also play a role. Li and Einstein [186] applied AE and DIC to study the progress of the process zone and crack propagation in a pre-notched specimen of Barre Granite under four-point bending. Theoretically, the macroscopic fracture produced under bending is considered a definite tensile crack. However, both AE and DIC results indicated that shear and tensile mechanisms are both present. Their AE results also revealed that the process zone consisted of much more shear than tensile cracks, especially immediately at the notch tip. Zafar et al. [45] investigated the microcracking mechanisms during the deformation of Barre Granite under unconfined compression using AE and DIC techniques and established a quantitative correlation between AE and DIC data. They reported that the cracking process initiated in tension followed by shear microcracks. In addition, their observations revealed a strong correlation between the evolution of shear and tensile microcracks from AE analysis with the inelastic shear and tensile strains from DIC analysis during the deformation process. In a recent experimental study, Guo and Zhao [226] employed AE monitoring to study the cracking behavior of granite, sandstone, and marble subjected to Mode I semi-circular bending tests. They found that the quantity of pre-existing microcracks in rocks controls the number of radiated AE events. The authors also reported that the source mechanisms of AE events were predominantly tensile in all rock types. However, granite exhibited a significantly higher number of shear events than other rock types.

Labuz et al. [227] employed ultrasonic probing and AE measurements to determine the granite fracture process zone (FPZ) and fracture toughness. They evaluated the effect of the microstructure, specifically the grain size, on the FPZ by studying the small and large grain-size granites. Their results indicated that the length of the FPZ was about 40 and 90 mm for granites with average grain sizes of 1 and 10 mm. Other researchers have studied the effect of the grain size on the PFZ and found that the extend of the FPZ increases with grain size [50], [228]–[230]. AE results from an experimental study conducted by Zietlow and Labuz [230] showed that the width of the FPZ is approximately correlated with the logarithm of the grain size for different rock types. Lei et al. [231] used AE monitoring to study the fracturing mechanisms in fine- and coarse-grained granites under triaxial compression. Their experiments showed a significant distinction between the source mechanisms of AE events for two granites. Shear fractures were dominant throughout the fracturing process in coarse-grained granite. However, in fine-grained granite, the tensile fracturing mechanism predominated up to 80% of the failure load, and shear fractures gradually dominated after this stress level. Lin et al. [219] used AE and DIC techniques to characterize the PFZ in medium- to fine-grained sandstone. Their results showed that the length of FPZ is approximately ten times longer than the maximum grain size, emphasizing the effect of grain size on the fracturing characteristics of rocks. Guo and Wong [42] examined the spatial-temporal evolution of AE events and the variation of AE energy to characterize the microcracking behavior and mechanisms of three granite rocks with different grain sizes in Mode I three-point bending tests. They found that the different

granite rocks showed distinct AE features throughout the fracturing process and concluded that the mineralogy and the grain size significantly affect the spatial and temporal evolution of microcracks and the energy of the radiated AEs.

In addition, the literature showed a difference between macro and micro failure mechanisms in rocks under different loading conditions in laboratory and field scales [27], [41], [44], [47], [232]. Conventionally, it is considered that hydraulic fracture initiation and propagation are predominantly governed by tensile mode cracks in the field scale. Likewise, it is well known that macroscopic fractures are tensile in the direct tensile and Brazilian splitting tests, two well-recognized experiments for determining rocks' tensile strength. However, by analyzing AE data from hydraulic fracture experiments in the laboratory on granite and shale, Li and Einstein [41] found that the shear cracking mechanism also contributes (to different extents) to hydraulic fractures at the microstructural scale. According to AE analysis results from a series of laboratory hydraulic fracturing experiments on granite specimens with pre-cut flaws, Li et al. [47] reported that the source mechanisms of most microcracks (55–60%) were shear, while only 25–30% was tensile. To determine the source mechanisms of AE events, the authors used the decomposition of moment tensors into isotropic (ISO), double-couple (DC), and compensated linear vector dipole (CLVD) components, according to Vavryčuk [211]. AE events were classified as shear when DC $\geq$ 50%. Events with a DC component of less than 50% were considered compaction or tensile based on their ISO and CLVD components. Furthermore, Maxwell and Cipolla [232] noted that in-situ microseismic data shows more shear than tensile deformations in hydraulic fracture development. This could be because, in hydraulic fracture processes, the amplitude of tensile mode fractures is too small to be detected by microseismic monitoring systems, rendering the tensile deformation as aseismic. In addition, Wang et al. [27] studied the dominant frequency of AE waveforms to determine the relationship between marble's micro and macro failure under direct tensile and Brazilian tests. Their results showed that macro tensile fractures in Brazilian and direct tensile tests are generated through a combination of shear and tensile cracks at the microscale. However, the proportion of shear cracks was more significant in Brazilian than in direct tensile tests. Finally, through a comprehensive experimental campaign, Einstein [44] concluded that a fracture that may appear as a tensile or shear crack on a larger scale could consist of both tensile and shear mechanisms coinciding spatially and temporally.

From the literature, it can be concluded that there is a discrepancy between the cracking mechanisms at the macro and micro scales. A fracture could be interpreted as a pure tensile fracture at a large scale, while it could be composed of both tensile and shear mechanisms at the microscopic scale. The same applies to macroscopic shear fractures [44]. For instance, direct tensile, hydraulic fracturing, bending, and Brazilian tests are all recognized by geomechanics communities as classic experiments in which tensile fracture is induced [44], [92], [233]. However, it has been shown that the generated macroscopic tensile fractures in all these tests comprised many shear microcracks; in some cases, even the shear mechanism was dominant.

Despite these significant findings, it is not fully understood yet 1) Why are cracking mechanisms different at micro and macro scales? and 2) How do loading conditions affect micro-cracking processes during tensile failure? In this study, we try to address these knowledge gaps by investigating the effects of grain size and stress state on the spatiotemporal evolution of micro-fracturing processes in granite specimens during tensile failure. We employed AE, DIC, and roughness scanning. For this purpose, coarse-grained granite and later fine-grained mortar specimens were subjected to two standard loading conditions, i.e., direct tension and Brazilian tests. The objectives of this study are to (1) improve our understanding of microstructural damage and strength in rocks, (2) explain the difference between macro and micro fracturing mechanisms in rocks, and (3) determine how well the measured tensile strength approximates the true tensile strength of the tested material. This could lead to more efficient and safer rock engineering designs.

4.2. Experiments

4.2.1. Materials and Specimen Preparation

The rock specimens were prepared from Stanstead granite, which is quarried in Stanstead (Eastern Township region, Québec, Canada). Stanstead Granite is a coarse-grained crystalline rock with an average grain size of 1.1 mm and a maximum grain size of 7 mm and is mainly composed of quartz, mica (biotite), alkali feldspar (orthoclase), plagioclase (albite), and opaque minerals [193]. The properties of Stanstead granite are given in Table 4.1.

Table 4.1. Mechanical and physical properties of Stanstead granite

Parameter	No. of Samples	Min	Max	Mean	SD*
Uniaxial compressive strength (MPa)	4	136.80	138.00	137.00	0.61
Direct tensile strength (MPa)	4	5.40	5.50	5.50	0.05
Brazilian tensile strength (MPa)	4	7.40	9.00	8.00	0.76
Elastic modulus (GPa)	3	49.90	51.10	50.60	0.62
Poisson's ratio	3	0.21	0.27	0.23	0.03
P-wave velocity (km/s)	4	4.07	4.17	4.12	0.02
Density (kg/m^3)	4	2636	2646	2643	4.85

* Standard deviation

Two groups of specimens were prepared, including four Φ75 × 30 mm cylindrical disc specimens and four prismatic specimens with dimensions 100 × 37 × 30 mm (length (L) × width (W) × depth (D)). The disc specimens (named B1 to B4) were tested under the Brazilian tensile loading, and the prismatic specimens (named D1 to D4) were tested under the direct tensile loading. A direct tensile test is regarded as valid only if the failure occurs at the midpoint of the specimen [22]. Therefore, to achieve this, two 5 mm notches were

cut on both sides of the specimens. The prismatic specimens' ends were polished and glued onto the loading plates with a strong adhesive epoxy. Fig. 4.1a and b show an example of the prepared specimens of each type. The International Society for Rock Mechanics and Rock Engineering (ISRM) recommendations were adopted for rock specimen preparation, including coring, cutting, grinding, and polishing [92], [129].

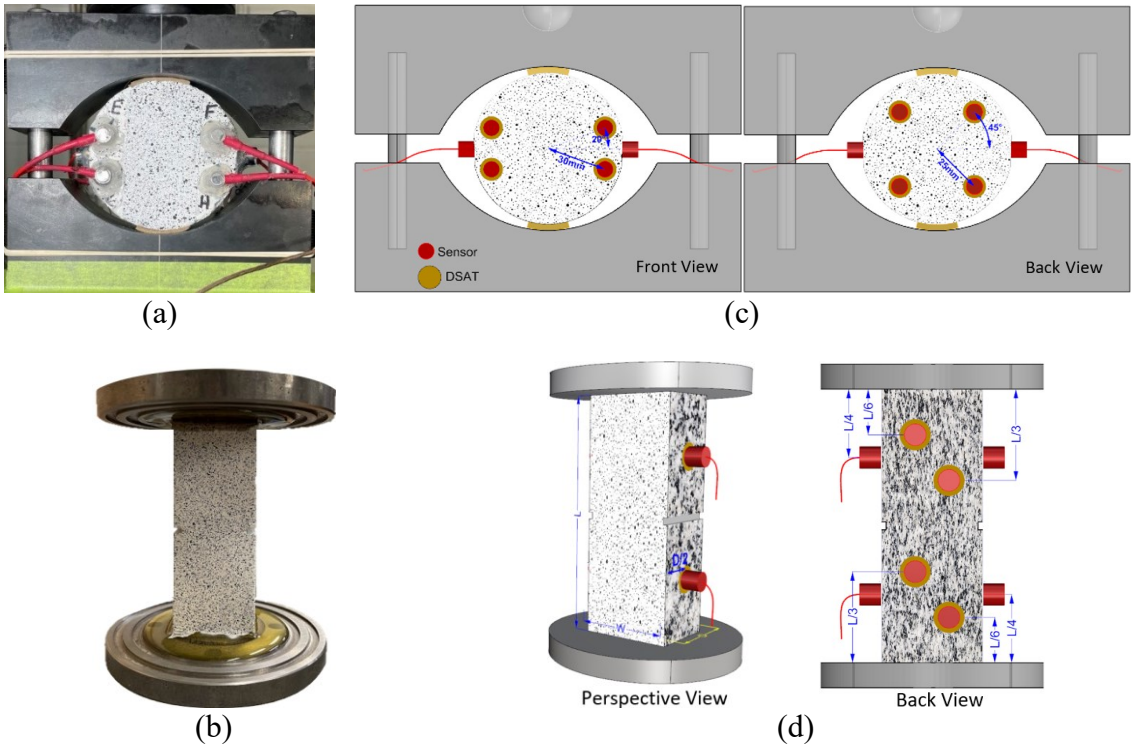

Fig. 4.1 Schematic view of (a) a disc specimen mounted on standard Brazilian jaws and (b) a prismatic specimen glued to loading platens. Locations of AE sensors for (c) Brazilian specimens and (d) specimens tested under direct tension.

4.2.2. Experimental Setup

4.2.2.1. Loading System

The Brazilian tests were conducted with servo-controlled material testing system (MTS) equipment. The load cell capacity was 225 KN. The direct tensile tests were performed with an INSTRON 4482 dual-column Universal Testing machine. The load cell capacity was 100 KN. The ISRM standard apparatus, consisting of two loading jaws, was used to perform the Brazilian test [92]. An excessive compressive stress concentration may cause premature fracture initiation under the loading ends, invalidating the Brazilian test results [63], [119], [194]. To mitigate the compressive stress concentration around the loading areas in Brazilian discs, two thin cardboard cushions with a thickness of 2.5 mm were inserted between jaws and specimens (Fig. 4.1a and c) [22], [63], [66], [108].

All tests were conducted at the Rock Mechanics Laboratory of Université de Sherbrooke. In both the Brazilian and direct tension experiments, the applied load (F) and the axial displacement in the vertical direction were recorded using two LVDT displacement transducers (Solartron Metrology, Model 925604 DCR15). All tests were performed under the displacement control mode at a rate of 0.1 μm/s to ensure the quasi-static loading condition. This loading rate, which is lower than the ISRM recommended loading rates [92], was adopted to better monitor and record the fracturing processes in specimens.

The Brazilian σ_{Bt} and direct σ_{Dt} tensile strengths for tested specimens were calculated as follows:

$$\sigma_{Bt} = \frac{2F_p}{\pi DT} \quad \text{Eq. 4.1}$$

$$\sigma_{Dt} = \frac{F_p}{A} \quad \text{Eq. 4.2}$$

where F_p is the applied external load at failure, D is the disc diameter, T is the disc thickness, and A is the nominal cross-sectional area of prismatic specimens.

4.2.2.2. Acoustic Emission (AE) Monitoring

The MISTRAS μ-SAMOS acoustic emission equipment with two PCI-8 cards (16 measurement channels) was employed to determine the cracks' temporal and spatial distribution throughout the experiments. Nano-30 AE sensors operating in the 125–750 kHz frequency range were used to capture AE signals. Fig. 4.1c and d show the AE sensor layout for the disc and prismatic specimens, respectively. Ten and eight AE sensors were mounted on the surface of the cylindrical and prismatic specimens, respectively. For the Brazilian specimens, four sensors were placed on the front surface, four sensors on the back surface, and two sensors on the sides to better obtain the 3D distribution of AE events (Fig. 4.1c). The locations of the sensors on the sides of the specimens were polished to provide a flat surface for coupling between the sensors and the specimens. For the specimens under direct tensile loading, four sensors were attached to the back surface and four to the left and right sides (Fig. 4.1d). The sensors were first attached to the surface of specimens using a double-sided adhesive tape (DSAT) and then glued to the specimens with hot glue. The efficiency of sensor-granite coupling was verified using the auto sensor test (AST) [234].

The AE signals were amplified with PAC 2/3/4 preamplifiers with a gain of 40 dB and they were recorded after passing a triggering threshold of 35 dB. The data acquisition system was set up with sampling frequency of 3 MHz, PDT (Peak Definition Time) of 200 μs, HDT (Hit Definition Time) of 800 μs, HLT (Hit Lockout Time) of 350 μs, and maximum duration of 10 ms. The AE waveforms were registered with a pre-trigger time of 50 μs and a sample length of 4k. The same settings were used for both Brazilian and direct tensile

tests. The location error was measured as ±2 mm using the pencil-lead break (PLB) tests [235] on the pre-defined locations.

For the AE source localization, the Akaike information criterion (AIC) [134], [151], [236]–[238] was employed to pick up the P-wave arrival times. A constant P-wave velocity model (4120 m/s), optimized using the downhill simplex optimization method [239], was applied to locate AE sources for a minimum distance error of 3 mm. We followed the procedure developed in Li et al. [47] for the source localization and the moment tensor inversion of the AE events. An AE event must be detected with at least four sensors to determine the event origin coordinates (*x, y, z*) and the event occurrence time (*t*).

Following determining the AE locations, the moment tensor inversion (MTI) technique was performed on the AE events, detected by at least six sensors, to determine their source mechanisms according to the 2D implementation of the SiGMA (Simplified Green's functions for Moment tensor Analysis) procedure [47], [134], [152], [195]. Moment tensors were decomposed into double-couple (DC), isotropic (ISO), and compensated linear vector dipole (CLDV) components for each event, according to Vavryčuk [211]. Then, AEs were regarded as tensile (ISO ≥ 15% and CLVD ≥ -15%), pore space collapse or compaction (ISO ≤ -15% and CLVD ≤ 15%), or shear (|ISO| < 15%) events [155].

In addition, the average focal amplitude (A_0) of the detected AE events was calculated by Eq. 4.3, considering geometrical spreading for a reference distance of 10 mm as in Zang et al. [210]:

$$A_0 = \sqrt{\frac{1}{n}\sum_{i=1}^{n}\left(A_i \frac{r_i}{10}\right)^2} \qquad \text{Eq. 4.3}$$

where n is the number of sensors receiving the same AE signal, A_i is the maximum signal amplitude received by the i^{th} sensor, and r_i (in mm) is the signal source distance to the i^{th} sensor.

4.2.2.3. Digital Image Correlation (DIC) Technique

DIC computes the displacement and strain fields by comparing images of the specimen's surface captured at different deformation stages. Firstly, a calculation area or a region of interest (ROI) is defined over the specimen's surface in the first image taken before loading (the reference image). The ROI is then divided into smaller regions called subsets. A correlation algorithm identifies the best match between a given subset in an undeformed image (i.e., the reference image) and a distorted image. Finally, the displacement and strain fields are determined by calculating the subsets' motion [157].

A Basler acA2440-75um camera with a Scheinder Xenoplan 1.9/35-0901 CM120 BK 15 compact lens was used to capture images of the specimen deformation process throughout each experiment. The images were acquired at a rate of 1 fps with a resolution of 2448 ×

2048 pixels (5 MP). The camera was placed perpendicularly to the specimen front surface 900 mm away to minimize the out-of-plane motions, increasing the accuracy of in-plane measurements. Given the specimens' small diameter, this distance ensures that the out-of-plane displacement remains below the allowable limit [240]. Two LED lights also provided stable and constant illumination of the specimen's surface, minimizing DIC post-possessing errors.

To resolve uniqueness issues of the surface of the granite specimens and, thus, to increase the accuracy of image correlation [157], a random speckle pattern was applied over the front surface of samples. The specimen's surface was first lightly coated with white paint, and black paint was then sprayed over the surface (Fig. 4.1). For more details on the DIC technique and the speckle patterns, readers are referred to CorelatedSolutions [178].

After image acquisition, the VIC-2D software, licensed by Correlated Solutions Inc. [178], was used to compute and visualize the evolution of displacement and strain fields over the surface of the tested specimens. The ROI over which the strains were measured was selected to cover the central part of specimens, where the ultimate macro fractures occurred (upper panel of Fig. 4.9). A subset size of 29 × 29 pixels was chosen to ensure a unique speckle pattern within each subset [157], [178]. Also, a step size of 7 pixels was picked between subset meshes to get independent and non-repetitive data points over the specimen surface [157], [178].

Before starting each test, all observational systems, i.e., loading, imaging, and AE monitoring systems, were synchronized to record experimental data simultaneously.

4.3. Results

4.3.1. Direct vs. Indirect Tensile Strength

Fig. 4.2a and b indicate the load-displacement responses from the Brazilian and direct tension tests, respectively. The insets in Fig. 4.2 show the specimens' tensile strength.

The average σ_{Bt} (Brazilian tensile strength) is approximately 8 MPa (standard deviation 0.76), while the average σ_{Dt} (direct tensile strength) is approximately 5.5 MPa (standard deviation 0.05). The average ratio of σ_{Dt}/σ_{Bt} is 0.69, which is very close to the value of 0.67 reported by Perras and Diederichs [22]. Additionally, the standard deviation values suggest that compared with the Brazilian tests, the direct tension tests yielded more consistent, repeatable results. A similar conclusion was reached in other studies [61], [62]. Fig. 4.2c also shows the average direct and Brazilian tensile strength of various granitic rocks from different literature and this study. The numbers given above bars represent the σ_{Dt}/σ_{Bt} ratio. There is a good agreement between σ_{Bt}, σ_{Dt}, and their ratio obtained from this study with those from literature.

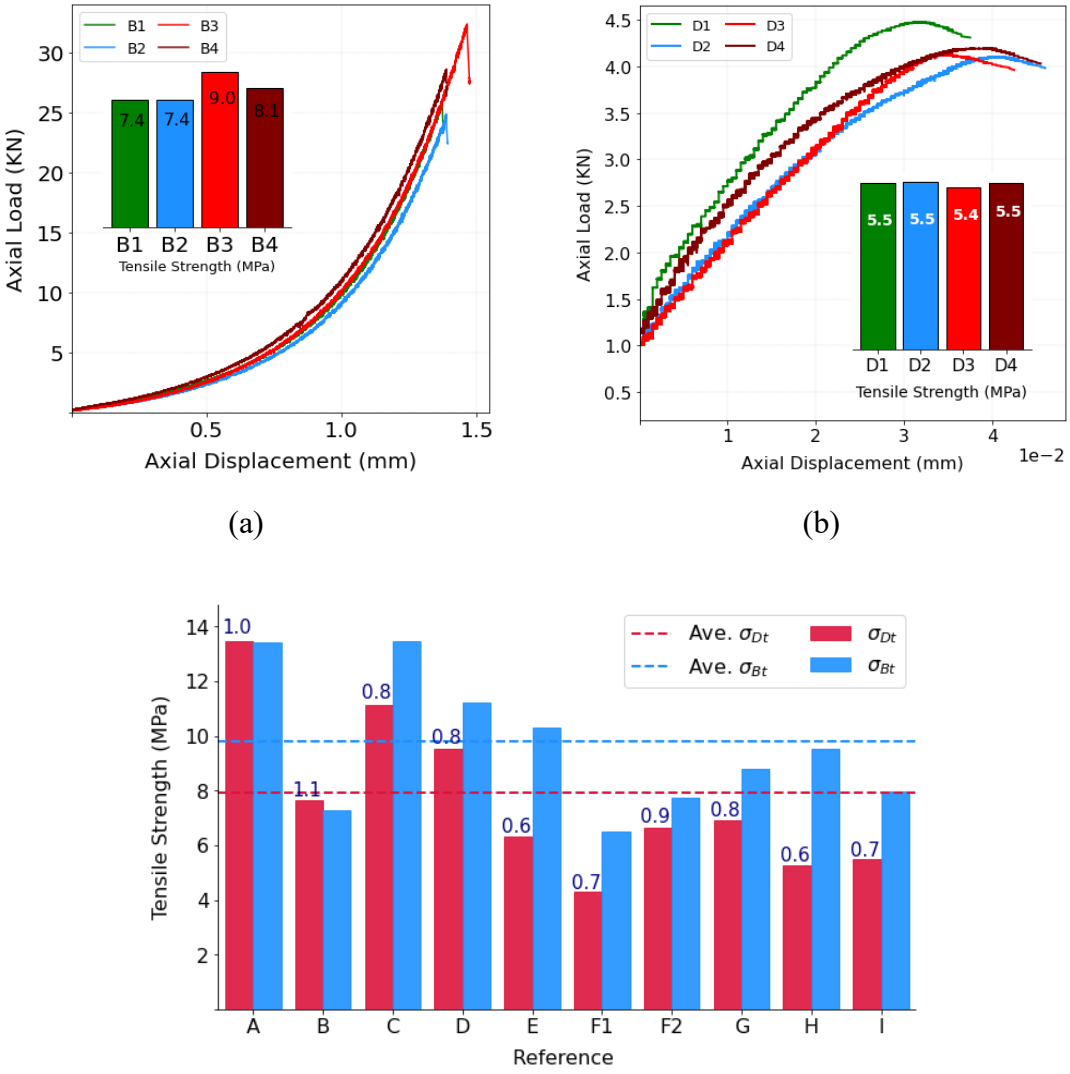

Fig. 4.2 Load-displacement curves for (a) Brazilian specimens, (b) specimens under direct tensile loading, and (c) the direct and Brazilian tensile strength of granite from literature: (A) Mellor and Hawkes [63], (B) Ramana and Sarma [65], (C) Alehossein and Boland [61], (D) Liu et al. [10], (E) Perras and Diederichs [22], (F1, and F2) Cacciari and Futai [62], (G) Qi et al. [64], (H) Efe et al. [31], and (I) this study. The blue and red dashed lines represent the average values of Brazilian and direct tensile strengths.

The experiments showed that the load-displacement behavior, AE, and DIC characteristics were relatively similar for all specimens of the same loading type. Thus, the experimental results of specimens B1 and B2 (for the indirect tensile loading) and D1 and D2 (for the direct tensile loading) were analyzed and discussed in more detail

4.3.2. Acoustic Observation of Tensile Fracturing

The AE waveforms were registered throughout the tensile loading. Fig. 4.3 displays different steps in picking an AE waveform (one from the Brazilian experiment and one from the direct tensile experiment).

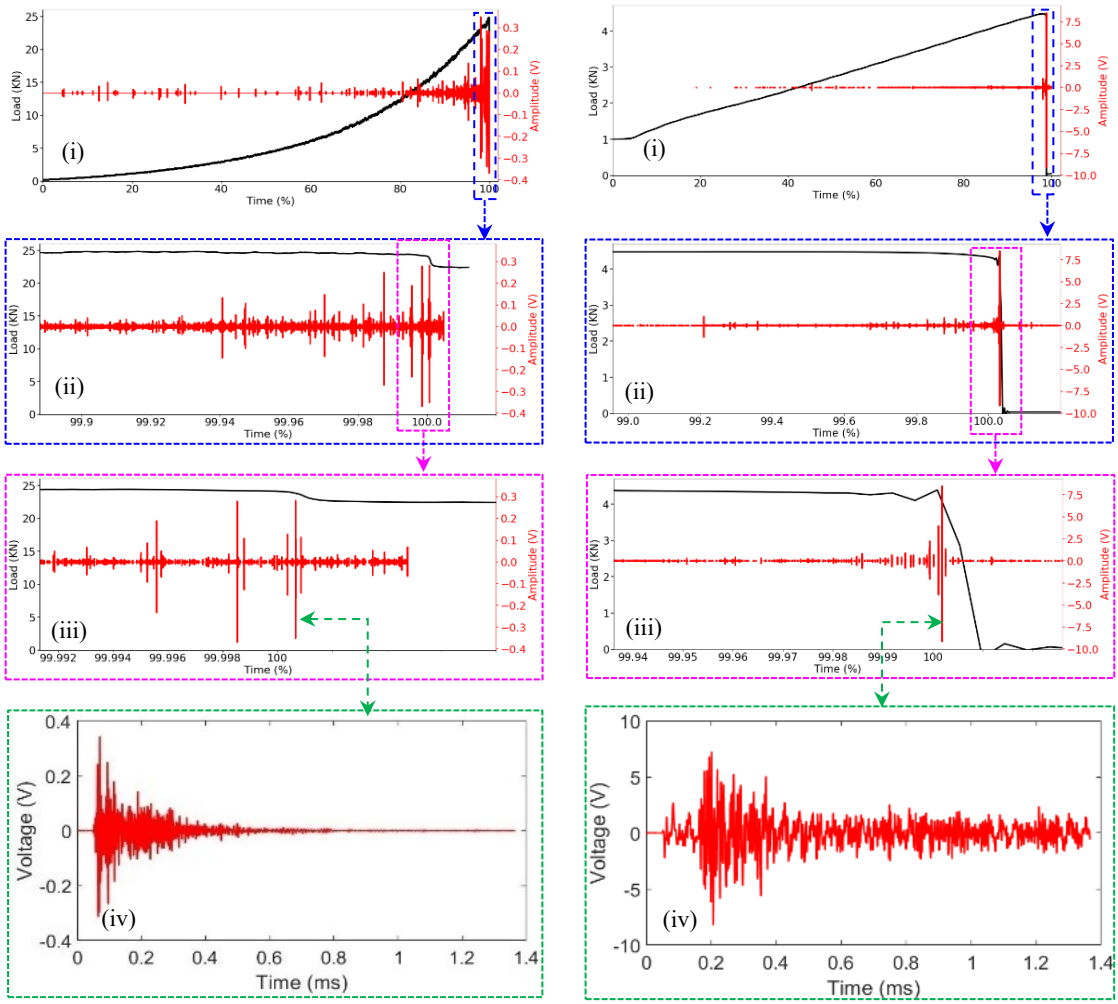

Fig. 4.3 Time series of the AE waveforms recorded during fracturing process for (a) B1 and **(b)** D1. The plots show the waveform for (i) the entire loading time, (ii) 25 seconds before the failure load, (iii) 2 seconds before the failure load, and (iv) a representative waveform at the failure point. For the B1, only the unclipped AE waveforms which are not saturated are presented here.

4.3.2.1. Temporal and Spatial Microcracking Processes

The typical temporal evolution of AE events during the loading process in Brazilian (B1 and B2) and direct (D1 and D2) tension tests are shown in Fig. 4.4. The AE event amplitude, the cumulative AE events, and the applied load are shown as a function of the loading time percentage. Each circle in the scatter plot represents an AE event that was captured if a given AE signal was detected by at least 6 AE sensors. The color of the AE events in Fig. 4.4 reflects the average focal amplitude (A_0) of the AEs determined by Eq. 4.3.

In the Brazilian tests, the AE system gets saturated at the failure point and AE waveforms are clipped and distorted. In this study only well-registered waveforms have been analyzed and therefore the number, amplitude, and located AE signals in this study are lower than the AE results presented in Shams et al. [241] (i.e., Chapter 3).

Fig. 4.4 points out that B1 and B2 show very similar AE activity in all three loading stages regarding the number of AE events and duration of each loading stage. The same applies to D1 and D2. This confirms the repeatability of the experimental results.

As indicated in Fig. 4.4, based on the rate of microcracks development (AE events), the deformation process of all specimens, up to the peak load, can be divided into three distinct stages. The first stage consists of almost no AE activity, as reflected by the absence of AE events. The second stage is distinguishable by a slight but constant increase in the AE rates for both test types. The small number of AE events with relatively higher amplitude values in this stage indicates the initiation and growth of microcracks within the specimens. The second stage, in which the specimen may undergo inelastic deformations, begins approximately at 25% and 60% of the failure loads for B and D specimens. Brace et al. [3] reported that the crack initiation (CI) threshold of granite specimens in a uniaxial compression test is reached at approximately 30 to 50% of the failure load. Thus, it may be inferred that the crack initiation limit of granite falls in the range of 30 to 50% of the peak load, regardless of the loading type.

Our investigation indicated that around 25% of the total microcracks were generated in D specimens during the second stage, while almost 10% were generated in B specimens in this stage. On the other hand, the second stage accounts for 36 and 56% of the whole applied load for D and B specimens (Fig. 4.4). This may show that the specimens under direct tensile loading underwent more damage in the stable cracking stage than the specimens subjected to indirect tensile loading. A remarkable number of microcracks with higher amplitude is generated in the last stage. The drastic increase in cumulative AE events illustrates an unstable propagation and coalescence of microcracks leading to the ultimate macro-fracture in specimens. Our results revealed that around 75% and 88% of the total AEs occurred in the third stage for D and B specimens. However, on average, the third stage, the unstable fracture growth stage, accounts for 2.5% and 17% of the entire applied load for D and B specimens (Fig. 4.4). This again suggests that microcracks initiated, propagated, and coalesced earlier under the direct tension than the Brazilian

loading. This could be because the macroscopic damage in Brazilian specimens is mainly composed of micro-shear cracks that gradually initiate and propagate inside granite. However, the macroscopic damage in specimens tested under direct tensile loading is primarily made up of micro-tensile cracks that initiate and propagate earlier than micro-shear cracks (Fig. 4.5, Fig. 4.6, Fig. 4.10, and Fig. 4.11 in sections 4.3.2.2 and 0).

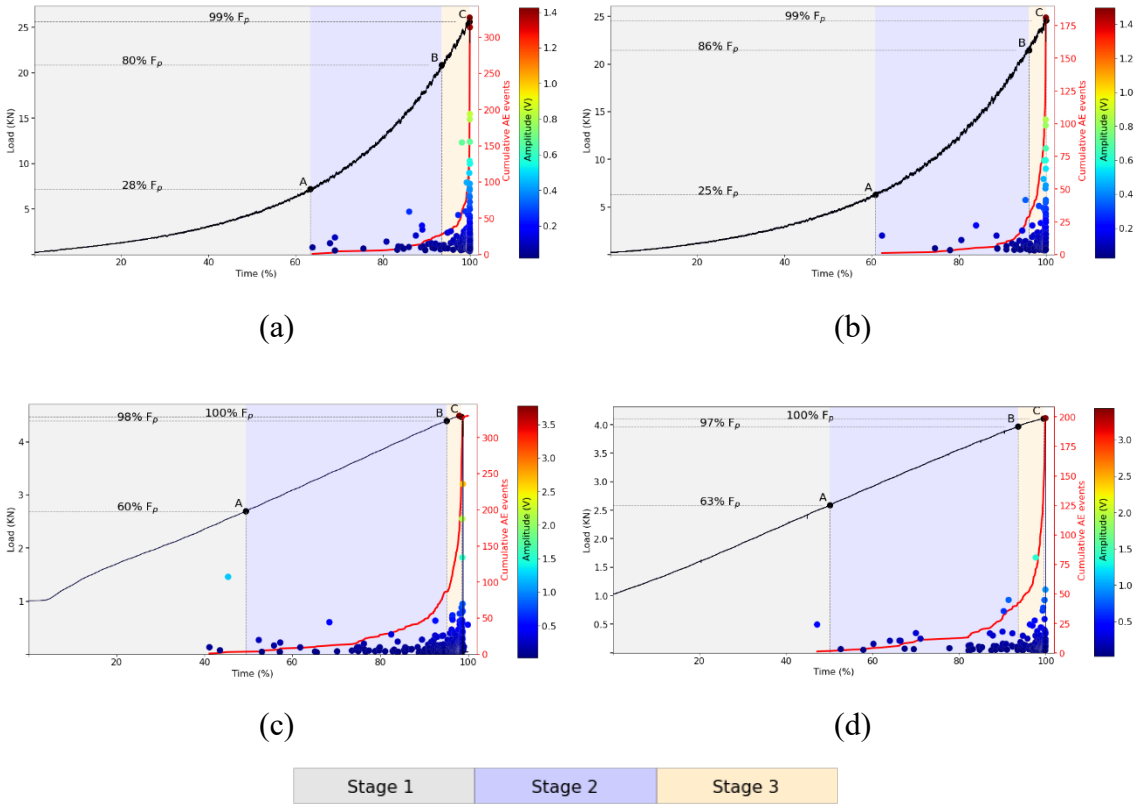

Fig. 4.4 AE events amplitude, cumulative AE events, and loads of the specimens (a) B1, (b) B2, (c) D1, and (d) D2 throughout the loading process.

4.3.2.2. AE Microcracking Mechanisms

The moment tensor inversion (MTI) technique was applied to determine the AE source mechanisms. Fig. 4.5a and e, and Fig. 4.6a and e illustrate the AE source distribution of AE events at the end of the third loading stage (i.e., at the failure load) for B1, B2, D1, and D2. The blue lines in Fig. 4.5 and Fig. 4.6 represent the macroscopic fracture path seen in specimens. The size and color of the AE events in these figures reflect the average focal amplitude (A_0) of the AEs given in Eq. 4.3. In Fig. 4.5 and Fig. 4.6, the percentages in brackets represent the ratio of the specified AE mechanisms to the total AEs detected for the given specimen.

In general, the location of AEs is in good agreement with the location of the final macro fracture for all specimens. Moreover, the general trend of AE activities for different specimens of the same type is highly consistent. Fig. 4.5a and e show that microcracks

were mainly accumulated in the middle part of disc specimens close to their center. This indicates that cracks initiated in the central part of specimens (also confirmed by the DIC results, see Fig. 4.9) and gradually extended toward the vertical ends, coalescing which formed the final fracture. Likewise, Fig. 4.6a and e indicate that AE events were mainly accumulated around the right notch of D1 and D2, showing that the macroscopic fracture initiated from the right side and propagated to the left. This is confirmed by the DIC strain fields shown later (Fig. 4.9).

The spatial distribution of different AE mechanisms is shown in Fig. 4.5b-d and Fig. 4.5f-h for B1 and B2 and in Fig. 4.6b-d and Fig. 4.6f-h for D1 and D2. Note that the orientation of line segments in Fig. 4.5b and f and Fig. 4.6b and f represents the orientation of the tensile microcracks. As expected, micro tensile cracks lay along the final macroscopic fractures in all specimens; they angled vertically to sub-vertically in Brazilian specimens and horizontal to sub-horizontal in specimens under direct tensile loading. Moreover, the color of the source mechanisms is scaled by the average focal amplitude (A_0) of the AEs

All three different cracking mechanisms, i.e., tension, compression, and shear, contribute to the fracturing behavior and the tensile strength of both prismatic and disc specimens. In other words, the tensile strength of specimens is controlled by a combination of different microcracks types, even in the direct tensile tests, which has been accepted as the most valid method for measuring the true tensile strength of rock [22], [92], [116].

Fig. 4.5 reveals that the majority of AEs are shear-type in Brazilian specimens (50% and 47% in B1 and B2). In comparison, they are mostly tensile (47% and 63% in D1 and D2) in specimens under direct tensile loading, as seen in Fig. 4.6. On average, there are 49% shear cracks and 23% tensile cracks in B specimens. In contrast, these values are 21% and 55% in D specimens. In indirect and direct experiments, the tensile-to-shear microcracks ratio is 0.47 and 2.62, respectively. This significant difference in the contribution of shear and tensile AEs in the Brazilian and direct tensile tests can explain the difference between the direct and indirect tensile strength of rock materials like granite. In brittle materials, the tensile strength (TS) is often less than the shear strength and much lower than the compressive strength, reflecting the importance of the TS in the resistance to failure of rock engineering materials [22], [24], [25]. These expressions also apply to micro-scale cracking. Therefore, the higher the proportion of the shear-type microcracks, the higher is the tensile strength. That is, the higher contribution of shear microcracks (which are stronger than tensile microcracks) in Brazilian experiments resulted in higher "indirect" than "direct" tensile strengths in tested granite (Fig. 4.2).

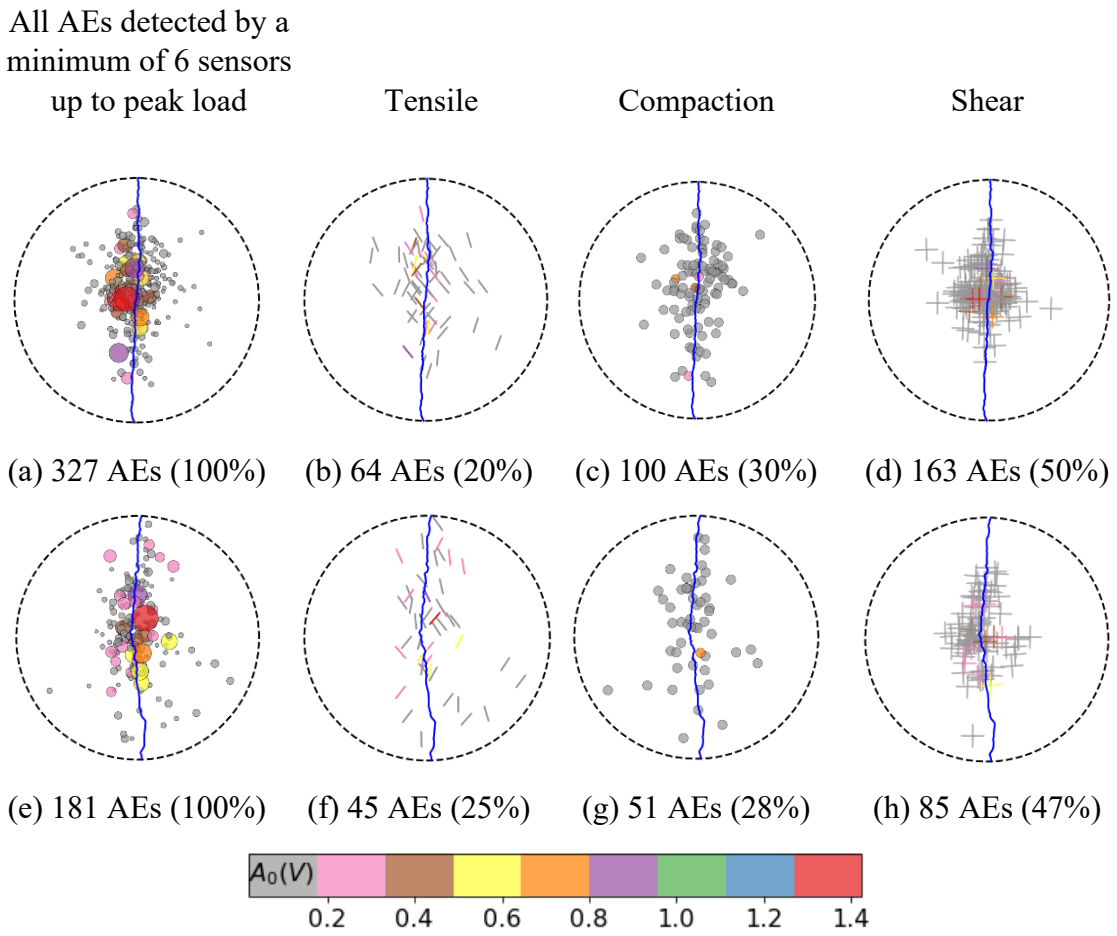

Fig. 4.5 Spatial distribution of AE events detected by a minimum of 6 sensors and AE source mechanisms for B1 (upper panel) and B2 (lower panel). The shear cracking mechanism is predominant in specimens tested under Brazilian loading. Percentages in brackets indicate the proportion of specific AE source mechanisms to the total AEs detected for the given specimen.

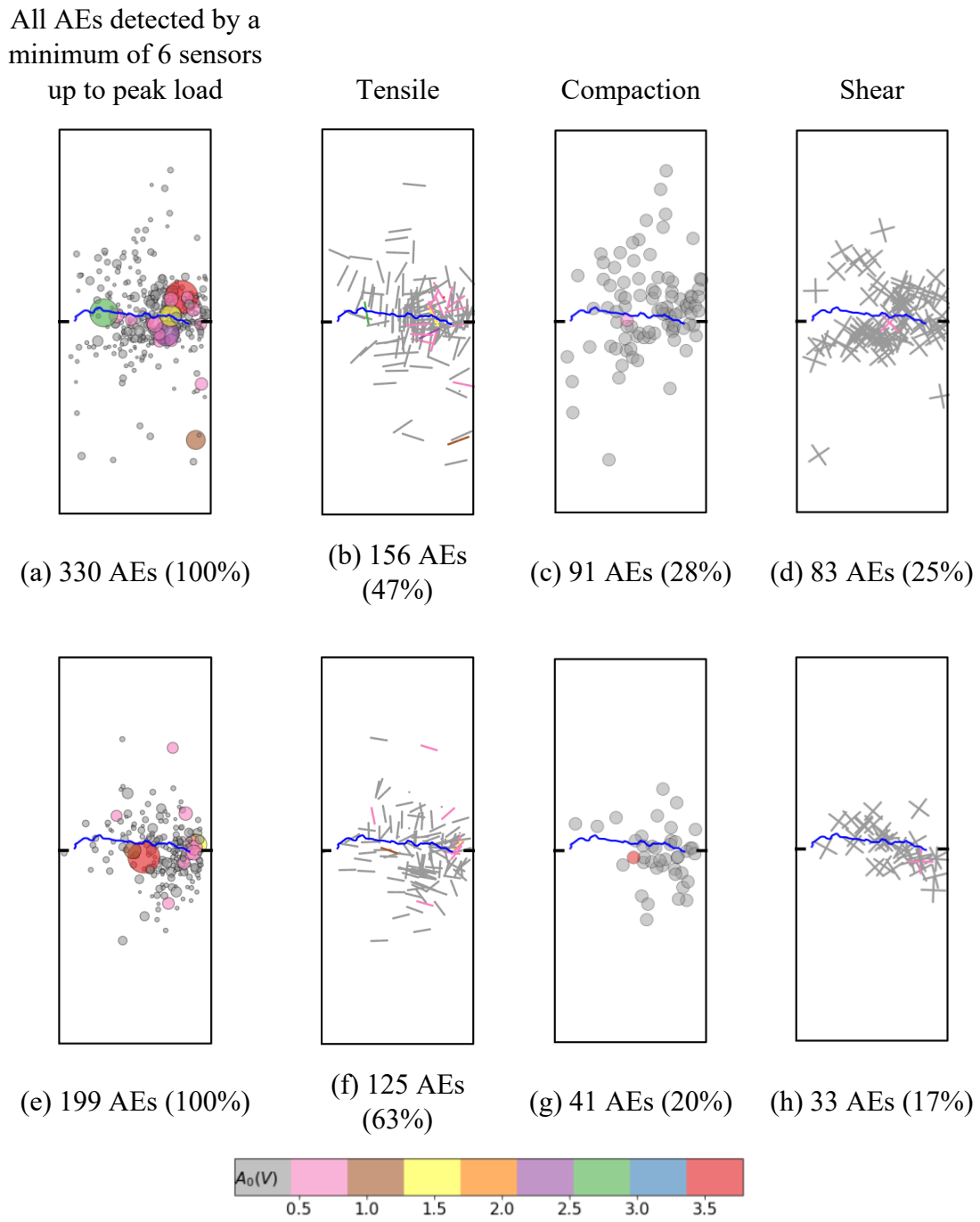

Fig. 4.6 Spatial distribution of AE events detected by a minimum of 6 sensors and AE source mechanisms for D1 (upper panel) and D2 (lower panel). The tensile cracking mechanism is predominant in specimens tested under direct tensile loading. However, shear microcracks' contribution to the formation of the macro fracture is still significant. Percentages in brackets indicate the proportion of specific AE source mechanisms to the total AEs detected for the given specimen.

The temporal evolution of AEs of different source mechanisms during the loading process is depicted in Fig. 4.7.

The absence of AEs in the first loading stage for B1 and B2 (Fig. 4.7a and b) suggests that all deformations could be considered elastic deformation at this stage. In stage 2, it is evident that both tensile and shear microcracks are simultaneously activated, though the quantity of tensile AEs is slightly higher. As the load approaches the end of the second stage, the compaction and shear AEs started to increase at a higher rate than the tensile AEs. Finally, as the load reaches its peak value, the shear microcracks dominate the fracturing mechanisms in Brazilian specimens.

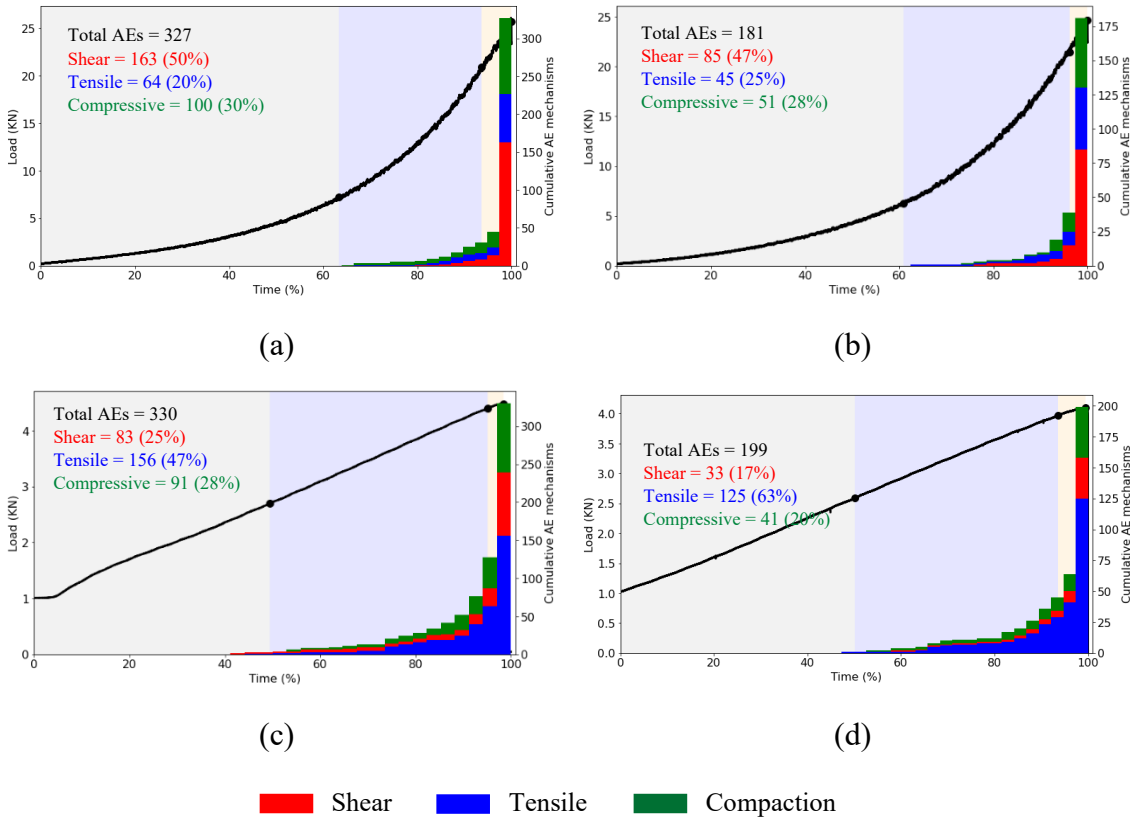

Fig. 4.7 Cumulative histogram of the temporal distribution of AE events of different source mechanisms for (a) B1, (b) B2, (c) D1, and (d) D2 during the loading process. The crack initiation is almost equally composed of tensile and shear cracking mechanisms for both Brazilian and direct tensile loadings. However, from the middle of the second loading stage, microcracks become predominantly shear for Brazilian loading and tensile for direct tensile loading.

Similarly, there are almost no AEs in the first stage for D1 and D2, as shown in Fig. 4.7c and d. In addition, both tensile and shear microcracks simultaneously occurred in direct experiments in the first half of the second stage, like B1 and B2. However, from the middle of the second stage, the tensile-type AEs increase sharply in D specimens, in contrast to B

specimens in which shear-type AEs increase more drastically. Finally, the third stage primarily consists of tensile AEs.

Regardless of the loading type, the tensile- and shear-type AEs occurred coincidentally throughout the deformation process of granite specimens. However, Fig. 4.7 suggests that the fracturing process is shear dominant in the Brazilian test and tensile dominant in direct tension tests, at least for this study's material and experimental conditions.

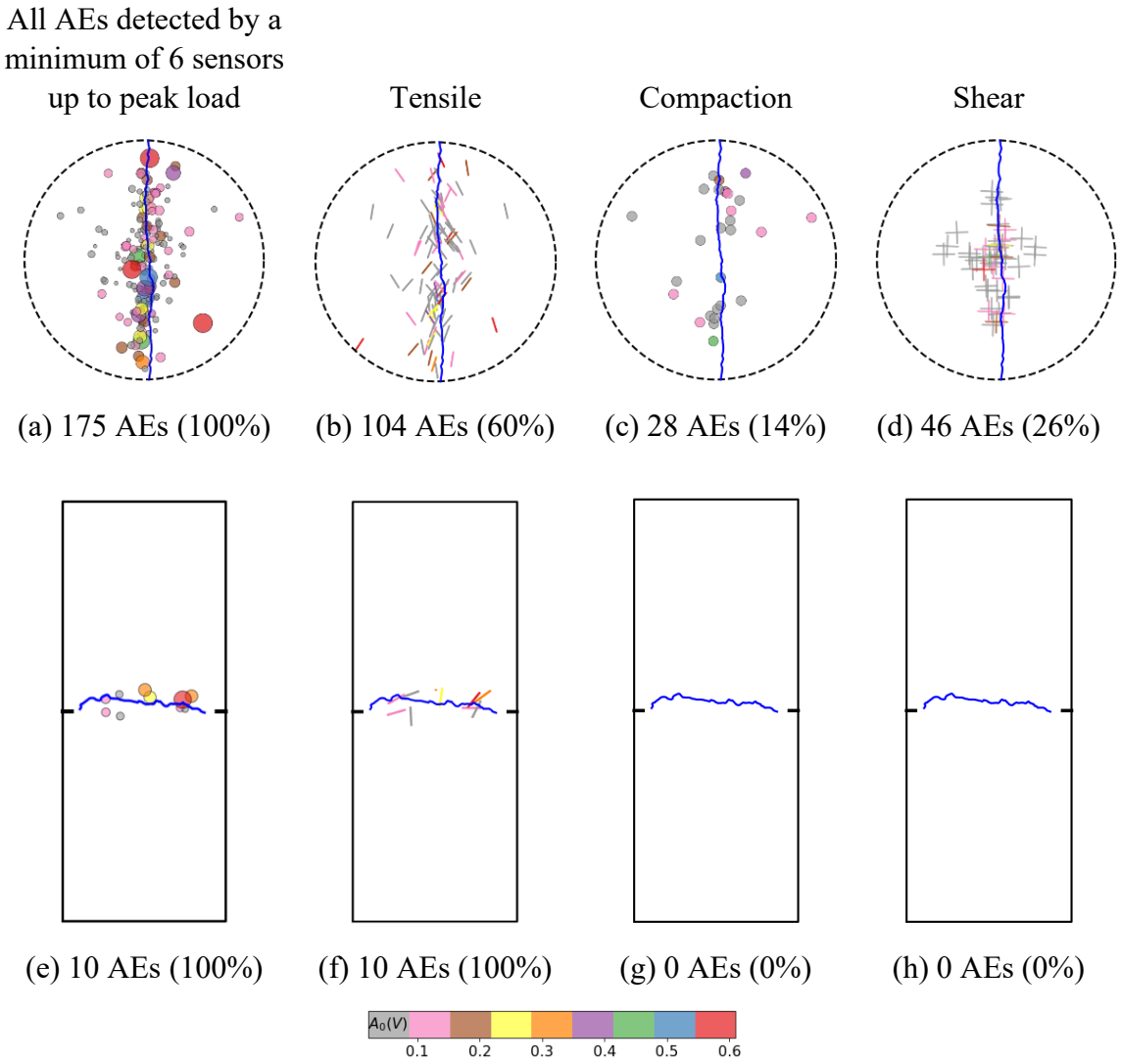

Fig. 4.8 Spatial distribution of AE events detected by a minimum of 6 sensors and AE source mechanisms for mortar specimens tested under Brazilian (upper panel) and direct tensile (lower panel) loading. Testing fine-grained mortar specimens, 60% and 100% tensile microcracks was observed in Brazilian and direct tensile experiments, respectively.

In addition, Brazilian and direct tensile tests were conducted on fine-grained mortar (rock-like) specimens as illustrated in Fig. 4.8. The mortar is SikaGrout 212 with an average grain size of 23 μm and a maximum grain size of 2 mm. Although a fine-grained granite would have been a better candidate for this comparison, in order to avoid the effects of the anisotropy and heterogeneity of different grains in granite, SikaGrout 212 mortar with a uniform grain size distribution was selected. The results of the mortar specimens tested under Brazilian and direct tensile loading are shown in Fig. 4.8. Reducing the grain size increased the contribution of tensile microcracks in the Brazilian specimen (compare 60% in Fig. 4.12b with 25% and 20% in Fig. 4.5b and 5f). Removing the compressive stress further increased the contribution of tensile microcracks in specimens tested under direct tension (compare 100% in Fig. 4.12f with 47% and 63% in Fig. 4.6b and f) .

4.3.3. Visual Observation of Tensile Fracturing

Because the deformation in brittle rocks is primarily due to the tensile stress concentration at the tip of pre-existing flaws [242], extensile strain distribution in the ROI was examined for B1, B2, D1, and D2. Considering the loading configuration in the direct and Brazilian tests, the extensile strain includes ε_{xx} (tensile strain in horizontal direction) for B1 and B2, and ε_{yy} (tensile strain in vertical direction) for D1 and D2.

AE events reflect the formation of inelastic damage in materials [10]. It is, therefore, more appropriate to determine the inelastic strain fields in the DIC analyses to compare the AE and DIC results. The strain field measured by the VIC-2D software is the nominal total strain (ε^t) that includes both the elastic ε^e and plastic ε^p strain components, i.e.,

$$\varepsilon^t = \varepsilon^e + \varepsilon^p \qquad \text{Eq. 4.4}$$

Thus, the elastic strain component must be subtracted from the total strain to determine the plastic strain component. From the AE analysis, it was assumed that the end of the first loading stage, i.e., point A in Fig. 4.4, can represent the elastic limits for all specimens. In fact, in this stage, less than 2% of AEs were captured in all experiments (Fig. 4.4). Hence, the maximum strain values corresponding to point A (in the horizontal and vertical directions for B and D specimens, respectively) were assumed to reasonably estimate the elastic strain limit, i.e., ε^e. The maximum elastic strain component for B1, B2, D1, and D2 was approximately 950, 640, 400, and 350 με, respectively.

The upper panel of Fig. 4.9 displays the plastic tensile strain component in horizontal (i.e., ε_{xx}^p for B1 and B2) and vertical (i.e., ε_{yy}^p for D1 and D2) directions over the given ROIs immediately before failure (i.e., point C in Fig. 4.4). The same color scale was used for the same specimen types to better compare the developed fracture process zones over their surfaces. The lowest value in the color bars was set to zero to facilitate distinguishing the zones of inelastic tension.

As illustrated in Fig. 4.9a and b (upper panel), in B specimens, the inelastic horizontal tensile strain mostly concentrated in the central region of discs and coincided with the path

of the final fractures. The maximum stain values occurred close to the center of B specimens, confirming the Brazilian test results' validity [102], [117]. The maximum tensile strain at failure was 3300 and 3100 με for B1 and B2. In addition, Fig. 4.9a and b (upper panel) show that the FPZ almost has the same extent in both specimens. However, the red-color zone in B1 is wider and longer than in B2, meaning that B1 underwent more microcracking during loading (remember that B1 and B2 have the same color scale). This agrees well with the number of detected AEs in B1 and B2, as shown in Fig. 4.5a and e.

Fig. 4.9c and d upper panel) show the inelastic tensile strain distribution in the vertical direction right before failure in D1 and D2. The tensile strain fields in D1 and D2 are also quite similar. In both D specimens, the vertical plastic extension accumulated in the middle of the specimens with the maximum values at the right notch. The strain concentration zones match the specimens' macro fracture paths very well. The red-color zones indicate that the macro fractures initiated from the right notch and propagated to the left side of specimens under direct tensile loading. Furthermore, the extent of the FPZ is also very similar in D1 and D2.

Overall, the DIC process zones in Fig. 4.9a-d (upper panel) are consistent with AE event distributions shown in Fig. 4.5a and e and Fig. 4.6a and e, respectively. In addition, Fig. 4.9 (lower panel) depicts the scatter plot of the detected AEs colored by AE density for B and D specimens. These plots represent the FPZ obtained from the AE analysis, in which darker shades of red indicate a higher concentration of AE events and darker shades of blue indicate lower AE activities.

The zones of the highest AE density in AE FPZ plots (darker reds) and the zones of the highest strain concentration in DIC FPZ plots (darker reds) match very well. In general, the trend of the DIC FPZ agrees well with the AE FPZ for all specimens. However, in all cases, the AE FPZ is larger than the DIC FPZ. This is because the AE events represent deformation occurring in the entire body of specimens, while the strain fields represent only those deformations that appear on the surface of specimens. Another reason for this discrepancy could be due to the errors associated with the AE source locations. That said, comparing the size of the same FPZ measured by different techniques (e.g., AE and DIC) must be considered cautiously, as the definition of the range of FPZs varies for different techniques.

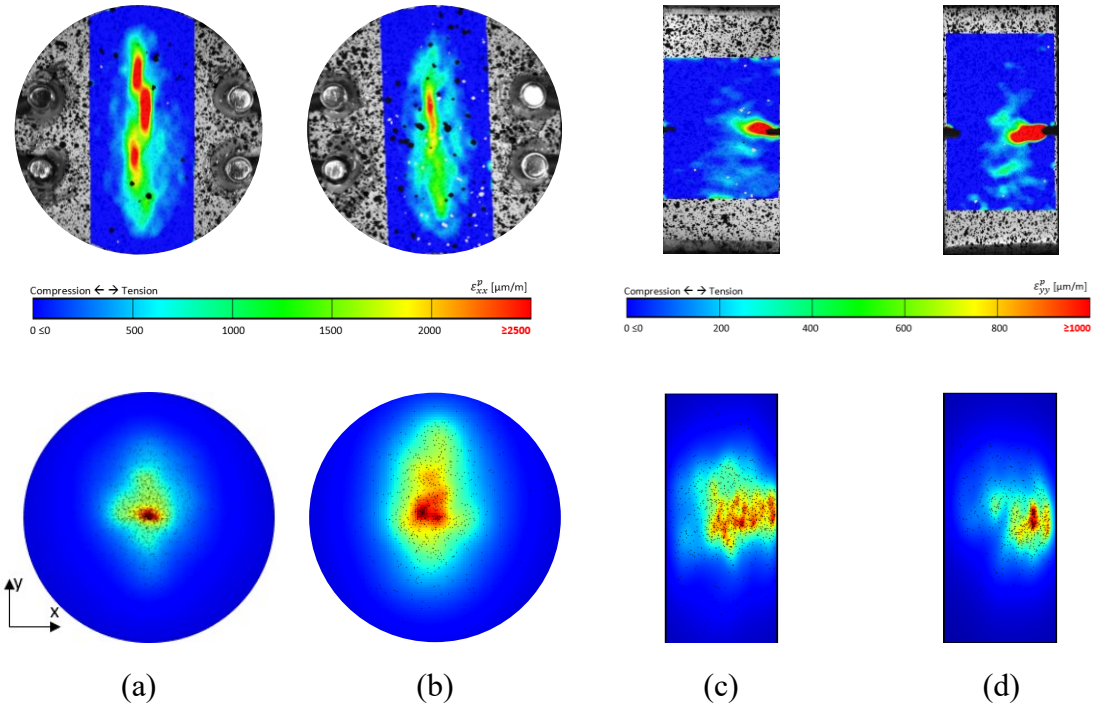

Fig. 4.9 Plastic strain field at failure (upper panel) and AE density plot at failure (lower panel) for (a) B1, (b) B2, (c) D1, and (d) D2. Darker shades of red indicate higher concentrations of AE events in AE density plots. Overall, the zones of the highest strain concentration (upper panel) coincide well with those of the highest AE density (lower panel). However, the AE-based process zones (lower panel) are slightly larger than the DIC-based process zones.

To determine the contribution of the different micro failure mechanisms during the fracturing process in granite specimens, the temporal evolution of total tensile (ε_{xx}^{t} for B1 and B2 and ε_{yy}^{t} for D1 and D2) and total shear (ε_{xy}^{t}) strains in different loading stages were evaluated as follows. Fig. 4.10 shows the histogram of the tensile strain (ε_{xx}^{t} for B1 and B2 and ε_{yy}^{t} for D1 and D2) distribution in the ROI at three loading stages (points A, B, and C in Fig. 4.4). Also, Fig. 4.11 illustrates the total shear strain (ε_{xy}^{t}) distribution at these loading points. Note that Fig. 4.10 and Fig. 4.11 represent the total strain values, including the elastic and plastic components. The total strains were used because it was not straightforward to determine the elastic limit of the shear strains. However, the total strain distributions are basically similar to the plastic strain distributions, so this will not affect the subsequent analyses and conclusions.

At point A (stage 1), the histograms show a narrow spread of tensile (Fig. 4.10) and shear (Fig. 4.11) strains for all specimens, reflecting the homogenous and uniform tensile/shear strain distribution in the ROI. The peak in the histograms represents the most frequent values in a data set. Accordingly, since the peak of the histograms corresponding to the first loading stage (green histograms in Fig. 4.10 and Fig. 4.11) occur in small strain values,

it is deduced that the majority of DIC grid points in the ROI underwent minimal tensile and shear strains during this deformation stage. With the increase of the applied load, histograms of ε_{xx}^{t} and ε_{yy}^{t} show smaller peaks, while their spread increases. This indicates the higher variation in the tensile strain field in the ROI, reflecting the local strain accumulation leading to damage in stages 2 and 3. By comparing the ε_{xx}^{t} distribution in B1 and B2 (upper panel in Fig. 4.10) with ε_{yy}^{t} distribution in D1 and D2 (lower panel in Fig. 4.10), one observes that the heterogeneity in the tensile strain is much more significant in Brazilian specimens than in specimens subjected to direct tension. In addition, Fig. 4.10 shows the presence of some compressive strain (negative sign strain) in ε_{xx}^{t} strain field for B1 and B2. This compressive strain is because the horizontal strain (ε_{xx}^{t}) in Brazilian discs become compressive beneath the loading jaws [127].

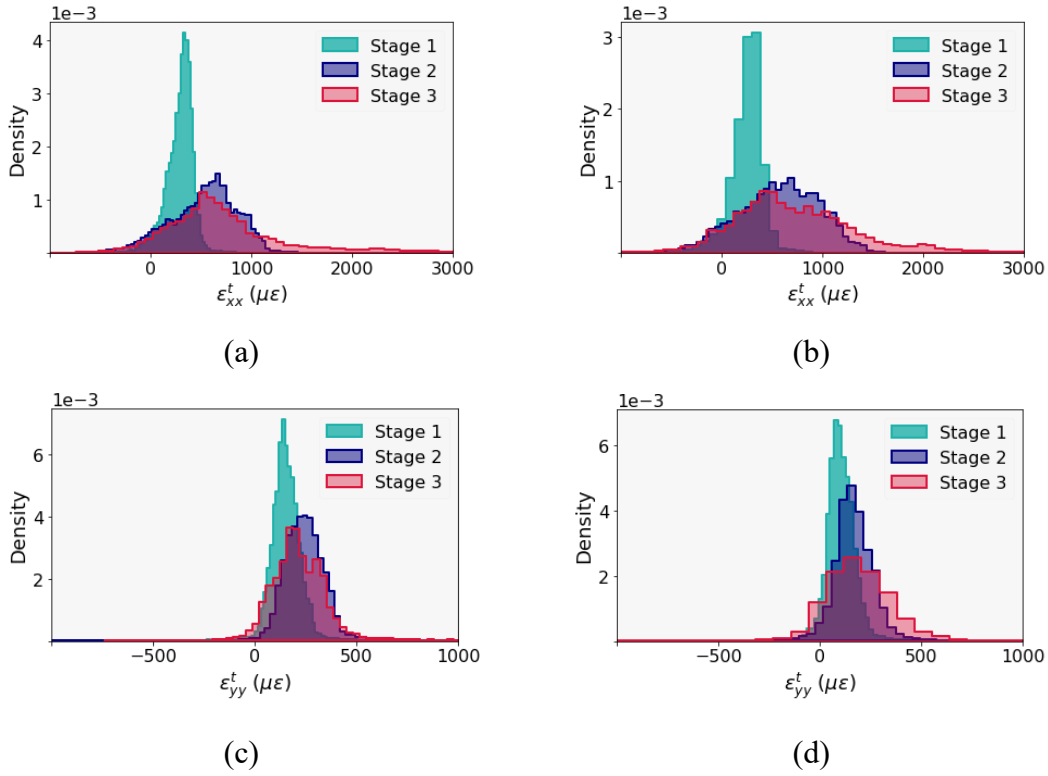

Fig. 4.10 Histograms of total extensile strain distribution in the ROI at different loading stages: ε_{xx} (horizontal strain, along the x-axis in Fig. 4.9) for (a) B1 and (b) B2, and ε_{yy} (vertical strain, along the y-axis in Fig. 4.9) for (c) D1 and (d) D2. Positive (+) and negative (-) strains represent tension and compression. The loading stages 1, 2, and 3 for each specimen are shown in **Erreur ! Source du renvoi introuvable.**. With the applied load, the heterogeneity in the tensile strain field (zones of tensile strain concentration) progressively developed in both Brazilian and direct tensile specimens, as reflected by the wider and shorter histograms in stages 2 and 3.

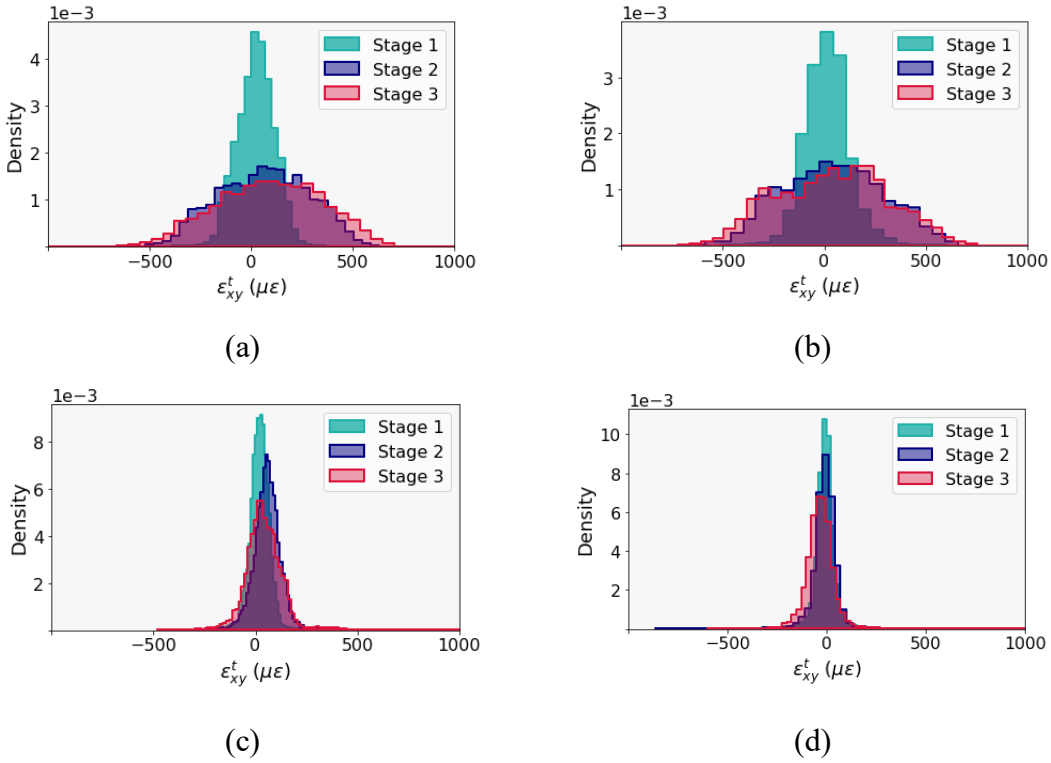

Fig. 4.11 Histograms of shear strain (ε_{xy}) distribution in the ROI at different loading stages for (a) B1, (b) B2, (c) D1, and (d) D2. The loading stages 1, 2, and 3 for each specimen are shown in Fig. 4.4. With the applied load, the heterogeneity in the shear strain field (zones of shear strain concentration) progressively developed in B1 and B2, as reflected by the wider and shorter histograms in the stages 2 and 3 in Fig. 4.11a and b. However, there is no significant change in the spread of the shear strain histogram for D1 and D2, suggesting that shear microcracking may not have played an essential role in the fracturing process of D1 and D2

Furthermore, Fig. 4.11 shows that as the applied load increased from stage 1 to stages 2 and 3, the spread in the histogram of shear strain (ε_{xy}^{t}) increased significantly for B1 and B2. In contrast, there is no significant change in the spread of the histogram of the shear strain (ε_{xy}^{t}) for D1 and D2. In other words, the heterogeneity in the shear strain distribution in the ROI increased remarkably with increasing load levels for B1 and B2, reflecting the local shear strain zones (damages) in Brazilian specimens. This points out the critical role of micro shear cracks in the fracturing process of Brazilian specimens. On the other hand, the absence of such shear strain heterogeneity for D1 and D2 suggests the less important role of shear damage in specimens subjected to direct tension. These results agree well with the contribution of shear and tensile AE mechanisms to the fracturing process of B and D specimens, as shown in Fig. 4.5 and Fig. 4.6.

4.4. Discussion

4.4.1. Macro- and Micro-scale Fracturing

Load-displacement results indicated that the tensile strength of granite specimens obtained from the indirect (Brazilian) tensile load is 46% higher than that obtained from the direct tension. The average Brazilian and direct tensile strengths were 8 and 5.5 MPa, respectively. From a macroscopic point of view, it has been accepted that the rock specimen fails under tensile failure mode in both Brazilian and direct tensile loadings. However, DIC (Fig. 4.10 and Fig. 4.11) and AE (Fig. 4.5, Fig. 4.6, and Fig. 4.7) results showed that this so-called tensile macroscopic failure of rock was composed of both tensile and shear cracks at the microscale. The proportion of tensile and shear cracking modes varied significantly according to the different loading configurations. Microcracks were 49% shear and 23% tensile in Brazilian tests. In contrast, they were 21% shear and 55% tensile in direct tensile tests. This different contribution of tensile and shear microcracks to the formation of the ultimate macroscopic fracture can explain the difference between the Brazilian and direct tensile strengths of rock specimens. These results indicate that the cracking mechanisms differ at micro and macro scales.

It is assumed that 1) the different loading configurations in Brazilian and direct tensile tests and 2) the grain size of tested materials are critical factors controlling their microcracking mechanisms and, thereby, the difference between their direct and Brazilian tensile strengths. This is explained as follows.

Fig. 4.12 illustrates a simplified schematic representation of the loading configuration in Brazilian and direct tensile tests and the induced normal and shear stresses at the grain scale. The direction of the induced tensile stress in both tests is shown with blue arrows. In the Brazilian test, the applied compressive load induces tensile stresses perpendicular to the loading direction (Fig. 4.12a). In the direct tension test, the applied tensile load generates tensile stresses parallel to the loading direction (Fig. 4.12b). We assume that the local tensile stresses are adequate to create tensile cracks (the blue zone) along grain boundaries (intergranular) or through grains (intragranular). The formation of tensile cracks (opening mode) requires some sliding along grain boundaries (the orange zones). The resultant normal stress (black arrows) over the grain boundaries is primarily compressive in Brazilian loading and extensile in direct tensile loading. Thus, generating micro sliding would be more difficult in the Brazilian loading than in the direct tension. This explains why many more shear AEs were detected in Brazilian tests than in the direct tensile tests. Therefore, the higher proportion of "*stronger*" shear microcracks in Brazilian specimens than in specimens tested under the direct tensile loading explains the difference between tensile strengths obtained from these tests. This strongly agrees with the findings reported by Qi et al. [64]. Based on their numerical study, the authors concluded that the difference in granite's direct and Brazilian tensile strengths is because the applied external load has to overcome both the tensile and shear strength along grain boundaries in the Brazilian test. In contrast, the applied external load has to only overcome the tensile strength along grain boundaries in the direct tensile test.

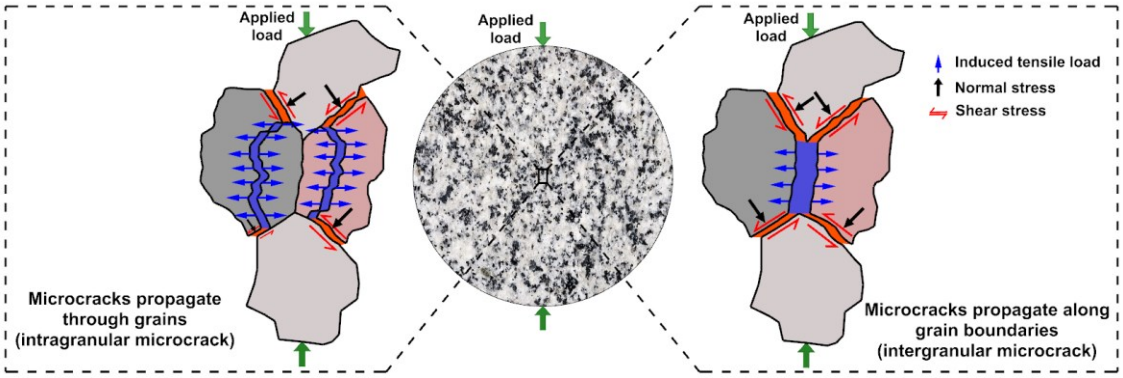

(a)

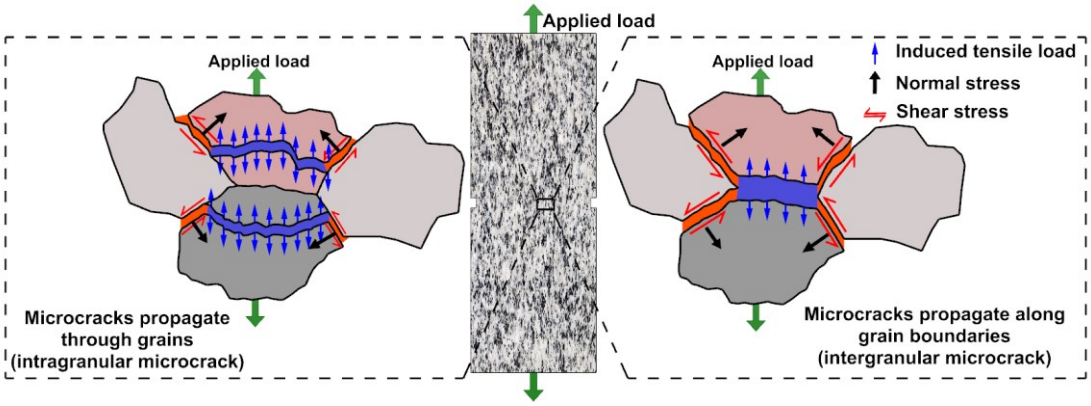

(b)

Fig. 4.12 A simplified representation of the load configuration and the induced normal and shear stresses at grain scale for (a) Brazilian and (b) direct tensile loading. Applied external load induces compressive and tensile stresses over grain boundaries in Brazilian and direct tensile loading, respectively (Adapted from Nicksiar and Martin [243] and Qi et al. [64]).

Therefore, it can be concluded that the fracturing processes in neither Brazilian nor direct tensile tests were composed of 100% tensile microcracks. However, these statements may only be valid for medium to coarse-grain materials like the granite rock tested in this study. Therefore, we tested fine-grained mortar (rock-like) specimens under the Brazilian and direct tensile loading (Fig. 4.8) to examine the effect of grain size on the microcracking mechanisms in rock materials.

As shown in the upper panel of Fig. 4.8, 175 AE events were captured for the Brazilian mortar discs (MB), including 104 tensile, 28 compaction, and 46 shear microcracks. Reducing the material grain size resulted in fewer shear and more tensile microcracks in the Brazilian specimen. The percentage of tensile events increased from 23% for granite disc specimens to 60% for the mortar disc specimen. On the other hand, the percentage of

shear AEs decreased from 49% to 26%. This indicates the effect of the grain size on the micro failure process in rock and rock-like materials. However, due to the compressive stress in the biaxial stress state in the Brazilian test (Fig. 4.12a), some shear microcracks (Fig. 4.8d) are still contributing to the formation of the final tensile macroscopic fracture. The lower panel in Fig. 4.8 represents the AEs detected for the mortar specimen tested under direct tensile loading (MD). Only ten events were detected, all of which are tensile (Fig. 4.8f). That is, by removing the grain size and compressive stress factors by conduction direct tensile tests on mortar specimens, 100% of the captured AEs are of tensile type. This means both macro and micro failure mechanisms are tensile, at least for this specific specimen.

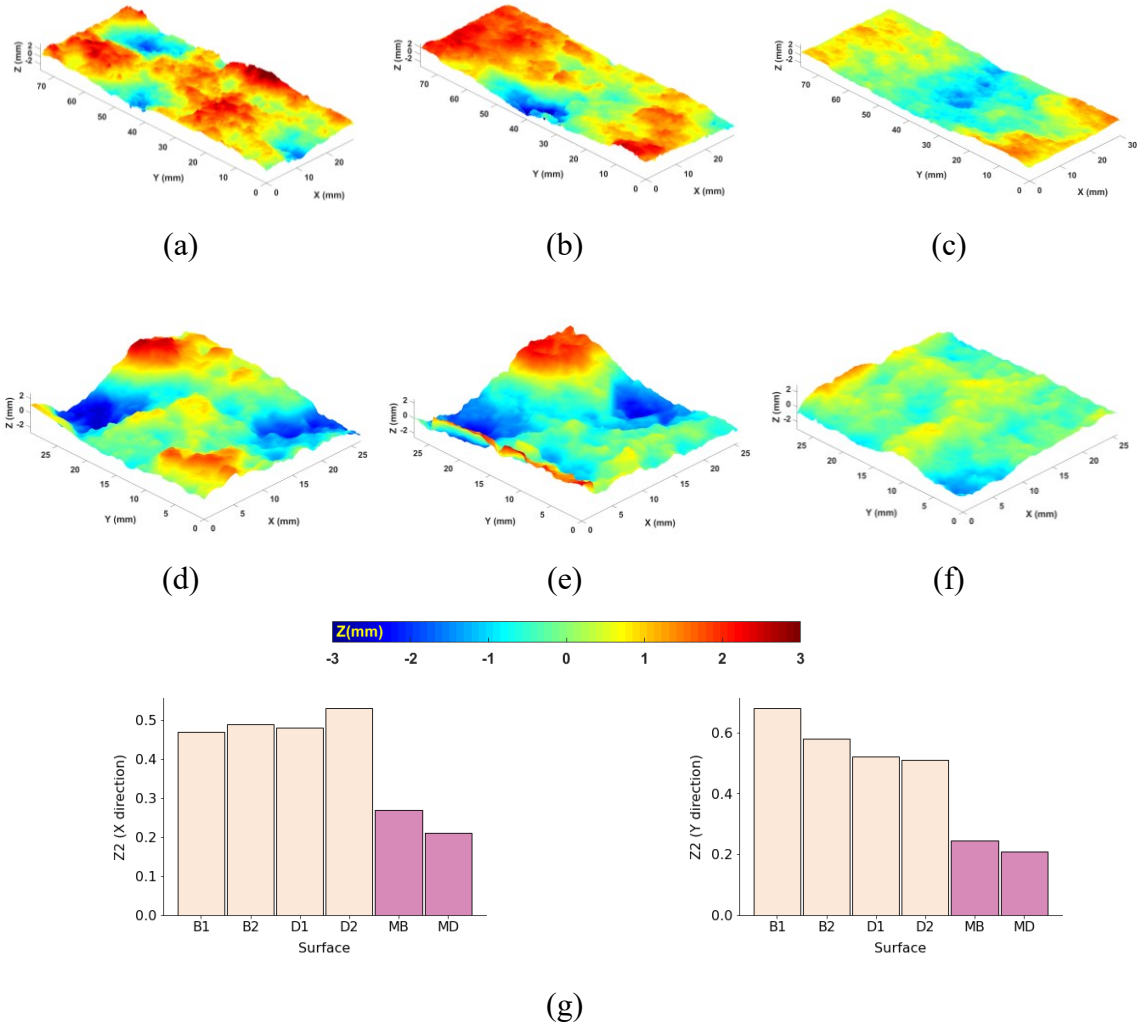

Fig. 4.13 Surface roughness geometry of the created macroscopic fracture after specimen failure for Brazilian specimens (a) B1, (b) B2, (c) MB (Brazilian mortar disc), and specimens tested under the direct tensile loading (d) D1, (e) D2, (f) MD (mortar specimen subjected to the direct tension), and (g) average Z2 value of the created fracture in x and y directions for all specimens.

As an additional evaluation of the effect of grain size on the failure mechanism, the roughness of the created macro fractures was studied. Fig. 4.13 depicts the geometry of the surface roughness of the generated macro fractures for granite and mortar specimens. The average Z2 value (root mean square of the first deviation of the roughness profiles [200]) is also given for comparison. Granite specimens (with coarse grain size) have a rougher fracture surface compared to mortar specimens (with fine grain size) [244].

Fig. 4.14a and b illustrate a simplified 2D roughness profile for a rough and smooth fracture surface. In order to create the fracture and break the specimen into two halves, there are two different fracturing processes. First, for the coarse-grained material, due to the grain interlocking over the rough surface, tensile cracks can be accompanied by some shear slippage on the wall of the fracture surface (Fig. 4.14a). Therefore, a considerable number of shear AE events were detected for granite specimens under the direct tension test. Second, there is no notable grain interlocking for the smooth surface (the fine-grained material); hence, the cracking mechanism is primarily tensile under direct tension (Fig. 4.14b).

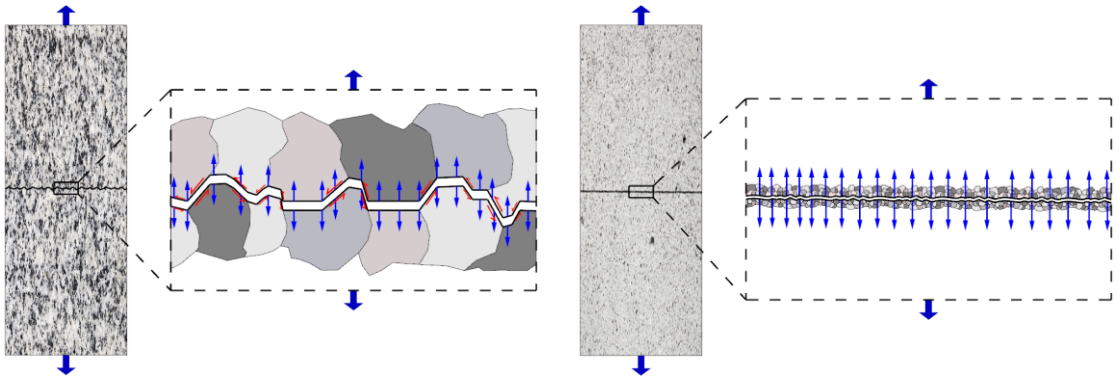

(a) (b)

Fig. 4.14 Direct tensile test on materials with coarse and fine grain sizes. A 2D roughness profile for (a) granite (coarse-grained material) and (b) mortar (fine-grained material). Due to the larger grain size in granite, the induced tensile damage is accompanied by some shear sliding along the grain boundaries. For mortar, shear sliding is basically absent.

4.4.2. Implication to Field Applications

This paper showed that both AE and DIC techniques could explain why macro and micro failure mechanisms differ in rocks under tensile loading. The findings of this study can be applied to explain the fracturing process in other laboratory and field-scale rock tests. For example, it can explain why we have many shear microcracks (sometimes it is the prominent cracking mechanism) in hydraulic fracturing (HF) tests (both on laboratory and field scale), while HF is known as a tensile fracturing process. Our results showed that this could be because: (1) hydraulic fracturing in enhanced geothermal systems is primarily

done in crystalline rocks with large grain size, and (2) due to depth, there is a lot of confining stresses where fractures are hydraulically created. These two parameters bring to mind what we observed in the Brazilian tests.

In addition, our results showed that the ratio of shear-to-tensile microcracks associated with the formation of macroscopic fractures determines to what extent the obtained strength gives a correct estimate of the true tensile strength of the rock. It was shown that with the removing the compressive stress in the Brazilian tests and decreasing the grain size, the micro failure mechanism in the direct tensile tests approaches to be purely tensile, indicating that the measured strength could represent the true tensile strength of the material. However, with the increase of the compressive stress and grain size, the shear microcracks contribute more to the formation of the macroscopic fractures in the Brazilian tests, meaning that the measured strength may overestimate the true tensile strength of the material. That is why Brazilian tensile strength was 1.45 (=8/5.5) times the direct tensile strength.

In hydraulic treatment, the fracture is created in opening or shear mode. The opening-mode deformation (associated with tensile AE events) can significantly impact fracture fluid flow and transport processes in the subsurface reservoir [245], [246]. Likewise, shear cracking (associated with shear AE events) induces slip along pre-existing or newly created fractures, increasing the permeability of the rocks at greater depths, where higher confining stresses exist [247]. However, tensile and shear fracturing mechanisms affect the reservoir permeability differently. The permeability produced by shear cracking is mostly irreversible, while that enhanced by tensile fractures could be completely reversible [247]. Therefore, a well-established knowledge of the relationship between stress state, fracture location, and fracturing mechanisms, derived from laboratory-scale experiments, can serve as a baseline in interpreting the field-scale seismic observations such as hydro-fracturing mapping in enhanced geothermal systems (EGS) and other geo-energy applications

4.5. Conclusions

Fractures that are simply referred to as shear or tensile at the macroscopic scale can be formed by a combination of tensile and shear with different proportions at the microscopic scale. This discrepancy between the macro and micro-scale cracking mechanisms can explain the differences in strengths measured under different experimental loadings performed on the same rock (e.g., Brazilian and direct tensile loading). This study used AE and DIC techniques to investigate the temporal and spatial changes in microcracking process in granite specimens subjected to direct and indirect tensile loadings. It was also attempted to address why cracking mechanisms differ at micro and macro scales, considering the loading conditions.

The findings indicated that the tensile strength obtained from direct tensile loading is approximately 70% of that obtained from Brazilian tensile loading. While the deformation processes were similarly divided into three loading stages for both direct and indirect tensile loadings, the evolution of microcracking mechanisms was significantly different.

Both AE and DIC results indicated that microcracks in granite were predominantly shear for specimens tested under Brazilian and tensile under direct tension. The tensile and shear cracking mechanisms contributed almost equally to the microcracking initiation in both experimental loadings. However, with increasing the load beyond the crack initiation limit, shear microcracks significantly outnumbered tensile microcracks in Brazilian loading, while the opposite was true for direct tensile loading.

Moreover, our results demonstrated that the difference in the evolution of the cracking mechanisms under direct and indirect tensile loadings, among other factors, is due to 1) the different loading configurations in Brazilian and direct tensile tests and 2) the grain size. The AE results of fine-grained mortar specimens and the fracture roughness characterization data provided further evidence for these assumptions.

Our observations could be a step ahead toward enhancing our understanding of the fracturing processes in rock materials in laboratory and field scales. For instance, it can explain the presence of shear microcracks and their contribution to the formation of hydraulically created so-called *tensile* fractures.

Future research should investigate the effect of grain size and compressive stress on the microcracking mechanisms in different rock types with different values of porosities under other rock strength tests. In addition, microstructural observations using scanning electron microscope (SEM) should be performed to further examine these findings about the effect of grain size on the microcracking mechanisms under direct and indirect tensile loadings

CHAPTER 5: TENSILE STRENGTH AND FAILURE BEHAVIOUR OF ROCK-MORTAR INTERFACES: DIRECT AND INDIRECT MEASUREMENTS

RÉSISTANCE À LA TRACTION ET COMPORTEMENT À LA RUPTURE DES INTERFACES ROCHE-MORTIER: MESURES DIRECTES ET INDIRECTES

Authors and Affiliation:

Ghasem Shams: Ph.D. Candidate, Civil Engineering and Building Engineering Department, Université de Sherbrooke, Sherbrooke, Québec, Canada.

Patrice Rivard: Professor, Candidate, Civil Engineering and Building Engineering Department, Université de Sherbrooke, Sherbrooke, Québec, Canada.

Omid Moradian: Lecturer, Department of Earth Sciences, Swiss Federal Institute of Technology (ETH), Zurich, Switzerland and Currently Research Associate Professor, Department of Civil and Environmental Engineering, Colorado School of Mines, Golden, Colorado, USA.

Journal Title and Paper Status:
Submitted to ***Journal of Rock Mechanics and Geotechnical Engineering*, October 2022**, **accepted with revision**.

Contribution to the Thesis

The previous chapter discussed the cracking mechanisms at micro and macro scales for intact rock specimens under direct and indirect tensile loadings. This chapter investigates the microcracking mechanisms in rock-mortar specimens subjected to direct and indirect (Brazilian) tensile tests. The relationship between direct and Brazilian tensile strengths of rock-mortar interfaces and between microcracking mechanisms and tensile strength of rock-mortar specimens are studied. Roughness characteristics of the surface of the generated fractures in specimens tested under two different experimental setups (i.e., direct and Brazilian tensile loadings) are also discussed in this chapter.

This chapter is aimed to address the following specific objectives (see Section 1.4):

1. Identify and describe the micromechanics of damage at the granite-mortar interface subjected to tensile loading.

Résumé

La résistance à la traction de l'interface roche-béton est l'un des facteurs cruciaux contrôlant les mécanismes de rupture des structures telles que les barrages-poids en béton. Malgré l'importance critique du mécanisme de rupture et de la résistance à la traction des interfaces roche-béton, nos connaissances et notre compréhension dans ce domaine sont encore très limitées. Cet article vise à étudier la résistance à la traction et les processus de fracturation aux interfaces roche-mortier soumises à des chargements de traction directs et indirects. Des techniques de corrélation d'images numériques (DIC) et d'émission acoustique (AE) ont été utilisées pour surveiller les mécanismes de rupture dans les échantillons soumises à une tension directe et indirecte (essais brésiliens). Les résultats ont montré que la résistance à la traction directe des échantillons de roche-mortier est inférieure à leur résistance à la traction indirecte, avec un rapport de résistance à la traction directe/indirecte de 65%. Les données de champ de déformation DIC et l'inversion du tenseur des moments des événements AE ont indiqué qu'un nombre important de microfissures de cisaillement se sont produites dans les échantillons soumis à l'essai brésilien. La présence de ces microfissures de cisaillement qui nécessitent une énergie plus élevée pour se rompre entraîne une résistance à la traction plus élevée dans les essais brésiliens. Au contraire, les microfissures étaient majoritairement en traction dans les échantillons soumises à une traction directe conduisant à une résistance à la traction plus faible. Cela a également été confirmé par les caractéristiques de rugosité de la surface des fractures générées, car les échantillons testés sous tension indirecte ont montré une rugosité plus faible avec des surfaces de fracture plus plates que les échantillons testés sous tension directe avec des surfaces de fracture irrégulières et rugueuses. Les résultats de cette étude peuvent aider à obtenir des prédictions plus précises de la résistance à la traction des interfaces roche-béton pour une conception plus sûre des structures.

Abstract

The tensile strength at the rock-concrete interface is one of the crucial factors controlling the failure mechanisms of structures such as concrete gravity dams. Despite the critical importance of the failure mechanism and tensile strength of rock-concrete interfaces, understanding of these factors remains very limited. This study investigated the tensile strength and fracturing processes at rock-mortar interfaces subjected to direct and indirect tensile loadings. Digital image correlation (DIC) and acoustic emission (AE) techniques were used to monitor the failure mechanisms of specimens subjected to direct tension and indirect loading (Brazilian tests). The results indicated that the direct tensile strength of the rock-mortar specimens was lower than their indirect tensile strength, with a direct/indirect tensile strength ratio of 65%. DIC strain field data and moment tensor inversions of AE events indicated that a significant number of shear microcracks occurred in the specimens

subjected to the Brazilian test. The presence of these shear microcracks, which require more energy to break, resulted in a higher tensile strength during the Brazilian tests. In contrast, microcracks were predominantly tensile in specimens subjected to direct tension, leading to a lower tensile strength. Spatiotemporal monitoring of the cracking processes in the rock-mortar interfaces revealed that they show AE precursors before failure under the Brazilian test, whereas they show a minimal number of AE events before failure under direct tension. Due to different microcracking mechanisms, specimens tested under Brazilian tests showed lower roughness with flatter fracture surfaces than those tested under direct tension with jagged and rough fracture surfaces. The results of this study shed light on better understanding the micromechanics of damage in the rock-concrete interfaces for a safer design of engineering structures.

Keywords: Rock-mortar, Rock-concrete, Moment tensor inversion, Acoustic emission, Digital image correlation, Tensile strength, Direct tensile test, Brazilian test

5.1. Introduction

In geomechanics, rock-concrete (RC) interfaces are frequently seen in civil and mining engineering applications such as concrete gravity dams founded on rock, concrete retaining walls, socketed piers, and shotcrete [71], [248]. In such structures, the interface between rock and concrete is usually considered the weakest structural zone, causing the initiation and growth of damage and final failure along the interface [249], [250]. During the last few decades, numerous studies have investigated the mechanical behavior of RC interfaces under compression [76], [77] and shear loading [58], [78]–[82]. However, very few studies have focused on the tensile interaction mechanism and tensile strength of RC interfaces. In brittle materials, tensile strength is often less than shear strength and much smaller than compressive strength, reflecting the importance of tensile strength in the resistance to failure of rock engineering materials and RC structures [22], [24], [25]. For instance, the tensile strength in dam-foundation interfaces resists the overturning moment at the toe zones of dams due to the acting forces of reservoirs [68], [69]. In addition, tensile failure at the rock-shotcrete interface is the source of instabilities and the failure mode in shotcrete, which, in turn, can influence the overall stability of structures [70]–[73]. Furthermore, the tensile strength and behavior at cement-cap rock interfaces are crucial factors controlling leakage from wells in the oil and gas industry [74], [75]. Therefore, to provide a safe design of elements incorporating RC interfaces, obtaining a reliable understanding of the tensile behavior of such bi-material interfaces and its impact on the fracturing processes of whole structures is essential.

It should be noted that there is no standard laboratory testing procedure for performing a tensile test on a RC or rock-mortar (RM) interface, with direct tension and Brazilian (indirect) tension tests typically being adopted [69], [71], [80]. Based on the existing literature, the failure properties and Brazilian tensile strength (BTS) of RC and RM specimens subjected to the Brazilian test are controlled by various parameters, including the interface roughness, interface inclination angle, rock type, and concrete/mortar properties [70], [71], [76], [83]–[85].

Some studies have reported that the BTS of RM specimens increases with interface roughness [70], [71], [83], [85]. According to Shams et al. [251], Zhu et al. [70], and Qiu et al. [85], increasing the interface roughness increases the contact area and interlocking effect (anchorage) between the rock and mortar along the interface. This contributes to an increase in the BTS of RM Brazilian discs. Luo et al. [83] observed that the BTS of RM interfaces is governed by the combined contribution of the adhesion and cohesion losses. Adhesion loss occurs when rock and concrete/mortar semi-samples are detached exactly along their interface, without any failure in the interface asperities. In cohesion loss, failure occurs at the asperities root, either in the concrete/mortar or rock.

The BTS of RM interfaces is also affected by the properties of the rock and mortar constituents. Chang et al. [71], Selçuk and Aşma [76], and Zhu et al. [70] showed that an increase in the mortar strength increases the BTS of bi-material discs. According to Selçuk and Aşma [76] and Zhu et al. [70], the mortar constituents and degree of hydration of the cement produce different adhesions between the rock and mortar that affect the BTS of specimens. Moreover, the mechanical properties of rocks seem to have a negligible effect on the BTS of bi-material specimens as long as the mortar is weaker than the rock [70], [85]. It has also been shown that the interface adhesive strength is affected by the physical properties of rocks, for example, porosity [70]. For instance, compared with granite and marble, sandstone adheres much more to mortar, thereby increasing the adhesion between rock and mortar and increasing the BTS of RM specimens [70].

The tensile strength of rock-mortar specimens under direct tension has rarely been studied. Bauret and Rivard [86] studied the effect of interface roughness on the direct tensile strength (DTS) of bi-material cylindrical specimens composed of high-strength and low-strength mortars. Their results indicated that the bond strength increased with roughness. A few studies have reported the DTS of RM and RC specimens without examining the effect of different parameters on the DTS [69], [72], [77], [80], [87]. Notably, RM and RC interfaces have a smaller yet considerable DTS compared to those of intact rock and intact mortar/concrete [69], [80] and, sometimes, DTS is comparable to that of intact mortar/concrete [87].

It is well known that the Brazilian test overestimates the tensile strength of "intact" rocks. The ratio of the DTS to BTS for different "intact" rock types ranges between 0.6 and 0.9 [5], [10], [22], [31], [62]–[64], [252]. This difference between the DTS and BTS is mainly attributed to the different loading configurations of the two testing methods [22], [66]. According to Perras and Diederichs [22], a key factor affecting the difference between the BTS and DTS of rocks is suppressed crack propagation in Brazilian discs because of the biaxial stress state in the Brazilian test. However, these very few studies have focused on the macroscale behavior of rocks under tensile loading. Based on a numerical study, Qi et al. [64] reported that the difference between the BTS and DTS of intact rocks arise because the applied external load must overcome both the tensile and shear strengths along the grain boundaries in the Brazilian test compared to only tensile strength along the grain boundaries in the direct tensile test. In an experimental study, Wang et al. [27] analyzed

the dominant frequency of acoustic emission (AE) hits produced in marble specimens under direct and Brazilian tensile tests. These authors suggested that tensile cracks produce low-dominant-frequency AE signals while shear cracks release high-dominant-frequency signals and concluded that the difference in DTS and BTS of marble results from a higher proportion of high-dominant-frequency waveforms (i.e., shear cracks) in Brazilian test specimens.

While the tensile fracturing processes of "intact" rocks under the Brazilian and direct tensile tests have been investigated to some extent, there are still critical scientific gaps in understanding the micromechanics of the tensile fracturing in bi-material interfaces such as rock-mortar or rock-concrete. Further research is needed to investigate: (1) When, where, and how microcracks nucleate and propagate in these interfaces under tensile loading; (2) Do bi-material interfaces show precursors before final failure?; (3) Do spatiotemporal evolutions of cracking processes in bi-materials differ in micro- and macro-scales? Answering these questions can significantly increase our knowledge for successful structural health monitoring of engineering structures.

This study investigated the fracturing processes in RM specimens at the microscopic scale by focusing on spatiotemporal crack initiation and propagation under direct and indirect (Brazilian) tensile tests. In addition, microcrack source mechanisms were examined during the tensile loading of RM interfaces to better understand the relationship between micro- and macro-cracking mechanisms and between the direct and indirect tensile strengths. A combination of strain measurements using digital image correlation (DIC) and moment tensor analysis of AE were used to track the microscopic cracking and damage mechanisms. The roughness values of the fractures produced under the two loading conditions were also compared. Our results provide insight into the fundamental mechanisms of rock-concrete interface fracturing under tensile loading.

5.2. Materials, Specimens, and Experimental Procedure

5.2.1. Materials and Specimen Preparation

The bi-material specimens were composed of rock and mortar. Two groups of RM specimens were prepared as follows: (1) cylindrical disc specimens subjected to Brazilian indirect tensile loading, and (2) rectangular prismatic specimens subjected to direct tensile loading. The rock was Stanstead granite, and the mortar was composed of water and SikaGrout 212 in a ratio of 2:11.

A granite panel with a saw-cut smooth surface was used to prepare the RM specimens. After preparing the granite panel, it was placed in a wooden mold and mortar was poured onto the rock surface in the mold. A plastic sheet was used to cover the cast mortar for 48 h, and once the mortar hardened, the RM blocks were kept in a wet room at room temperature for 28 d.

Cylindrical cores (diameter, D = 75 mm) were subsequently drilled from the RM blocks, and the drilling axis was parallel to the RM interface. Careful attention was paid to ensure

that the interface passed through the center of the cores. Subsequently, the cores were cut into cylindrical discs (D = 75 mm, thickness (T) = 37.5 mm) as specimens for Brazilian indirect tensile testing (Fig. 5.1a); with a T/D ratio of 0.5, as suggested by the International Society for Rock Mechanics and Rock Engineering (ISRM) [92]. Both sides of the discs were then ground and polished. Furthermore, the RM block was cut into small cuboid samples (length (L) = 37 mm, width (W) = 30, height (H) = 100 mm) as specimens for direct tensile testing (Fig. 5.1b). The ends of the prismatic specimens were polished and then glued onto the loading plates using a strong adhesive epoxy (Fig. 5.1b). The entire preparation procedure, including coring, cutting, grinding, and polishing, was performed according to ISRM recommendations [92], [253].

High-contrast black speckles were made on a white layer of paint on the surfaces of the specimens to achieve more accurate displacement measurements using the digital image correlation (DIC) technique, as depicted in Fig. 5.1a and b. In addition, cylindrical and disc specimens of intact mortar and granite were prepared to determine basic mechanical and physical properties, as listed in Table 5.1.

5.2.2. Experimental System and Testing Methodology

5.2.2.1. Loading System

Brazilian tests were performed using a servo-controlled material testing system (MTS). The load cell capacity for the Brazilian tests was 225 KN. Direct tensile tests were performed with an INSTRON 4482 dual-column Universal Testing machine, for which the load cell capacity was 100 KN.

ISRM standard loading jaws [92] were used to perform the experimental Brazilian tests (Fig. 5.1a). In addition, two cardboard cushions (T = 2.5 mm) were inserted between the jaws and specimens (Fig. 5.1a) to avoid an excessive concentration of compressive stress at the jaw–specimen contact [22], [63], [108], which would otherwise cause premature fracture initiation and invalidate the test results [63], [119], [194].

All the tests were performed at the Rock Mechanics Laboratory of the Université de Sherbrooke. Two LVDT displacement transducers (Solartron Metrology, Model 925604 DCR15) were used to record the axial displacement in the vertical direction in both direct and Brazilian tests. To ensure that the experiments were performed under a quasi-static loading condition, they were conducted in the displacement control mode at a rate of 0.1 μm/s. The average test durations for the Brazilian and direct tensile tests were 196 min and 42 min, respectively. This loading rate, which was lower than the ISRM recommendation [92], was adopted to better monitor and record the fracturing processes in the specimens.

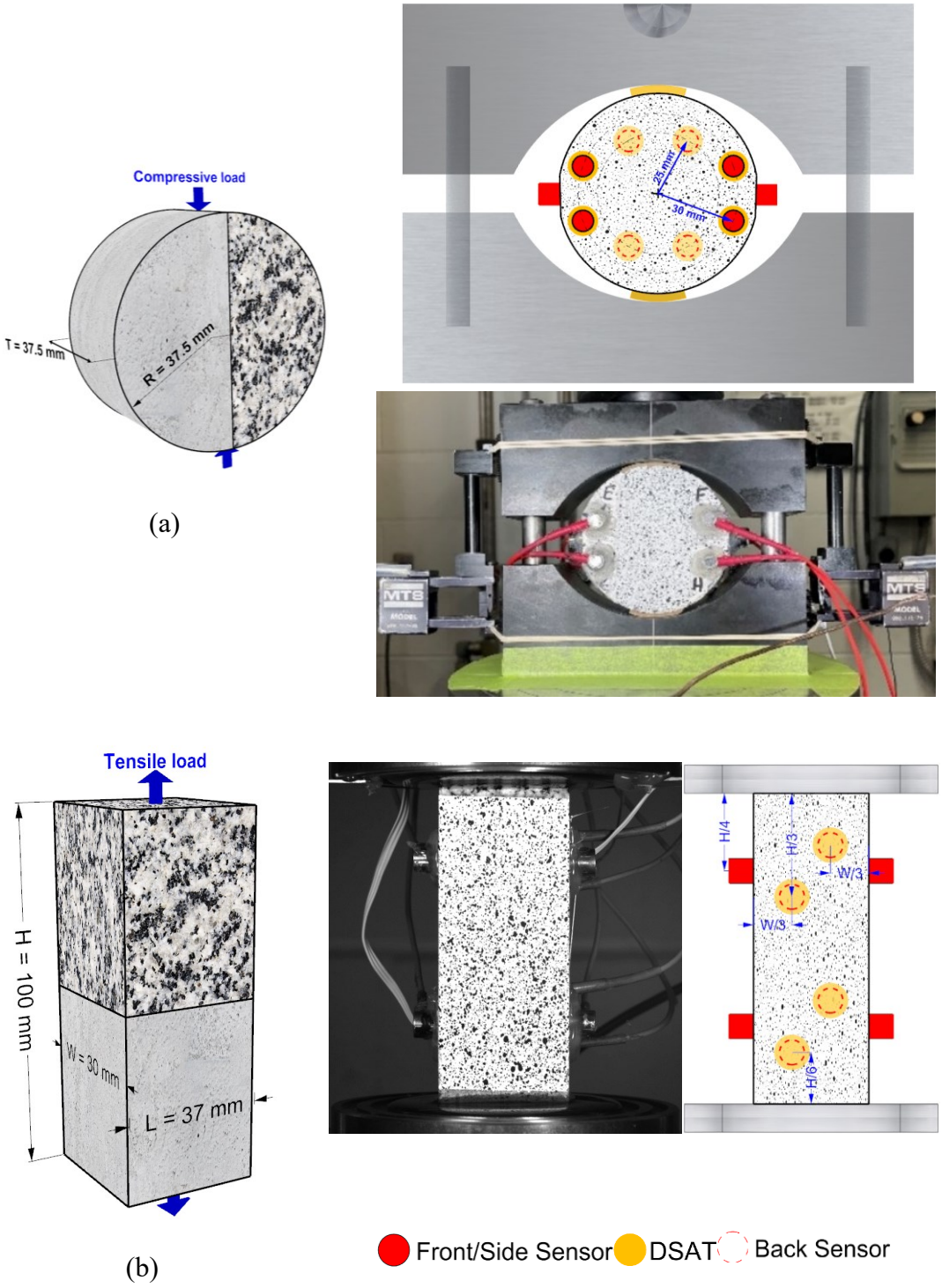

Fig. 5.1 Specimen dimension, location of AE sensors, and speckle pattern created over the front faces of specimens for the (a) Brazilian and (b) direct tension tests.

Table 5.1 Mechanical and physical properties of Stanstead granite and mortar

Property	Granite			Mortar		
	No.*	Min Max	Mean [SD**]	No.*	Min Max	Mean [SD**]
UCS (MPa)	4	136.8 138.0	137.0 [0.6]	3	56.2 59.3	58.1 [1.7]
σ_D (MPa)***	4	5.4 5.5	5.5 [0.05]	4	4.0 4.8	4.3 [0.3]
σ_B (MPa) ***	4	7.4 9.0	8.0 [0.8]	4	5.2 6.1	5.8 [0.4]
E (GPa)	3	49.9 51.1	50.6 [0.6]	3	28.2 29.8	29.0 [0.8]
ν	3	0.21 0.27	0.23 [0.03]	3	0.18 0.20	0.19 [0.01]
V_p (km/s)	4	4.07 4.17	4.12 [0.02]	3	4.17 4.18	4.17 [0.01]
ρ (kg/m^3)	4	2,636 2,646	2,643 [5]	3	2,262 2,269	2,265 [4]

* Number of Samples, ** Standard deviation, *** Tensile strength measured with a loading rate of 0.1 μm/sec for both direct and Brazilian tests.
UCS: Uniaxial compressive strength, σ_D: Direct tensile strength, σ_B: Brazilian tensile strength, E: Modulus of elasticity, *v*: Poisson's ratio, V_p: P-wave velocity, ρ: Density

5.2.2.2. Acoustic Emission (AE) Monitoring

MISTRAS μ-SAMOS AE equipment with two PCI-8 cards (16 measurement channels) was employed to detect the spatiotemporal evolution of AE events (microcracking) in the specimens throughout the experiments. Nano-30 AE sensors operating in the 125–750 kHz frequency range, with a resonant frequency of 300 kHz, recorded AE signals. Fig. 5.1a and b show the AE sensor arrangement for the Brazilian and prismatic specimens, for which ten and eight AE sensors were attached, respectively. To obtain the 3D spatial distribution of the AE events: (1) for the Brazilian specimens, four sensors were mounted on the front surface, four on the back surface, and two on the sides (Fig. 5.1a); and (2) for the specimens under direct tensile loading, four sensors were placed on the back surface and four on the left and right sides (Fig. 5.1b). The sides of the discs were slightly flattened to provide better coupling between the sensors and the specimens. The sensors were first attached to the surfaces of the specimens using double-sided adhesive tape (DSAT) and then glued to the specimens with hot glue. The efficiency of the sensor-specimen coupling was verified using an auto-sensor test (AST) [234].

PAC 2/3/4 preamplifiers with a gain of 40 dB were employed to amplify the low-amplitude AE signal produced by the AE sensors. To avoid ambient noise as much as possible, AE signals were recorded using a threshold value of 35 dB. The sampling frequency was 3

MHz with a pre-trigger of 50 μs and a sample length of 4k. To compute the AE features, the Peak Definition Time (PDT), Hit Definition Time (HDT), and Hit Lockout Time (HLT) were set as 200, 800, and 350 μs, respectively. The maximum duration was 10 ms. The same settings were used for both the Brazilian and direct tensile tests.

AE source localization was performed by determining the arrival times of the P-waves using the Akaike information criterion (AIC) [134], [151]. A constant P-wave velocity field model optimized using the "fmincon" function in MATLAB was applied to locate the AE sources for a minimum distance error of 3 mm. We followed the procedure developed by Li et al. [47] for the source localization and moment tensor inversion of AE events. It should be noted that the source localization procedure requires that each event triggers a minimum of four observation points (AE sensors) to determine the four unknowns, including the event origin coordinates (x, y, z) and event time (t). Therefore, we applied the minimum four-sensor criterion to locate the AE events. In addition, the AE source mechanism was analyzed using the moment tensor inversion method to gain insights into microscale cracking during the loading process [47]. Source localization was performed for a minimum of six AE sensors when the AE source mechanisms were investigated using moment tensor inversion (MTI).

A sensitivity analysis was conducted to determine the effect of the P-wave velocity on the location and number of captured AE events. The results indicated a negligible error in the location and number of detected AE events for the range of P-wave velocities from 4.12 Km/s (average for granite, see Table 5.1) to 4.17 Km/s (average for mortar). Thus, a constant P-wave velocity of 4.15 Km/s was employed to monitor the AE events in the tested RM specimens.

5.2.2.3. Imaging System and Digital Image Correlation Technique

The DIC technique determines the displacement and strain fields by comparing images of the specimen surface captured at different loading times. First, an image of the specimen surface was taken before loading, called the reference image. A region of interest (ROI) was then defined on the surface of the reference image, over which the deformation was determined. The ROI was composed of smaller regions called subsets. The correlation algorithm identifies the best match between a given subset in an undeformed image (i.e., the reference image) and a distorted image (i.e., taken at different loading stages). Finally, the displacement and strain fields were determined by calculating the motion of the subsets [157].

A Basler acA2440-75um camera with a Scheinder Xenoplan 1.9/35-0901 CM120 BK 15 compact lens was employed to capture images of the specimen during the entire loading process. Images were acquired at a rate of 1 fps with a resolution of 2,448 × 2,048 pixels. The same imaging rate was employed for both types of tests. To minimize out-of-plane motion and thereby increase the accuracy of the in-plane displacement measurements, the camera was placed 90 cm from the front surface of each specimen. Simultaneously, the lens axis was perpendicular to the specimen surface. Given the small dimensions of the

specimens, this distance ensured that the out-of-plane displacement did not exceed the acceptable range [240]. Two LED lights also cast stable, constant illumination over the surfaces of the specimens, thereby minimizing DIC post-processing errors.

To increase the accuracy of the DIC post-processing, a random speckle pattern was applied over the front surface of the specimens [157]. The surfaces of the specimens were lightly coated with white paint, and black paint was sprayed over the surface (Fig. 5.1a and b). Further details on the DIC technique and the speckle patterns are provided by CorelatedSolutions [178]. After capturing the images, the VIC-2D DIC measurement system [178] was used to compute and visualize the displacement and strain fields over the surfaces of the granite specimens.

Following image acquisition, the spatiotemporal evolution of strain fields over the specimen surfaces was computed using VIC-2D software, a DIC measurement system licensed by Correlated Solutions Inc. [178]. The ROI for the specimens tested under the Brazilian and direct tensile loadings were selected such that they covered the area where the final macroscopic fractures occurred (see Fig. 5.4 and Fig. 5.6). A subset size of 29 × 29 pixels was selected to ensure a unique speckle pattern within each subset [157], [178]. In addition, a step size of seven pixels was selected between the subset meshes to obtain independent and non-repetitive data points over the specimen surfaces [157], [178]. Before each experiment, all observational systems, including the loading, AE monitoring, and imaging systems, were triggered simultaneously to acquire synchronized experimental data.

5.3. Experimental Results

5.3.1. Tensile Strength

Fig. 5.2 Fig. 5.2 shows the load-axial displacement curves of the specimens subjected to Brazilian (six B specimens) and direct tensile (four D specimens) loadings (insets show the corresponding tensile strengths of the specimens). The direct and indirect tensile strengths of the specimens were determined in compliance with ISRM standards (Bieniawski and Hawkes, 1978). As the ISRM suggested equation for determining the BTS is valid for isotropic brittle materials [32], [92], this was used to calculate the *nominal* BTS of the RM specimens for comparison. The *nominal* tensile strengths (σ_B) of B1 to B6 ranged from 3.0 to 3.4 MPa with an average of 3.2 MPa (Fig. 5.2a), and those of D1 to D4 (σ_D) ranged from 2.0 to 2.2 with an average of 2.1 MPa (Fig. 5.2b). Thus, on average, the tensile strength of the RM specimens obtained under direct tension was lower than that under indirect (Brazilian) tension, and the ratio of the average direct to Brazilian tensile strength of the RM specimens (σ_D/σ_B) was 0.66. For comparison, reported equivalent ratios for intact rock materials range between 0.6 and 0.9 [10], [22], [31], [62], [64]. Thus, the tensile strength ratio of the RM specimens fell within the range of intact rock materials.

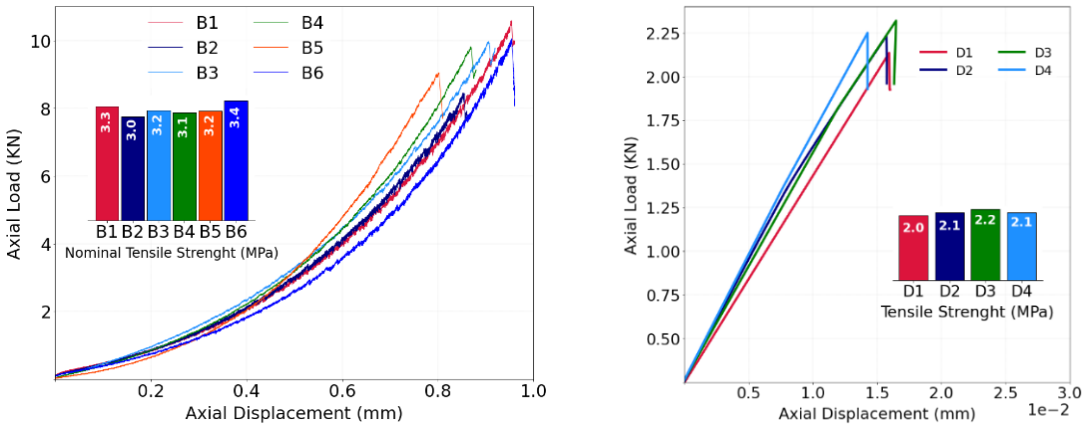

(a) (b)

Fig. 5.2 Load-axial displacement of (a) B and (b) D specimens. The insets show the tensile strength values.

5.3.2. Acoustic (AE) and Visual (DIC) Observations of Fracturing Processes

Fig. 5.3 shows the applied load, instantaneous AE hits, and cumulative AE hits versus loading time (represented as a percentage) for B1 and B2. The scatter plot represents instantaneous AE hits colored by amplitude. To obtain a more representative deformation response of the entire specimen, the AE hits captured by all AE sensors are plotted in Fig. 5.3 and Fig. 5.5.

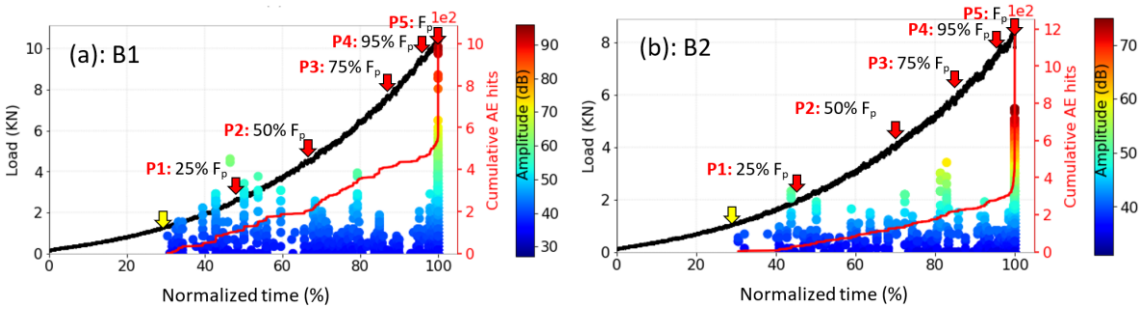

Fig. 5.3 Instantaneous hits, cumulative hits, and load against the normalized time (t/t_{max}) × 100 for (a) B1 and (b) B2.

AE hits reflect the internal damage of the loaded specimens, and an increasing hit rate reflects more severe damage [187], [234]. Hence, the lack of AE hits for loads lower than 1 KN (indicated by yellow arrows in Fig. 5.3a and b) indicates that no microcracks occurred in B1 or B2 during the initial loading phase. For loads higher than 1 KN, microcracks

appeared in both B1 and B2, and progressively accumulated until failure. The constantly increasing trend in the cumulative hit curves in Fig. 5.3a and b reveals that the fracturing processes of both B1 and B2 occurred at a continuous progressive rate. Because the trends of the instantaneous and cumulative hit curves (i.e., fracturing processes) were similar between B1 and B2 (Fig. 5.3a and b), for the sake of brevity, only the fracturing process of B1 is further discussed.

Fig. 5.4a- illustrate the AE and DIC results for B1 at five different loading levels, including 25, 50, 75, 95, and 100% of the failure load (F_p); points P1–P5 are shown by red arrows on the load-time curve (Fig. 5.3a). The major principal strain (extensile strain, ε_1) distribution was investigated at points P1–P5. Considering the loading configuration in the direct and Brazilian tests, the major principal strain concentration occurred in the horizontal direction owing to the induced horizontal tensile stress. By contrast, in the direct tension test, the major principal strain was concentrated in the vertical direction. Moreover, because shear damage in brittle materials occurs along the plane of maximum shear strain γ_{max} [45], [254], the maximum shear strain distribution was also examined to study the shear micro-damage in the specimens. γ_{max} was computed using Eq. 5.1 [254]:

$$\gamma_{max} = \left| {}^{(\varepsilon_1 - \varepsilon_2)}/_{2} \right| \qquad \text{Eq. 5.1}$$

where ε_2 is the minor principal strain.

In Fig. 5.4a-e, the upper panel (UP) depicts the spatiotemporal evolution of the major principal strain (ε_1) fields, the middle panel (MP) represents the spatiotemporal evolution of the maximum shear strain (γ_{max}) fields, and the lower panel (LP) shows the spatiotemporal development of AE events. Here, the AE signals captured by at least four AE sensors were considered events. In total, 94 AE events were observed during the deformation of B1, as shown in Fig. 5.4e, in which the colors of the AE events (circles) reflect the microcrack occurrence time. The positive strains are referred to as tensile in the strain plots, whereas the negative strains are compressive. Thus, ε_1 was predominantly tensile (+) in the entire ROI, whereas some compressive (-) strain zones developed around the loading jaws because of the compressive stress field in the vicinity of the jaw-specimen contact area [126], [127].

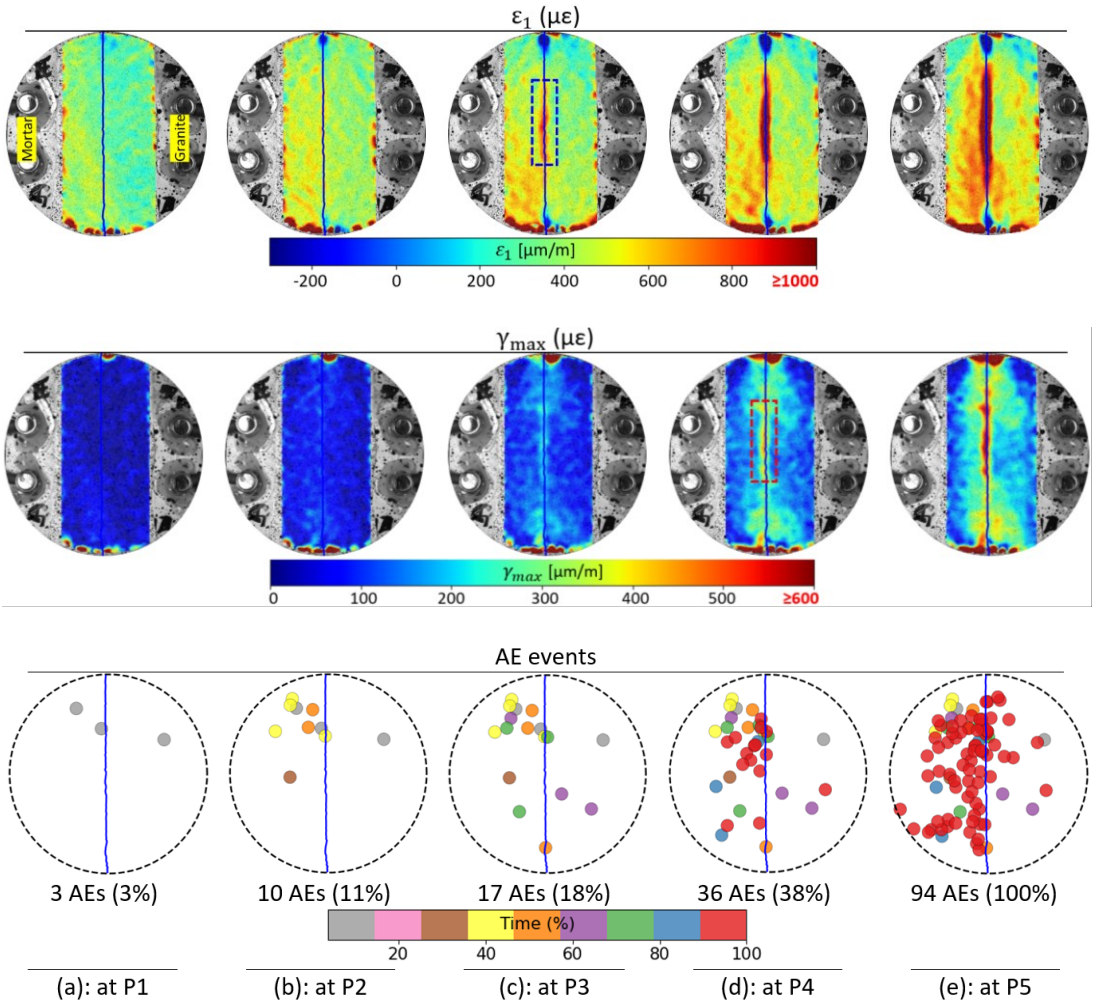

Fig. 5.4 (a)–(e) AE and DIC results for B1 corresponding to points P1 to P5 (as shown in Fig. 5.3a). Upper panel: Full-field major principal strain (ε_1) obtained by DIC. Lower panel: Spatial distribution of AEs. The blue line represents the observed macroscopic fracture path. (f) Specimen failure pattern and interfacial failure morphology with projected AE events. Black lines indicate the mortar remaining on the surface of the granite.

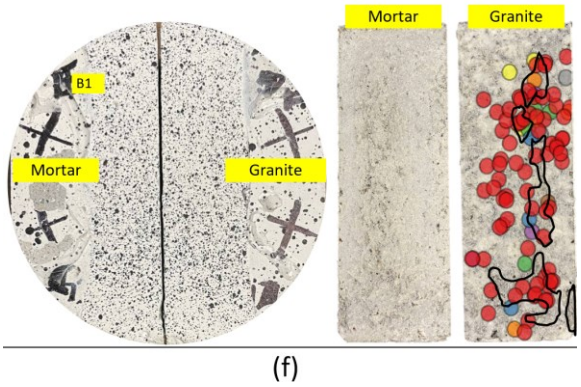

Similar to the hit plot in Fig. 5.3a, the spatial distribution of AE events at points P1–P5 in the LP in Fig. 5.4a-e indicates a continuous evolution of microcracks in B1 from small

loading values up to the failure load. As shown in Fig. 5.4a, approximately 3% of the total detected AE events (3 AEs) occurred up to P1 (25% F_p). Furthermore, Fig. 5.4a indicates a small heterogeneity in the ε_1 strain field, whereas the γ_{max} strain field remained entirely homogenous. That is, at 25% F_p, the ε_1 strain plot shows zones of small tensile strain accumulation in B1, whereas there is no visible shear strain accumulation within the specimen. Note that the tensile strain values in the mortar were greater than those in the granite, which is attributed to the heterogeneity of the mechanical properties of the RM specimens and the difference in Young's modulus—29 GPa for mortar versus 50.6 GPa for granite (Table 5.1). When the load increased to 50% and 75% F_p (points P2 and P3 in Fig. 5.3a, respectively), 10 and 17 AE events were captured in B2, accounting for 11% and 18% of the total events, respectively (Fig. 5.4b and c). The locations of the AE events reveal progressive damage in the mortar with a few random microcracks in the granite. The ε_1 strain fields at points P2 and P3 (Fig. 5.4b and c) display higher values of tensile strain accumulation in the mortar, which is consistent with the development of the AE events. At 75% F_p, a tensile stress concentration zone began to appear along the interface at the center of B1 (blue rectangle in Fig. 5.4c); however, the tensile strain values in the mortar were still greater than the tensile strain along the interface. The shear strain plots at P2 and P3 (Fig. 5.4b and c) suggest that the heterogeneity of the γ_{max} strain field remained minimal, meaning no significant shear zone concentration formed in B2 up to 75% F_p. At 95% F_p, approximately 38% of the total AE events were captured, most of which were in the mortar (Fig. 5.4d). In addition, while the tensile strain in the mortar was still more significant than in the granite, the highest tensile strain values appeared to be concentrated along the interface rather than in the mortar (Fig. 5.4d). In addition, the γ_{max} strain field at 95% F_p revealed that some shear strain started to occur and accumulated along the interface at this load level (shown by the red rectangle in Fig. 5.4d). This increase in the heterogeneity of the γ_{max} strain fields at high loading levels (at > 75% of the peak load) has been previously reported [254]–[256]. Finally, 58 new AE events (62% of the total) were captured from 95% to 100% F_p (P4 to P5 in Fig. 5.3a), indicating that considerable damage within B1 occurred during a short loading period. Interestingly, in Fig. 5.4e, the 58 newly detected AE events (red circles) were predominantly located either at the exact interface (or in the mortar but very close to the interface) where the highest tensile (ε_1) and shear (γ_{max}) strain concentrations were also observed (Fig. 5.4e). Specimen B1 eventually failed along the interface despite the previous internal microcracking in the mortar (Fig. 5.4f).

Fig. 5.4f shows the specimen failure pattern and interfacial failure morphology of specimen B1, in which the spatial distribution of the AE events captured up to the failure time is projected over the interface surface. Some mortar remained on the granite surface along the interface (black lines). That is, B1 failed in both the adhesive (detachment along the interface) and cohesive (internal damage in mortar) loss modes. This suggests that the internal micro-damage in the mortar, which began at lower load levels and accumulated under the gradually increasing load, significantly affected the strain distribution along the interface. Therefore, at higher load levels, the strain concentration rate along the interface

exceeded that within the mortar (Fig. 5.4d and e). Thus, the combined damage to the mortar and interface led to strength degradation and final failure along the interface.

Fig. 5.5a and b show the instantaneous and cumulative hits and the applied load against the loading time (as a percentage) for D1 and D2. The low number of low-amplitude instantaneous hits and the slow growth of cumulative hits indicate that no significant microcracking occurred in these samples until the peak load was reached. Indeed, for both D1 and D2, the cumulative hit number increased dramatically (with high-amplitude hits) at approximately the peak load, leading to ultimate failure, which is indicative of brittle failure.

As the trends in AE hits—and thus microcracking processes—were similar for D1 and D2, only the evolution of DIC strain and AE events in D1 are further considered. Thus, the progression of the ε_1 and γ_{max} strain fields and AEs for DI were evaluated at four different loading levels, namely 50, 75, 95, and 100% of the failure load (F_p), and points P1–P4 are indicated by red arrows in Fig. 5.5a.

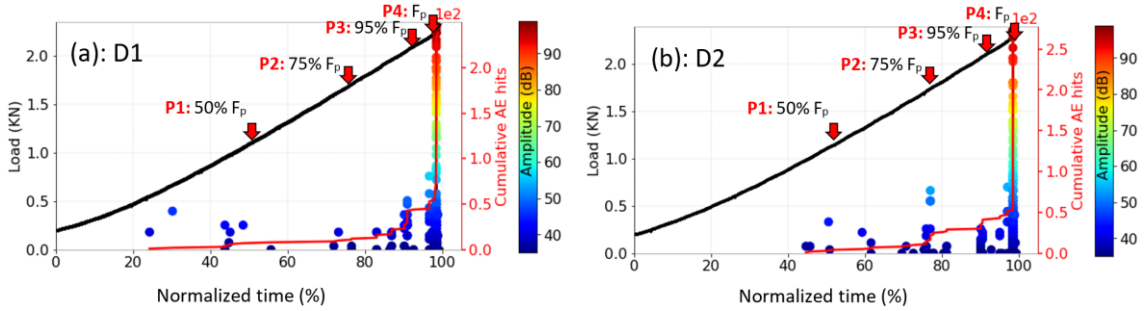

Fig. 5.5 Instantaneous hits, cumulative hits, and load vs. the percentage of the normalized time $(t/t_{max}) \times 100$ for (a) D1 and (b) D2.

The AE distributions in Fig. 5.6a-c indicate that no microcracking occurred in D1 for load levels below 95% F_p. This was confirmed by the ε_1 and γ_{max} strain fields. The shear strain values were minimal, almost up to P3 (95% F_p), and the γ_{max} strain field remained homogenous with little/no visible shear strain concentration. Moreover, the ε_1 strain field remained homogenous until 75% F_p, whereas some tensile strain concentration zones started forming along the interface at load values of approximately 95% F_p. In addition, like B1, the tensile strain values were more significant in the mortar than in granite. As the applied load approached its maximum value, nine new microcracks (almost 82% of the total AE events) occurred inside D1 within a short period (red circles in Fig. 5.6d); the coalescence and propagation of these microcracks led to the brittle failure of D1. These AE events mainly accumulated on the right side of the specimen, primarily inside the mortar and around the interface. The ε_1 and γ_{max} strain fields both showed their highest strain accumulations at the right side of the specimen and along the final macroscopic fracture.

The locations of the highest strain concentration zones strongly matched the AE locations at failure (Fig. 5.6d). It should be noted that (1) the tensile strain values in the mortar exceeded those in the granite during the entire loading process, and (2) the maximum values of ε_1 and γ_{max} at failure were approximately 980 and 300 με, respectively. The point at which the shear strain was far smaller than the tensile strain at failure may indicate the minor role of shear microcracking in the entire failure process of D1.

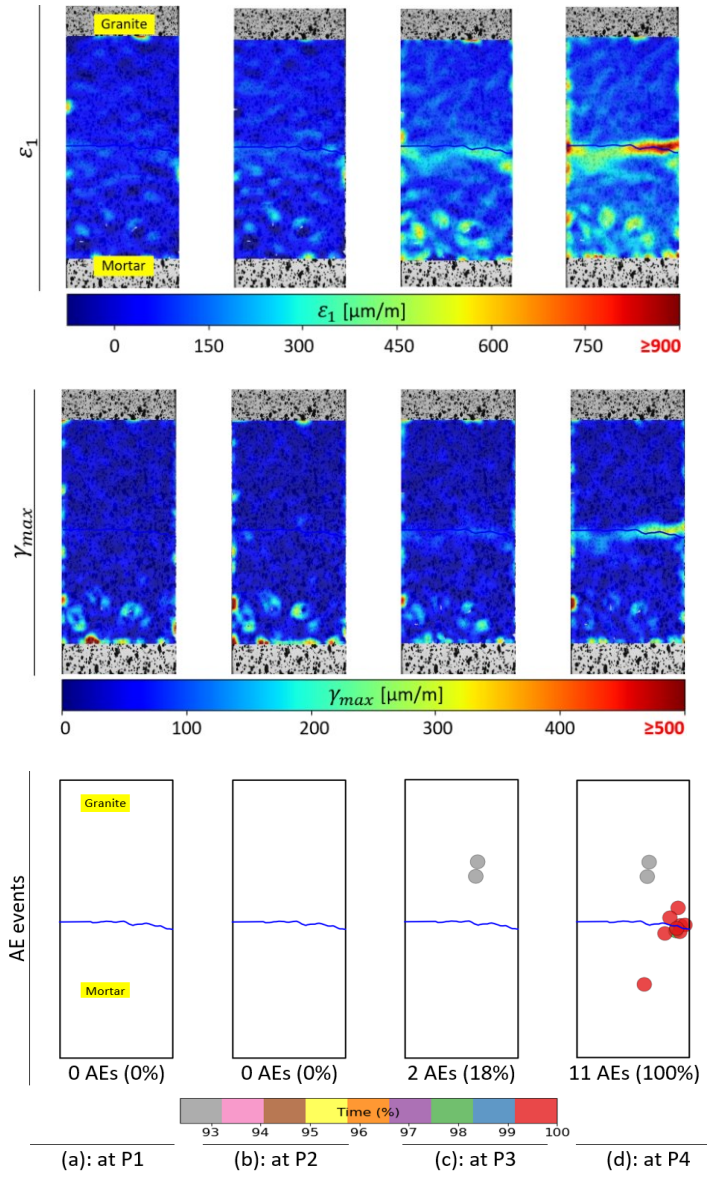

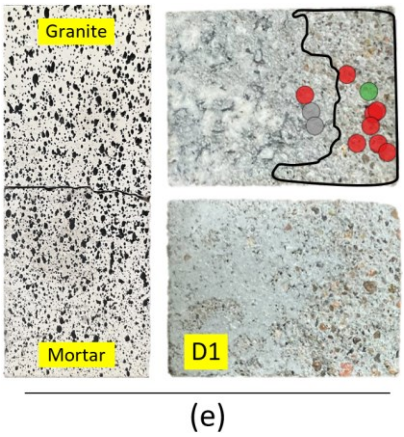

Fig. 5.6 (a)–(d) AE and DIC results for D1 corresponding to points P1 to P4 (as shown in Fig. 5.5a). Upper panel: Full-field major principal strain (ε_1) obtained by DIC. Lower panel: Spatial distribution of AE events. Blue lines represent the observed macroscopic fracture paths. (e) Specimen failure pattern and interfacial failure morphology, with AE events projected over the interface. Black lines indicate the mortar remaining on the surface of the granite.

Fig. 5.6e depicts the failure pattern of D1 and its interfacial failure morphology. Some mortar remains on the granite surface (as shown by the black lines), while no damage was observed in the granite. AE events are also projected onto the interface in Fig. 5.6e. Notably, the location of the AE events is consistent with the location of the damage in the mortar. In addition, the interfacial failure morphology reveals that macroscopic failure

occurred via a combination of adhesive loss (RM detachment at the interface) and cohesive loss (damage in the mortar). In other words, it appears that the tensile strength of D1 was governed by both the interface and mortar properties

5.3.3. AE Microcracking Source Mechanisms

To further investigate the damage mechanisms in the specimens subjected to direct and Brazilian tensile tests, the cracking mechanisms in B1 and D1 were determined by MTI analysis of the AE events according to the 2D implementation of the simplified Green's function for the moment tensor analysis (SiGMA) [47]. Moment tensors were decomposed into double-couple (DC), isotropic (ISO), and compensated linear vector dipole (CLDV) components for each event, according to Vavryčuk [211]. AE events were subsequently classified as tensile (ISO ≥ 15% and CLVD ≥ -15%), compaction (ISO ≤ -15% and CLVD ≤ 15%), or shear (|ISO| < 15%) events [155].

In the MTI analysis, only AE events with a minimum of six P-wave arrival detections were selected for further analysis. Accordingly, 37 and seven AE events (with at least six P-wave arrivals) were obtained for B1 and D1, respectively, as shown by the colored circles in Fig. 5.7a and Fig. 5.8a. The size and color of the AE events (circles) reflect their average focal amplitude (A_0), calculated considering geometrical spreading for a reference distance of 10 mm, following Zang et al. [210]:

$$A_0 = \sqrt{\frac{1}{n}\sum_{i=1}^{n}\left(A_i \frac{r_i}{10}\right)^2} \qquad \text{Eq. 5.2}$$

where n is the number of sensors receiving the same AE signal, A_i is the amplitude (V) of the first motion signal received by the i^{th} sensor, and r_i (in mm) is the signal source distance to the i^{th} sensor.

In Fig. 5.7 and Fig. 5.8, the blue lines indicate the observed ultimate macroscopic failure paths, and the black squares represent the AE events with at least four P-wave arrivals, as shown in Fig. 5.4 and Fig. 5.6.

The spatial distribution of different AE source mechanisms at the failure time is illustrated Fig. 5.7b-d for B1 and Fig. 5.8b-d for D1. The number and percentage of each AE mechanism are shown below the corresponding subplots, and the blue lines indicate the final macro-fracture path. It should be noted that the orientations of the tensile AE events in Fig. 5.7b and Fig. 5.8b represent the orientations of the tensile microcracks. Further details on determining the orientation of AE events can be found in Grosse and Ochtsu [234]. The orientation of the tensile AE events followed the direction of the ultimate macro-fractures in both specimens, which were vertical to sub-vertical in B1 and horizontal to sub-horizontal in D1.

As shown in Fig. 5.7, the microcracks of B1 consisted of 27% tensile (10 AE events), 32% compaction (12 AE events), and 41% shear (15 AE events) microcracks. Thus, the fracturing processes and tensile strength of B1 were governed by the different contributions of all three microcrack types. In addition, the locations of the tensile and shear microcracks in Fig. 5.7 were consistent with the locations of the tensile and shear strain concentration zones in Fig. 5.4.

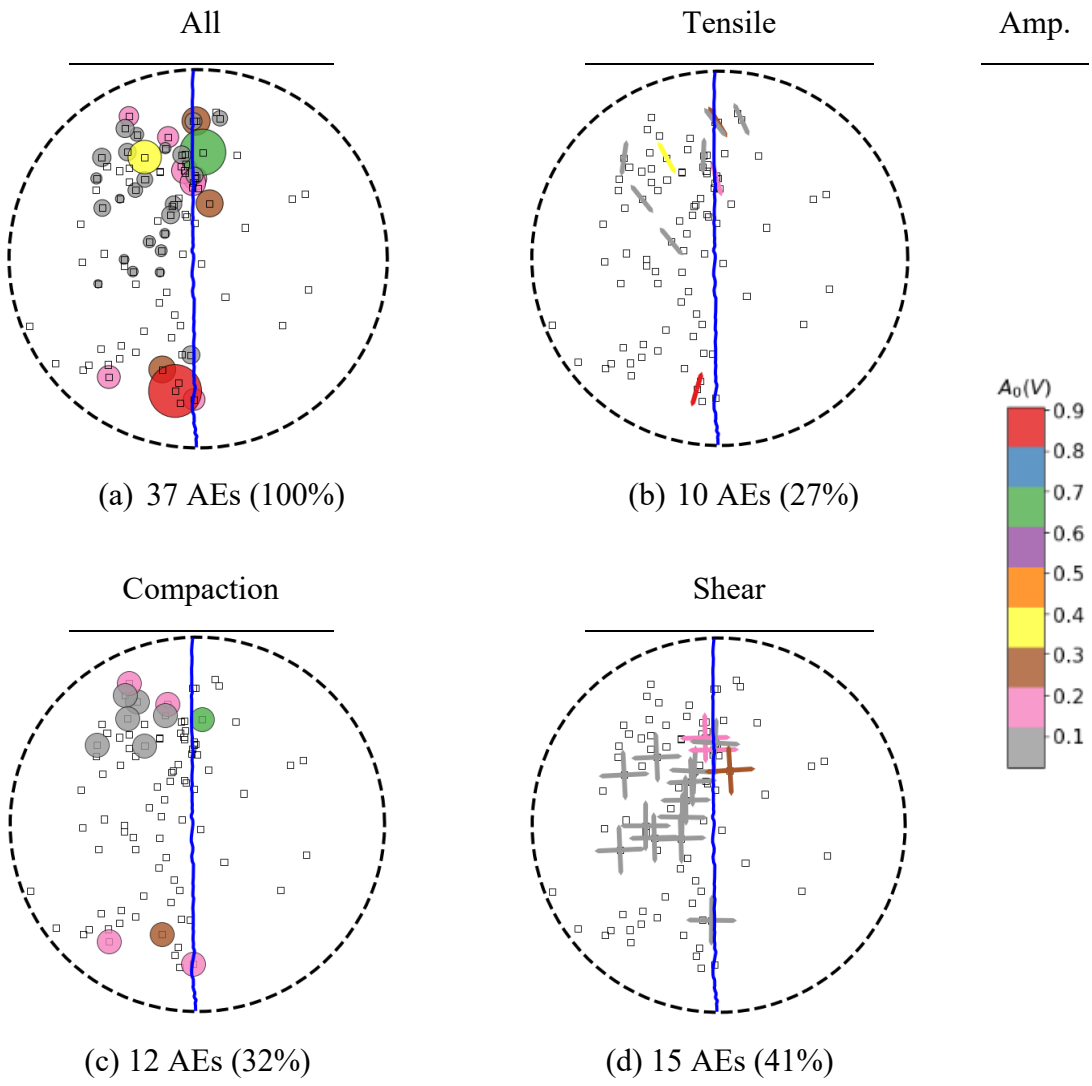

Fig. 5.7 Spatial distribution of AE events up to failure and AE focal mechanisms for B1. (a) AE events with at least six P-wave arrivals, (b) tensile microcracks, (c) compaction microcracks, and (d) shear microcracks. The color bar corresponds to the average focal amplitude (A_0) of AE events (Eq. 5.2), where the unit of the amplitude is V.

For D1, the microcracks were composed of 86% tensile (6 AE events), 14% compaction (1 AE event), and 0% shear (0 AE events) cracks ((Fig. 5.8). This strongly agrees with the

corresponding ε_1 and γ_{max} strain fields at failure for this sample (Fig. 5.6d). Compared with the ε_1 strains in Fig. 5.6d, the magnitude of the γ_{max} strains remained very small, even at the failure time. This shows that D1 failed under a predominantly tensile mode, whereas shear microcracking had a minimal effect on the overall fracturing process, which tallies with the MTI results shown in Fig. 5.8.

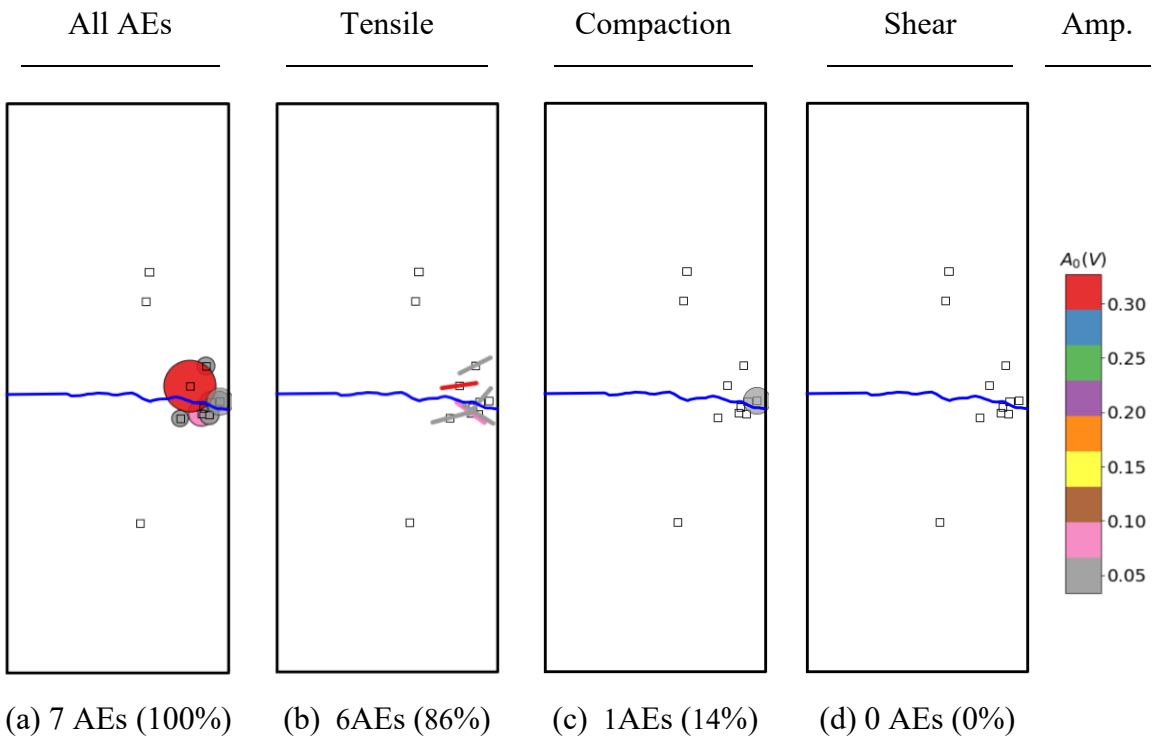

Fig. 5.8 Spatial distribution of AE events up to failure and AE focal mechanisms for specimen D1. (a) AE events with at least six P-wave arrivals, (b) tensile microcracks, (c) compaction microcracks, and (d) shear microcracks. The color bar corresponds to the average focal amplitude (A_0) of AE events (Eq. 5.2), where the unit of the amplitude is V.

From a macroscopic point of view, it is accepted that rock specimens fail under a tensile failure mode under both Brazilian and direct tensile loadings [22], [92], [116]. However, the DIC strain fields (Fig. 5.4 and Fig. 5.6) and AE source mechanisms (Fig. 5.7 and Fig. 5.8) indicate that the so-called macroscopic tensile failure of the RM specimens consisted of tensile, compaction, and shear cracks at the microscale, while the relative proportions of these cracking modes varied between the loading configurations.

5.3.4. Fracture Surface Roughness Characterization

To characterize the surface roughness of the macroscopic fractures generated after specimen failure, 3D coordinates defining the fracture surfaces were acquired using a high-accuracy profilometer 3D laser scanner (Kreon Zephyr© 25). The fracture surface

morphologies of the granite and mortar semi-samples after specimen failure are shown in Fig. 5.9a and b for B1 and Fig. 5.9c and d for D1. Because the interface surface morphology of the mortar part matched well with that of the granite part, only the roughness parameters of the mortar semi-samples were analyzed further, which were subject to the greatest level of damage.

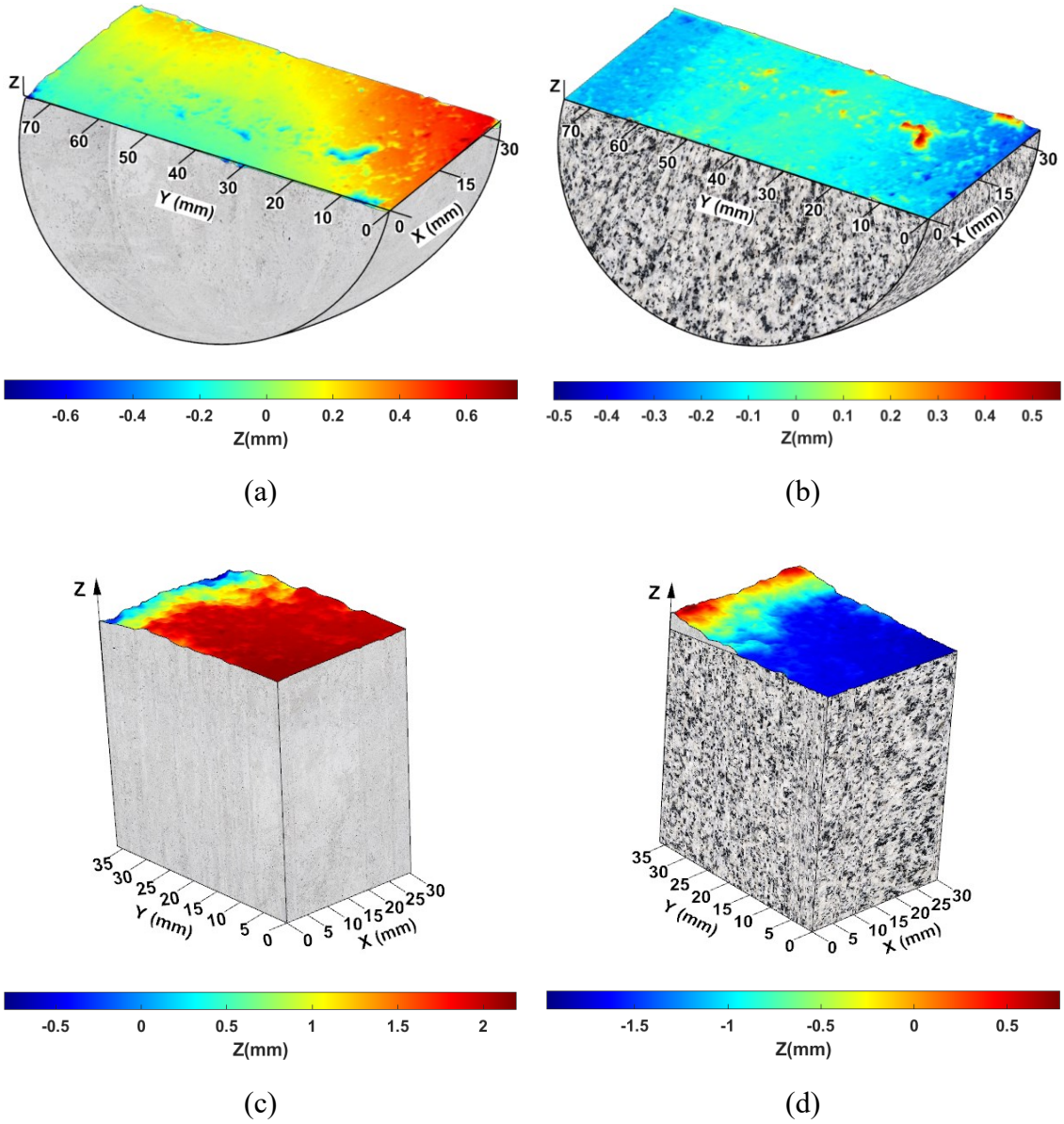

Fig. 5.9 Interface surface roughness geometry of generated macro fractures for (a) B1: mortar, (b) B1: granite, (c) D1: mortar, and (d) D1: granite.

Fig. 5.10a and b illustrate the distribution of the absolute values of asperity heights over the mortar surface for B1 (corresponding to Fig. 5.9b) and D1 (corresponding to Fig. 5.9d),

respectively. The minimum, maximum, mean, and standard deviation (SD) of asperity heights are shown in Fig. 5.10a and b. In addition, the roughness parameter z2, the root mean square of the first deviation of the roughness profiles (z2) [200], and the fractal dimension, D [203], were calculated. Higher values of z2 and D indicate a rougher surface. Note that the roughness parameters were calculated only along the fracture-propagation direction (i.e., the Y-axis in Fig. 5.9).

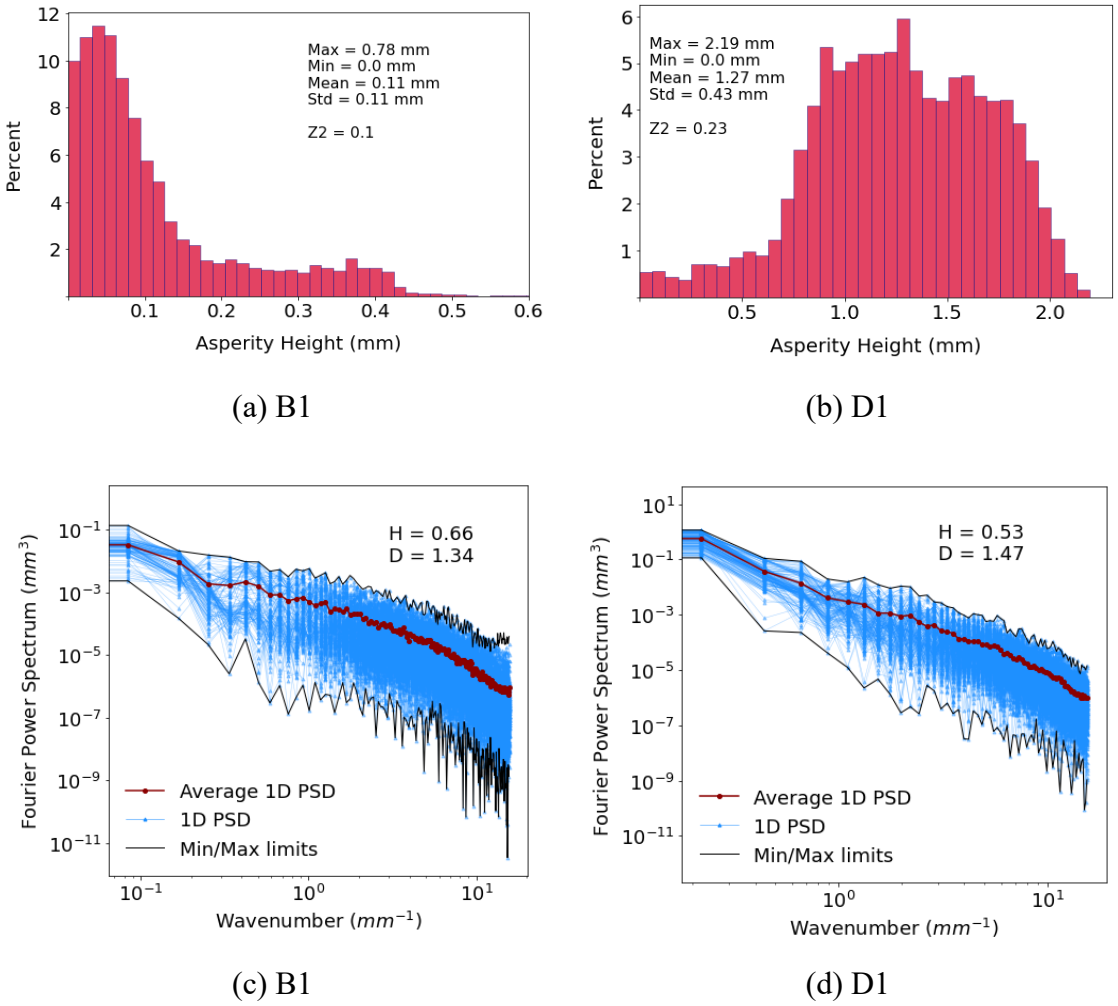

(a) B1 (b) D1

(c) B1 (d) D1

Fig. 5.10 Histogram of absolute asperity height over the fracture surface for (a) B1 and (b) D1. The minimum, maximum, mean, and standard deviation of asperity heights as well as the z2 values are given in (a) and (b). Average power spectra (red lines) of the fracture surfaces of (c) B1 and (d) D1 are shown. Blue lines represent the power spectra of a 2D profile extracted from the corresponding fracture surfaces. The Hurst exponent (H) and fractal dimension (D) values are indicated in (c) and (d). All roughness parameters and plots suggest that the fracture surface was rougher in the specimen subjected to direct tension than that subject to the Brazilian tensile test.

To determine D, Hurst exponents (H) were first computed for the 2D roughness profiles extracted from the fracture surface along the Y-axis. Values of H for the entire fracture surface were then obtained by stacking and averaging all the 2D Fourier spectra. After determining the average H for each surface, the corresponding fractal dimensions were calculated as D = 2–H [203], [212].

Fig. 5.10c and d show the typical average power spectra of the fractured surfaces of B1 and D1. The blue lines represent the spectra of the individual roughness profiles, the black lines represent the maximum and minimum limits, and the red lines indicate the average power spectra of the fracture surfaces. Corresponding H values were obtained as the slope of the linear fit of the red graph. More details on z2, the Hurst exponent, and the fractal dimension can be found in Belem et al. [203], Candela et al. [212], and Tse and Cruden [200].

For B1, z2 and D values were 0.1 and 1.34 (Fig. 5.10a and c) compared to 0.23 and 1.47 for D1 (Fig. 5.10b and d), respectively. The interface surface roughness geometries (Fig. 5.9) and their corresponding asperity height distributions, z2, and D values (Fig. 5.10) suggest that the surface of the fracture in D1 was rougher than that in B1. As previously discussed, the fractures in the Brazilian specimens (e.g., B1) were mostly formed by the initiation, propagation, and coalescence of non-tensile microcracks. In contrast, the fracture in D1 was predominantly composed of tensile microcracks. This was further confirmed by the fracture surface roughness characteristics (z2, D, and asperity heights) of these specimens. It has been previously shown that tensile fractures are generally rougher than shear fractures. For instance, Vogler et al. [257] investigated the surface roughness characteristics of shear and tensile fractures from crystalline rock, and reported that shear fractures have lower roughness values than tensile fractures.

5.4. Discussion

5.4.1. Tensile behavior of RM specimens under direct vs. Brazilian tensile tests

The direct tensile strength of the RM specimens was 66% of their Brazilian tensile strength, which is similar to the reported ratios for the intact rocks [22]. In Brazilian loading, a compressive load is applied to the specimen, and the RM interface is subjected to compression-induced (indirect) tension. However, a tensile load is applied to the specimen under direct tensile loading, and the RM interface is subjected to a directly induced tension. From a macroscopic perspective, the interface is subjected to tension under both direct and indirect tensile loading, but this is different at the microscale. In our previous work, this difference in the cracking mechanisms under micro- and macro-scales has also been observed for intact mortar and granite specimens [258].

The DIC strain fields in Fig. 5.4 and the AE source mechanisms in Fig. 5.7 indicate that both tensile and non-tensile (compaction and shear) microcracks contributed to the formation of macro-fractures in the Brazilian specimens (i.e., B1). Fig. 5.4e shows that at

failure, the maximum value of γ_{max} (660 με) was comparable to the maximum value of ε_1 (1,090 με). Moreover, Fig. 5.7 indicates that at failure, the microcracks were composed of 27% tensile and 41% shear cracks. In contrast, the DIC strain fields in Fig. 5.6 and the AE source mechanisms in Fig. 5.8 show that only tensile microcracks occurred in the specimens subject to direct tension (i.e., D1). Fig. 5.6d shows that, at failure, the maximum value of γ_{max} (300 με) was substantially lower than the maximum value of ε_1 (980 με). Moreover, 86% of the microcracks were tensile (i.e., almost all AE events), with no contribution from shear-type cracks (Fig. 5.8).

Based on these findings, microcracking occurred predominantly via the tensile mode (e.g., 86% tensile compared to 14% non-tensile AE events, Fig. 5.8) for the RM specimen tested under direct tension (i.e., D1). In contrast, microcracking occurred predominantly via the non-tensile mode (27% tensile compared to 73% non-tensile AE events in Fig. 5.7) for the RM specimen tested under Brazilian loading (i.e., B1). The different contributions of tensile and shear microcracks to the formation of the final macro-fracture can, therefore, explain the differences between the tensile strengths of the RM interfaces under different loading states.

Previous studies have reported that the tensile strength of brittle materials is often less than the shear strength and much lower than the compressive strength [22], [24], [25], [259]. Likewise, microcracks have a lower resistance to tension than to compression and shear. Thus, the higher contribution of non-tensile microcracks in the Brazilian experiments (73% for B1 against 14% for D1) led to higher tensile strengths in the tested RM specimens (Fig. 5.2). This indicates that RM interfaces that experience confining pressure show higher tensile strength than those under lower or zero confinement.

In general, fractures propagate according to the principle of minimal energy. This means that fractures follow the easiest paths in the rock, particularly if the available energy is not high. Based on Fig. 5.2, under Brazilian loading, the accumulated strain energy was higher than that in the direct tests, as a greater loading was required to induce failure. Indeed, under Brazilian loading, the input energy was higher, which in turn resulted in higher energy release. This high released energy can easily break the cohesive bonds and create a straight fracture with less tortuosity (see Fig. 5.9a and b). On the other hand, for the specimens under direct tension, the input and released energies are both low; therefore, the fractures find the easiest path with minimal energy. This means that the fracture will deviate significantly and, thus, result in a jagged surface and a tortuous path for the RM interfaces under lower or zero confinement (see Fig. 5.9c and d).

Fig. 5.11 shows the typical failure modes of rocks in terms of Mohr circles and envelopes [2]. The induced stresses along the RM interfaces under Brazilian loading resemble the confined tension failure mode (blue circle in Fig. 5.11). In this case, there is normal compressive stress over the microcracks (owing to the biaxial stress field in the Brazilian test), resulting in higher shear strength values along the microcracks. Therefore, the presence of more shear microcracks with higher strengths during the failure process in B1 increased the overall tensile strength. In contrast, the stress states along the RM interfaces

under the direct tensile test were equivalent to the uniaxial tension failure mode (red circle in Fig. 5.11). In the uniaxial tension failure mode, there was no compression or confinement over the microcracks (owing to the applied external load). Therefore, the shear strength along the microcracks was minimal (as shown by the red circle in Fig. 5.11), highlighting the minor role of shear microcracking in the overall failure and tensile strength of specimen D1. This suggests that the RM interfaces show higher strength under confined tension than those under unconfined tension.

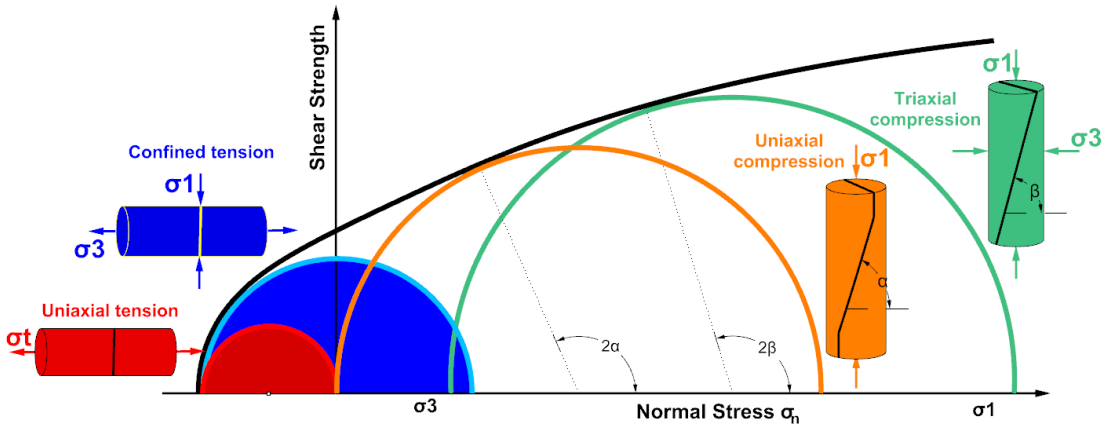

Fig. 5.11 Stress states for typical failure modes of rocks [2], [44]. In Brazilian specimens, normal compressive stress acts over the surfaces of microcracks due to the applied compressive load, meaning that these microcracks may be produced under the confined tension failure mode (blue circle). In contrast, microcracks in specimens under direct tension are predominantly produced in the uniaxial tension failure mode (red circle). Microcracks that fail under confined tension (Brazilian) have greater strength than those that fail under unconfined tension.

5.4.2. Limitations and future studies

In this study, a constant V_p field model was applied to determine the spatial distribution of AE events. This is because both granite and mortar showed similar V_p values. However, owing to the heterogeneity of granite (different grain sizes, pre-existing cracks, etc.) and the presence of two different propagation media (i.e., rock and mortar), this assumption may not always apply and result in AE location errors. Although our velocity sensitivity analysis showed that this error was negligible for the materials tested, to localize AE events more accurately, a 3D velocity model that considers both the inherent and stress-induced anisotropy of rocks is required.

In addition, only specimens with a smooth interface surface were considered when evaluating the tensile strength and tensile fracturing behavior of the rock-mortar specimens. To generalize these results, further experiments should be conducted on rock-

mortar specimens considering different values of interface roughness. In this study, the mortar had a lower strength than granite; therefore, most of the fracturing processes occurred either in the interface or the mortar. Testing bi-material interfaces with different mechanical properties of the rock and mortar/concrete is also needed to explore how cracks initiate and propagate for cases in which rock has lower strength, or the two materials have the same strength. The geometry and size of the specimens may affect the tensile strength of the RM interfaces, which are also needed to be investigated.

Lastly, AE and DIC techniques should be employed in other tensile-mode fracture mechanics tests of rock-mortar specimens to gain further insight into fracturing behaviors. For example, the progressive rock fracture mechanism in cracked-chevron-notched Brazilian discs of rock-mortar interfaces should be studied to determine the Mode I fracture toughness of bi-materials [260], [261]. Further work is also needed to examine the effect of tensile loading type, specimen shape, notch type, and interface geometry on the fracturing and mechanical properties of rock-mortar interfaces (e.g., PFZ, cracking mechanisms, and fracture toughness). The experimental and numerical investigations conducted by Wei et al. [262] and Wei et al. [261] provide useful examples of such work

5.5. Conclusions

We investigated the tensile strength and failure behavior of rock-mortar specimens under direct and indirect tensile loading. AE and DIC techniques were employed to evaluate the microcracking mechanisms of the RM specimens. Based on the obtained results, the following conclusions can be drawn:

- The DTS/BTS ratio of the RM specimens was 66%, which falls within the reported range of ratios for intact rocks.
- Monitoring of cracking processes in the RM interfaces revealed that if the failure in the RM interfaces happens under confined tension, they show AE precursors before failure, both temporally and spatially; however, they may not show considerable AE activity before failure under direct tension.
- The stress state was an essential factor affecting the fracturing mechanisms and, consequently, the tensile strengths of the RM specimens. The AE and DIC results indicate that microcracks were predominantly non-tensile for specimens under confined tension (Brazilian) and predominantly tensile in those subjected to direct tension.
- Due to different fracturing mechanisms, the surfaces of the ultimate macro-fractures were rougher in the specimens tested under direct tension than those tested under indirect tension.

The findings of this study can aid in understanding when, where, and how fracturing happens in the RM interfaces and whether we see precursors before the catastrophic failure,

which are essential factors for successful structural health monitoring in engineering structures.

CHAPTER 6: CONCLUSIONS, LIMITATIONS, AND RECOMMENDATIONS

6.1. Conclusions (Français)

Ce projet de recherche a utilisé l'émission acoustique (EA) et la corrélation d'images numériques (CIN) pour étudier les processus de microfissuration, les mécanismes de fracturation et leur influence sur la résistance à la traction et le comportement à la traction des matériaux rocheux et des interfaces roche-mortier sollicités en traction directe et en traction indirecte. Les conclusions sont les suivantes:

Selon nos résultats, le rapport entre la résistance à la traction directe et brésilienne (DTS/BTS) du granite intact était d'environ 0,7 (Fig. 4.2). Ce rapport était d'environ 0,65 pour les échantillons de roche-mortier (RM) (Fig. 5.2), ce qui indique que le rapport DTS/BTS pour les spécimens de RM demeure dans la même plage que le rapport DTS/BTS pour les roches intactes.

Les résultats EA basés sur les paramètres (*Parametric-based EA analysis*) (c'est-à-dire, les EA *hits* et l'énergie) et la réponse charge-déplacement des échantillons de granite soumis à l'essai brésilien ont indiqué que le processus de rupture en traction dans les disques brésiliens est composé de quatre étapes de déformation, quel que soit le taux de chargement axial (Fig. 3.4). Cependant, un taux de chargement plus élevé a provoqué le début de la formation de la ZPF à un stade de chargement relativement plus précoce (Fig. 3.4).

Les résultats de l'inversion du tenseur des moments des signaux EA ont indiqué que la soi-disant fracture macroscopique de traction dans les disques brésiliens était formée d'une combinaison de microfissures de traction, de cisaillement et de compression, quel que soit le taux de chargement (Fig. 3.7, Fig. 3.8, et Fig. 4.5). De même, la soi-disant rupture macroscopique de traction dans les spécimens testés sous tension directe était composée de différentes proportions de microfissures de traction, de cisaillement et de compression. (Fig. 4.6).

Cependant, l'évolution des différents mécanismes de microfissuration et leurs contributions à la rupture finale étaient significativement différentes dans les échantillons testés sous des charges de traction directes et indirectes (Fig. 4.7).

Les microfissures étaient principalement des modes de cisaillement et de traction pour les échantillons soumis respectivement aux essais de traction brésilienne et directe (Fig. 4.5 à Fig. 4.7). Dans les deux chargements expérimentaux, les mécanismes de fissuration par traction et par cisaillement ont contribué presque également à l'initiation de la microfissuration, qui s'est produite respectivement à 25% et 60% de la charge de rupture pour le chargement de traction brésilien et direct. Cependant, avec l'augmentation de la charge au-delà de la limite d'initiation de fissure, les microfissures de cisaillement étaient

nettement plus nombreuses que les microfissures de traction dans le chargement brésilien, alors que l'inverse était vrai pour le chargement de traction directe (Fig. 4.7).

En ce qui concerne les échantillons de roche-mortier, les microfissures n'étaient principalement pas développées en traction (cisaillement et compression) dans les échantillons brésiliens (Fig. 5.7) et principalement en traction dans les échantillons soumis à la tension directe (Fig. 5.8).

Il a été montré que la différence dans l'évolution et les proportions de différents types de microfissures (c'est-à-dire, traction, cisaillement et compression) sous des chargements de traction directs et indirects, entre autres facteurs, est associé 1) aux différentes configurations de chargement dans les essais de traction indirecte (essai brésilien) et directe et, 2) au type de matériau testé (granit à gros grains vs mortier à grains fins) (Fig. 4.12 à Fig. 4.14).

De même, les analyses EA et CIN ont indiqué que les mécanismes de fracturation des échantillons de roche-mortier, par conséquent, leurs résistances à la traction sont affectées, entre autres facteurs, par la configuration de la charge (charge de traction directe ou indirecte). En fait, le nombre plus élevé de microfissures de cisaillement dans les disques roche-mortier (Fig. 5.7) résultait de la contrainte de confinement dans l'essai brésilien. Par conséquent, il a été conclu que la résistance à la traction brésilienne dépasse la résistance à la traction directe des échantillons de roche-mortier, car davantage de ruptures par micro-cisaillement, probablement avec une résistance plus élevée, se produisent pendant l'essai brésilien (Fig. 5.11).

L'évolution et l'étendue de la ZPF dans les disques brésiliens déterminées par EA et CIN concordaient bien ; cependant, la zone de traitement basée sur l'EA était légèrement plus large (Fig. 2.9 à Fig. 2.11). De plus, l'étendue de la ZPF a augmenté avec le taux de chargement dans les disques brésiliens de granite.

La rugosité de surface de la fracture macroscopique produite dans les échantillons de granite a augmenté avec la diminution du taux de chargement dans les essais brésiliens (Fig. 3.14 à Fig. 3.17).

Nos résultats n'ont montré aucune corrélation entre l'emplacement et l'ampleur des EA détectés et la rugosité de surface des fractures macroscopiques produites dans des échantillons de granite sous rupture de traction indirecte (Fig. 3.18).

Pour les échantillons de roche-mortier, la surface des fractures macroscopiques produites dans les spécimens testés sous tension directe était plus rugueuse que celle des échantillons soumis à l'essai brésilien (Fig. 5.9 et Fig. 5.10). La rugosité plus élevée de la surface de rupture après l'essai de traction directe est attribuée au fait que la fracture macroscopique était principalement formée de microfissures de traction; par conséquent, il est considéré comme une fracture de traction. En revanche, la fracture macroscopique plus lisse générée dans les échantillons brésiliens était principalement composée de microfissures de

cisaillement, ce qui signifie que la fracture macroscopique doit être considérée comme une fracture de cisaillement dans les essais brésiliens.

En résumé, les fractures macroscopiques sont typiquement considérées comme des fractures de traction. Ceci est également vrai pour les macro-fractures qui sont simplement appelées fractures de cisaillement. Les travaux de cette thèse indiquent plutôt que diverses combinaisons de différents modes de microfissures forment des macro-fractures dans des matériaux rocheux. Les mécanismes de microfissuration affectent de manière significative la résistance des matériaux testés et la rugosité de surface des macro-fractures produites. La contribution de divers mécanismes de microfissures aux macro-endommagements des matériaux est influencée par différents facteurs, notamment le cadre expérimental et le type de matériau testé (granit à gros grains vs mortier à grains fins).

Dans l'ensemble, cette thèse de doctorat est proposée comme une recherche fondamentale pour mieux comprendre le mécanisme de rupture des géomatériaux sous chargement de traction. Cette thèse peut être considérée comme une base pour de nouvelles recherches sur les micro-endommagements des géomatériaux sous différents essais de résistance des roches, conduisant à un aperçu plus précis des facteurs contrôlant la résistance et le comportement des roches sous diverses conditions de chargement.

Par exemple, nos résultats ont montré que le rapport entre les microfissures de cisaillement et de traction dans la formation de fractures macroscopiques détermine dans quelle mesure la résistance obtenue donne une estimation correcte de la véritable résistance à la traction des roches. Il a été montré qu'avec la diminution du confinement et de la taille des grains, le mécanisme de microrupture se rapproche d'être purement en traction, ce qui signifie que la résistance mesurée pourrait représenter la véritable résistance à la traction du matériau. Cependant, avec l'augmentation du confinement et de la taille des grains (granit à gros grains vs mortier à grains fins), les microfissures de cisaillement contribuent de plus en plus à la formation des fractures macroscopiques, ce qui signifie que la résistance obtenue peut surestimer la véritable résistance à la traction du matériau. Cela peut également être considéré pour expliquer l'augmentation de la résistance à la compression de la roche avec la pression de confinement sous compression triaxiale.

En outre, les connaissances acquises grâce à ces travaux expérimentaux apportent des contributions importantes aux applications sur le terrain telles que les caractéristiques hydrauliques des roches dans les systèmes géothermiques améliorés (SGA) et les projets d'extraction de gaz de schiste, où l'objectif critique est de maximiser le volume du réservoir stimulé pour améliorer le taux de production. Par exemple, la relation entre les micro et macro dommages dans les géomatériaux, la relation entre le taux de chargement et l'étendue de la zone de processus de fracture, et la relation entre le taux de chargement et la rugosité de surface des fractures produites peuvent contribuer à une meilleure conception de la fracturation hydraulique.

De plus, les résultats issus de cette étude peuvent contribuer à améliorer la modélisation des micro-endommagements des géomatériaux. De nos jours, les simulations numériques

basées sur les grains sont largement utilisées pour modéliser explicitement le traitement de fracturation fragile dans les matériaux de type roche. Ces modèles nécessitent de nombreux paramètres d'entrée de micropropriétés, dont la plupart ne peuvent pas être obtenus par des mesures en laboratoire. Ces paramètres d'entrée doivent être déterminés via un processus de calibration afin que le comportement du modèle numérique représente mieux le comportement réel de la roche. Par conséquent, les données d'écoute acoustique, y compris la distribution spatio-temporelle et les mécanismes focaux des évènements détectés lors d'expériences en laboratoire, peuvent être utilisées pour calibrer des modèles numériques.

6.2. Conclusions (English)

This research project employed acoustic emission (AE) and digital image correlation (DIC) to investigate the microcracking processes, fracturing mechanisms, and their influence on the tensile strength and tensile behaviour of rock and rock-mortar materials under direct and indirect tensile loadings. The findings are the following:

According to our results, the ratio of direct to Brazilian tensile strength (DTS/BTS) of intact granite was approximately 0.7 (Fig. 4.2). This ratio for rock-mortar (RM) specimens was around 0.65 (Fig. 5.2), indicating that the DTS/BTS ratio for RM specimens remains in the same range as the DTS/BTS ratio for intact rocks.

Parametric-based AE results (i.e., AE hits and energy) and the load-displacement response of granite specimens subjected to the Brazilian test indicated that the tensile failure process in Brazilian discs is composed of four deformation stages, regardless of the axial loading rate (Fig. 3.4). However, higher loading rate caused the formation of the FPZ to begin at a relatively earlier loading stage (Fig. 3.4).

The results of the Moment tensor inversion of AE signals indicated that the *so-called* tensile macroscopic fracture in Brazilian discs was formed by a combination of tensile, shear, and compressive microcracks, regardless of the loading rate (Fig. 3.7, Fig. 3.8, and Fig. 4.5). Similarly, the *so-called* tensile macroscopic fracture in specimens tested under direct tension was composed of different proportions of tensile, shear, and compressive microcracks (Fig. 4.6).

However, the evolution of different microcracking mechanisms and their contributions to the finale failure were significantly different in specimens tested under direct and indirect (Brazilian) tensile loadings (Fig. 4.7).

Microcracks were predominantly shear and tensile for specimens tested under Brazilian and direct tension tests, respectively (Fig. 4.5 to Fig. 4.7). In both experimental loadings, the tensile and shear cracking mechanisms contributed almost equally to the microcracking initiation, which occurred at 25% and 60% of the failure load for Brazilian and direct tensile loading, respectively. However, with increasing the load beyond the crack initiation limit, shear microcracks significantly outnumbered tensile microcracks in Brazilian loading, while the opposite was true for the direct tensile loading (Fig. 4.7).

Regarding RM specimens, the microcracks were predominantly non-tensile (shear and compressive) in the Brazilian specimens (Fig. 5.7) and predominantly tensile in specimens subjected to direct tension (Fig. 5.8).

It was shown that the difference in the evolution and the proportions of different types of microcracks (i.e., tensile, shear, and compressive) under direct and indirect tensile loadings, among other factors, is due to 1) the different loading configurations in Brazilian and direct tensile tests and 2) the tested material type (coarse-grained granite vs. fine-grained mortar) (Fig. 4.12 to Fig. 4.14).

Likewise, the AE and DIC analyses indicated that the fracturing mechanisms of RM specimens, therefore, their tensile strengths, are affected by, among other factors, the loading setup (direct versus indirect tensile loading). In fact, the higher number of shear microcracks in RM Brazilian discs (Fig. 5.7) resulted from the confining stress in the Brazilian test. Therefore, it was concluded that the Brazilian tensile strength exceeds the direct tensile strength of RM specimens because more micro-shear failures, probably with higher strength, occur during the Brazilian test (Fig. 5.11).

The evolution and the extent of the PFZ in Brazilian discs determined by AE and DIC agreed well; however, the AE-based process zone was slightly wider (Fig. 3.5Fig. 3.9 to Fig. 3.11). Also, the extent of the FPZ increased with the loading rate in granite Brazilian discs.

The surface roughness of the produced macroscopic fracture in granite specimens increased with decreasing the loading rate in Brazilian tests (Fig. 3.14 to Fig. 3.17).

Our results did not show any correlation between the location and the magnitude of detected AEs and the surface roughness of the produced macro fractures in granite specimens under Brazilian tensile failure (Fig. 3.18).

For RM specimens, the surface of the produced macro fractures in specimens tested under direct tension was rougher than that of specimens tested under the Brazilian test (Fig. 5.9 and Fig. 5.10). The higher roughness of the fracture surface in the direct tensile test is attributed to the fact that the macro fracture was predominantly formed by tensile microcracks; hence, it is regarded as a tensile fracture. In contrast, the smoother macro fracture in Brazilian specimens was mainly composed of shear microcracks, meaning that the macro fracture should be seen as a shear fracture in Brazilian tests.

In summary, macroscopic fractures are conventionally regarded as tensile fractures under direct and indirect tensile testing methods. This is also true for macro-fractures that are simply called shear fractures. However, this study indicated that macro-fractures are formed by various combinations of different cracking modes at the microscale. The microcracking mechanisms significantly affect the strength of tested materials and the surface roughness of the produced macro-fractures. The contribution of various microcrack mechanisms to materials' macro-damage is influenced by different factors, including the

experimental setting and the tested material type (coarse-grained granite vs. fine-grained mortar).

Overall, this PhD thesis is proposed as fundamental research to better understand the failure mechanism in geomaterials under tensile loading. This study can be regarded as a basis for further research on the micro-damage of geomaterials under different rock strength tests leading to a more accurate insight into the factors controlling the strength and the behaviour of rocks under various loading conditions.

For example, our results showed that the ratio of shear to tensile microcracks in the formation of macroscopic fractures determines to what extent the obtained strength gives a correct estimate of the true tensile strength of the rocks. It was shown that with the decrease of the confinement and the grain size, the micro failure mechanism approaches to be purely tensile, meaning that the measured strength could represent the true tensile strength of the material. However, with the increase of the confinement and grain size (coarse-grained granite vs. fine-grained mortar), the shear microcracks contribute more and more to the formation of the macroscopic fractures, meaning that the obtained strength may overestimate the true tensile strength of the material. This can also be adopted to explain how and why the compressive strength of rock increases with the confining pressure under triaxial compression.

In addition, the insights gained through this research provide significant contributions to field applications such as hydraulic characteristics of the rocks in enhanced geothermal systems (EGS) and shale-gas extraction projects, where the critical goal is to maximize the stimulated reservoir volume to enhance the production rate. For example, the relationship between micro- and macro damage in geomaterials, the relationship between loading rate and the extent of the fracture process zone, and the relationship between loading rate and the surface roughness of the produced fractures can contribute to a better hydraulic fracturing design.

Furthermore, this study can contribute to improving the micro-damage modeling of geomaterials. Nowadays, grain-based numerical simulations are widely used to model brittle fracturing processing in rock-like materials explicitly. These models require many micro-properties input parameters, most of which cannot be obtained through laboratory measurements. These input parameters must be determined via a calibration process so that the numerical model's behaviour better represents the rock's real behaviour. Therefore, the AE data, including spatiotemporal distribution and the focal mechanisms of detected AEs during laboratory experiments, can be used to calibrate numerical models.

6.3. Research Limitations

The experimental results reported herein should be considered in light of some limitations. The most important limitations are:

1. The results were obtained based on one rock and one mortar type. Different rocks and mortars should be tested to validate and generalize the acquired results.

2. Parameters such as water content, porosity, mineralogy, grain heterogeneity, grain shape, and grain size distribution may significantly affect the microcracking process in tested materials. These factors were not studied in this research.
3. The effect of compressive stress on the microcracking process and cracking modes was studied considering the stress state in the Brazilian loading setup. The effect of confinement on microcracking mechanisms should be explicitly evaluated in other rock tests, such as triaxial compression.
4. To localized AE events, a constant P-wave velocity model was used. This model may cause some important location errors.
5. In some cases, the AE system used in this study was saturated at the failure point, which caused losing some AE events. In addition, due to the applied threshold voltage, some low-magnitude signals might not have been detected (tensile tests produce low-energy cracks). A low triggering threshold, a good noise filtration strategy, and a high-resolution data acquisition system should be used to overcome these limitations.
6. The resolution of the employed camera significantly decreased with increasing the imaging rate. A high-speed imaging system with high resolution is suggested for DIC analysis.

6.4. Recommendations

The current research tried to take a step towards better understanding and evaluating the fracturing and strength properties of rocks and rock-mortar interfaces. However, additional studies are recommended to deliver a well-established and reliable assessment of rock-like materials' tensile behavior in large-scale rock engineering structures.

The rock materials used in this study were Stanstead granite, an igneous rock that is known to be medium to coarse-grained rock, and fine-grained mortar. Different rock and mortar types of different grain sizes should be tested under tensile loadings to better evaluate the effect of grain size and material properties on the microcracking mechanisms and the surface roughness characteristics of final macroscopic fractures. The effect of parameters such as mineralogy, grain heterogeneity, grain shape, grain size distribution, etc., on the microcracking mechanisms should also be evaluated in future studies. What’s more, as it is known, the water content impacts the wave propagation in materials. On the other hand, the AE source localization directly depends on the wave propagation velocity in materials. Therefore, water content affects the accuracy of AE source localization. Thus, the effect of water content on the AE results should be the subject of future studies.

In addition, the effect of confinement stress on the microcracking mechanisms was only evaluated under the Brazilian loading configuration. Future research should investigate the effect of confinement stress on the microcracking mechanisms in other rock strength tests, such as triaxial compression.

Other experimental studies, such as scanning electron microscope (SEM) observations, could be a valuable addition for further examining the effect of grain size and experimental setup on the microcracking mechanisms in rock materials.

Based on the concept that macro-damage is formed by a combination of different microcracking modes, it might be possible, for example, to develop a correlation chart between the contribution of different micro-failure mechanisms and the strength values in similar rock strength tests. Similarly, by regulating the average contribution of micro-failure modes to the formation of macro-fractures in different rock tests, it might be possible to convert a rock strength type to another (e.g., tensile strength to uniaxial or triaxial compressive strength and vice versa).

This study applied a constant P-wave velocity (Vp) field model to determine the spatial distribution of AE events. This model requires a pre-measured V_p of the propagation medium as input and takes it as the average wave velocity to determine the location of AEs. However, due to the heterogeneity of granite (different grain sizes, pre-existing cracks, etc.) and the presence of two different propagation media (i.e., rock and mortar), the assumption of a single constant V_p may cause substantial location error and divergence in the computation. In addition, this assumption doesn't consider the effect of cracking on the wave velocity of the propagation medium. Therefore, to improve the source location accuracy of AEs (i.e., microcracks), a variable 3D velocity model that considers both the inherent and stress-induced anisotropy of rocks is required. A velocity-free model might also be another solution for increasing the accuracy of AE source localization.

In addition, only a smooth interface surface was considered to evaluate the tensile strength and fracturing behaviour of small-scale rock-mortar specimens. To verify the results of this study and generalize them to field-scale applications, experiments should be conducted on bi-material specimens of larger scales (scale effect) incorporating different values of interface roughness.

Furthermore, research on rock-concrete interfaces should be carried out because concrete is composed of fine to coarse aggregates, which may significantly affect the fracture capabilities of bi-material interfaces, a missing factor in mortar.

APPENDICES

APPENDIX 1: Roughness measurement procedure

Fig.A1. 1a and b illustrate an example of the fracture surface of a Brazilian specimen after failure and its corresponding raw 3D digitized surface, respectively. Following the digitization of fracture surfaces, the raw 3D point clouds were processed and aligned (rotated) to obtain an accurate and consistent roughness characterization. For this purpose, a best-fit plane was established through the 3D data using the least-squares regression method (the blue plane in Fig.A1. 1). Then, the data was rotated and transformed so that the best-fit plane is the "horizontal" XY plane (i.e., the z = 0 plane) with the y-axis aligned with the loading direction in Brazilian specimens (see Fig.A1. 1c).

Fig.A1. 1d represents an example of a 2D profile extracted from the 3D surface before and after alignment. The best-fit plane is used as the reference plane to calculate the surface roughness (e.g., asperity height distribution) from the aligned 3D surfaces.

The roughness parameters SF, R_a, R_p, R_q, z2, $Z2_s$, and D_{1d} were employed to quantify the fracture surfaces [200], [263]–[266]. The SF, R_a, R_p, R_q, z2, and D1d are 2D roughness parameters calculated along 2D profiles. Therefore, 2D roughness profiles were extracted from the 3D surface with a sampling interval of $\Delta x = 0.2$ mm in the X-direction, as shown in Fig.A1. 1d. The pseudo-3D roughness values for the entire surface of the fractures were then obtained by calculating the arithmetical mean of the corresponding profile parameters [206], [264]. The parameter $Z2_s$, on the other hand, explicitly defines the joint roughness in three dimensions [206]. These parameters are expressed as follows:

z2, R_a, R_q, R_p, and SF describe the irregularity of 2D profiles and provide a measure of the average amplitude (or the asperity heights) of the roughness profile relative to a best-fit line and are determined by the following equations:

$$R_a = \frac{1}{L_y} \sum_{i=1}^{N_y - 1} |z_i| \Delta y \qquad \text{Eq. A1. 1}$$

$$R_q = \left[\frac{1}{N_y} \sum_{i=1}^{N_y - 1} {z_i}^2 \Delta y \right]^{1/2} \qquad \text{Eq. A1. 2}$$

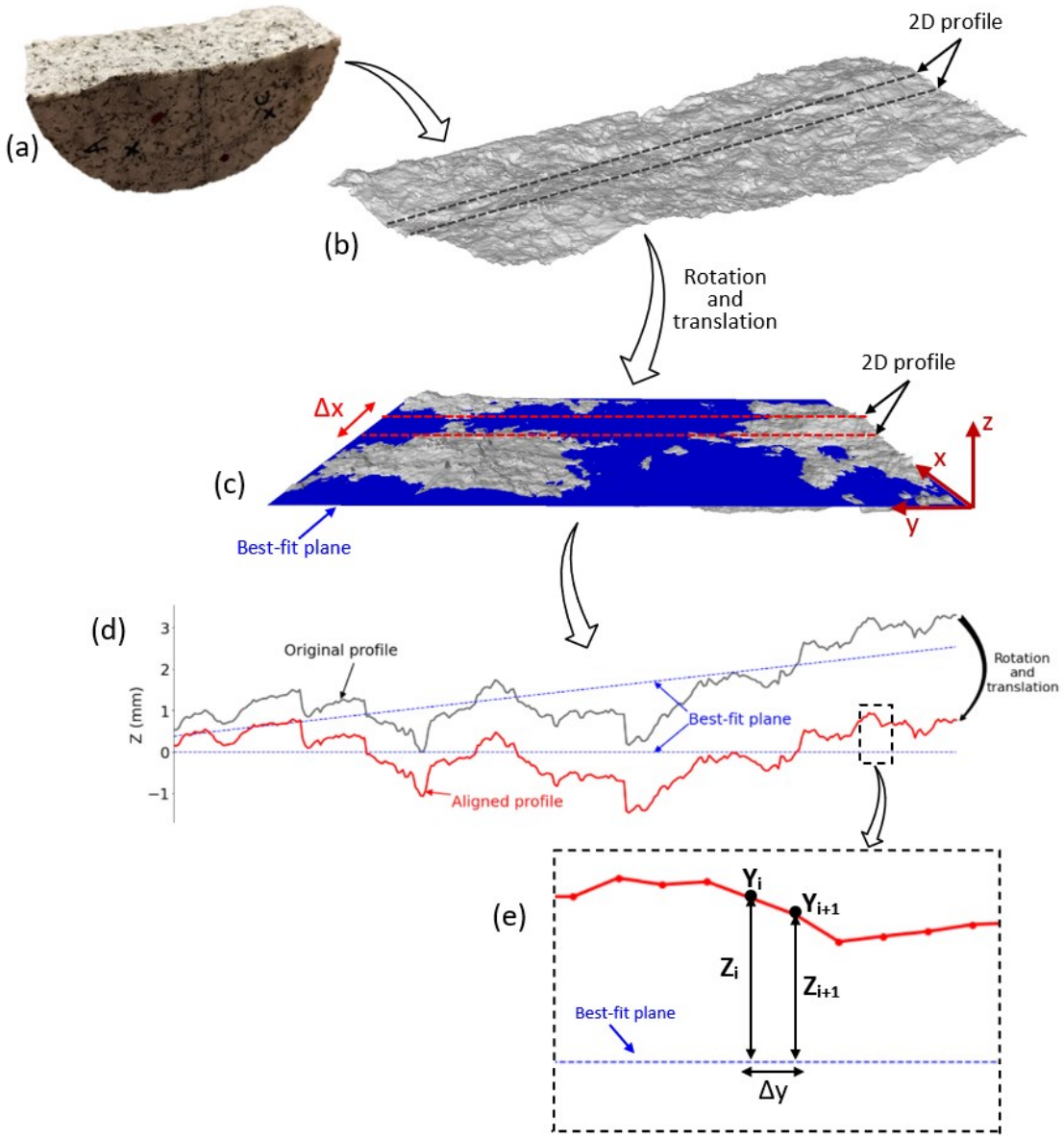

Fig.A1. 1 (a) Photograph indicating an example of the macro fracture surface generated in the Brazilian test, (b) raw scanned surface (gray dashed lines are examples of 2D profiles), (c) aligned scanned surface (the blue plane is the best-fit plane, the red dashed lines represent the gray dashed lines in (b) after the alignment, and $\Delta x = 0.2$ is the distance between 2D profiles in X-direction), (d) an example of 2D roughness profile extracted from the 3D surface (the gray profile is the 2D profile before alignment, and the red profile is the same profile after alignment, and (e) a zoomed view of the aligned 2D profile (Z_i and Z_{i+1} are the height of the profile at Y_i and Y_{i+1}, respectively. $\Delta y = 0.2$ is the distance between two adjacent measurements along Y-axis).

$$R_p = \frac{L_t}{L_y} = \frac{\sum_{i=1}^{N_y-1}[(y_{i+1}-y_i)^2 + (z_{i+1}-z_i)^2]^{1/2}}{L_y} \quad \text{Eq. A1. 3}$$

$$SF = \frac{1}{L_y}\sum_{i=1}^{N_y-1}(z_{i+1}-z_i)^2\Delta y \quad \text{Eq. A1. 4}$$

$$z2 = \left[\frac{1}{L_y}\sum_{i=1}^{N_y-1}\frac{(z_{i+1}-z_i)^2}{y_{i+1}-y_i}\right]^{1/2} \quad \text{Eq. A1. 5}$$

$Z2_s$, which represents the average roughness slope over the entire fracture surface, can be determined by:

$$Z2_s = \left[\frac{1}{(N_x-1)(N_y-1)}\left[\frac{1}{\Delta x^2}\sum_{i=1}^{N_x-1}\sum_{j=1}^{N_y-1}\frac{(z_{i+1,j+1}-z_{i,j+1})^2 + (z_{i+1,j}-z_{i,j})^2}{2} + \frac{1}{\Delta y^2}\sum_{j=1}^{N_y-1}\sum_{i=1}^{N_x-1}\frac{(z_{i+1,j+1}-z_{i+1,j})^2 + (z_{i,j+1}-z_{i,j})^2}{2}\right]\right]^{1/2} \quad \text{Eq. A1. 6}$$

Where L_y is the length of the profile projected onto its best-fit line, L_t is the true profile length, N_x and N_y are the number of discrete points along the x and y axes, z_i is the amplitude of the roughness about the best-fit line for 2D parameters and about the best-fit plane for 3D parameters, $\Delta x = 0.2$ and $\Delta y = 0.2$ are the constant intervals between adjacent points along x and y axes. All variables are demonstrated in Fig.A1. 1.

D_{1d} is determined by the following expression:

$$D_{1d} = 2 - H \quad \text{Eq. A1. 7}$$

Where H is the Hurst roughness exponent describing the self-affinity of the fracture surface and can be determined from the Fourier power spectrum (FPS), which follows a power law for a 2D self-affine profile [207], [213]. For each 2D roughness profile, the FPS $P(\omega)$ was first calculated as a function of wave number ω using the Fast-Fourier-Transform (FFT). The spectrum of the entire fracture surface was then obtained from staking and averaging all calculated 1-D Fourier transforms. The power spectrum $P(\omega)$ is characterized based on the following power law, which appears as a linear plot in log-log space:

$$P(\omega) \propto \omega^{-1-2H} \quad \text{Eq. A1. 8}$$

The Hurst exponent H can, therefore, be obtained from the slope of the linear fit to the $P(\omega)$-ω graph in log-log coordinates (e.g., Fig. 3.17) [212], [213].

APPENDIX 2: Analysis of variability and reproducibility of results

This appendix summarizes the experimental results obtained for all tested specimens. The following bar charts illustrate the variability/repeatability of the tensile strength (direct and indirect), microcracking (AE) mechanisms, and roughness characteristics of the final macro-fractures among each group of conducted experiments in this research study.

The detailed experimental data, including photographs of specimens, the load-displacement behaviour, the spatial distribution of AEs and the corresponding microcracking mechanisms, and the 3D surface of the macroscopic fractures for all samples are plotted and presented in APPENDIX 3.

In all figures below, the rightmost bar (the blue bar) represents the average value of the specific parameter of the given group of specimens. In addition, "CV" above the blue bars stands for the coefficient of variation.

For example, the upper leftmost bar chart in Fig.A2. 1 shows the tensile strength of GI specimens, which have been subjected to the Brazilian test with a loading rate of 1 μm/sec (high-loading rate), as explained in CHAPTER 3. As seen, in total, five samples have been tested for this group. The figure indicates that the tensile strength of GI specimens ranged from 8.8 MPa to 10.3 MPa, with an average of 9.6 MPa and a coefficient of variation of 5.8%.

As another example, the bottom leftmost bar chart in Fig.A2. 2 illustrates the percentage of tensile-mode microcracks (AEs) detected during the deformation process of bi-material granite-mortar discs under Brazilian loading (discussed in CHAPTER 5). As shown, six samples have been tested for this group of specimens. The percentage of tensile AEs varies between 27% to 48%, with an average of 31.8% and a coefficient of variation of 25.6%.

Please note that some data is missing for some samples due to various reasons, such as problems with AE sensors, corrupted data files, etc. Therefore, the bar chart is labeled "No data here" in the following figures where applicable.

As the coefficient of variation (CV) is a measure of relative variability for variables of different units, it can be used to compare the variability/repeatability of obtained different experimental data for different groups of specimens.

In Fig.A2. 1, the small CV values indicate the small variability or high reproducibility of the measured tensile strengths (Brazilian and direct) for all groups of tested specimens.

Because for some specimens, the percentage of tensile, compressive, and/or shear AEs is zero, it is more appropriate to evaluate the variability/repeatability of AEs mechanisms by considering the AEs as Tensile and Non-tensile (i.e., compressive + shear). This way, we can better understand the variation of the contribution of different microcracking modes to the failure of a given type of specimens. Hence, Fig.A2. 2 and Fig.A2. 3 represent the bar charts of tensile and Non-tensile AEs for each group of tested specimens. The average

percentage of tensile and Non-tensile AEs and their corresponding CV values are also given. The maximum CV value is 16%, which confirms that the variation of AEs mechanisms among specimens of the same group is relatively small, confirming the discussion and the interpretation given in CHAPTERS 3 to 5.

Furthermore, Fig.A2. 6 to Fig.A2. 10 depict the roughness parameter characteristics of the produced macro-fractures for all tested specimens. These parameters include Z2, Z2s, SF, and Rp. For more information about these parameters, please see APPENDIX 1. Similarly, the small values of the coefficient of variation strongly support the interpretation expressed in CHAPTERS 3 to 5 about the surface roughness of the created macro-fractures.

Finally, Fig.A2. 11, Fig.A2. 12, and Fig.A2. 13 summarize the average values of the measured tensile strength, AEs mechanisms, and roughness characteristics parameters for different groups of specimens.

According to Fig.A2. 11, in general, for all specimen types, i.e., intact granite, intact mortar, and bi-material granite-mortar, specimens' indirect (Brazilian) tensile strength is greater than their direct tensile strength. The intact granite samples subjected to the Brazilian test with a loading rate of 1 μm/sec (high-loading rate) have the highest tensile strength, while the lowest tensile strength corresponds to the granite-mortar specimens under direction tension. Additionally, the CV values indicate that, in general, the direct tension test yielded more consistent, repeatable results than the Brazilian test.

Fig.A2. 12 provides a summary of the average percentage of AEs mechanisms for all specimens. The lower left and lower right bar charts show the average percentage of tensile and Non-tensile AEs, respectively. As observed, in general, microcracks are predominantly tensile-mode for specimens tested under direct tension (regardless of the material type), especially for fine-grained materials, as discussed in CHAPTERS 3 and 4. On the other hand, AEs are, in general, mostly shear for specimens tested under Brazilian loading, especially for coarse-grained material. In addition, the small CV values confirm the reliability of the data and the given interpretations.

Fig.A2. 12 summarizes the roughness parameters for all tested specimens. Generally, the surface of macro-fractures of specimens subjected to direct tension is (slightly) rougher than those tested under Brazilian loading. This is because, in direct tension, the macroscopic fractures are mostly formed by tensile microcracks (as seen in Fig.A2. 12). As explained, tensile microcracks are assumed to propagate between grains boundaries, resulting in a rougher final macro-fracture. On the other hand, as shear microcracks may have enough energy to path through grains, the final macro-fracture may have a relatively smoother surface. This might explain why macro-fractures in Brazilian disc specimens (regardless of material type) are smoother than those in specimens tested under direct tension.

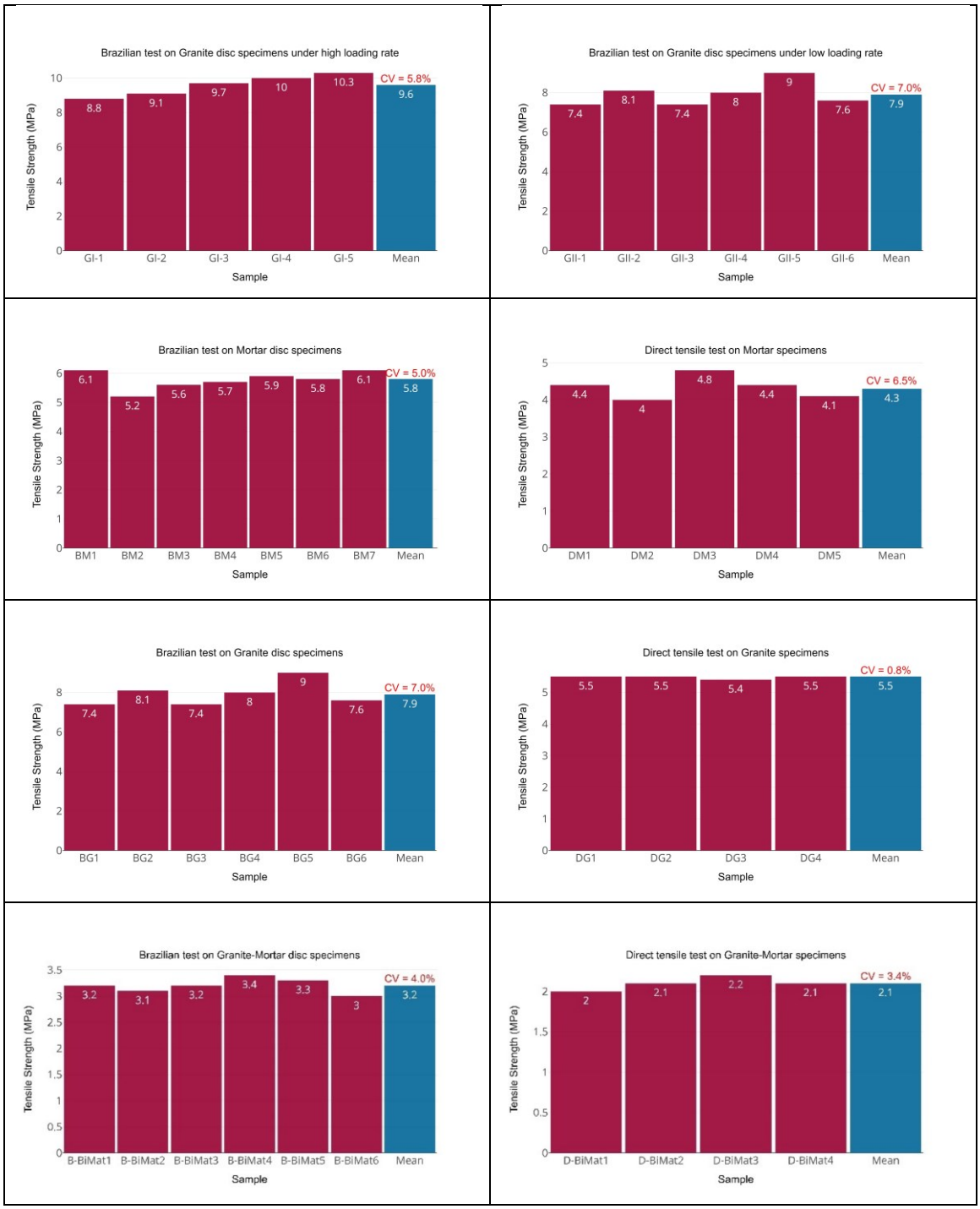

Fig.A2. 1. Tensile strength (direct and indirect) for different groups of tested specimens and their corresponding average values (the blue bar).

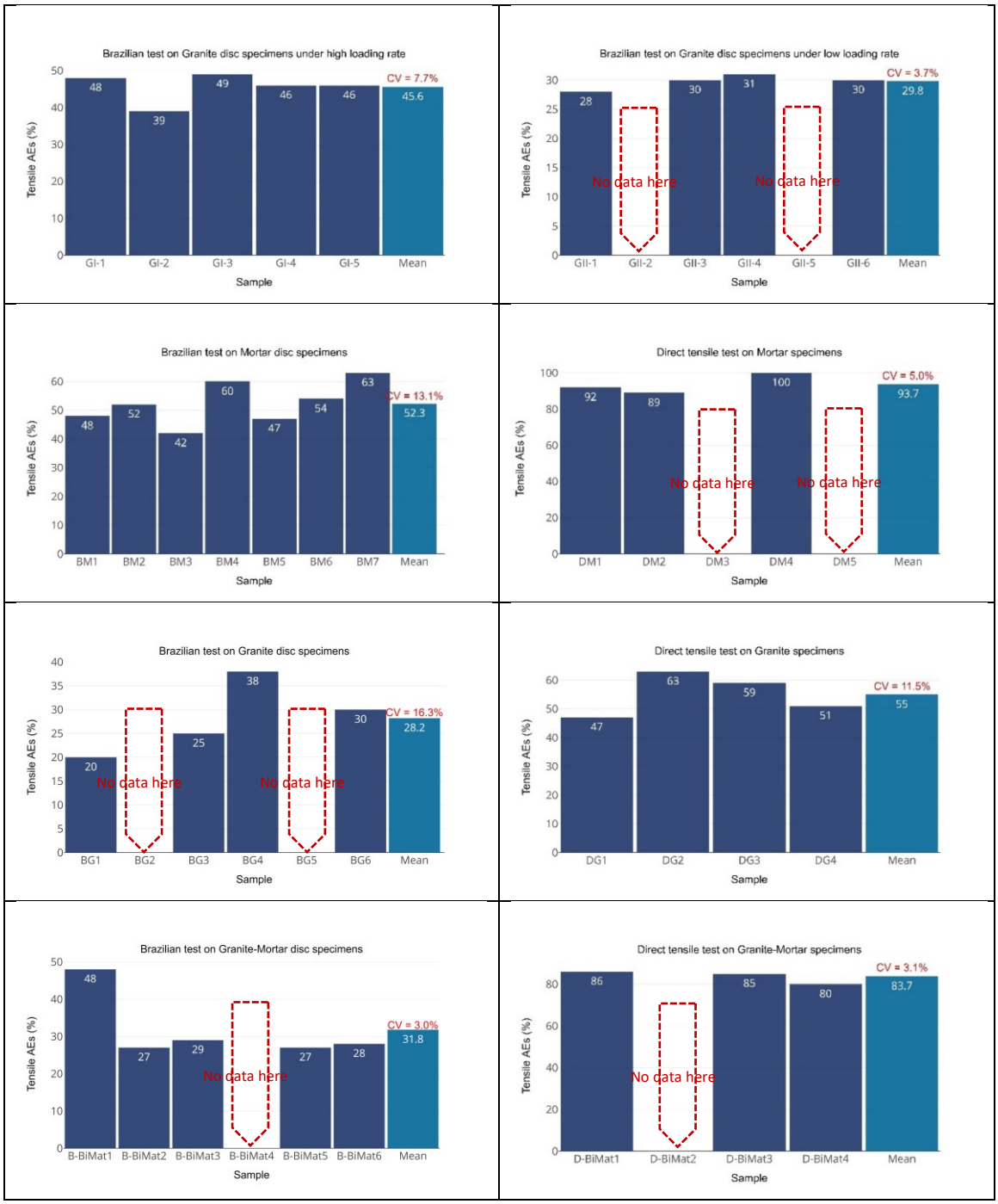

Fig.A2. 2. Percentage of the captured tensile AEs for different groups of tested specimens and their corresponding average values (the blue bar).

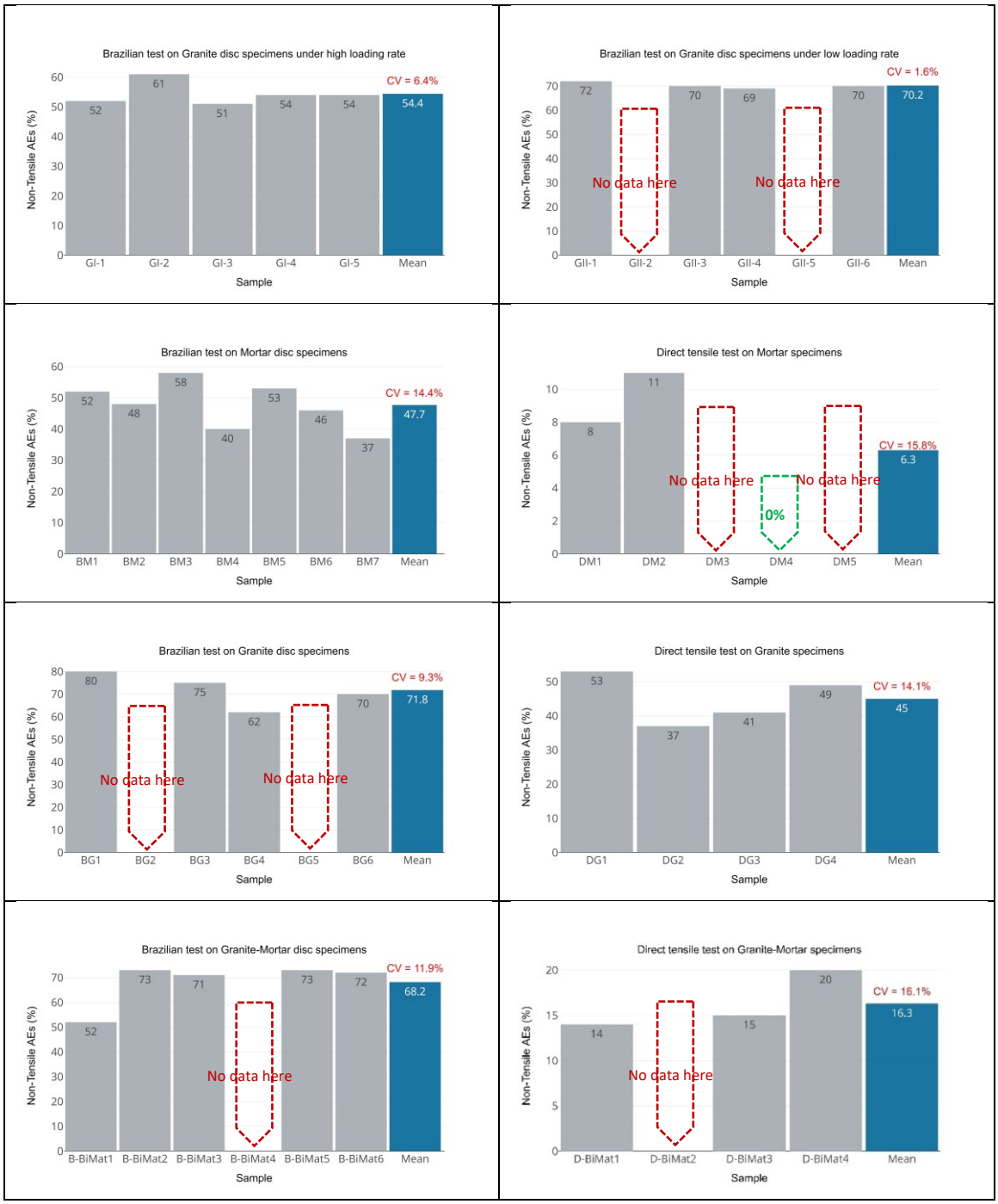

Fig.A2. 3. Percentage of Non-tensile (i.e., compressive + shear) AEs for different groups of tested specimens and their corresponding average values (the blue bar).

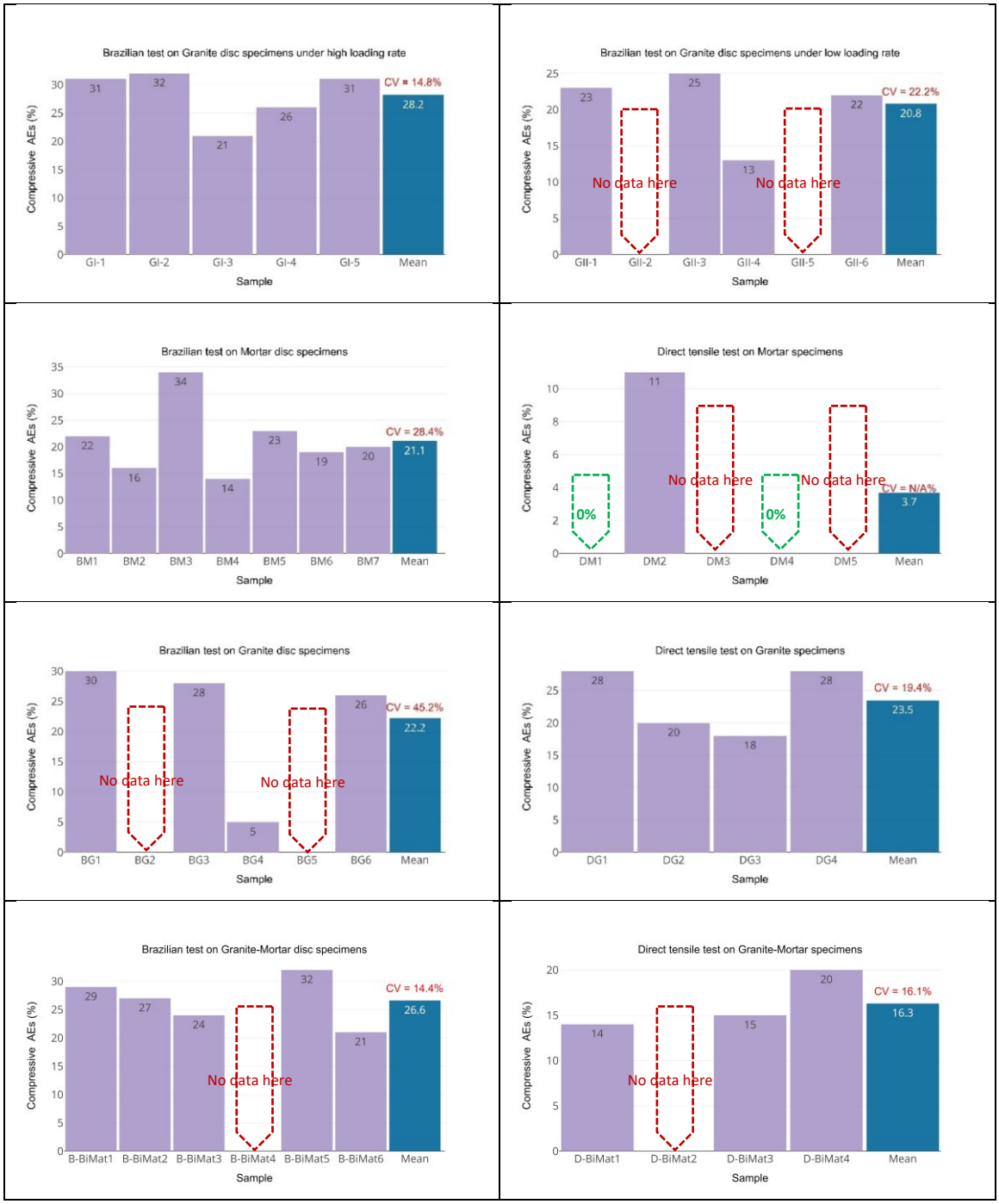

Fig.A2. 4. Percentage of the captured compressive AEs for different groups of tested specimens and their corresponding average values (the blue bar).

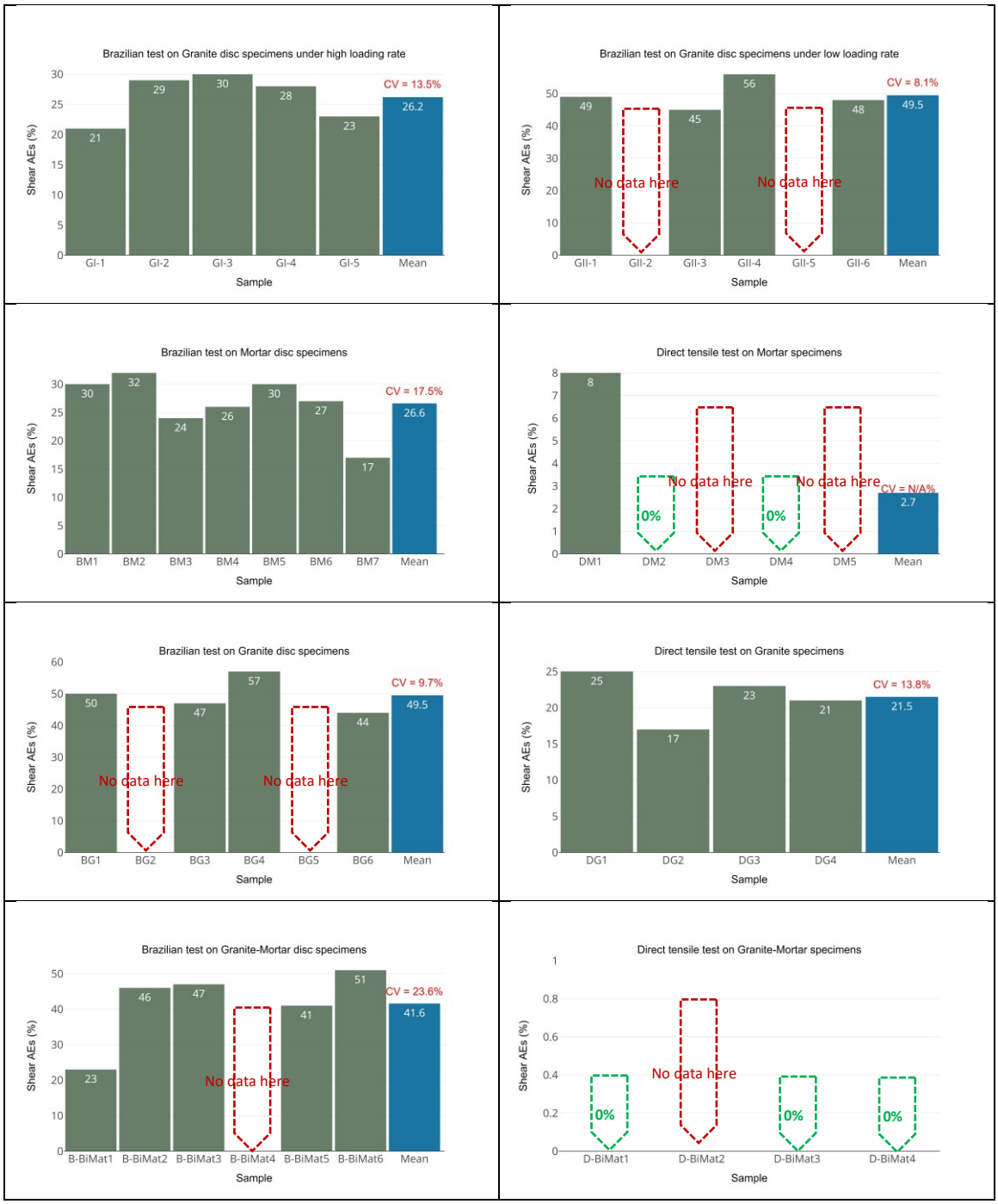

Fig.A2. 5. Percentage of the captured shear AEs for different groups of tested specimens and their corresponding average values (the blue bar).

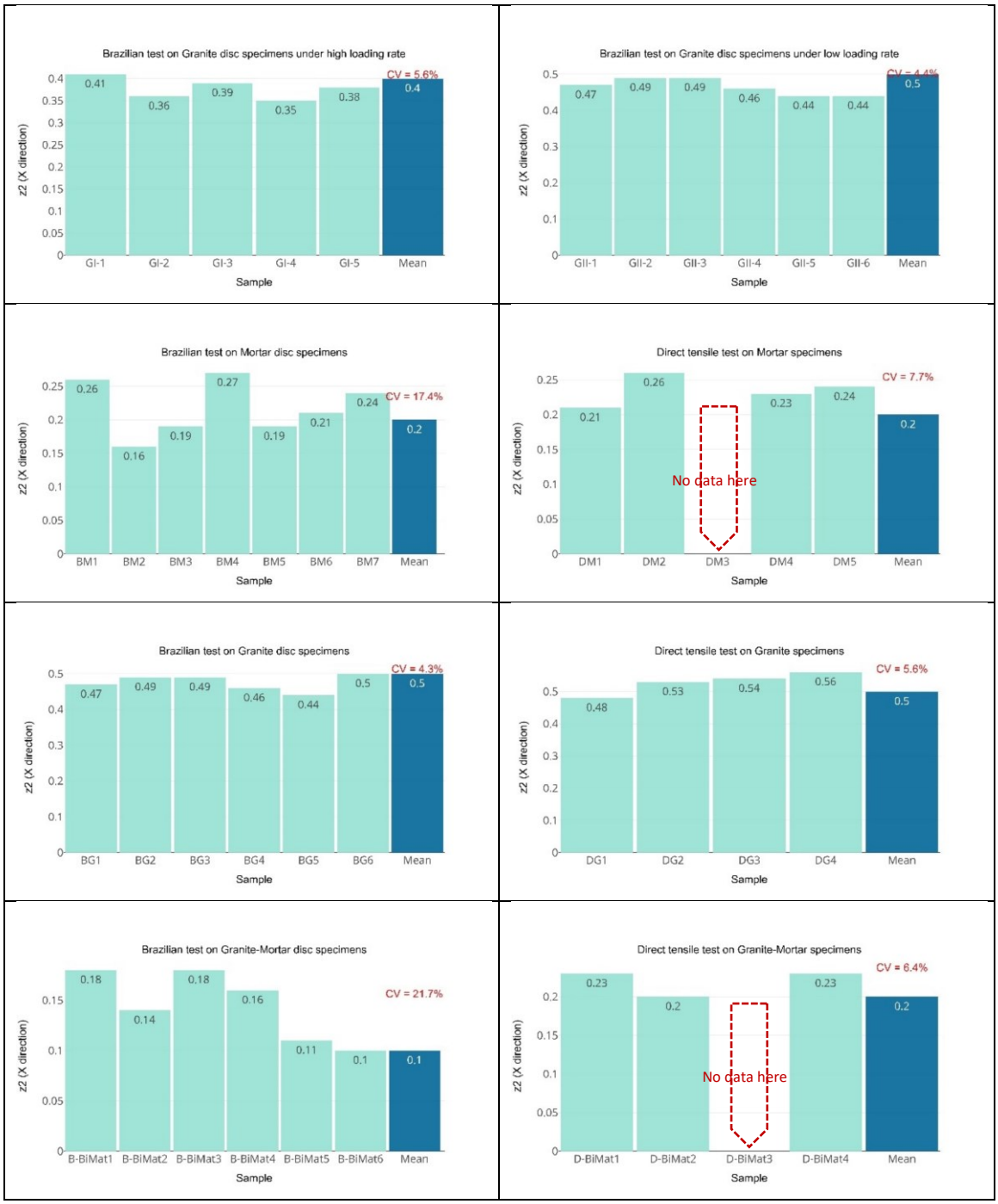

Fig.A2. 6. Z2 roughness parameter (in the x direction) for different groups of tested specimens and their corresponding average values (the blue bar). The x and y directions are depicted on surface roughness geometry plots (e.g., see Fig.A3. 20 and Fig.A3. 21).

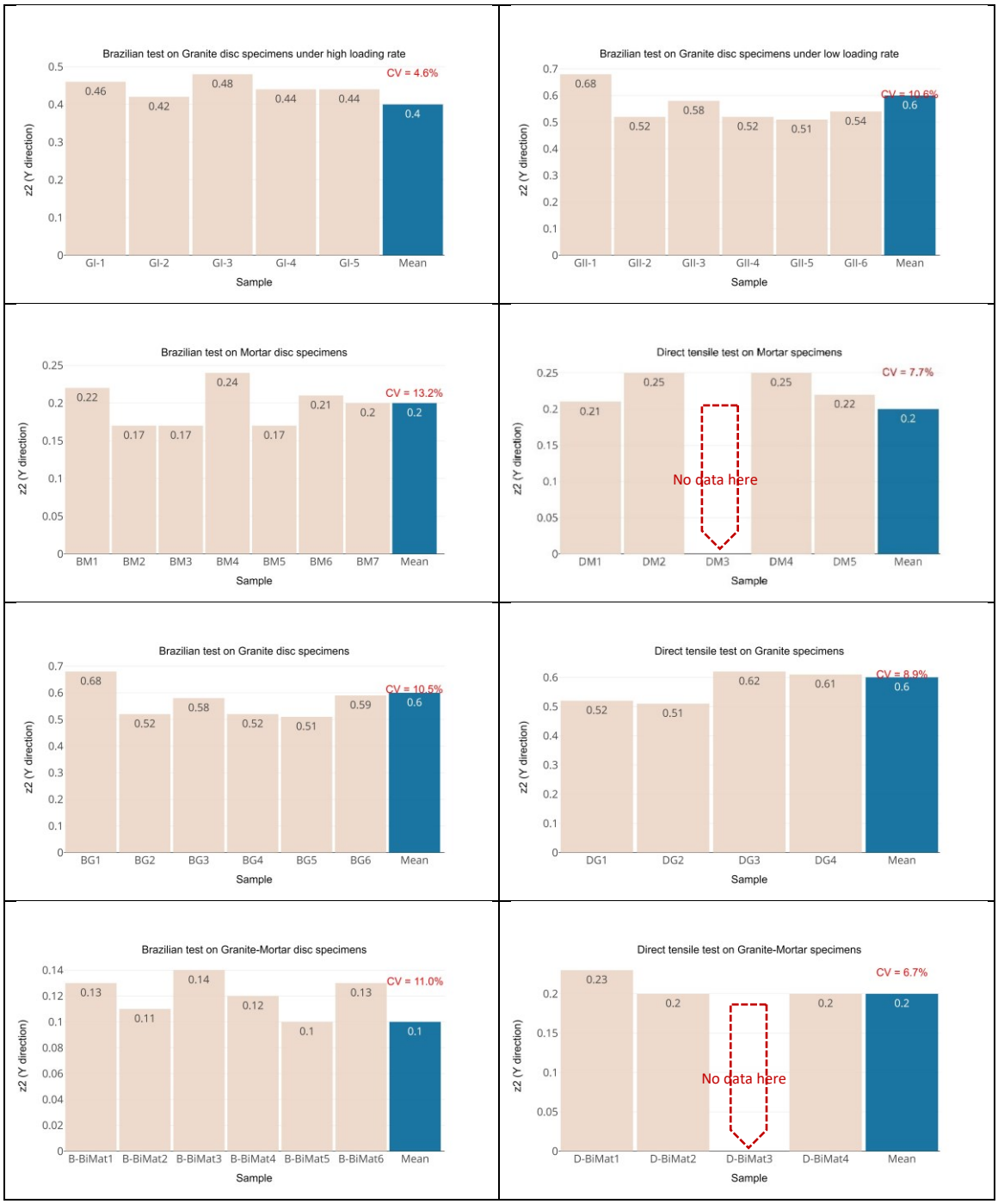

Fig.A2. 7. Z2 roughness parameter (in the y direction) for different groups of tested specimens and their corresponding average values (the blue bar). The x and y directions are depicted on surface roughness geometry plots (e.g., see Fig.A3. 20 and Fig.A3. 21).

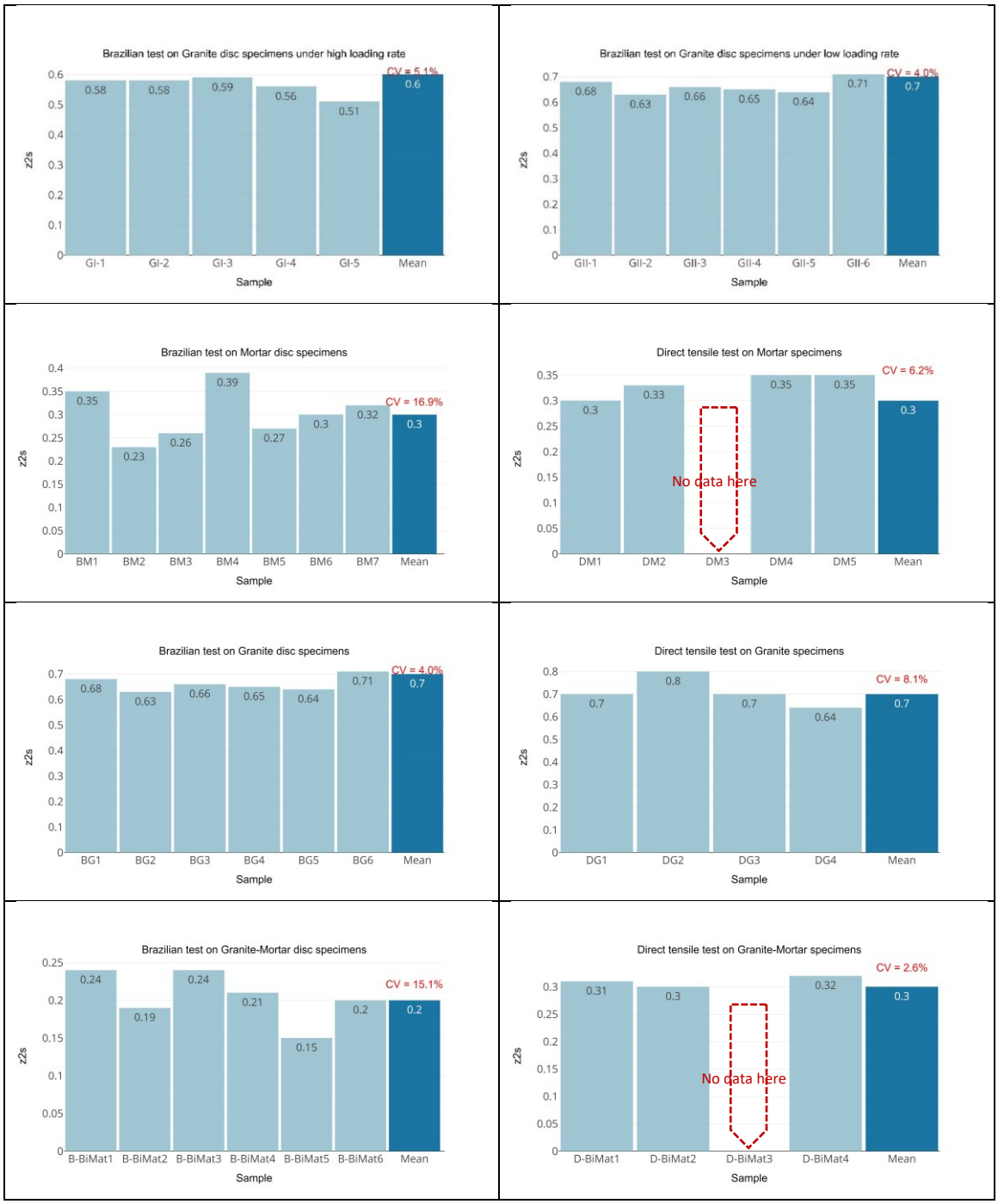

Fig.A2. 8. Z2s roughness parameter for different groups of tested specimens and their corresponding average values (the dark blue bar).

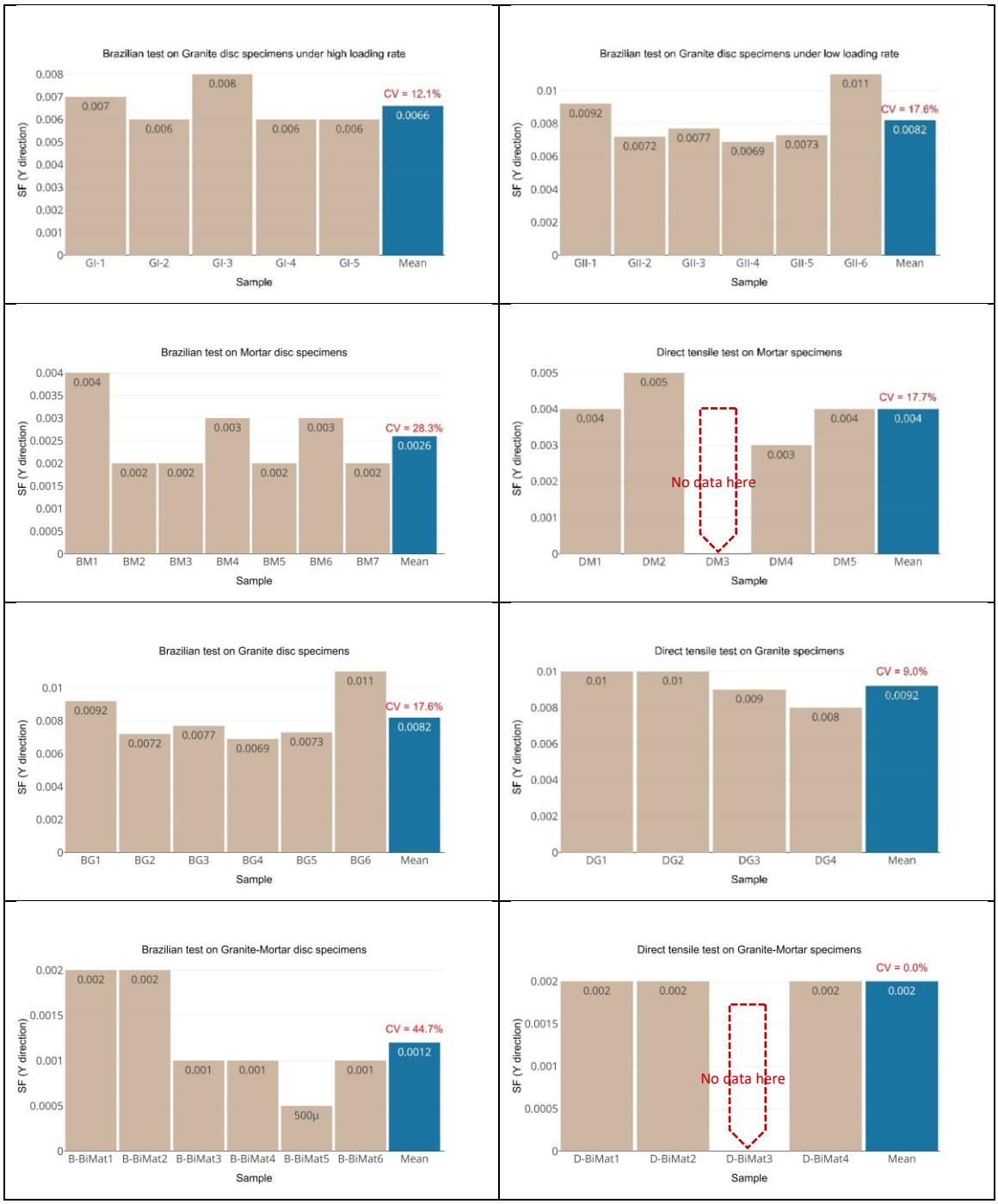

Fig.A2. 9. SF roughness parameter (in the y direction) for different groups of tested specimens and their corresponding average values (the blue bar). The x and y directions are depicted on surface roughness geometry plots (e.g., see Fig.A3. 20 and Fig.A3. 21).

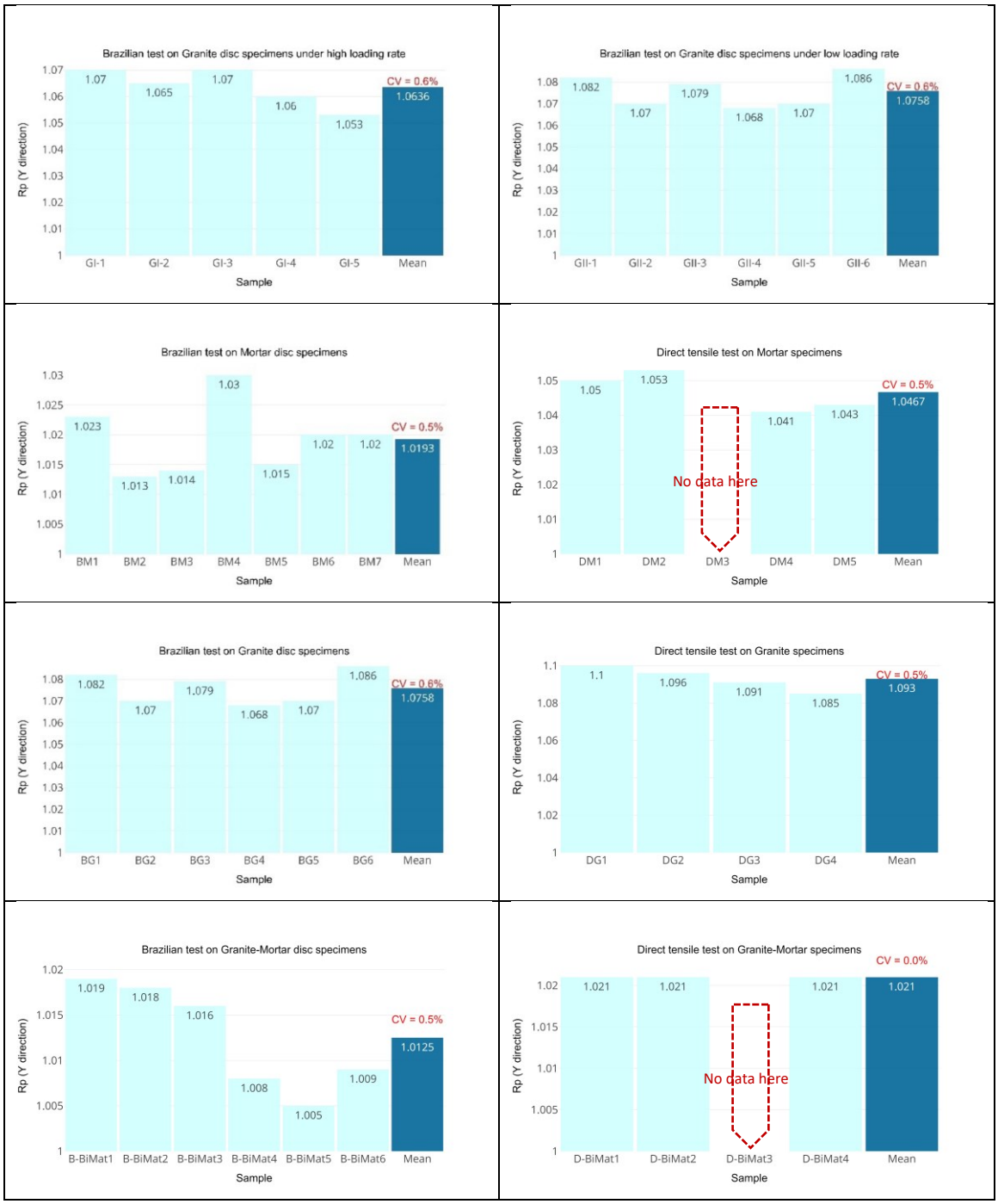

Fig.A2. 10. Rp roughness parameter (in the y direction) for different groups of tested specimens and their corresponding average values (the blue bar). The x and y directions are depicted on surface roughness geometry plots (e.g., see Fig.A3. 20 and Fig.A3. 21).

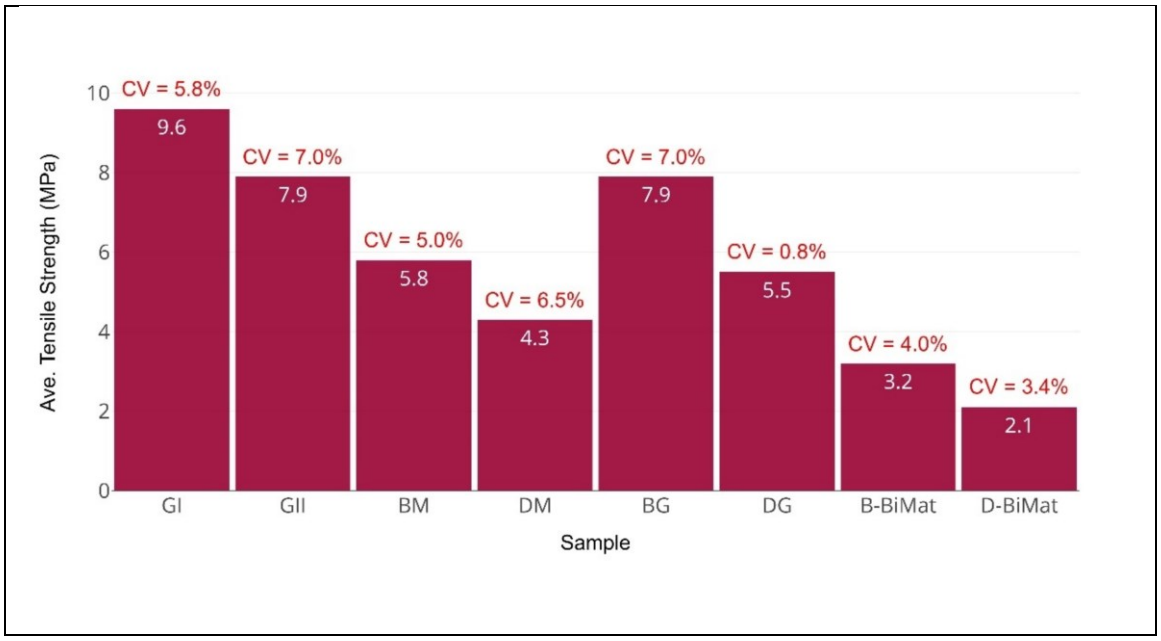

Fig.A2. 11. Summary of the average tensile strength for all tested specimens.

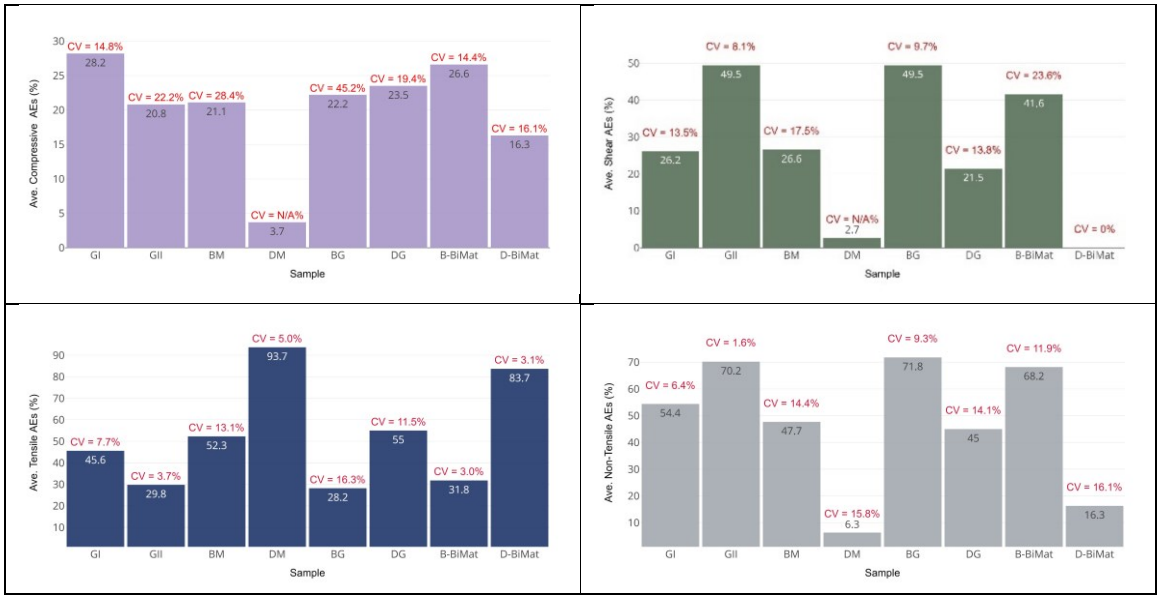

Fig.A2. 12. Summary of the average percentage of compressive, shear, tensile, and Non-tensile AEs for all tested specimens.

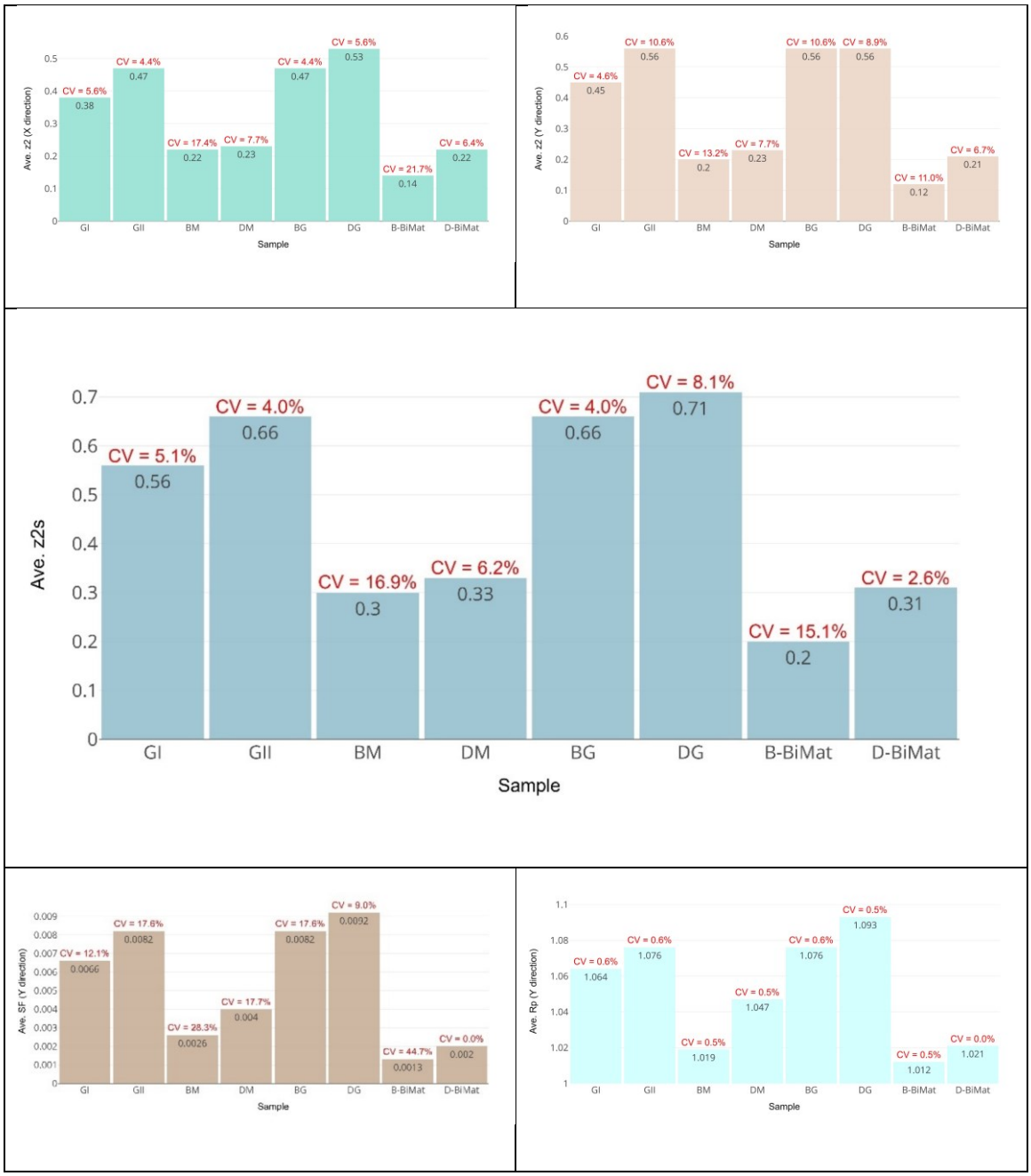

Fig.A2. 13. Summary of the average roughness parameters, z2, z2s, SF, and Rp for all tested specimens.

APPENDIX 3: All tested samples and their corresponding data

This chapter presents all tested specimens and their related test results (i.e., the macroscopic fracture path, load-displacement behaviour, tensile strength, detected acoustic emissions, the roughness of the produced fractures, etc.).

In the following, samples are named using abbreviations in the same way as in CHAPTERS 3 to 5, which are as follows:

- **GI** (GI-1 to GI-5 [5 samples]) in CHAPTER 3: **G**roup **I** of intact Granite discs subjected to Brazilian test under a higher loading rate
- **GII** (GII-1 to GII-6 [6 samples]) in CHAPTER 3: **G**roup **II** of intact granite discs subjected to Brazilian test under a lower loading rate
- **BM** (BM1 to BM7 [7 samples]) in CHAPTER 4: Intact **M**ortar discs subjected to **B**razilian test
- **DM** (DM1 to DM5 [5 samples]) in CHAPTER 4: Intact **M**ortar discs subjected to **D**irect tension test
- **BG** (BG1 to BG6 [6 samples]) in CHAPTER 4: Intact **G**ranite discs subjected to **B**razilian test
- **DG** (DG1 to DG4 [4 samples]) in CHAPTER 4: Intact **G**ranite discs subjected to **D**irect tension test
- **B-BiMat** (B-BiMat1 to B-BiMat6 [6 samples]) in CHAPTER 5: **Bi-mat**erial granite-mortar discs subjected to **B**razilian test
- **D-BiMat** (D-BiMat1 to D-BiMat4 [4 samples]) in CHAPTER 5: **Bi-mat**erial granite-mortar discs subjected to **D**irect tension test

Please note that some data is missing for some samples due to various reasons, such as problems with AE sensors, corrupted data files, etc. Therefore, data is shown as N/A in the tables below where applicable.

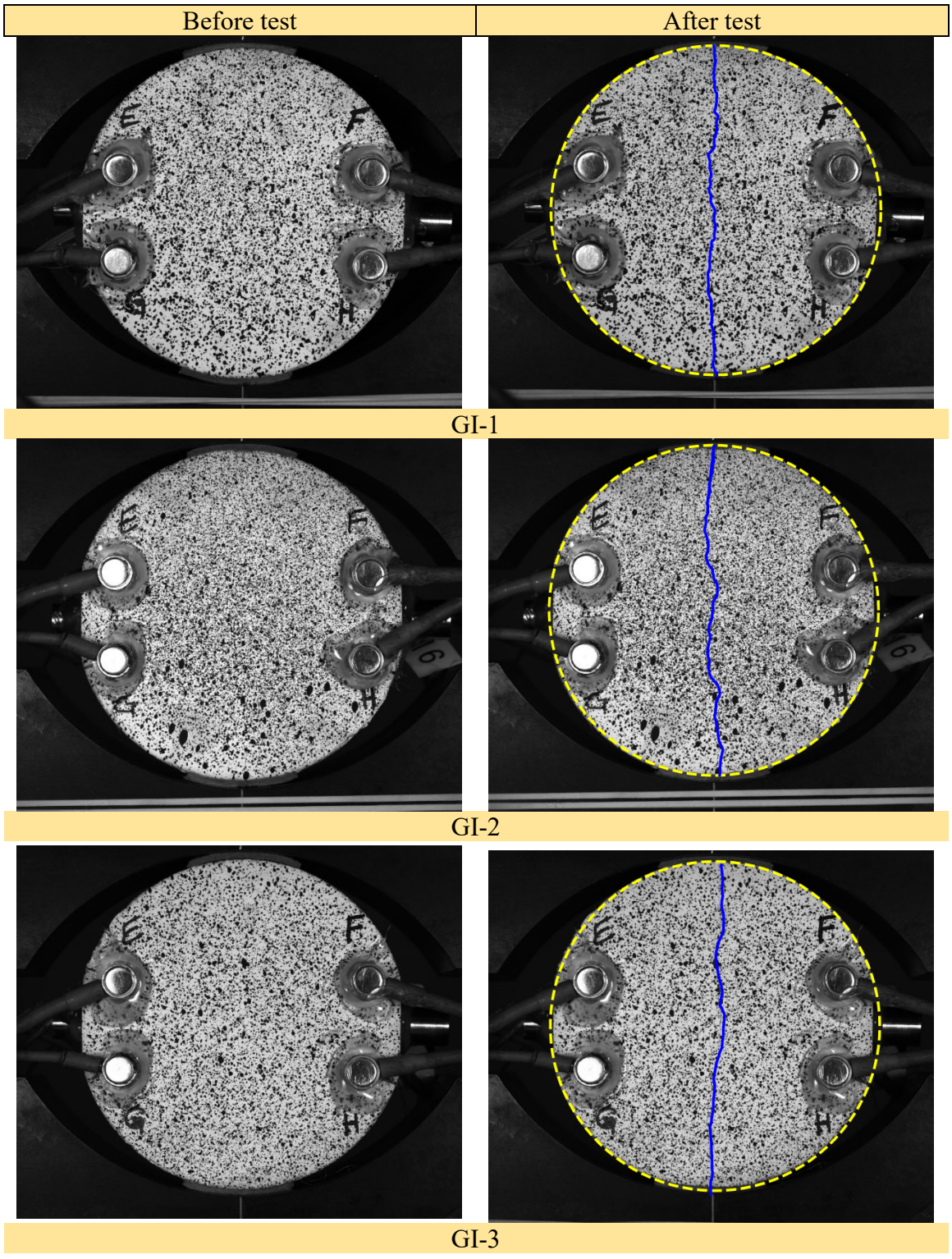

Fig.A3. 1. Macroscopic failure pattern of GI-1 to GI-5 representing the group I specimens subjected to the Brazilian test with a loading rate of 1 μm/sec (high-loading rate). The blue lines represent the macro fracture path at the failure.

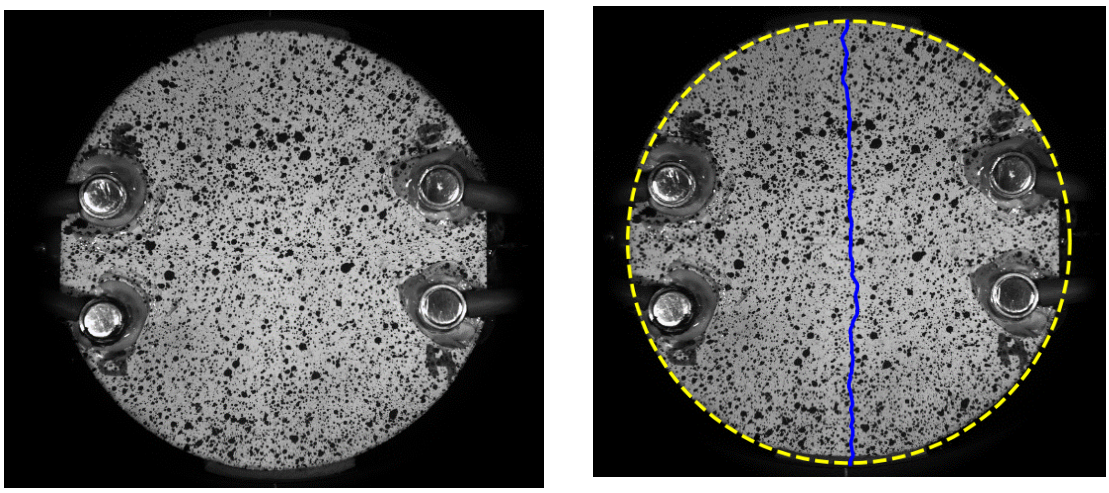

GI-4

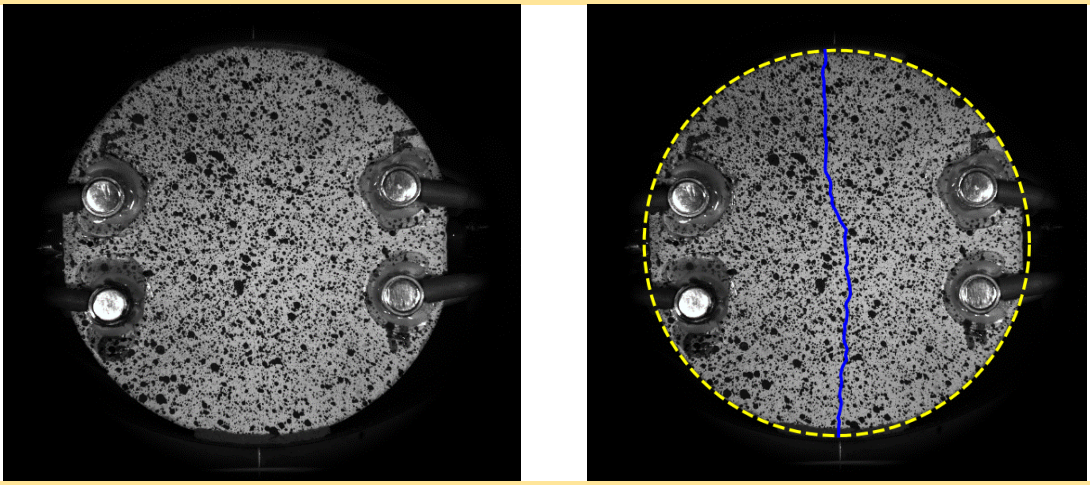

GI-5

Fig.A3. 1. Continue…

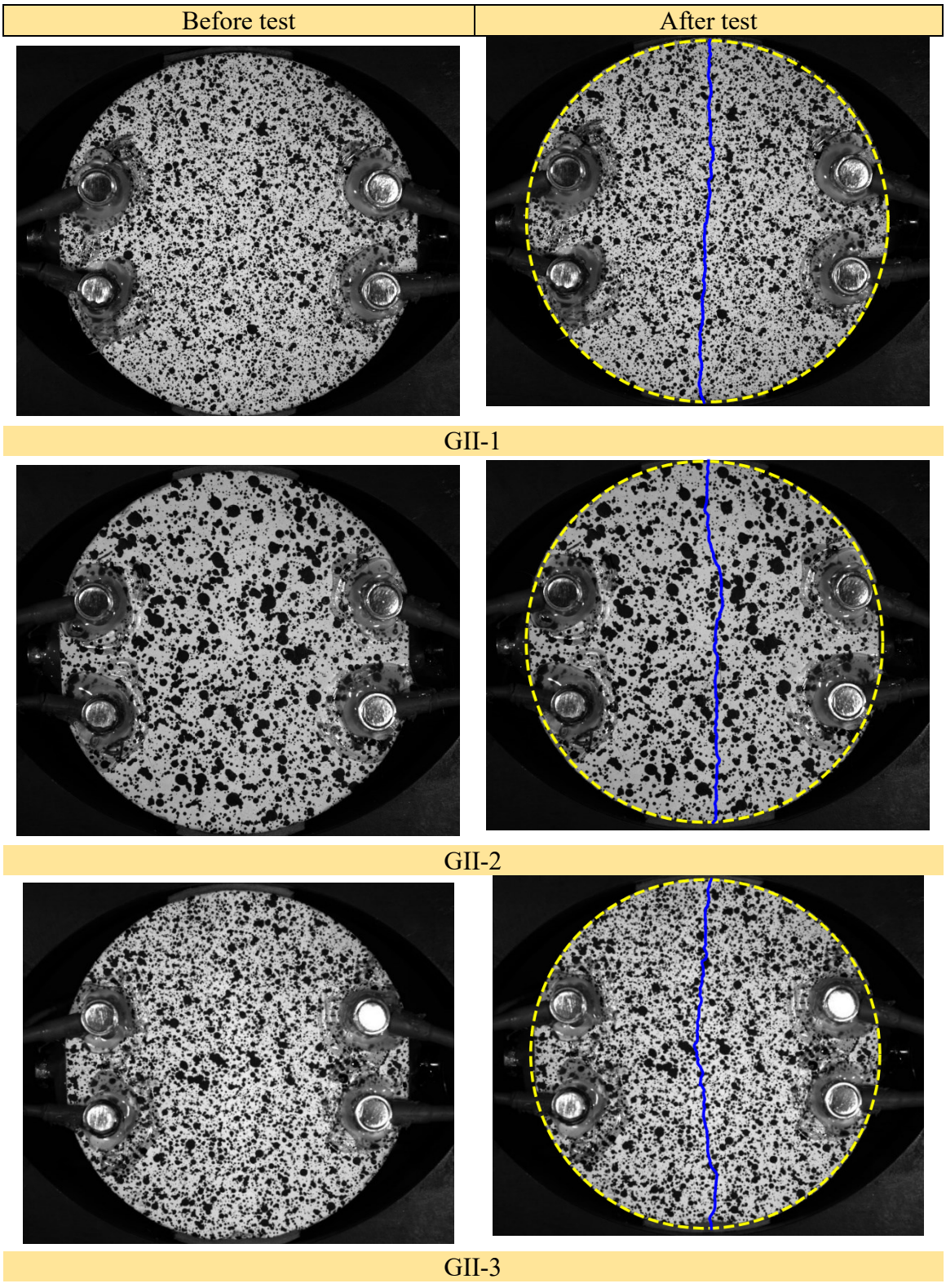

Fig.A3. 2. Macroscopic failure pattern of GII-1 to GII-6 representing the group II specimens subjected to the Brazilian test with a loading rate of 0.1 µm/sec (low-loading rate). The blue lines represent the macro fracture path at the failure.

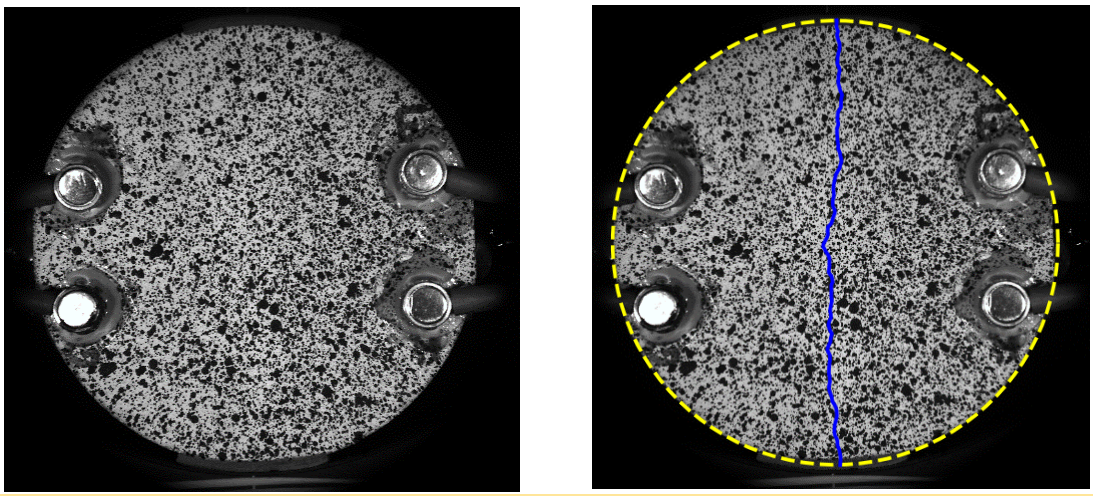

GII-4

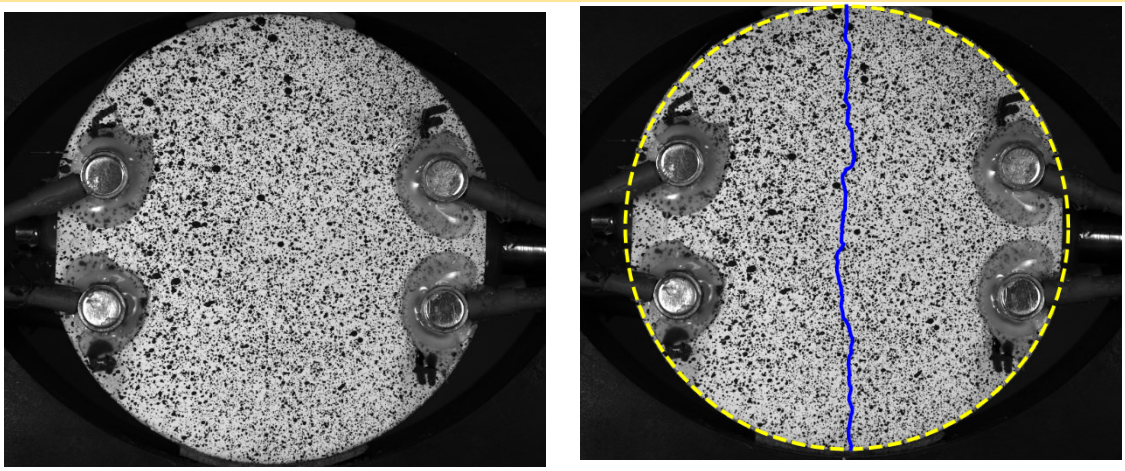

GII-5

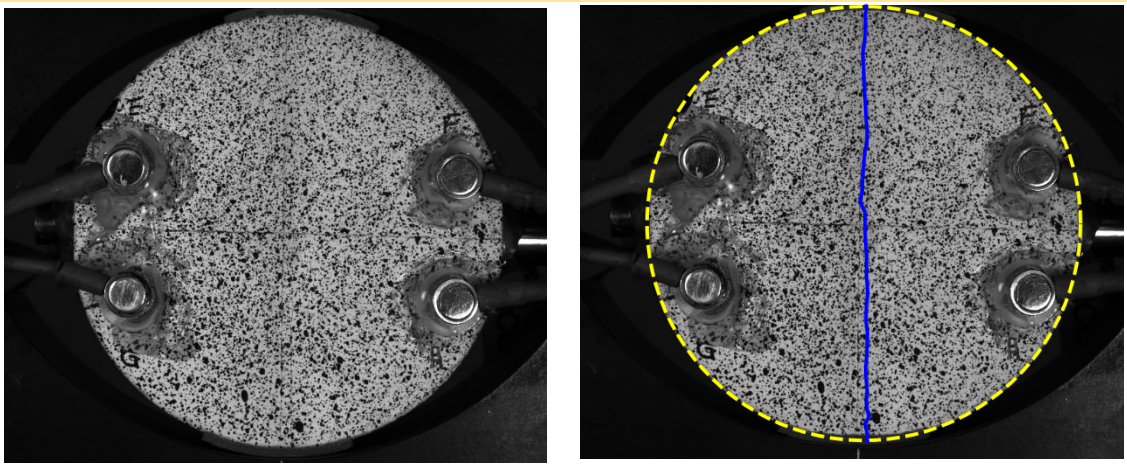

GII-6

Fig.A3. 2. Continue …

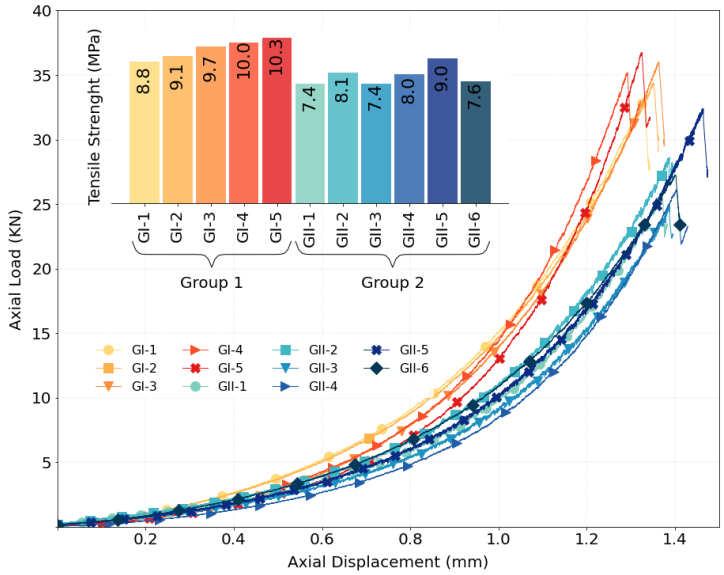

Fig.A3. 3. Load-displacement curves for group I and II Brazilian discs. The inset shows the tensile strength of specimens. Specimens GI-1 to GI-5 were tested with a loading rate of 1 µm/sec (high-loading rate), and specimens GII-1 to GII-6 were tested with a loading rate of 0.1 µm/sec (low-loading rate).

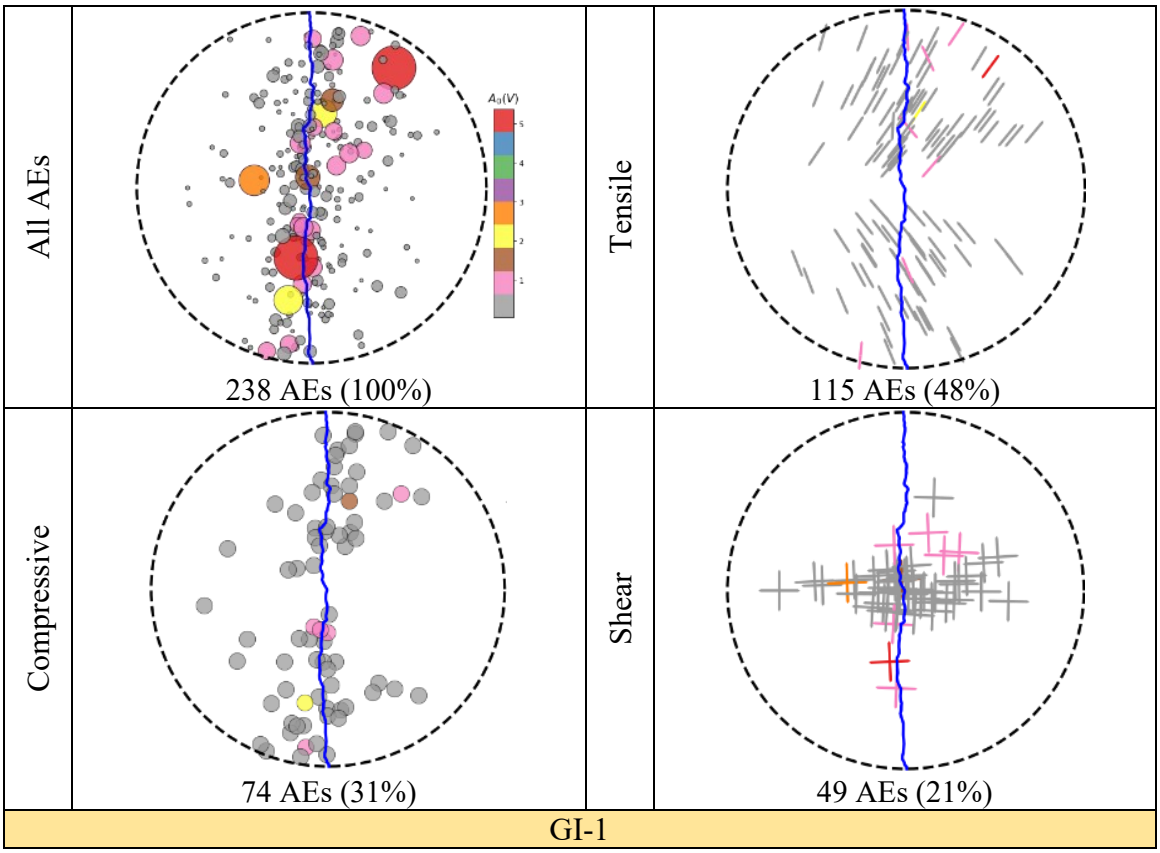

Fig.A3. 4. Spatial distribution of AE events at failure load detected by a minimum of 6 sensors decomposed into different focal mechanisms for group I specimens (GI-1 to GI-5) with a loading rate of 1 µm/*sec* (high-loading rate). The color codes represent the average focal amplitude (A_0) of AEs. The upper left column indicates all detected AE events, while the other subplots show the distribution of tensile, compressive, and shear AE sources. The percentages in brackets represent the ratio of the specified AE mechanisms to the total AEs detected for the given specimen.

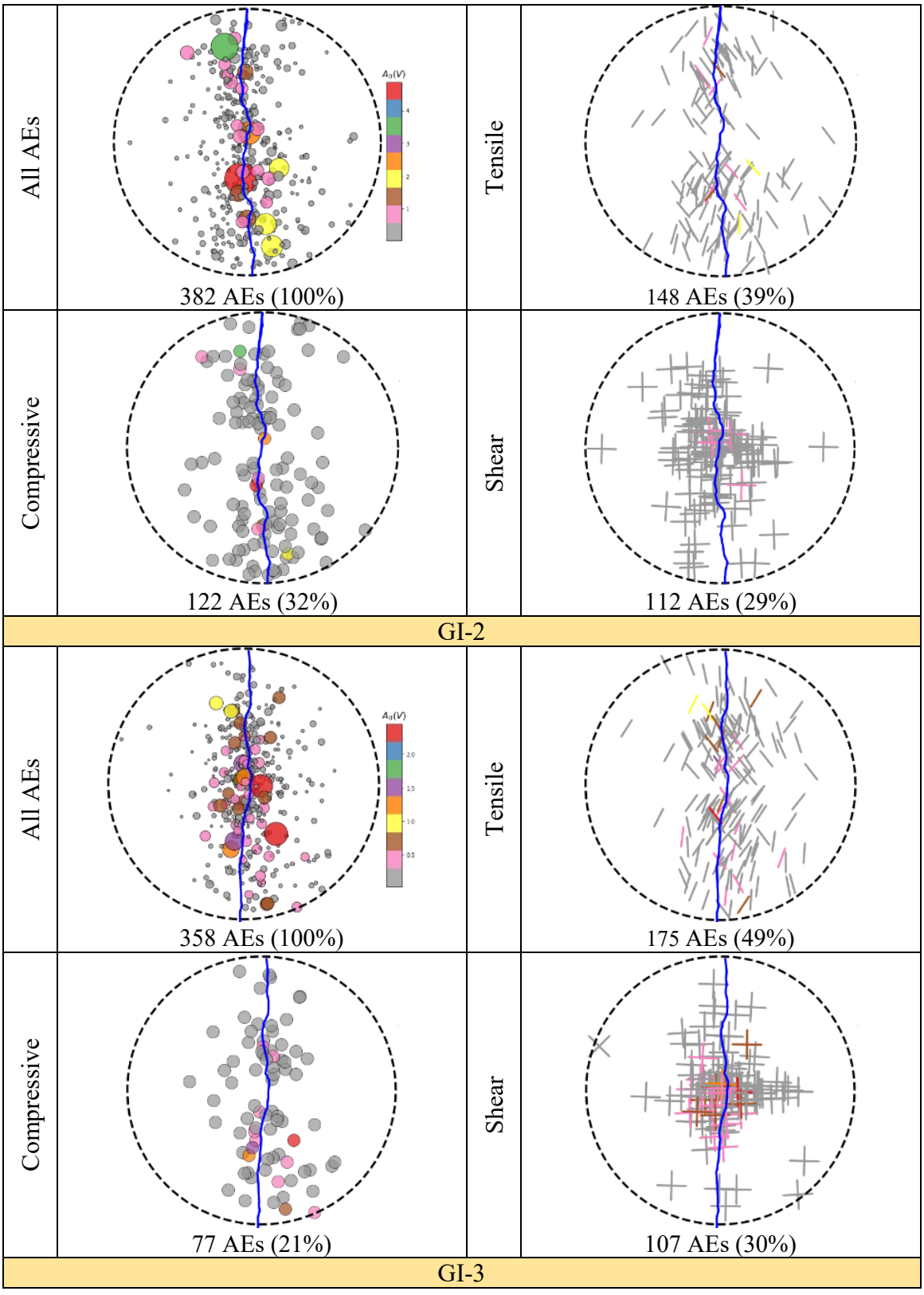

Fig.A3. 4. Continue …

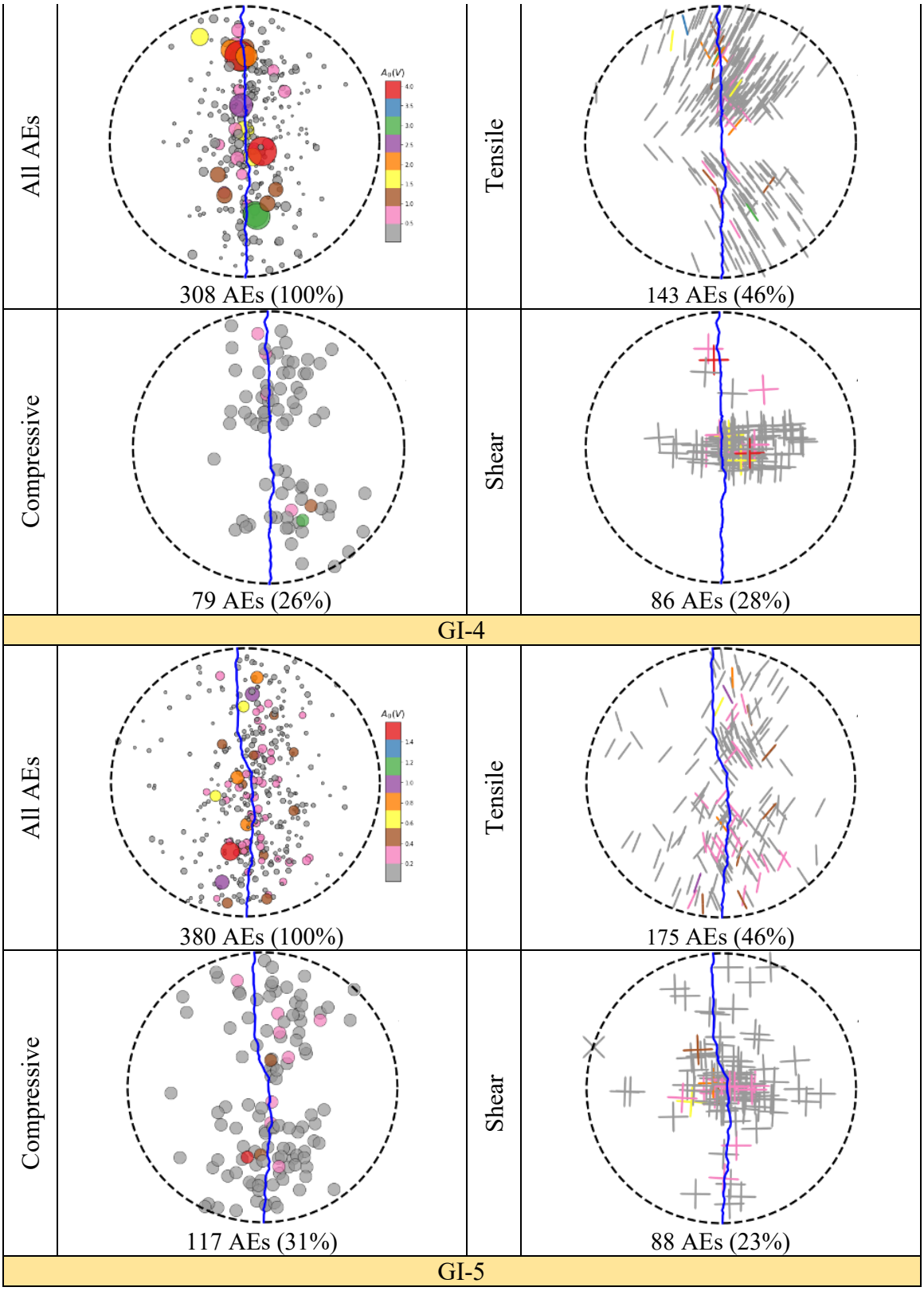

Fig.A3. 4. Continue …

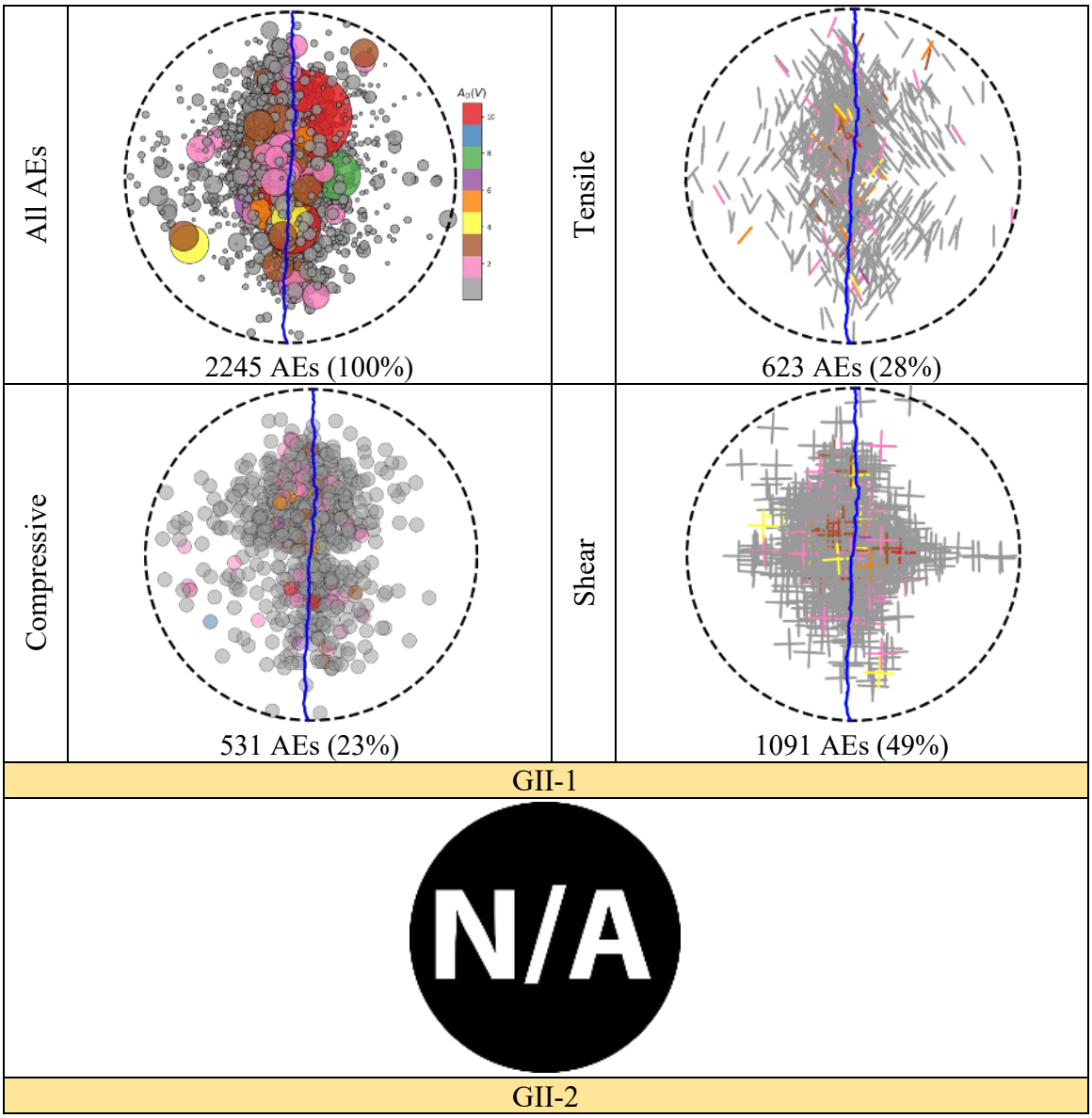

Fig.A3. 5. Spatial distribution of AE events at failure load detected by a minimum of 6 sensors decomposed into different focal mechanisms for group II specimens (G II -1 to G-II -6) with a loading rate of 0.1 µm/*sec* (low-loading rate). The color codes represent the average focal amplitude (A_0) of AEs. The upper left column indicates all detected AE events, while the other subplots show the distribution of tensile, compressive, and shear AE sources. The percentages in brackets represent the ratio of the specified AE mechanisms to the total AEs detected for the given specimen.

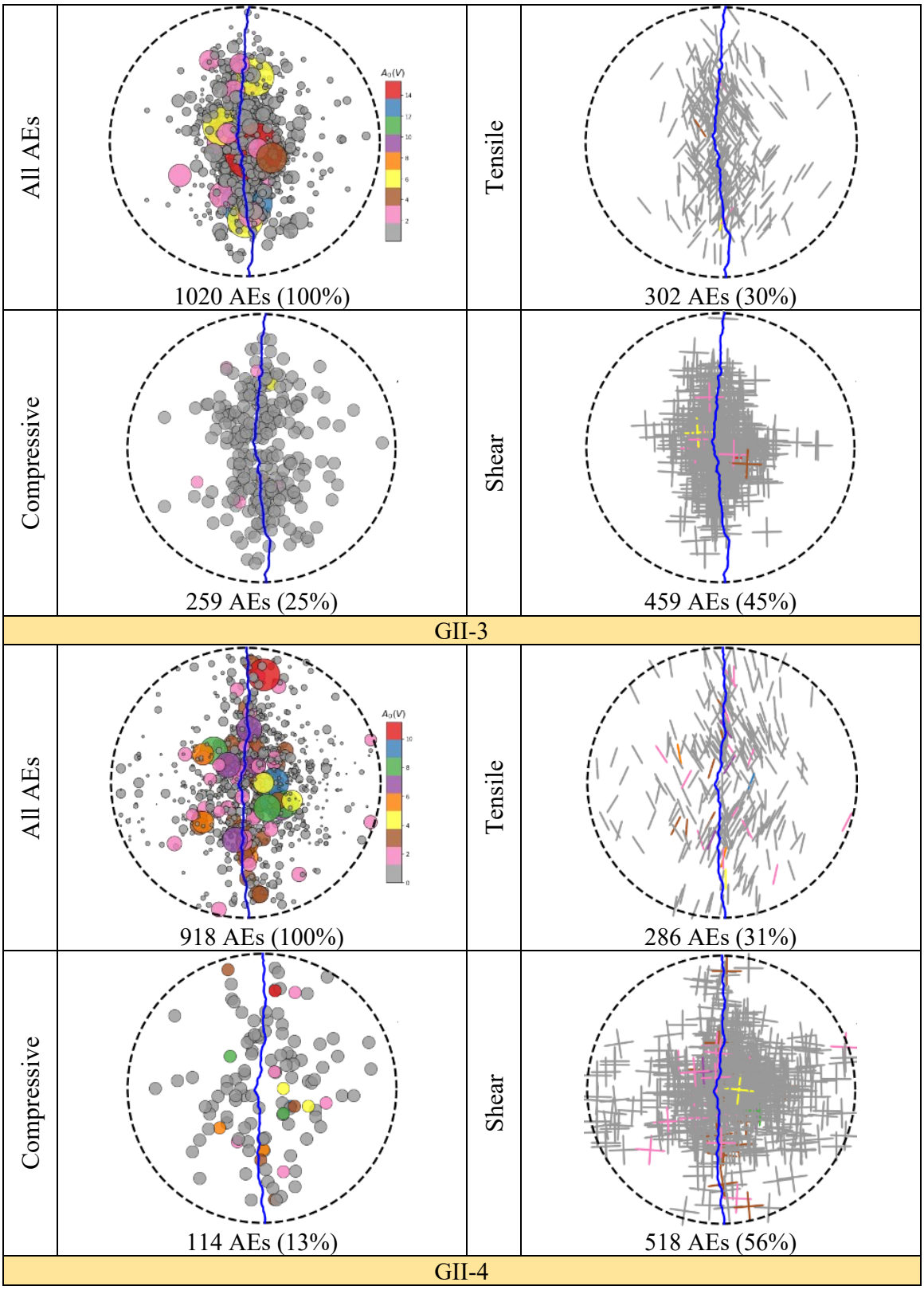

Fig.A3. 5. Continue …

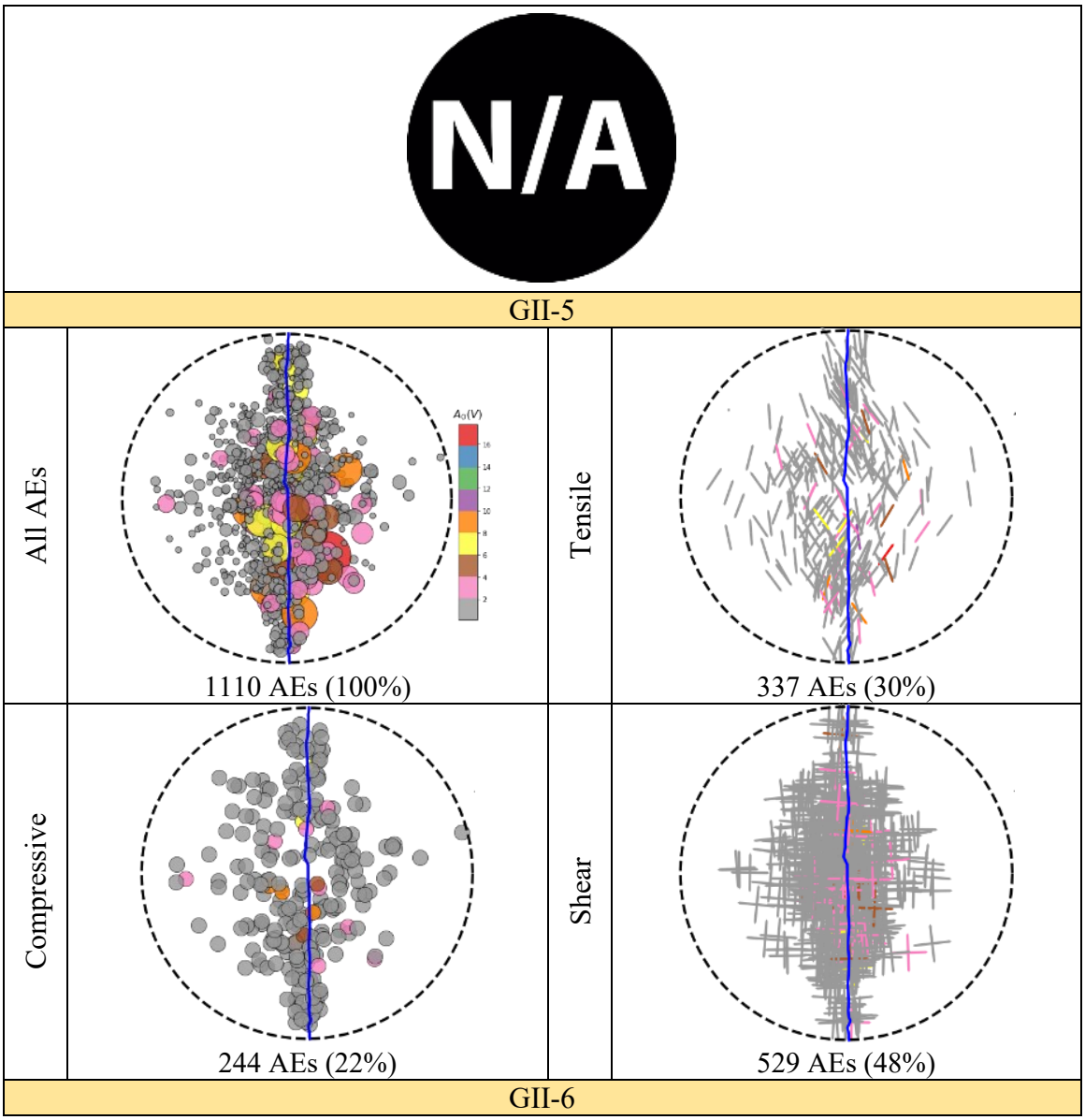

Fig.A3. 5. Continue …

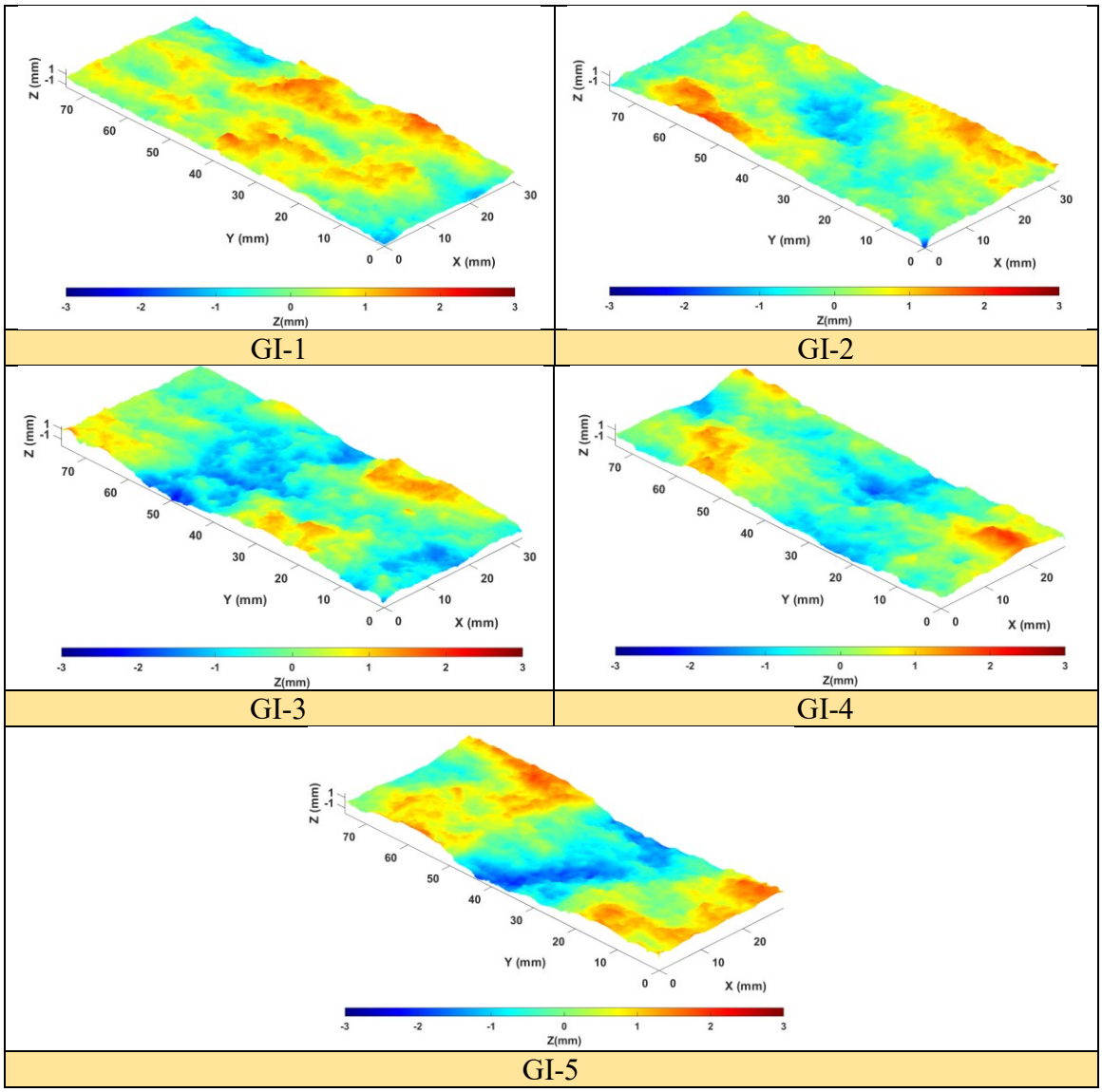

Fig.A3. 6. Surface roughness geometry of the created macroscopic fracture after specimen failure for group I Brazilian specimens (GI-1 to GI-5).

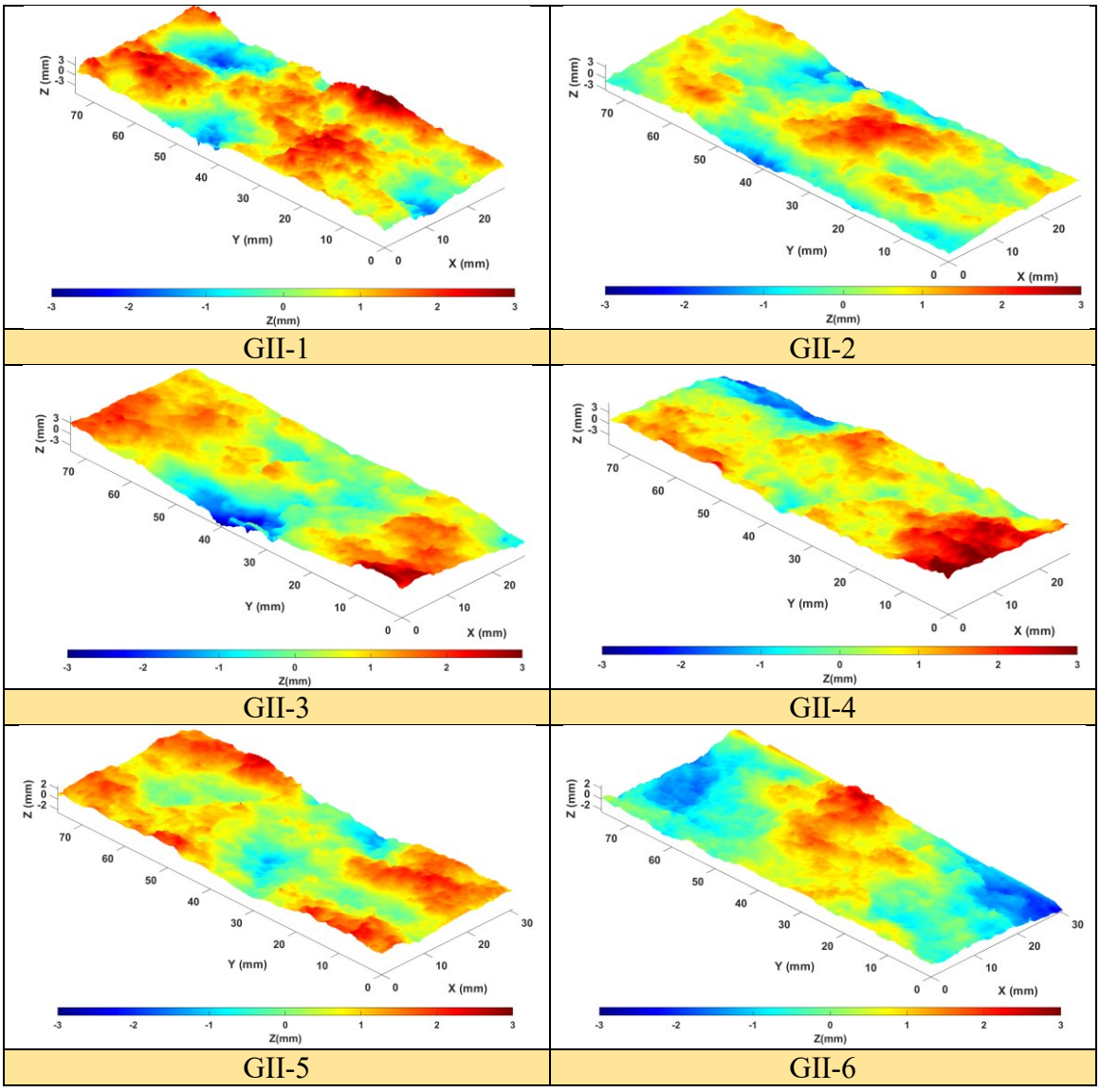

Fig.A3. 7. Surface roughness geometry of the created macroscopic fractured after specimen failure for group II Brazilian specimens (GII-1 to GII-6).

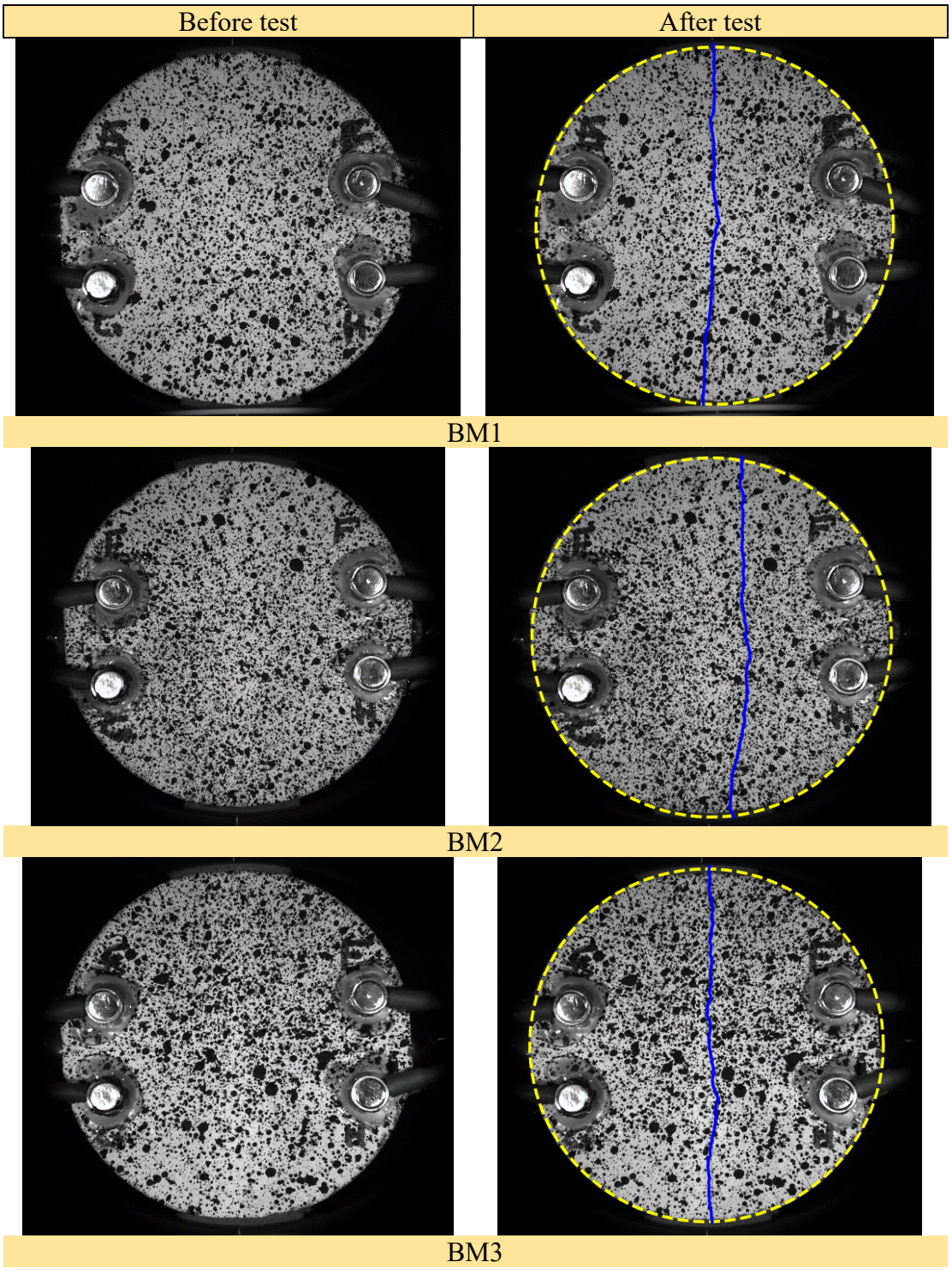

Fig.A3. 8. Macroscopic failure pattern of BM specimens subjected to Brazilian test. The blue lines represent the macro fracture path at the failure.

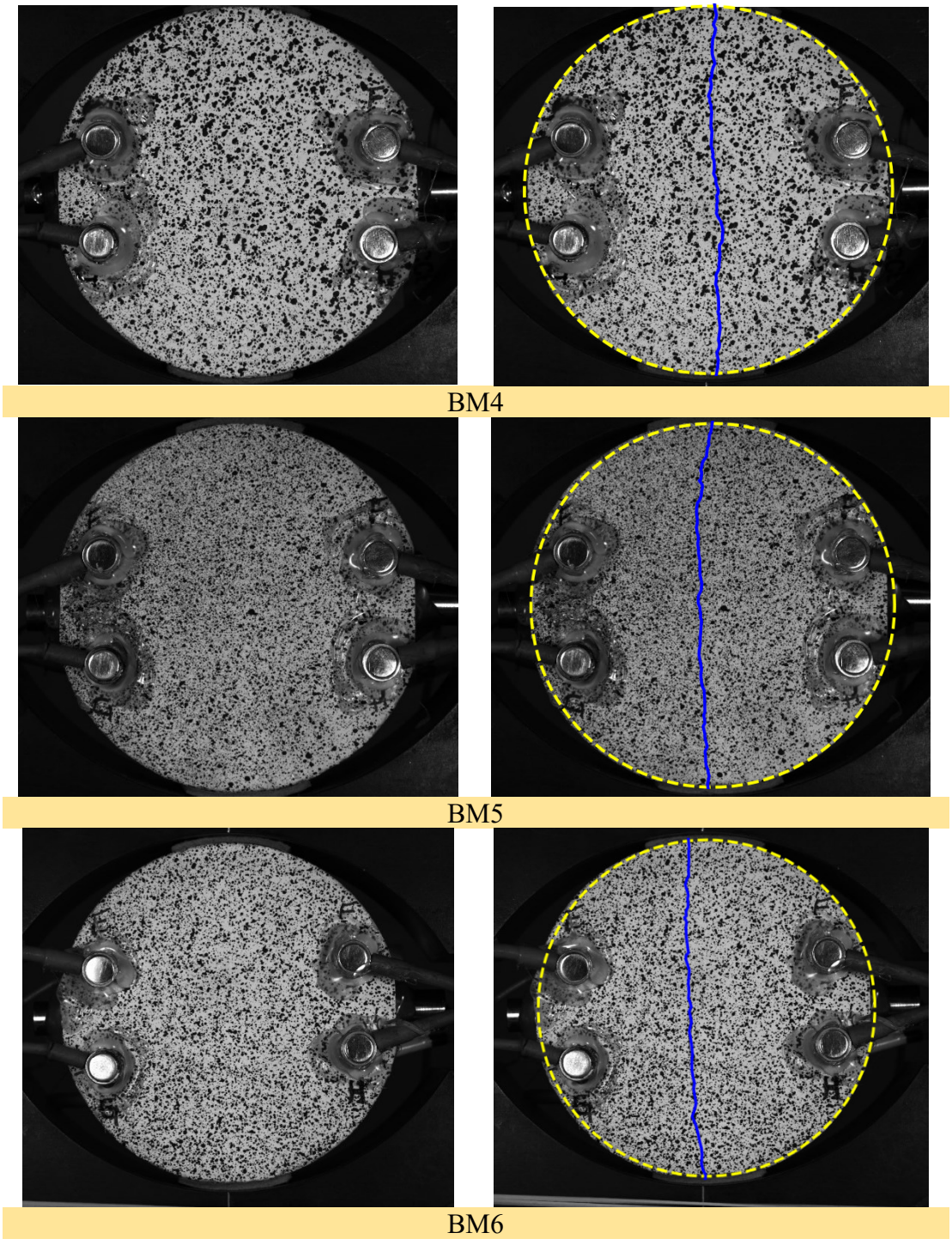

Fig.A3. 8. Continue …

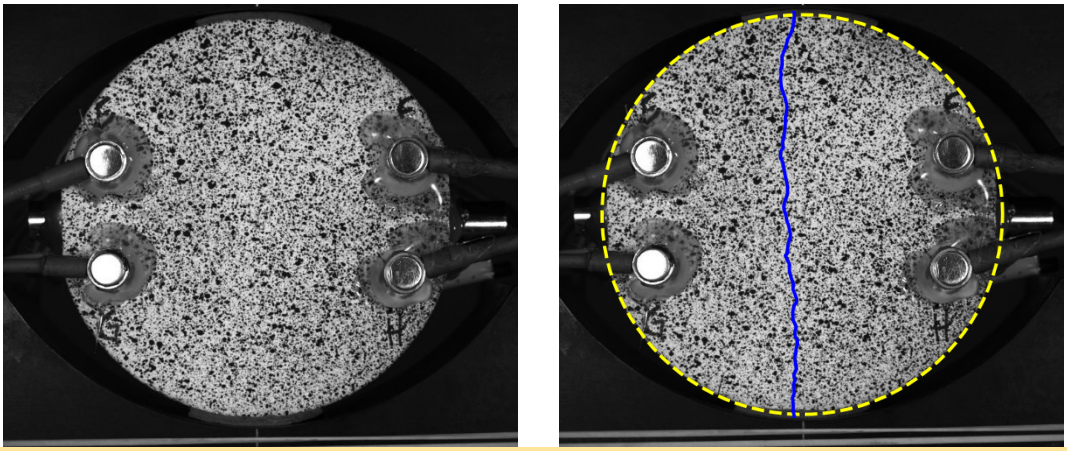

BM7

Fig.A3. 8. Continue …

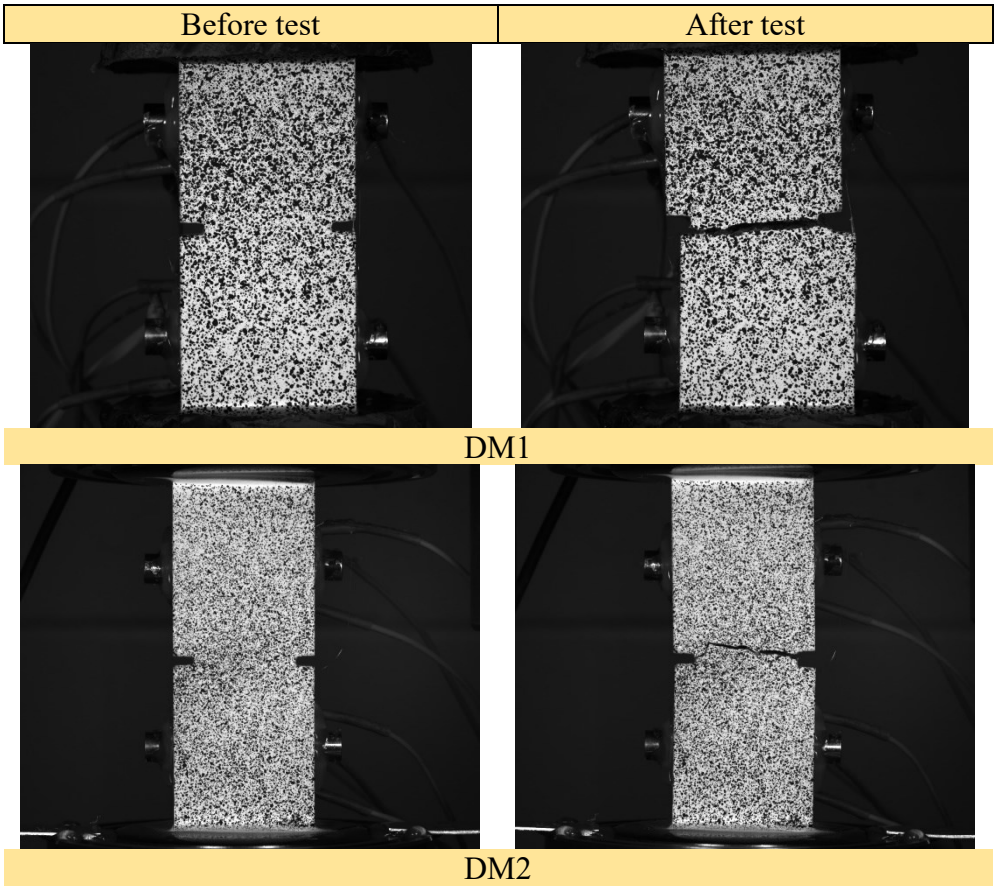

Fig.A3. 9. Macroscopic failure pattern of DM specimens subjected to direct tensile test.

DM3

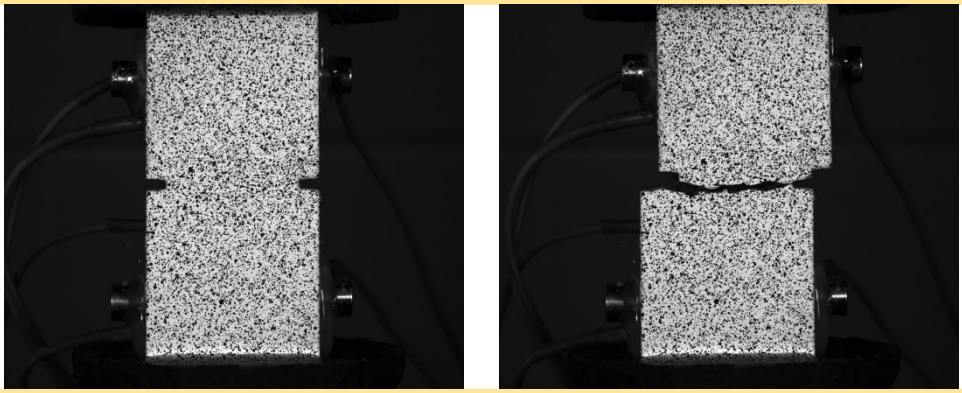

DM4

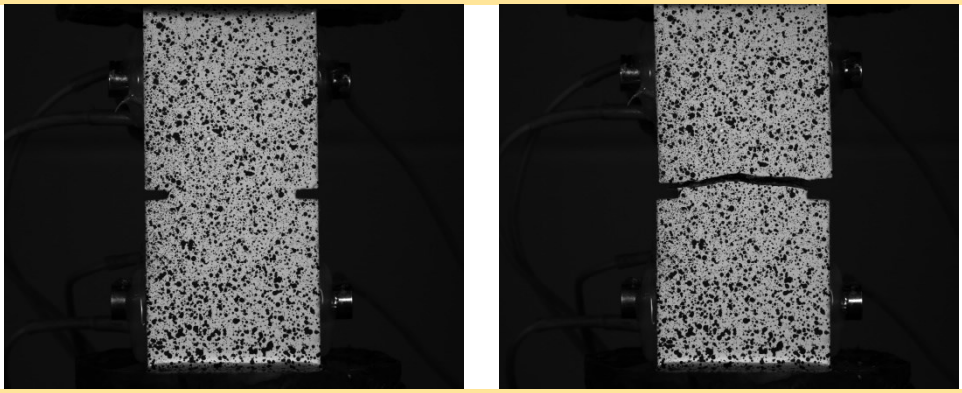

DM5

Fig.A3. 9. Continue …

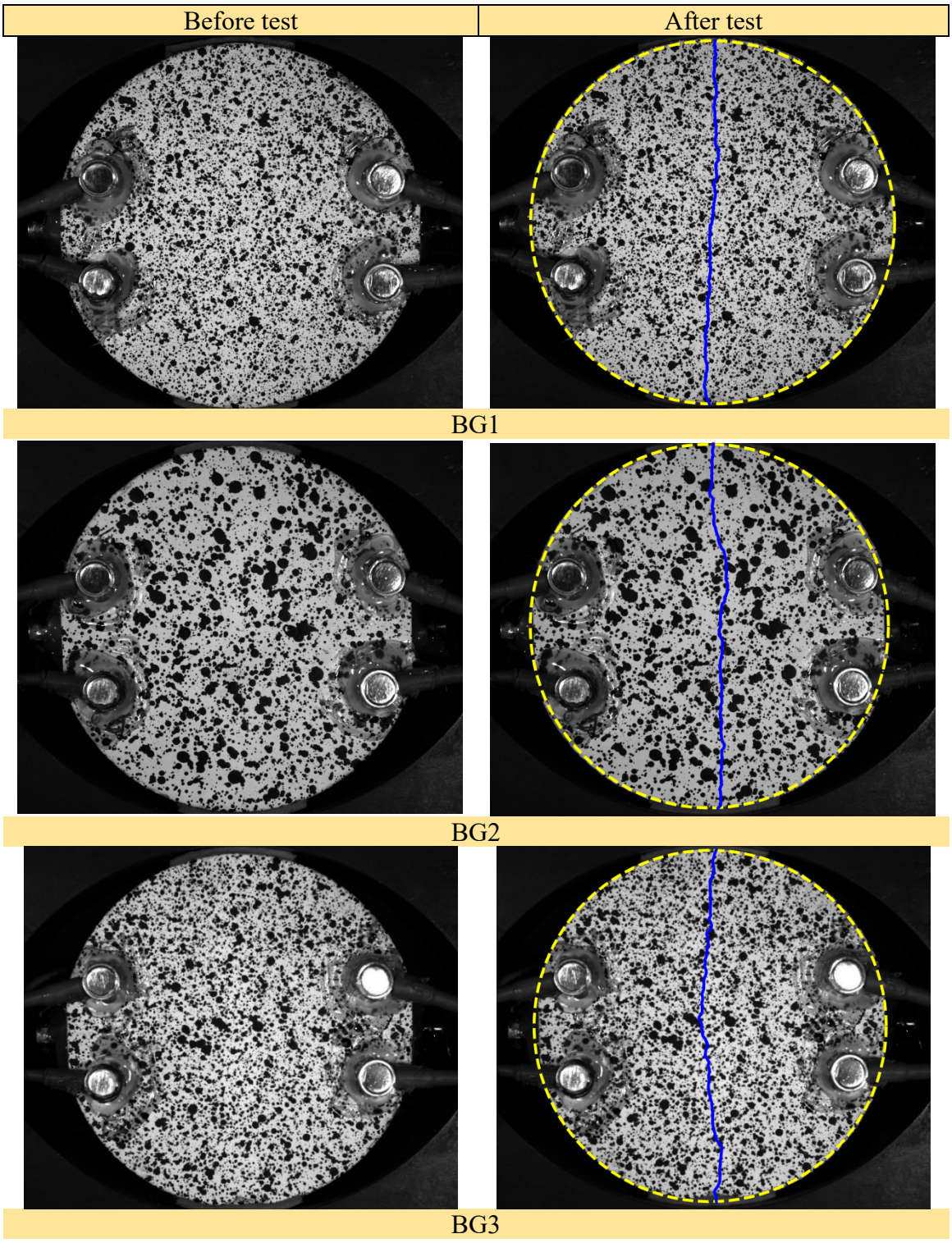

Fig.A3. 10. Macroscopic failure pattern of BG specimens subjected to Brazilian test. The blue lines represent the macro fracture path at the failure.

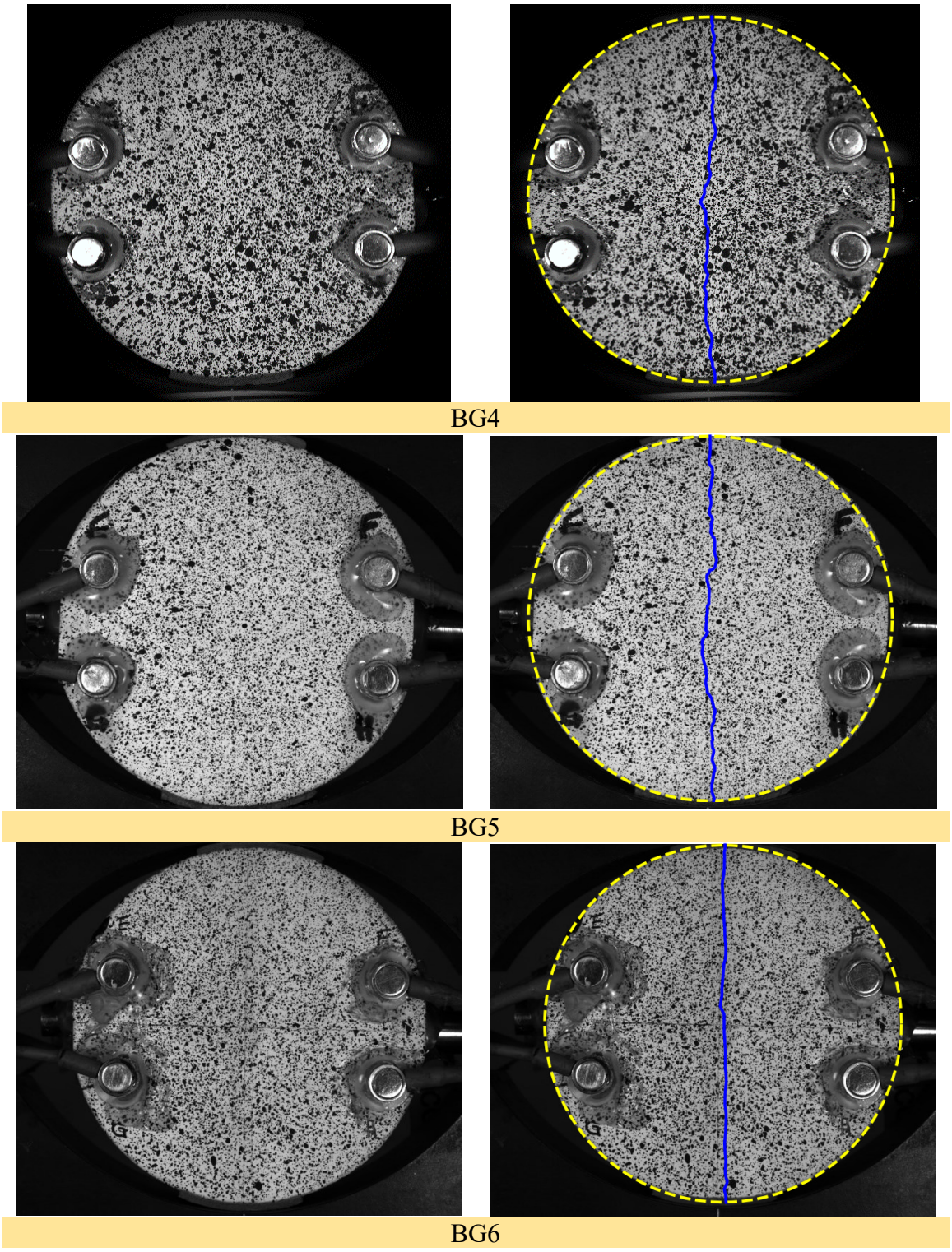

Fig.A3. 10. Continue …

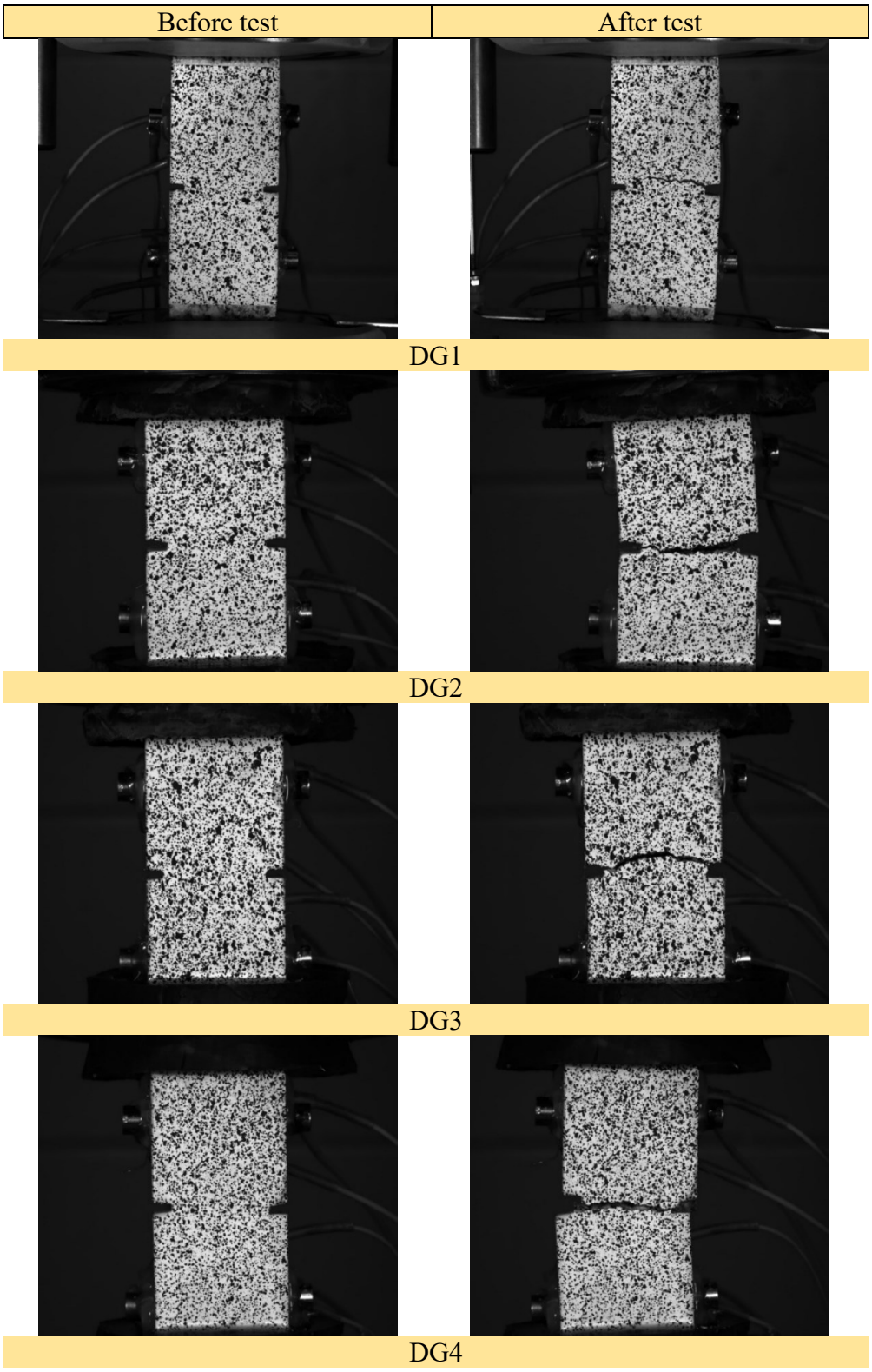

Fig.A3. 11. Macroscopic failure pattern of DG specimens subjected to direct tensile test.

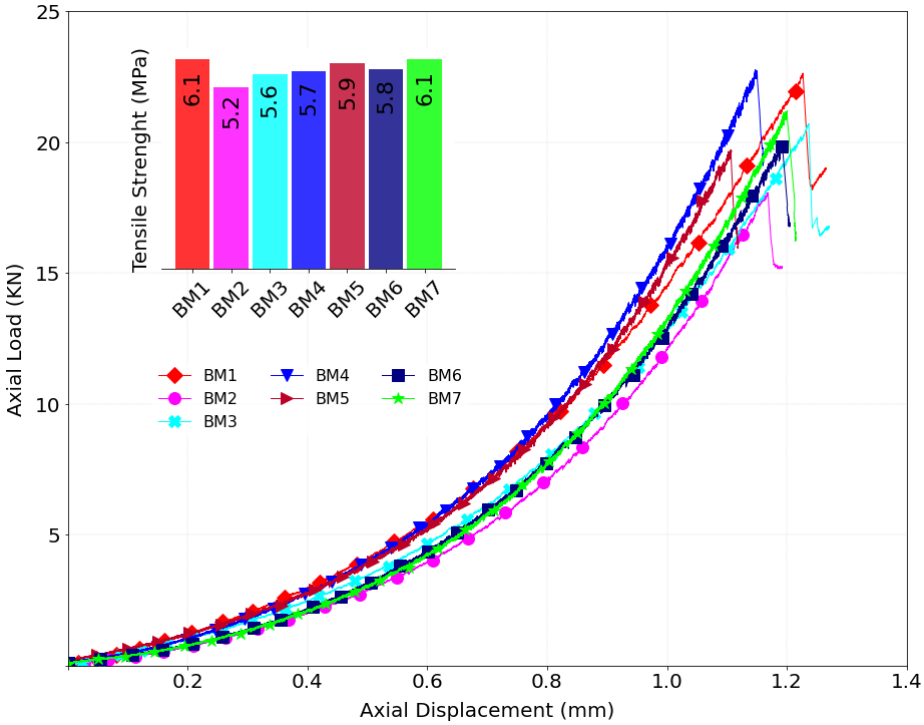

Fig.A3. 12. Load-displacement curves for BM specimens. The inset shows the tensile strength of specimens.

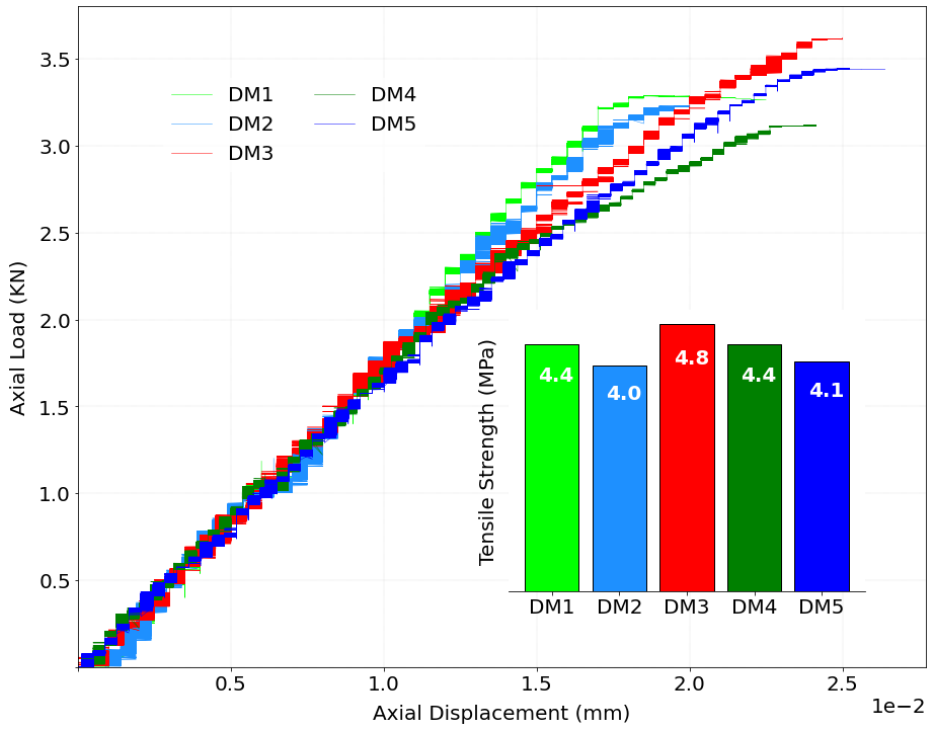

Fig.A3. 13. Load-displacement curves for DM specimens. The inset shows the tensile strength of specimens.

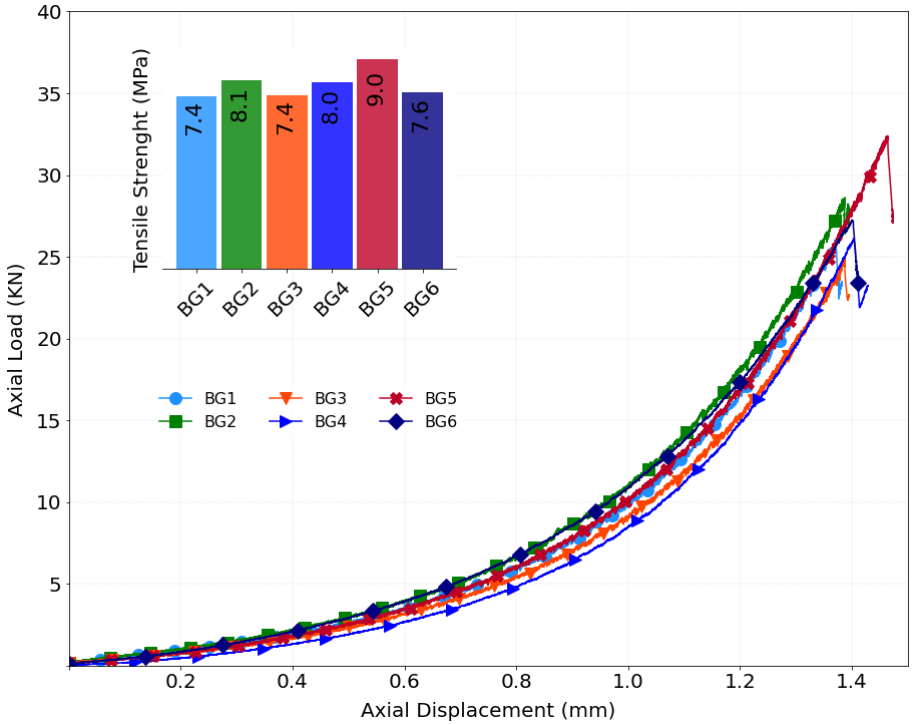

Fig.A3. 14. Load-displacement curves for BG specimens. The inset shows the tensile strength of specimens.

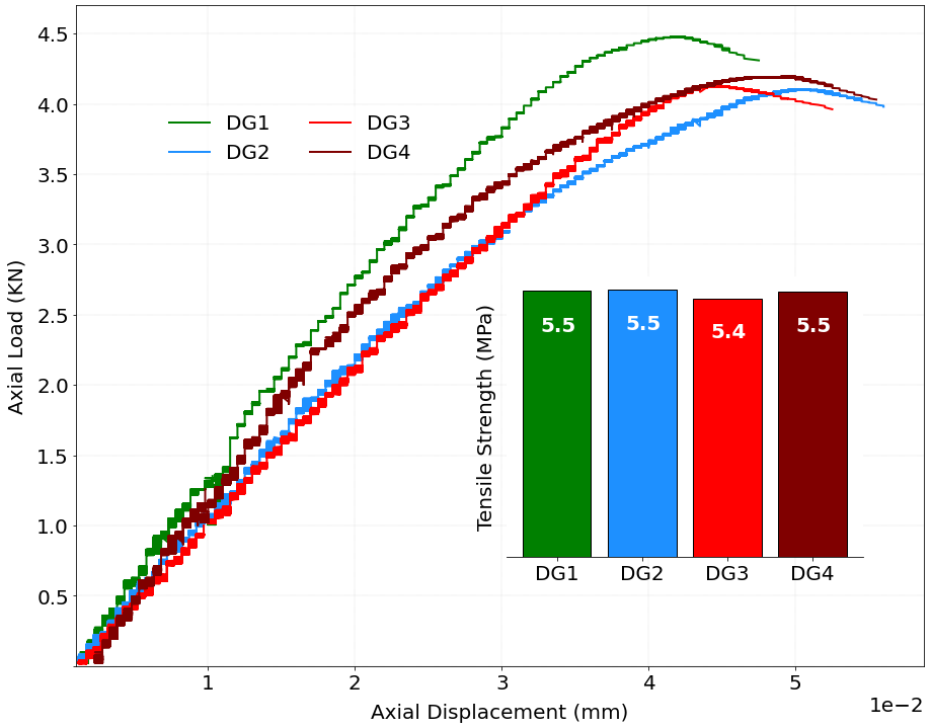

Fig.A3. 15. Load-displacement curves for DG specimens. The inset shows the tensile strength of specimens.

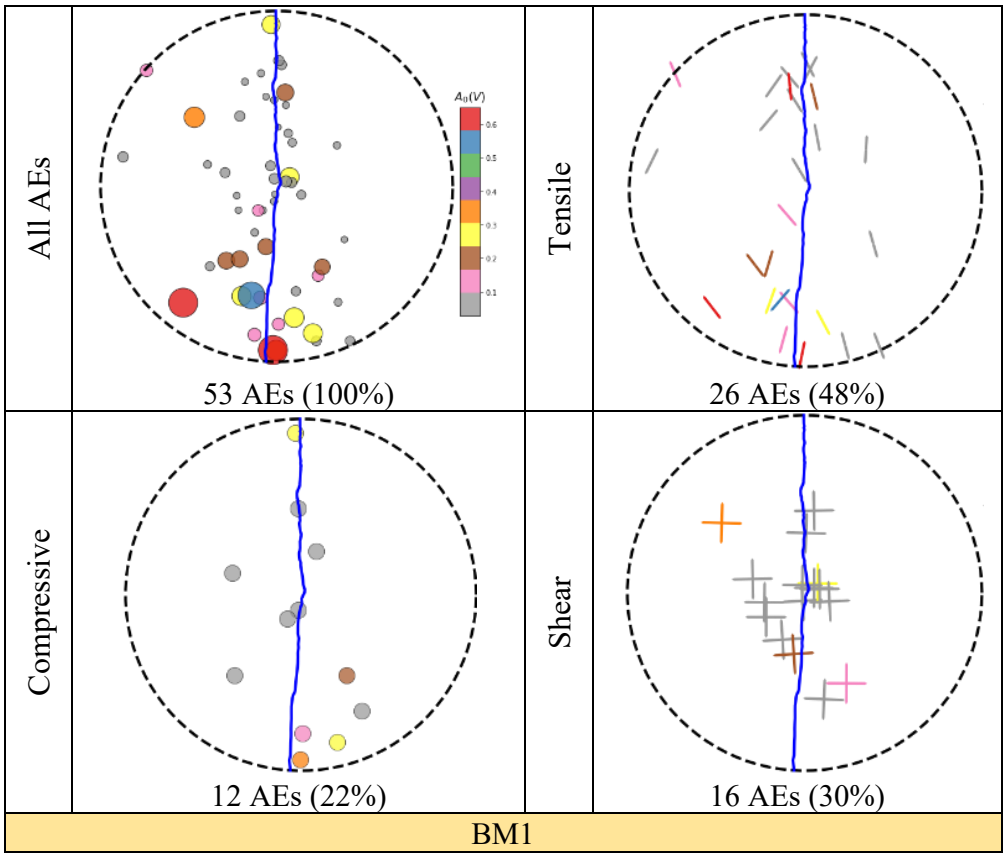

Fig.A3. 16. Spatial distribution of AE events at failure load detected by a minimum of 6 sensors decomposed into different focal mechanisms for BM specimens. The color codes represent the average focal amplitude (A_0) of AEs. The upper left column indicates all detected AE events, while the other subplots show the distribution of tensile, compressive, and shear AE sources. The percentages in brackets represent the ratio of the specified AE mechanisms to the total AEs detected for the given specimen.

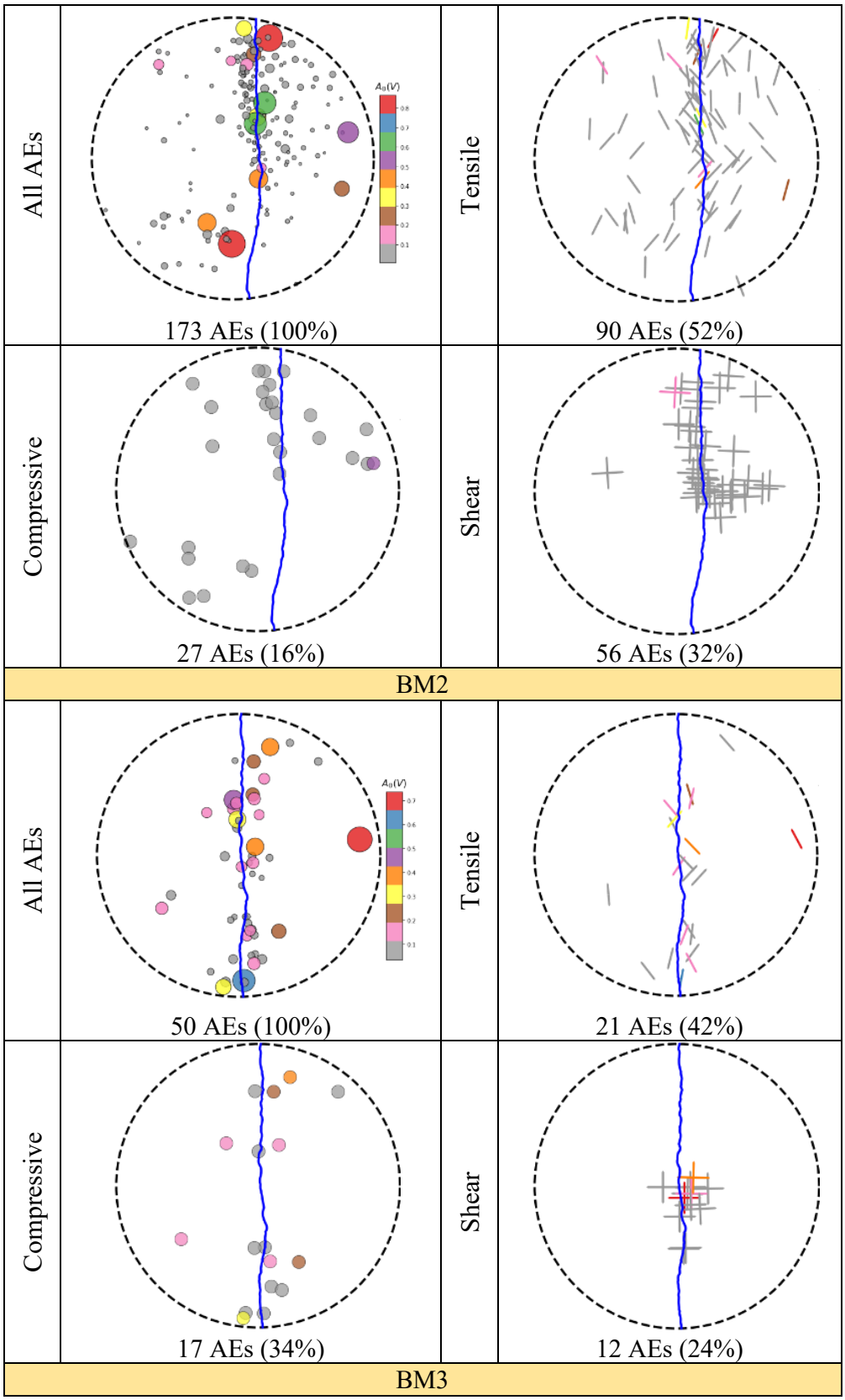

Fig.A3. 16. Continue …

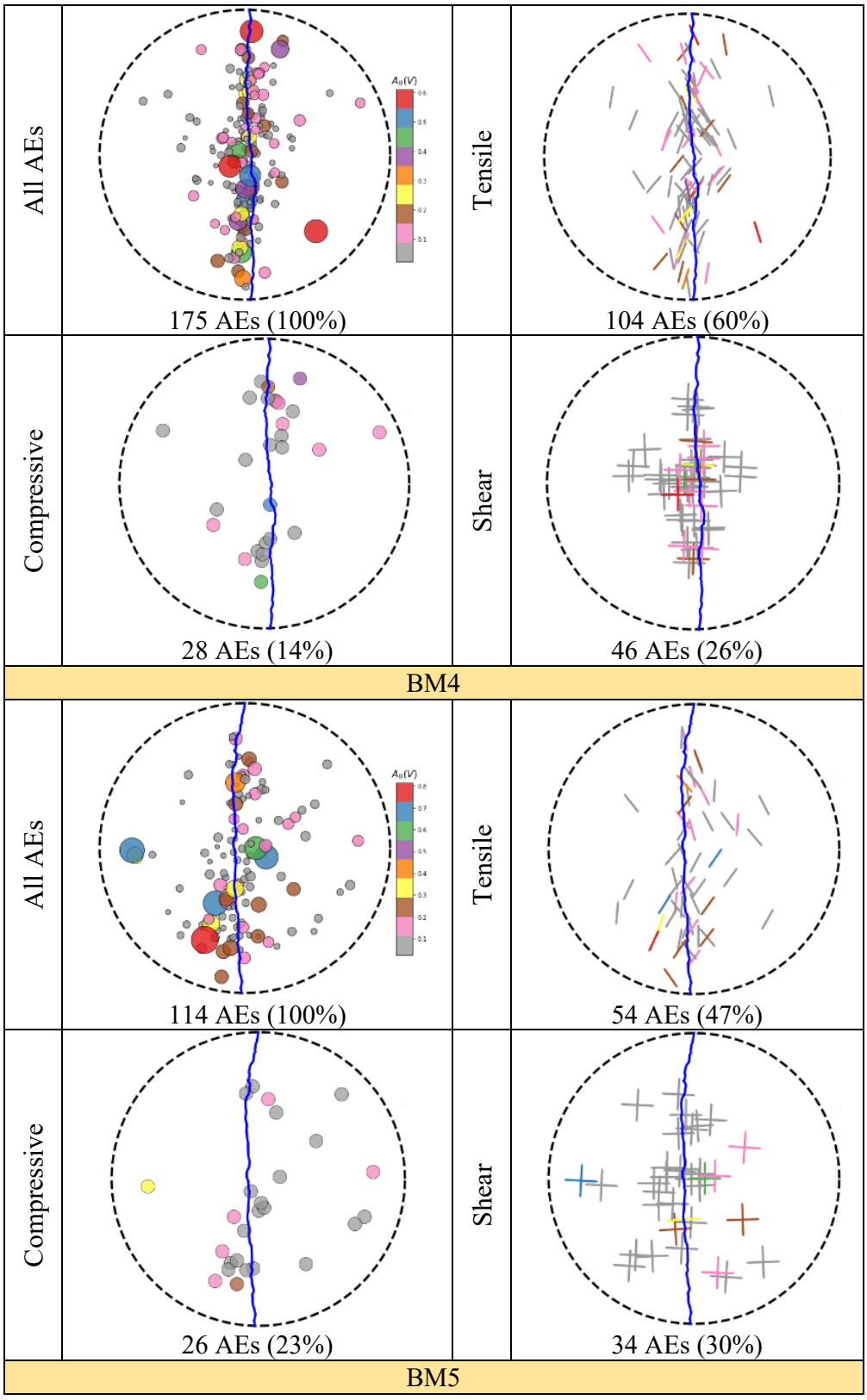

Fig.A3. 16. Continue …

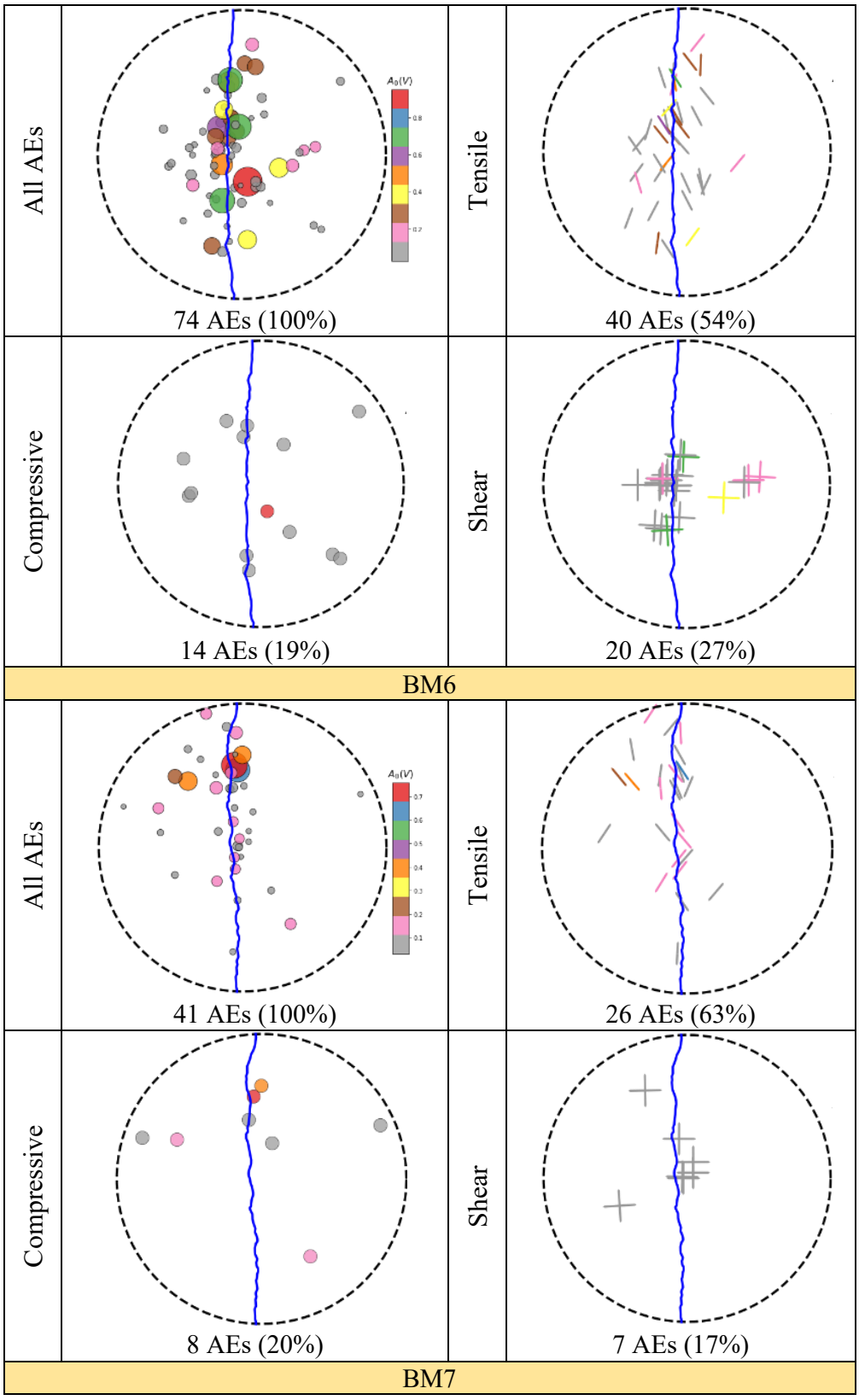

Fig.A3. 16. Continue …

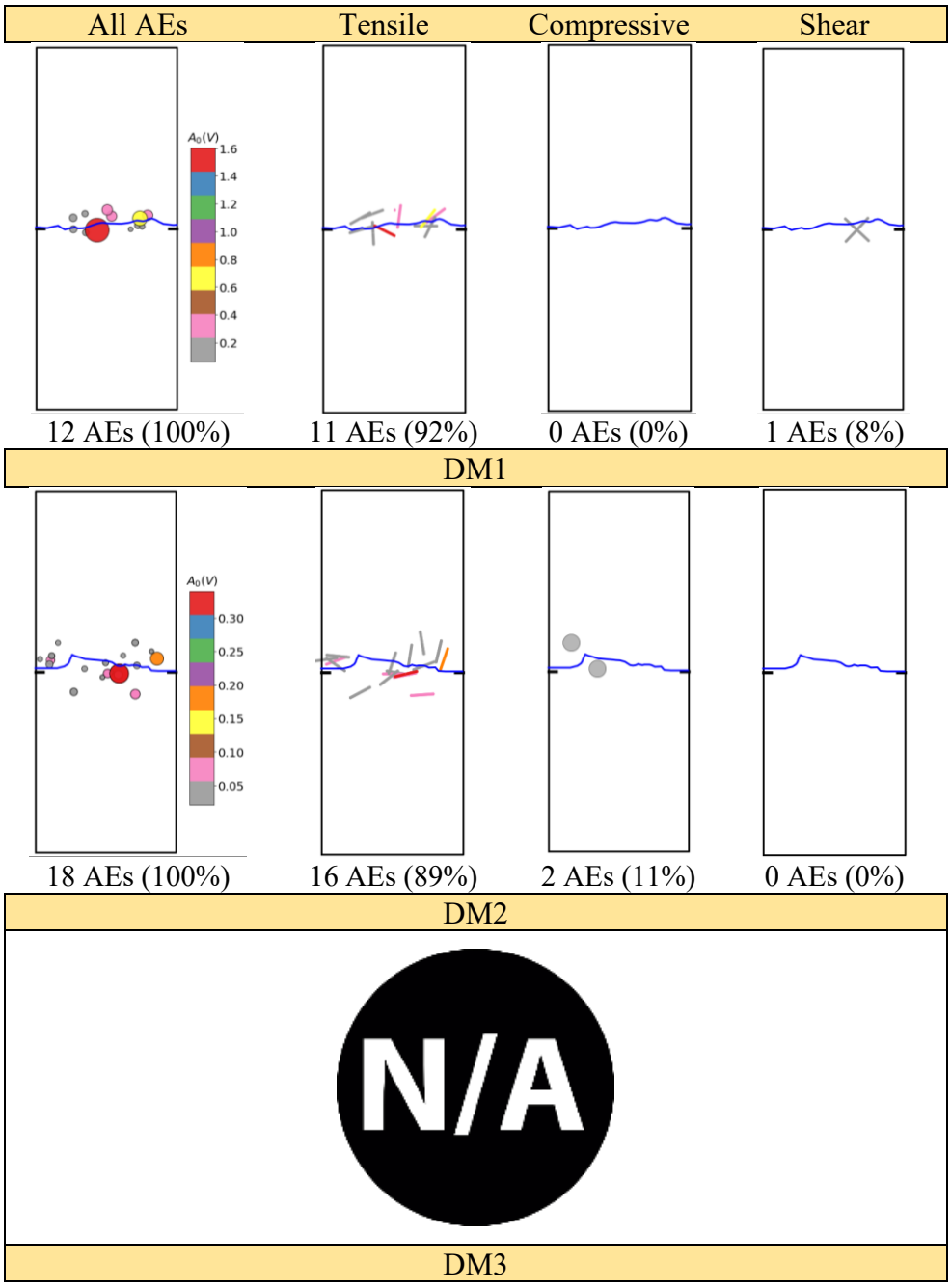

Fig.A3. 17. Spatial distribution of AE events at failure load detected by a minimum of 6 sensors decomposed into different focal mechanisms for DM specimens. The color codes represent the average focal amplitude (A_0) of AEs. The leftmost column indicates all detected AE events, while the other three columns show the distribution of tensile, compressive, and shear AE sources. The percentages in brackets represent the ratio of the specified AE mechanisms to the total AEs detected for the given specimen.

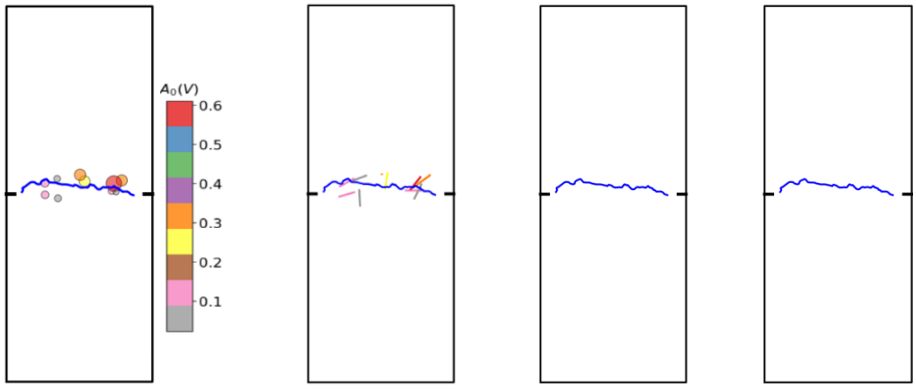

10 AEs (100%) | 10 AEs (100%) | 0 AEs (0%) | 0 AEs (0%)

DM4

N/A

DM5

Fig.A3. 17. Continue …

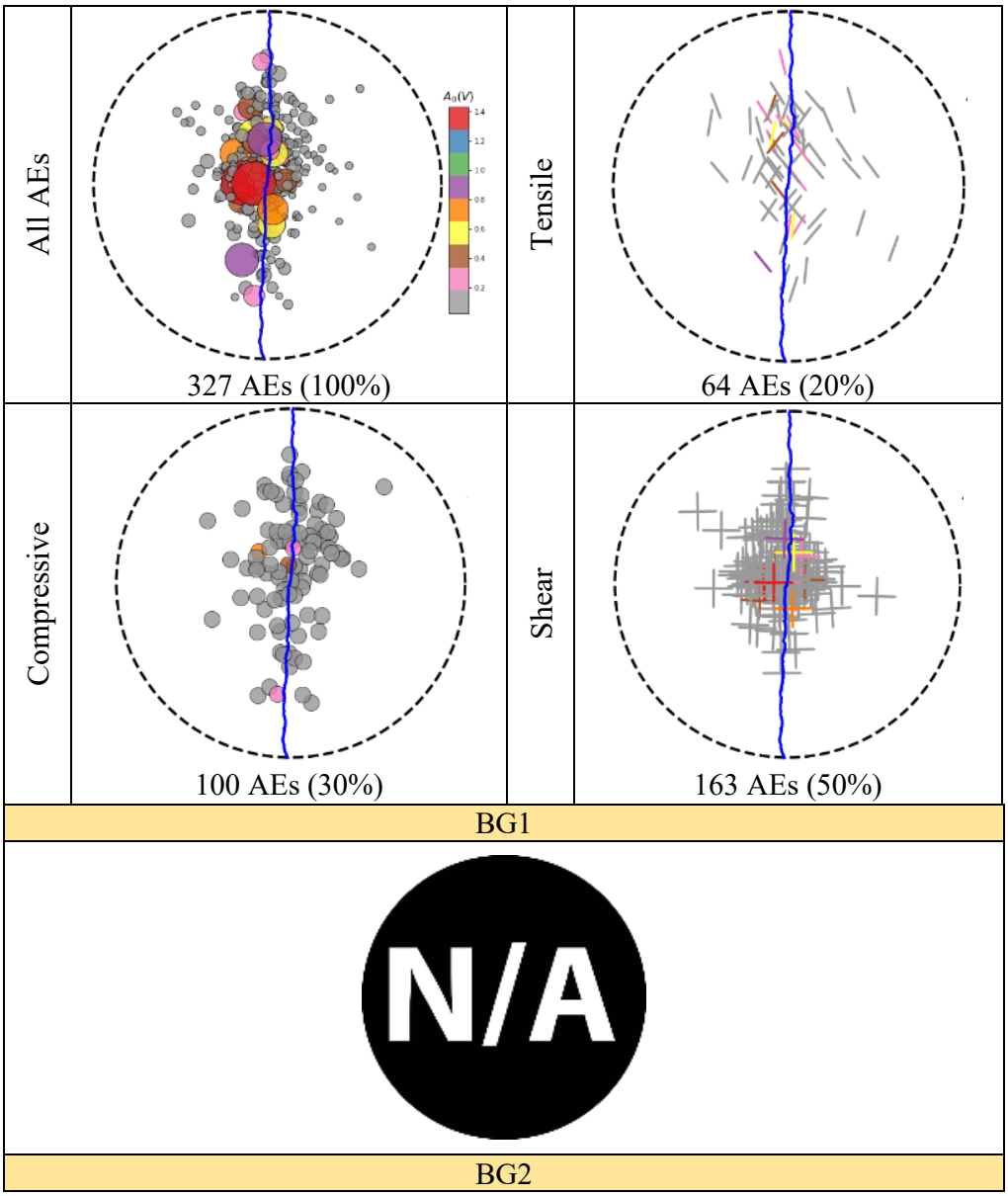

Fig.A3. 18. Spatial distribution of AE events at failure load detected by a minimum of 6 sensors decomposed into different focal mechanisms for BG specimens. The color codes represent the average focal amplitude (A_0) of AEs. The upper left column indicates all detected AE events, while the other subplots show the distribution of tensile, compressive, and shear AE sources. The percentages in brackets represent the ratio of the specified AE mechanisms to the total AEs detected for the given specimen.

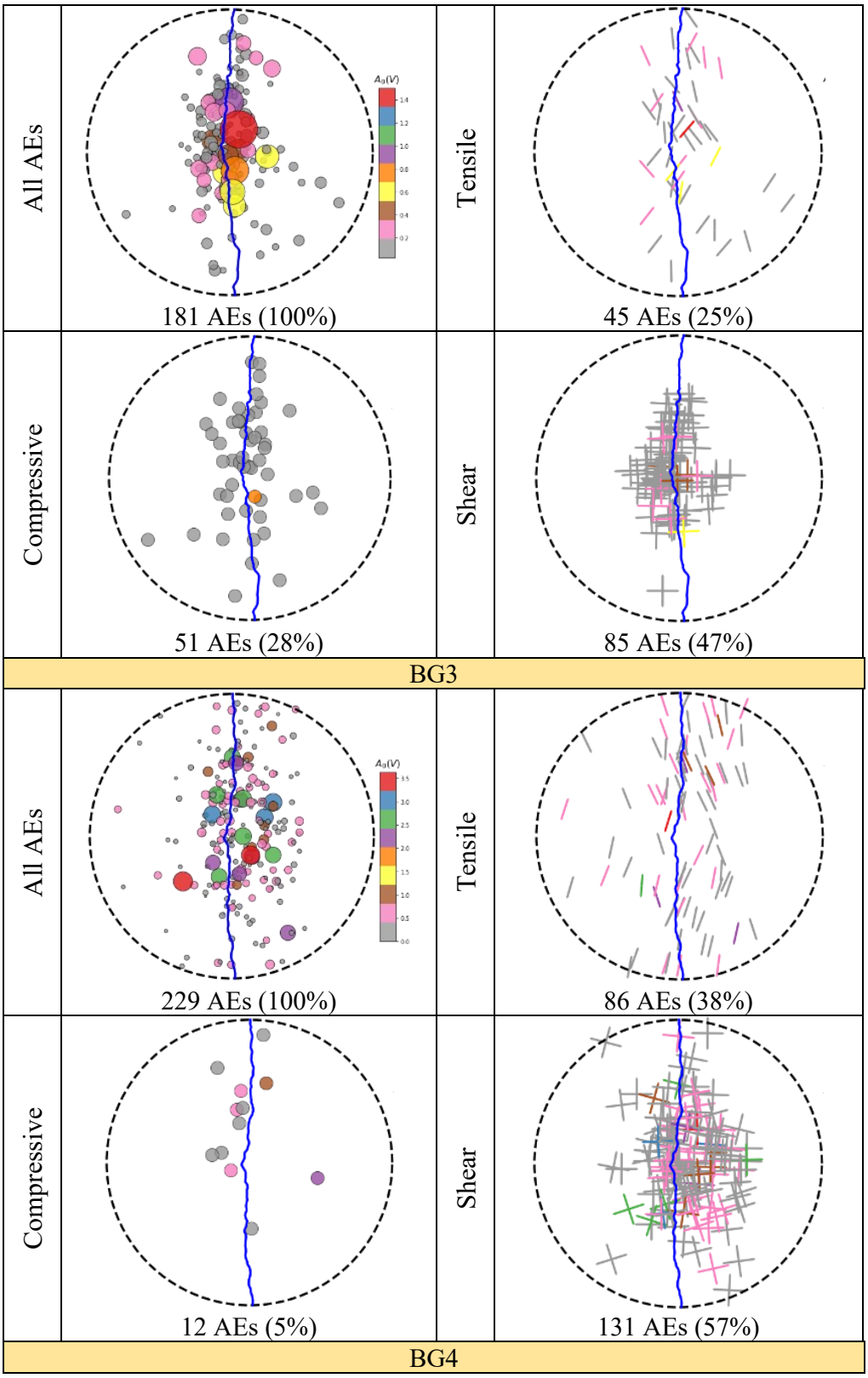

Fig.A3. 18. Continue …

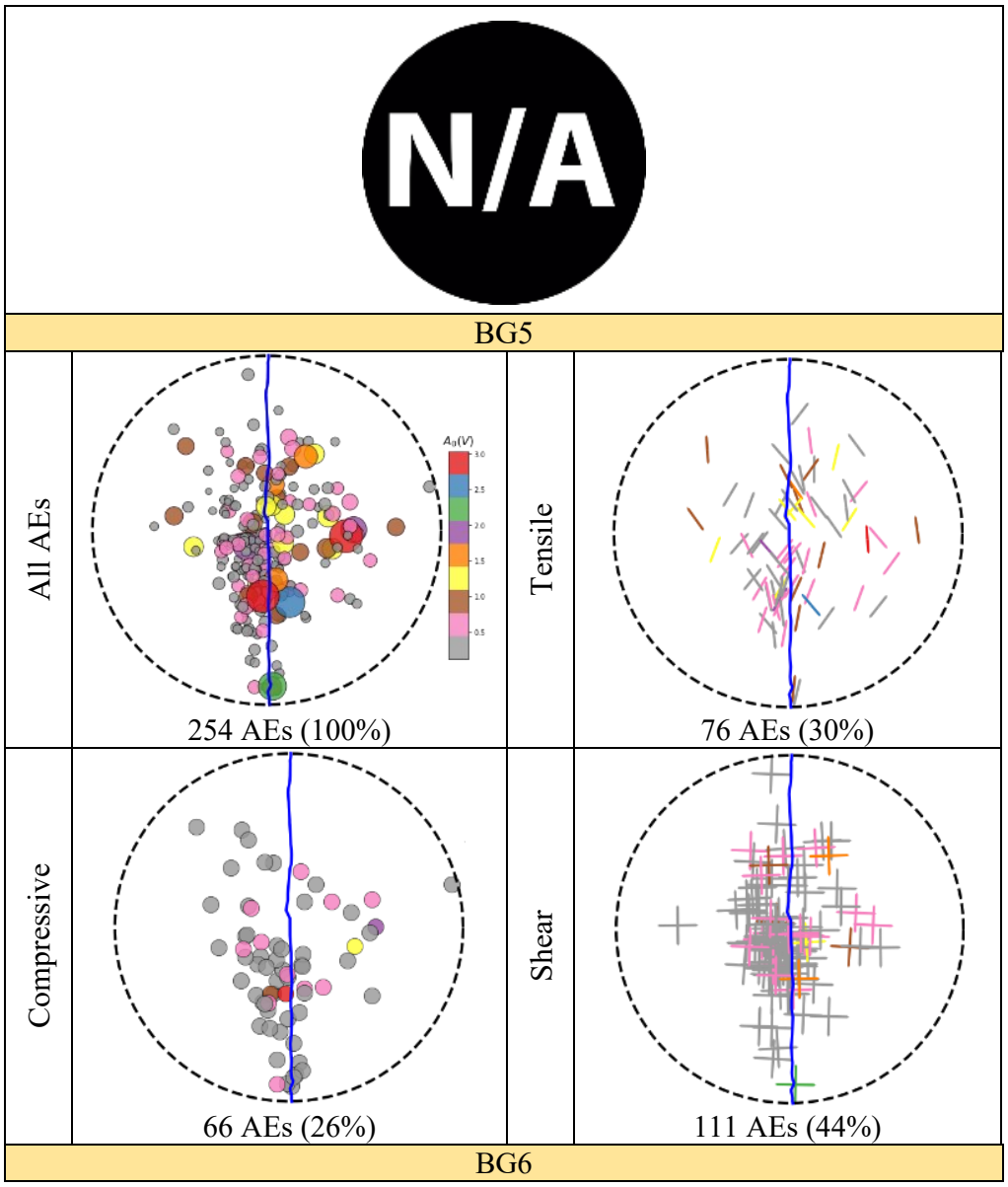

Fig.A3. 18. Continue …

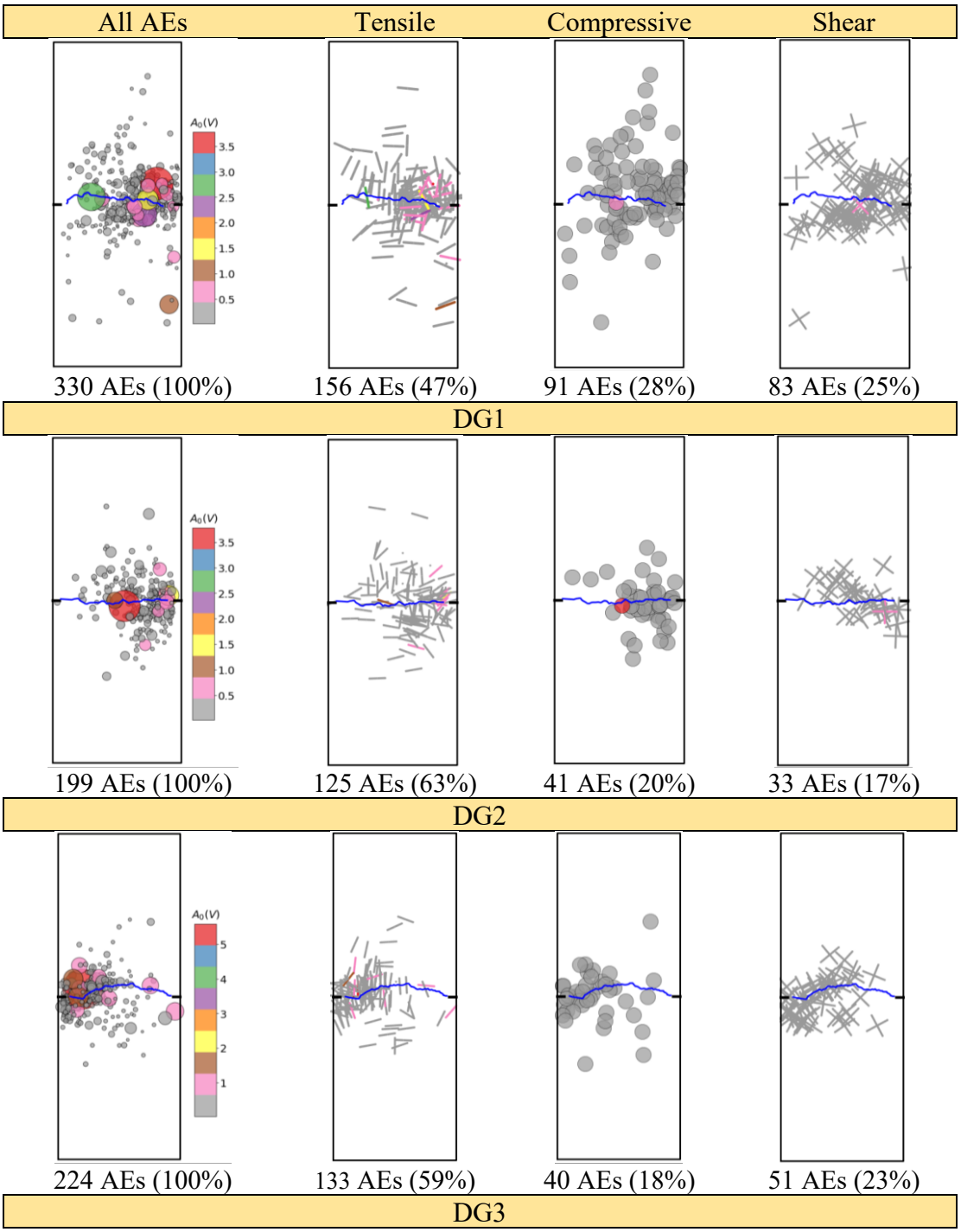

Fig.A3. 19. Spatial distribution of AE events at failure load detected by a minimum of 6 sensors decomposed into different focal mechanisms for DG specimens. The color codes represent the average focal amplitude (A_0) of AEs. The leftmost column indicates all detected AE events, while the other three columns show the distribution of tensile, compressive, and shear AE sources. The percentages in brackets represent the ratio of the specified AE mechanisms to the total AEs detected for the given specimen.

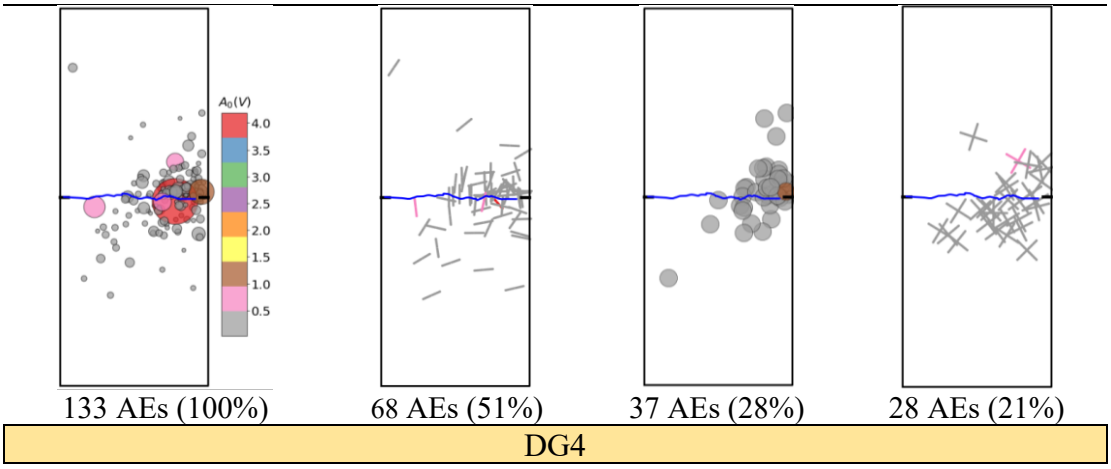

Fig.A3. 19. Continue …

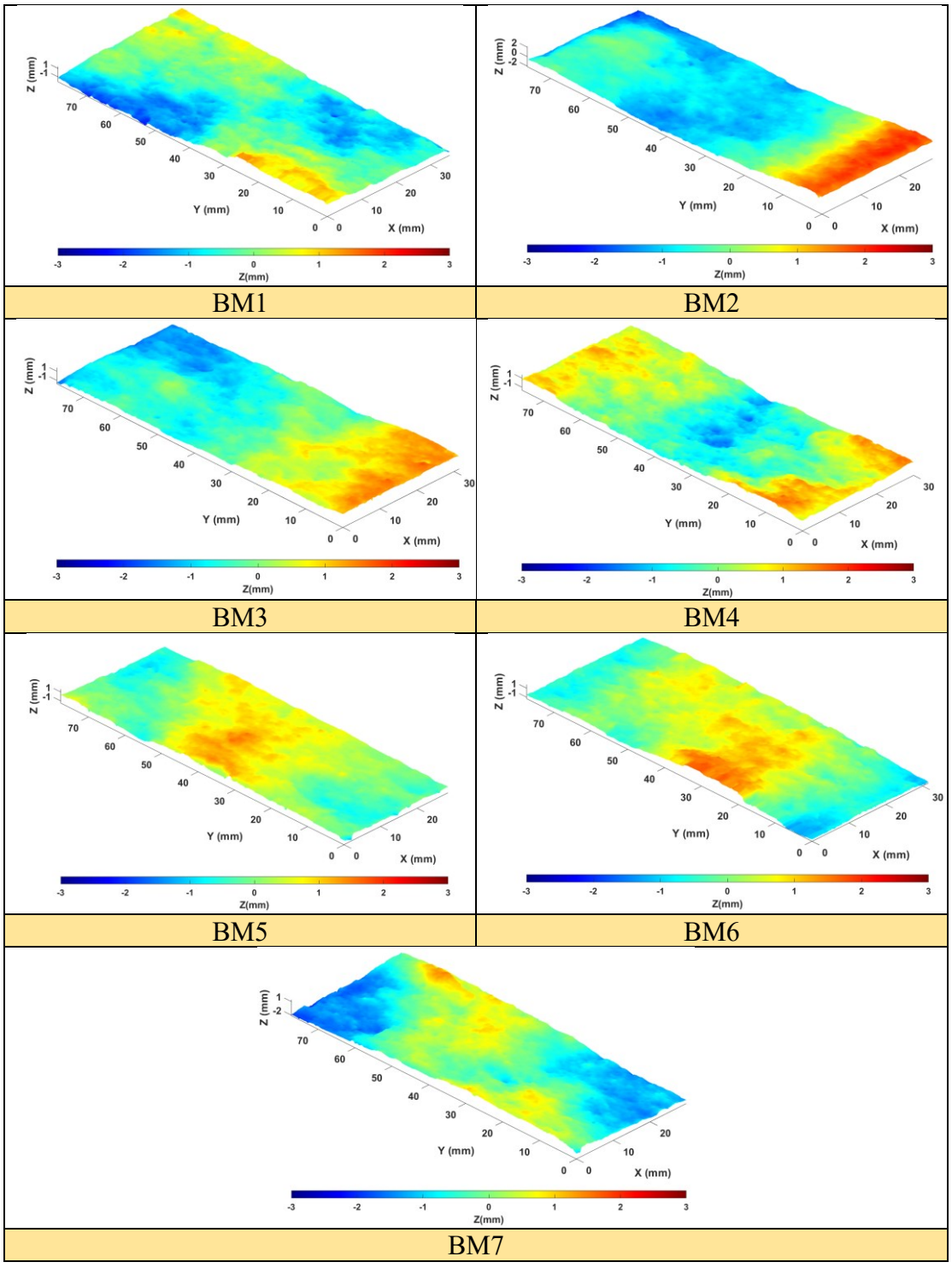

Fig.A3. 20. Surface roughness geometry of the created macroscopic fractured after specimen failure for BM specimens (BM1 to BM7).

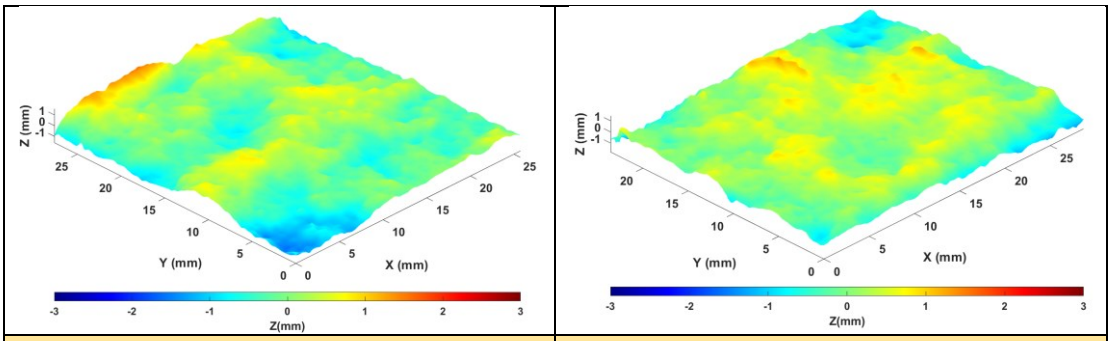

DM1

DM2

N/A

DM3

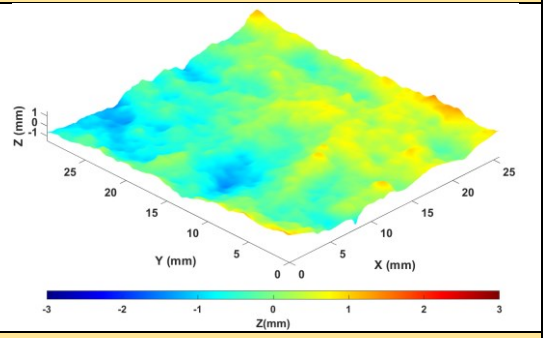

DM4

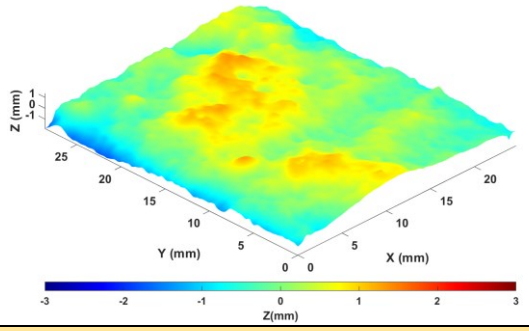

DM5

Fig.A3. 21. Surface roughness geometry of the created macroscopic fractured after specimen failure for DM specimens (DM1 to DM5).

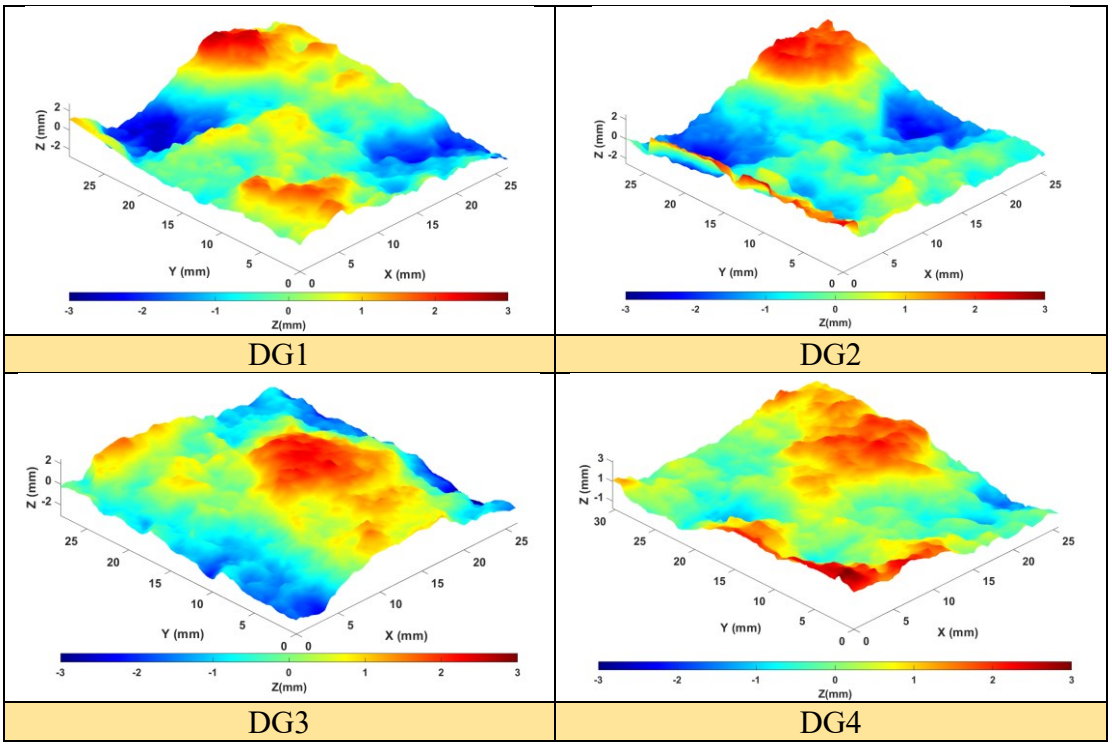

Fig.A3. 22. Surface roughness geometry of the created macroscopic fractured after specimen failure for DG specimens (DG1 to DG4).

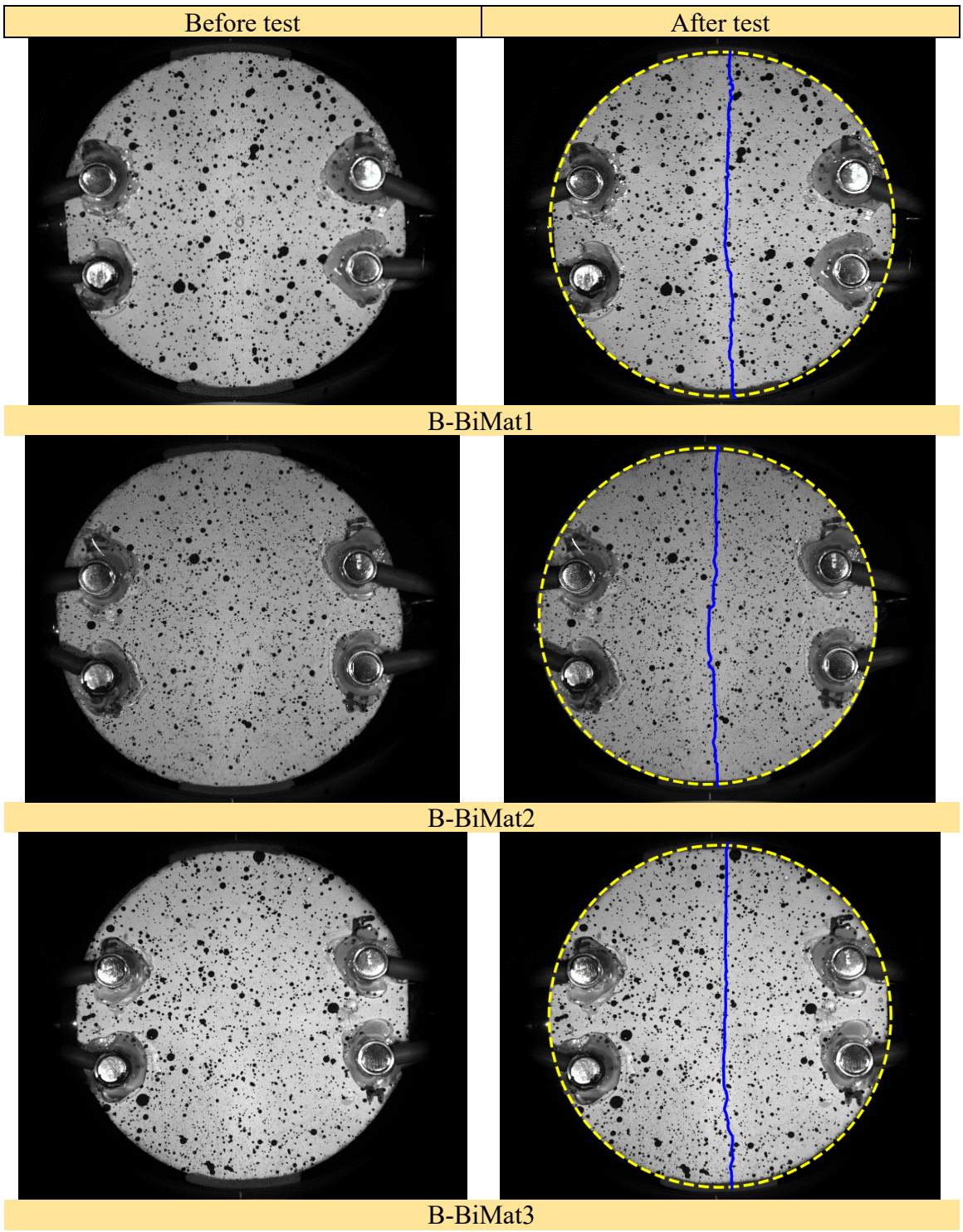

Fig.A3. 23. Macroscopic failure pattern of B-BiMat specimens subjected to Brazilian test. The blue lines represent the macro fracture path at the failure.

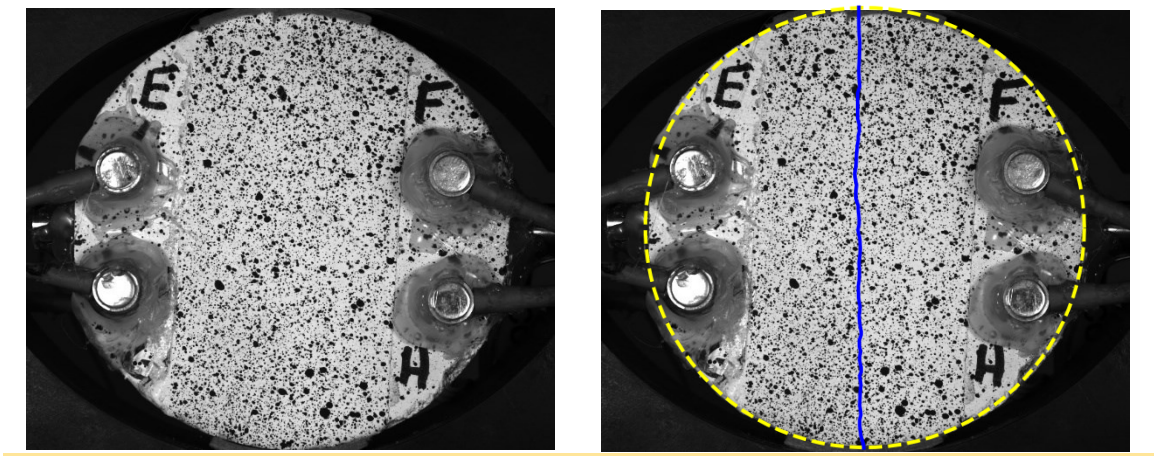

B-BiMat4

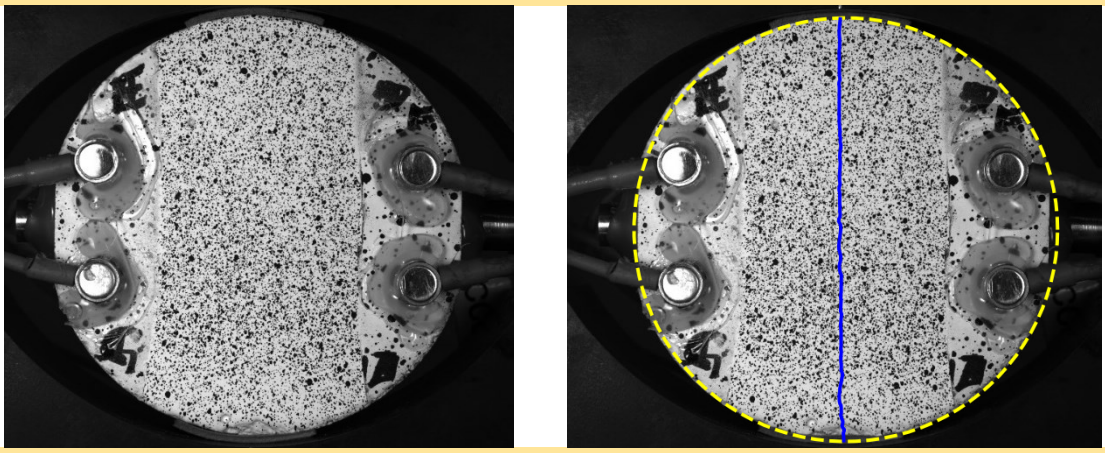

B-BiMat5

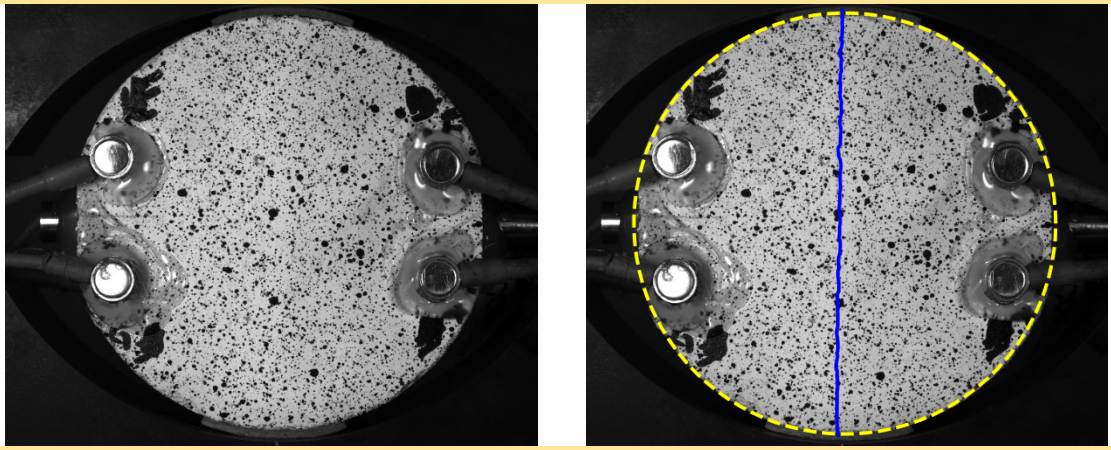

B-BiMat6

Fig.A3. 23. Continue …

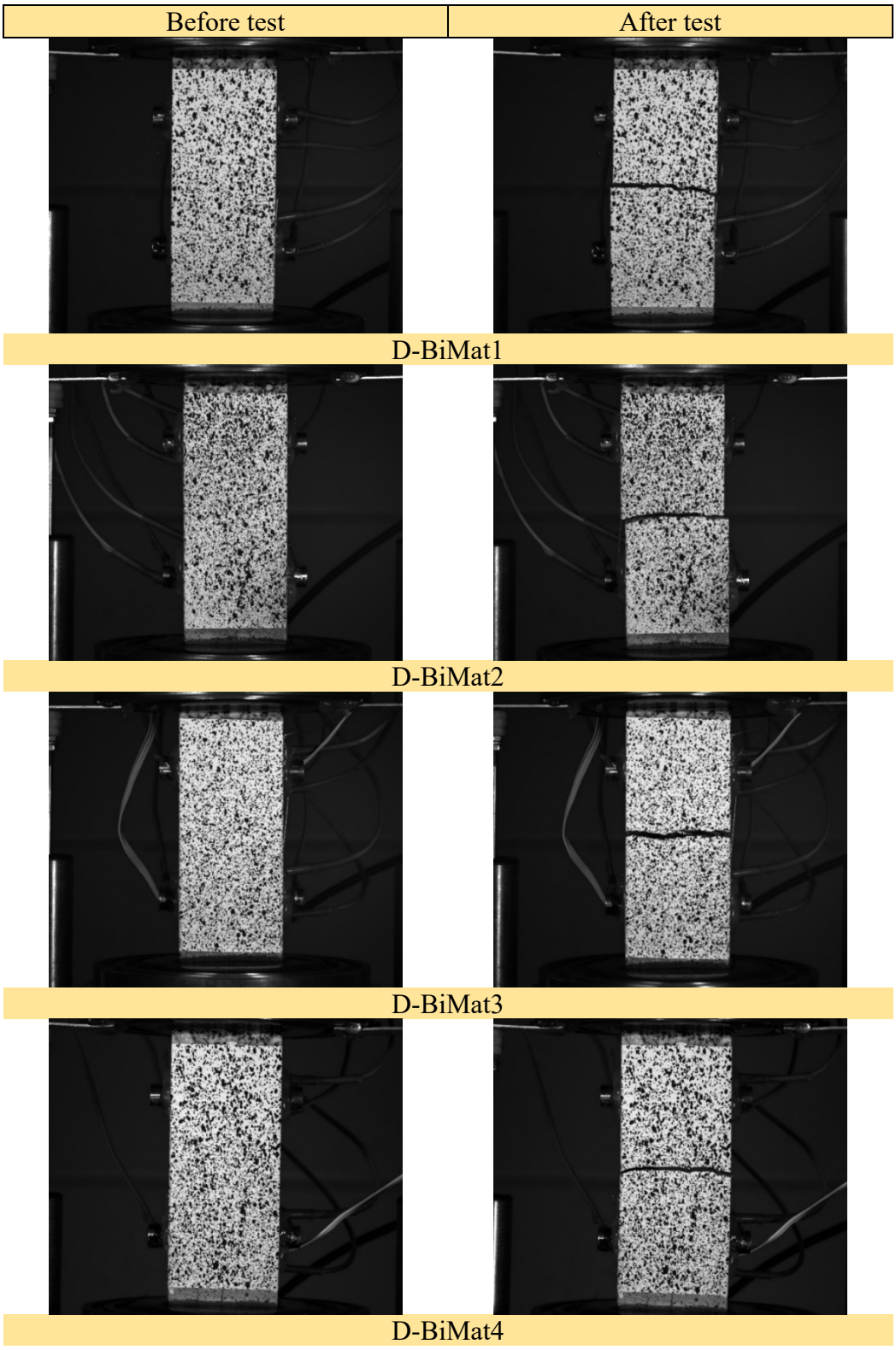

Fig.A3. 24. Macroscopic failure pattern of D-BiMat specimens subjected to direct tensile test.

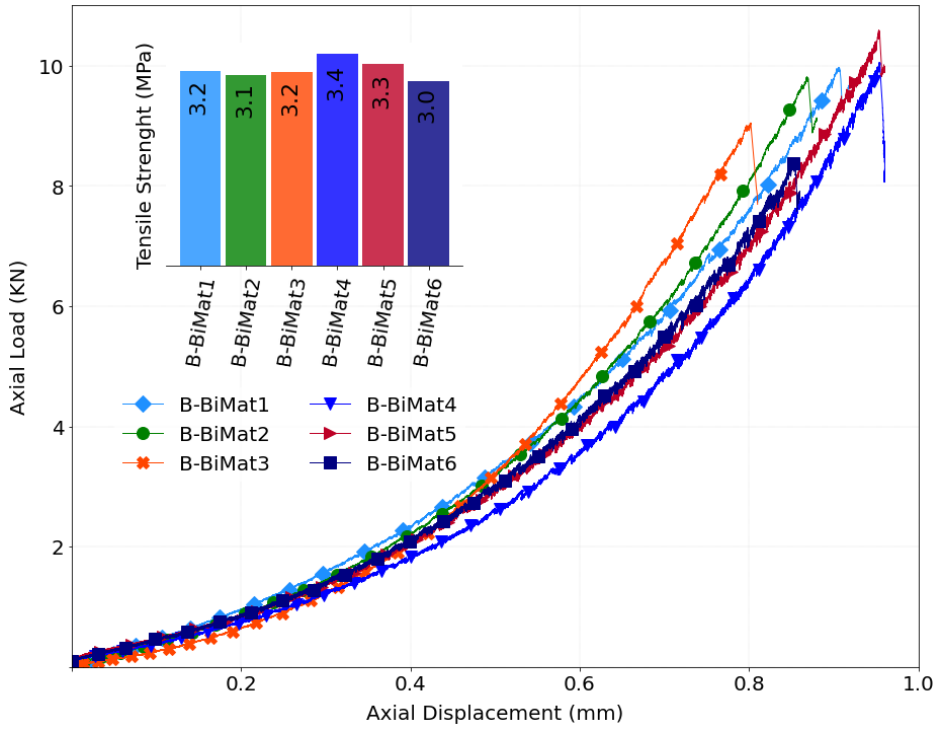

Fig.A3. 25. Load-displacement curves for B-BiMat specimens. The inset shows the tensile strength of specimens.

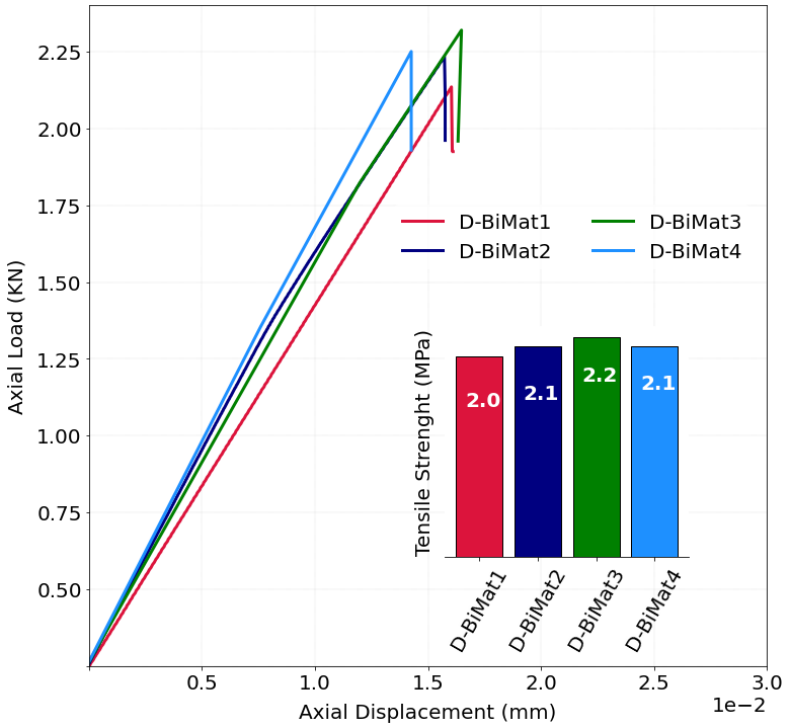

Fig.A3. 26. Load-displacement curves for D-BiMat specimens. The inset shows the tensile strength of specimens.

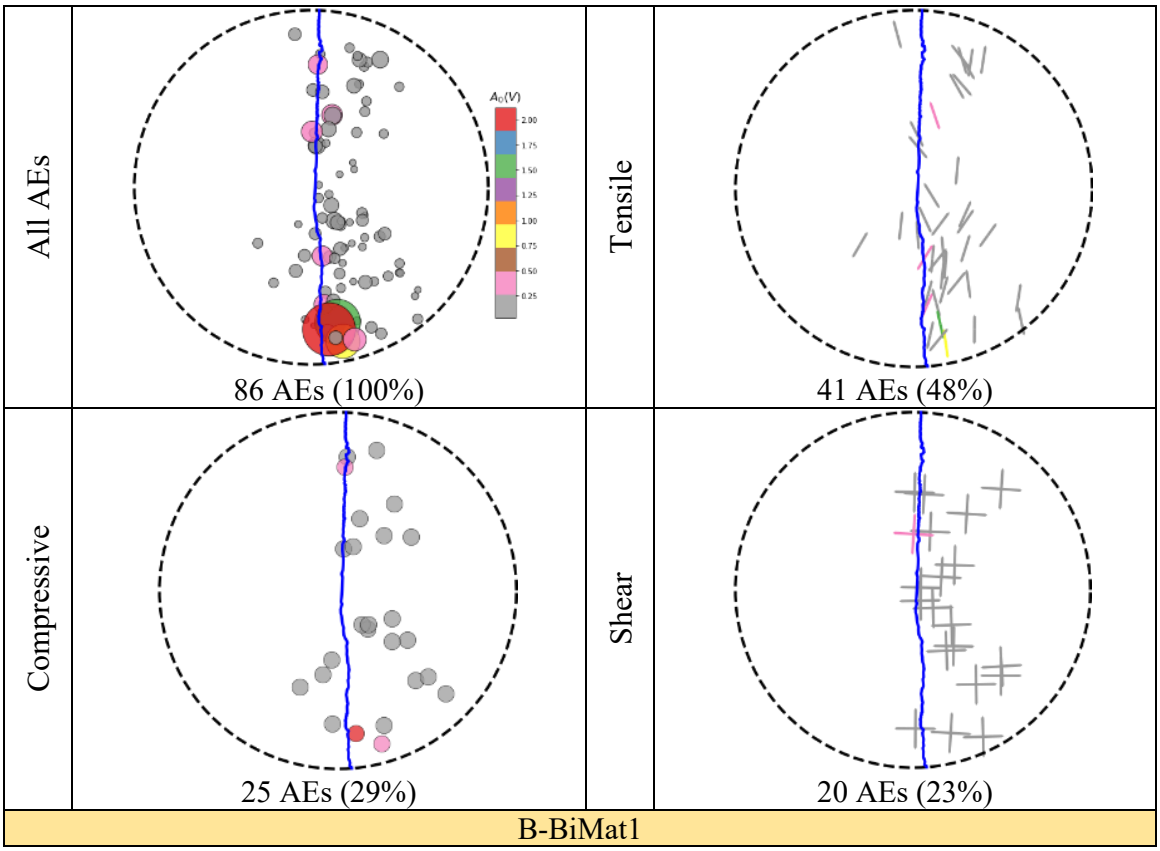

Fig.A3. 27. Spatial distribution of AE events at failure load detected by a minimum of 6 sensors decomposed into different focal mechanisms for B-BiMat specimens. The color codes represent the average focal amplitude (A_0) of AEs. The upper left column indicates all detected AE events, while the other subplots show the distribution of tensile, compressive, and shear AE sources. The percentages in brackets represent the ratio of the specified AE mechanisms to the total AEs detected for the given specimen.

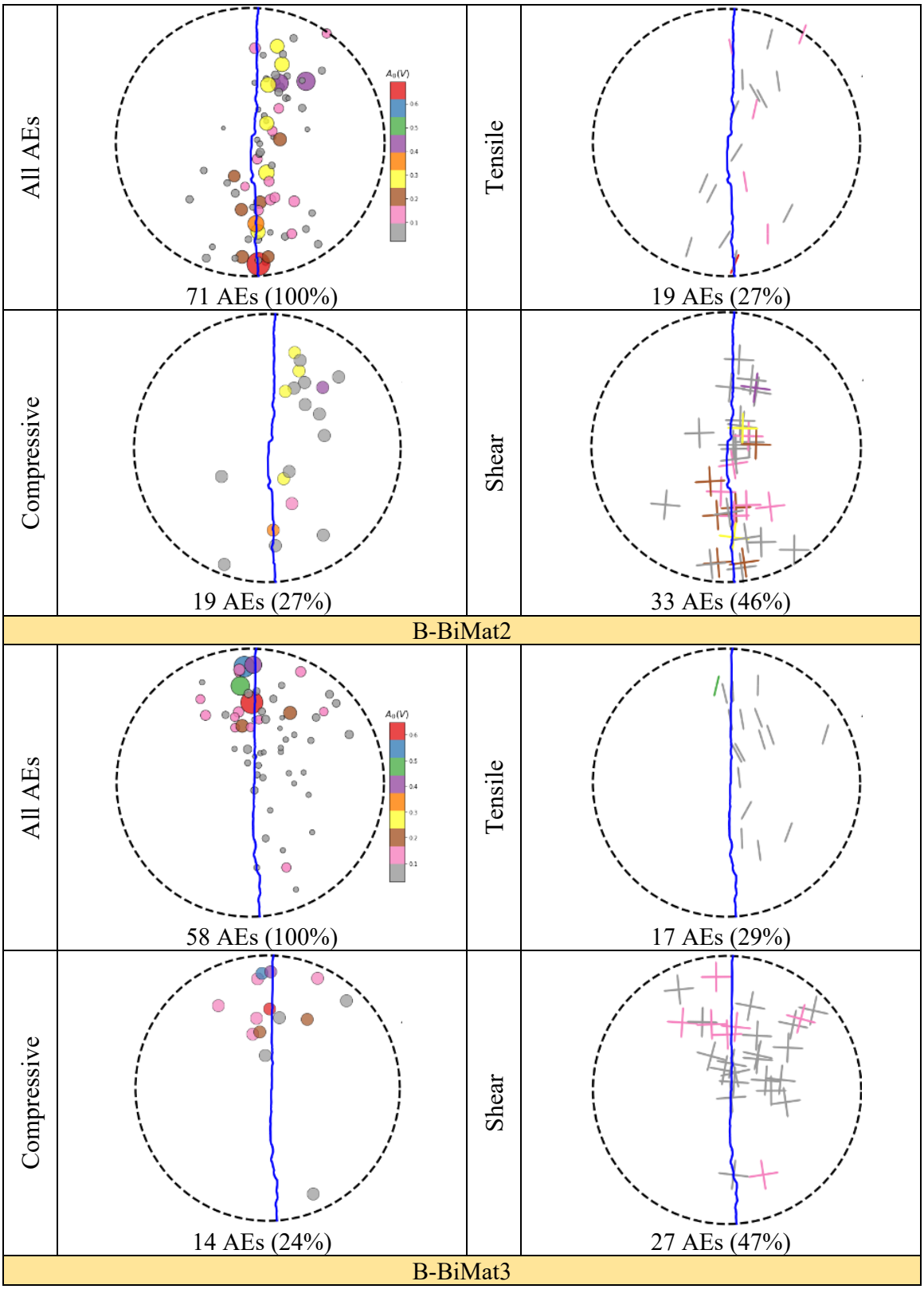

Fig.A3. 27. Continue …

B-BiMat4			
All AEs	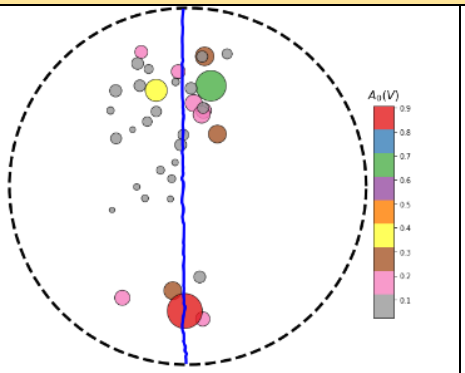 37 AEs (100%)	Tensile	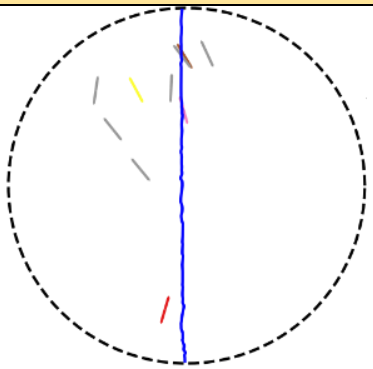 10 AEs (27%)
Compressive	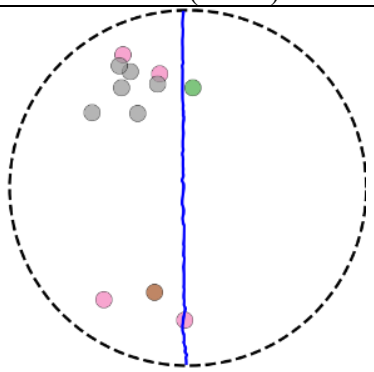 12 AEs (32%)	Shear	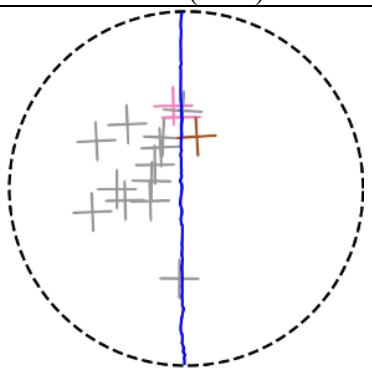 15 AEs (41%)
B-BiMat5			
All AEs	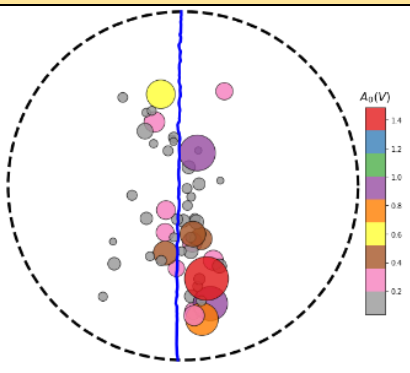 53 AEs (100%)	Tensile	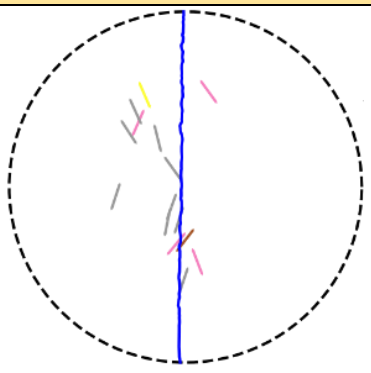 15 AEs (28%)

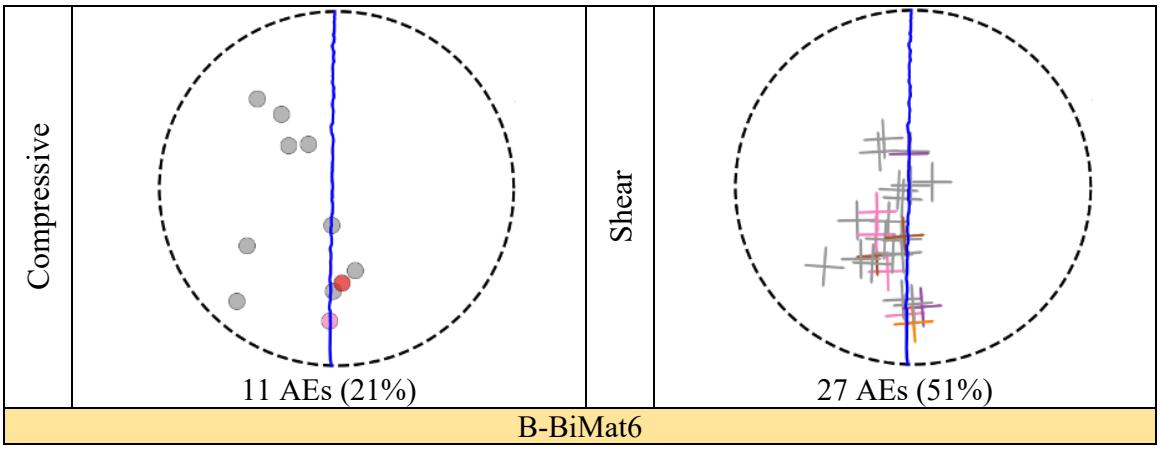

Fig.A3. 27. Continue …

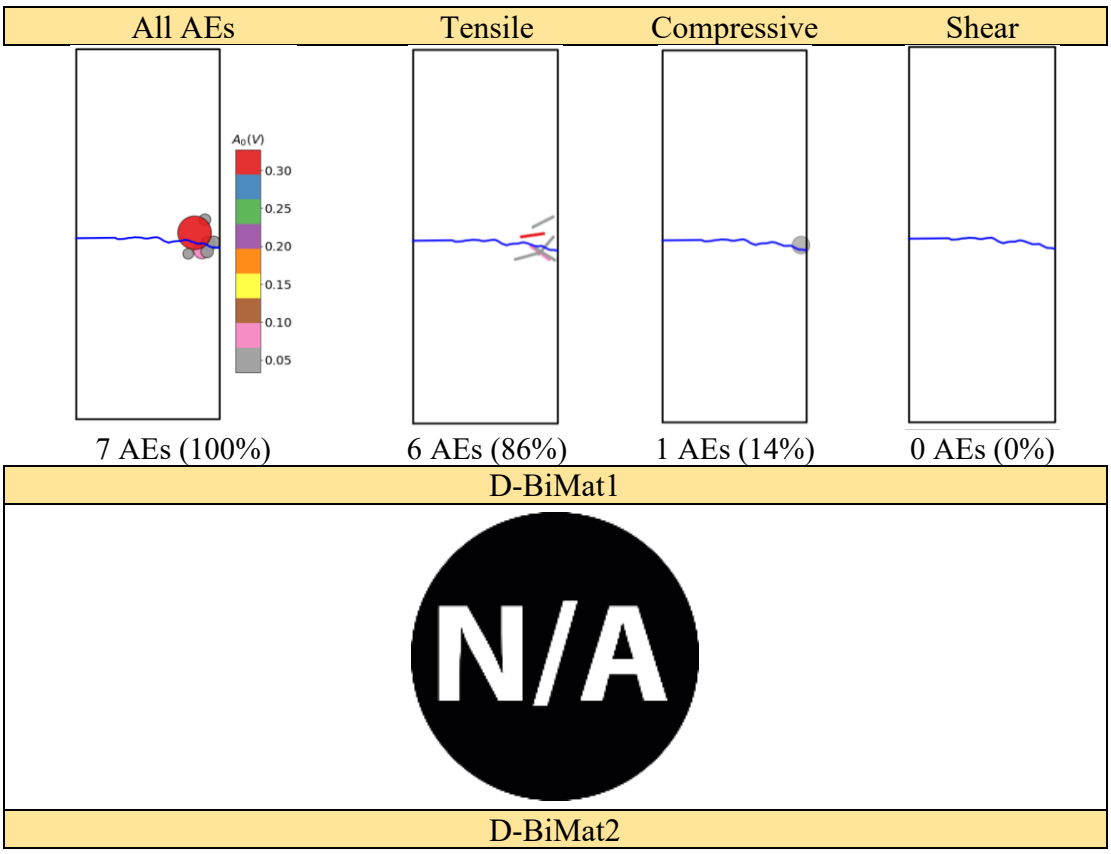

Fig.A3. 28. Spatial distribution of AE events at failure load detected by a minimum of 6 sensors decomposed into different focal mechanisms for D-BiMat specimens. The color codes represent the average focal amplitude (A_0) of AEs. The leftmost column indicates all detected AE events, while the other three columns show the distribution of tensile, compressive, and shear AE sources. The percentages in brackets represent the ratio of the specified AE mechanisms to the total AEs detected for the given specimen.

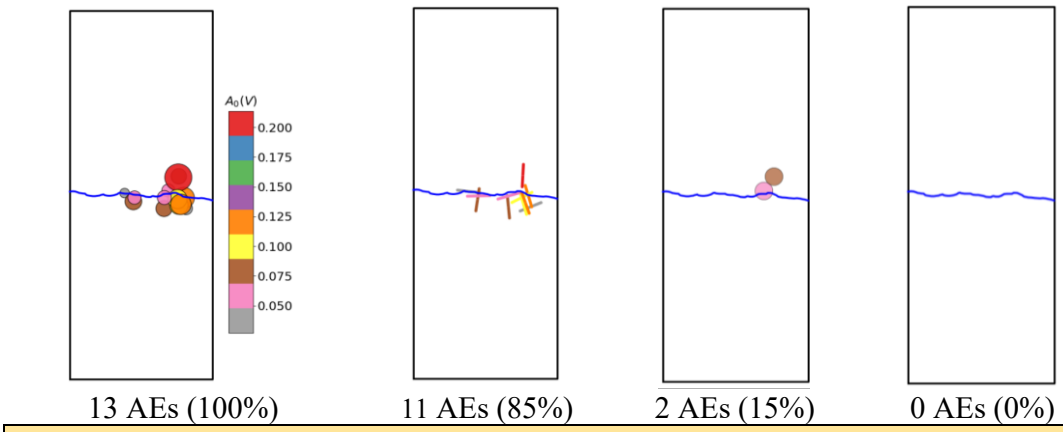

Fig.A3. 28. Continue …

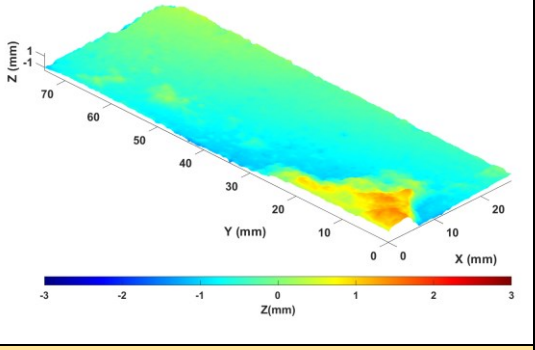

B-BiMat1

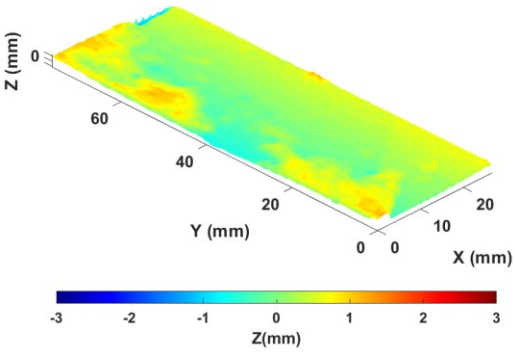

B-BiMat2

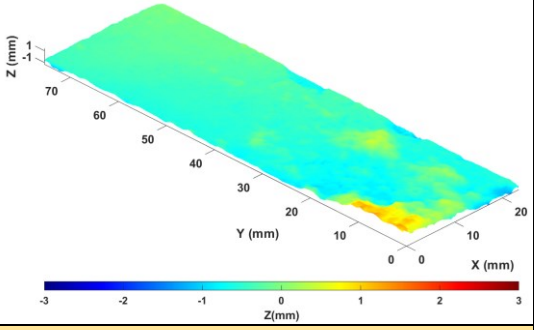

B-BiMat3

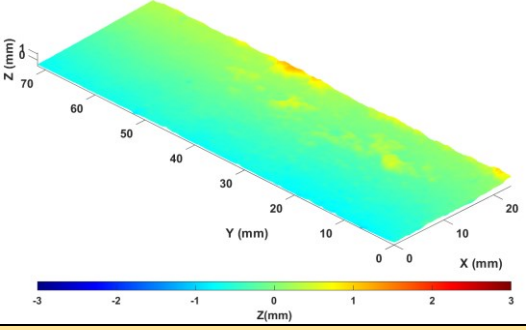

B-BiMat4

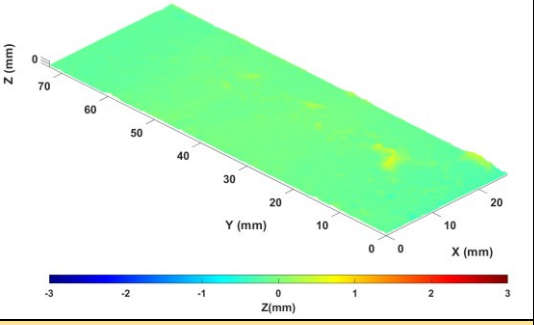

B-BiMat5

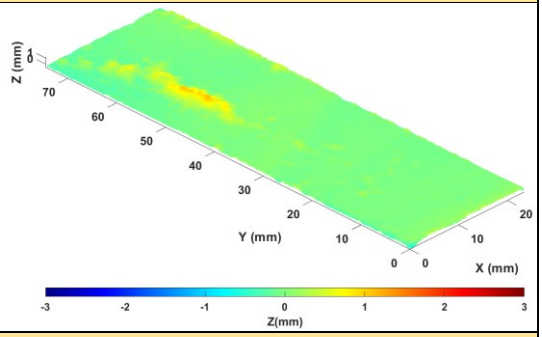

B-BiMat6

Fig.A3. 29. Surface roughness geometry of the created macroscopic fractured after specimen failure for B-BiMat specimens (B-BiMat1 to B-BiMat6).

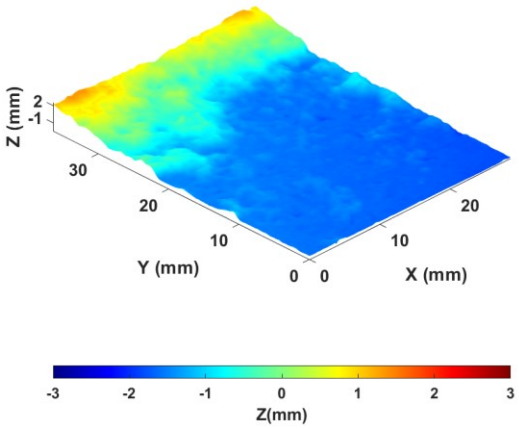

D-BiMat1

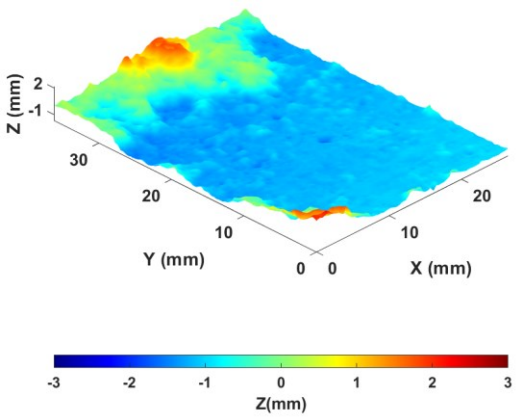

D-BiMat2

N/A

D-BiMat3

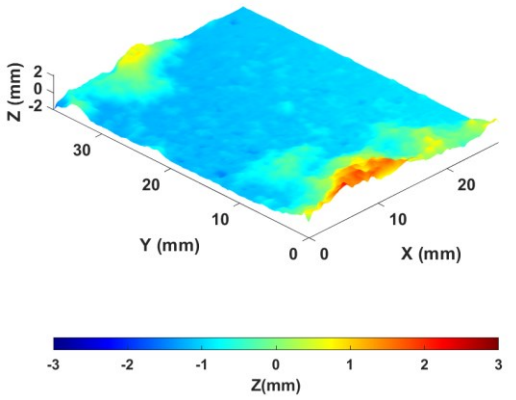

D-BiMat4

Fig.A3. 30. Surface roughness geometry of the created macroscopic fracture after specimen failure for D-BiMat specimens (D-BiMat1 to D-BiMat4).

REFERENCES

[1] R. L. Kranz, "Microcracks in rocks: A review," *Tectonophysics*, vol. 100, no. 1–3, pp. 449–480, 1983, doi: 10.1016/0040-1951(83)90198-1.

[2] E. Hoek and C. D. Martin, "Fracture initiation and propagation in intact rock - A review," *J. Rock Mech. Geotech. Eng.*, vol. 6, no. 4, pp. 287–300, 2014, doi: 10.1016/j.jrmge.2014.06.001.

[3] W. F. Brace, B. W. Paulding, and C. Scholz, "Dilatancy in the fracture of crystalline rocks," *J. Geophys. Res.*, vol. 71, no. 16, pp. 3939–3953, 1966, doi: 10.1029/jz071i016p03939.

[4] Z. T. Bieniawski, "Mechanism of brittle fracture of rock: Part I—theory of the fracture process," *Int. J. Rock Mech. Min. Sci. Geomech. Abstr.*, vol. 4, no. 4, pp. 395–406, 1967, doi: https://doi.org/10.1016/0148-9062(67)90030-7.

[5] C. D. Martin and N. A. Chandler, "The progressive fracture of Lac du Bonnet granite," *Int. J. Rock Mech. Min. Sci.*, vol. 31, no. 6, pp. 643–659, 1994, doi: 10.1016/0148-9062(94)90005-1.

[6] P. Tapponnier and W. F. Brace, "Development of Stress-Induced Microcracks in Westerly Granite," *Int. J. Rock Mech. Min. Sci. Geomech. Abstr*, vol. 13, pp. 103–112, 1976.

[7] L. N. Y. Wong and H. H. Einstein, "Crack coalescence in molded gypsum and carrara marble: Part 1. macroscopic observations and interpretation," *Rock Mech. Rock Eng.*, vol. 42, no. 3, pp. 475–511, 2009, doi: 10.1007/s00603-008-0002-4.

[8] S. Q. Yang, D. S. Yang, H. W. Jing, Y. H. Li, and S. Y. Wang, "An experimental study of the fracture coalescence behaviour of brittle sandstone specimens containing three fissures," *Rock Mech. Rock Eng.*, vol. 45, no. 4, pp. 563–582, 2012, doi: 10.1007/s00603-011-0206-x.

[9] X. P. Zhou, J. Bi, and Q. H. Qian, "Numerical Simulation of Crack Growth and Coalescence in Rock-Like Materials Containing Multiple Pre-existing Flaws," *Rock Mech. Rock Eng.*, vol. 48, no. 3, pp. 1097–1114, 2015, doi: 10.1007/s00603-014-0627-4.

[10] J. Liu *et al.*, "Characterizing the mechanical tensile behavior of Beishan granite with different experimental methods," *Int. J. Rock Mech. Min. Sci.*, vol. 69, pp. 50–58, 2014, doi: 10.1016/j.ijrmms.2014.03.007.

[11] M. Nicco, E. A. Holley, P. Hartlieb, R. Kaunda, and P. P. Nelson, "Methods for Characterizing Cracks Induced in Rock," *Rock Mech. Rock Eng.*, vol. 51, no. 7, pp. 2075–2093, 2018, doi: 10.1007/s00603-018-1445-x.

[12] B. M. Gonçalves da Silva, "Fracturing processes and induced seismicity due to the

hydraulic fracturing of rocks," Doctoral dissertation, Massachusetts Institute of Technology, 2016.

[13] W. Dong, Z. Wu, X. Zhou, N. Wang, and G. Kastiukas, "An experimental study on crack propagation at rock-concrete interface using digital image correlation technique," *Eng. Fract. Mech.*, vol. 171, pp. 50–63, 2017, doi: 10.1016/j.engfracmech.2016.12.003.

[14] S. Muralidhara, B. K. R. Prasad, H. Eskandari, and B. L. Karihaloo, "Fracture process zone size and true fracture energy of concrete using acoustic emission," *Constr. Build. Mater.*, vol. 24, no. 4, pp. 479–486, 2010, doi: https://doi.org/10.1016/j.conbuildmat.2009.10.014.

[15] W. R. Wawersik and C. H. Fairhurst, "A study of brittle rock fracture in laboratory compression experiments," in *International Journal of Rock Mechanics and Mining Sciences & Geomechanics Abstracts*, 1970, vol. 7, no. 5, pp. 561–575.

[16] H. Zhang, C. P. Lu, B. Liu, Y. Liu, N. Zhang, and H. Y. Wang, "Numerical investigation on crack development and energy evolution of stressed coal-rock combination," *Int. J. Rock Mech. Min. Sci.*, vol. 133, no. June, p. 104417, 2020, doi: 10.1016/j.ijrmms.2020.104417.

[17] L. Liu, H. Li, X. Li, D. Wu, and G. Zhang, "Underlying Mechanisms of Crack Initiation for Granitic Rocks Containing a Single Pre-existing Flaw: Insights From Digital Image Correlation (DIC) Analysis," *Rock Mech. Rock Eng.*, vol. 54, no. 2, pp. 857–873, Feb. 2021, doi: 10.1007/s00603-020-02286-x.

[18] B. Bahrami, M. Nejati, M. R. Ayatollahi, and T. Driesner, "Theory and experiment on true mode II fracturing of rocks," *Eng. Fract. Mech.*, vol. 240, no. June, 2020, doi: 10.1016/j.engfracmech.2020.107314.

[19] W. Sun and S. Wu, "A study of crack initiation and source mechanism in the Brazilian test based on moment tensor," *Eng. Fract. Mech.*, vol. 246, no. January, p. 107622, 2021, doi: 10.1016/j.engfracmech.2021.107622.

[20] C. He, J. Yang, and Q. Yu, "Laboratory study on the dynamic response of rock under blast loading with active confining pressure," *Int. J. Rock Mech. Min. Sci.*, vol. 102, no. 5, pp. 101–108, 2018, doi: 10.1016/j.ijrmms.2018.01.011.

[21] T. Backers, "Fracture Toughness Determination and Micromechanics of Rock Under Mode I and Mode II Loading," no. August, 2004.

[22] M. A. Perras and M. S. Diederichs, "A Review of the Tensile Strength of Rock: Concepts and Testing," *Geotech. Geol. Eng.*, vol. 32, no. 2, pp. 525–546, 2014, doi: 10.1007/s10706-014-9732-0.

[23] L. R. Myer, J. M. Kemeny, Z. Zheng, R. Suarez, R. T. Ewy, and N. G. W. Cook, "Extensile cracking in porous rock under differential compressive stress," 1992.

[24] A. Griffith, "The theory of rupture," in *First Int. Cong. Appl. Mech*, 1924, pp. 55–63.

[25] M. You, “Strength criterion for rocks under compressive-tensile stresses and its application,” *J. Rock Mech. Geotech. Eng.*, vol. 7, no. 4, pp. 434–439, Aug. 2015, doi: 10.1016/j.jrmge.2015.05.002.

[26] D. Q. Dan, H. Konietzky, and M. Herbst, “Brazilian tensile strength tests on some anisotropic rocks,” *Int. J. Rock Mech. Min. Sci.*, vol. 58, pp. 1–7, 2013, doi: 10.1016/j.ijrmms.2012.08.010.

[27] Y. S. Wang, J. H. Deng, L. R. Li, and Z. H. Zhang, “Micro-failure Analysis of Direct and Flat Loading Brazilian Tensile Tests,” *Rock Mech. Rock Eng.*, vol. 52, no. 11, pp. 4175–4187, 2019, doi: 10.1007/s00603-019-01877-7.

[28] M. S. Diederichs and P. K. Kaiser, “Tensile strength and abutment relaxation as failure control mechanisms in underground excavations,” *Int. J. Rock Mech. Min. Sci.*, vol. 36, no. 1, pp. 69–96, 1999, doi: 10.1016/S0148-9062(98)00179-X.

[29] R. Nova and A. Zaninetti, “An investigation into the tensile behaviour of a schistose rock,” *Int. J. Rock Mech. Min. Sci. Geomech. Abstr.*, vol. 27, no. 4, pp. 231–242, 1990, doi: https://doi.org/10.1016/0148-9062(90)90526-8.

[30] T. D. Le, R. Mitra, J. Oh, and B. Hebblewhite, “Study on caving mechanism in longwall top coal mining using discontinuous modelling,” in *ISRM International Symposium-EUROCK 2016*, 2016.

[31] T. Efe, S. Demirdag, K. Tufekci, N. Sengun, and R. Altindag, “Estimating the direct tensile strength of rocks from indirect tests,” *Arab. J. Geosci.*, vol. 14, no. 14, 2021, doi: 10.1007/s12517-021-07539-9.

[32] J. Claesson and B. Bohloli, “Brazilian test: Stress field and tensile strength of anisotropic rocks using an analytical solution,” *Int. J. Rock Mech. Min. Sci.*, vol. 39, no. 8, pp. 991–1004, 2002, doi: 10.1016/S1365-1609(02)00099-0.

[33] A. Coviello, R. Lagioia, and R. Nova, “On the measurement of the tensile strength of soft rocks,” *Rock Mech. Rock Eng.*, vol. 38, no. 4, pp. 251–273, 2005, doi: 10.1007/s00603-005-0054-7.

[34] S. Yagiz, “Utilizing rock mass properties for predicting TBM performance in hard rock condition,” *Tunn. Undergr. Sp. Technol.*, vol. 23, no. 3, pp. 326–339, 2008, doi: https://doi.org/10.1016/j.tust.2007.04.011.

[35] K. Sippakorn, “Direct tension testing of rock specimens.” School of Geotechnology Institute of Engineering Suranaree University of …, 2010.

[36] J. J. Zhang, “Chapter 3 - Rock strengths and rock failure criteria,” J. J. B. T.-A. P. G. Zhang, Ed. Gulf Professional Publishing, 2019, pp. 85–131.

[37] G. Q. Zhang and M. Chen, “Dynamic fracture propagation in hydraulic re-fracturing,” *J. Pet. Sci. Eng.*, vol. 70, no. 3–4, pp. 266–272, 2010.

[38] C.-L. Zhang, “Thermo-hydro-mechanical behavior of clay rock for deep geological disposal of high-level radioactive waste,” *J. Rock Mech. Geotech. Eng.*, vol. 10, no. 5, pp. 992–1008, 2018, doi: https://doi.org/10.1016/j.jrmge.2018.03.006.

[39] L. Zhuang and A. Zang, “Laboratory hydraulic fracturing experiments on crystalline rock for geothermal purposes,” *Earth-Science Rev.*, vol. 216, p. 103580, 2021.

[40] B. Q. Li, B. Gonçalves da Silva, and H. Einstein, “Laboratory hydraulic fracturing of granite: Acoustic emission observations and interpretation,” *Eng. Fract. Mech.*, vol. 209, pp. 200–220, Mar. 2019, doi: 10.1016/J.ENGFRACMECH.2019.01.034.

[41] B. Q. Li and H. H. Einstein, “Direct and Microseismic Observations of Hydraulic Fracturing in Barre Granite and Opalinus Clayshale,” *J. Geophys. Res. Solid Earth*, vol. 124, no. 11, pp. 11900–11916, Nov. 2019, doi: 10.1029/2019JB018376.

[42] T. Y. Guo and L. N. Y. Wong, “Microcracking behavior of three granites under mode I loading: Insights from acoustic emission,” *Eng. Geol.*, vol. 278, no. September, p. 105823, 2020, doi: 10.1016/j.enggeo.2020.105823.

[43] B. N. Whittaker, R. N. Singh, and G. Sun, “Rock fracture mechanics. Principles, design and applications,” 1992.

[44] H. H. Einstein, “Fractures: Tension and Shear,” *Rock Mech. Rock Eng.*, vol. 54, no. 7, pp. 3389–3408, 2021, doi: 10.1007/s00603-020-02243-8.

[45] S. Zafar, A. Hedayat, and O. Moradian, “Evolution of tensile and shear cracking in crystalline rocks under compression,” *Theor. Appl. Fract. Mech.*, vol. 118, no. November 2021, p. 103254, 2022, doi: 10.1016/j.tafmec.2022.103254.

[46] M. A. Lotidis, P. P. Nomikos, and A. I. Sofianos, “Laboratory Study of the Fracturing Process in Marble and Plaster Hollow Plates Subjected to Uniaxial Compression by Combined Acoustic Emission and Digital Image Correlation Techniques,” *Rock Mech. Rock Eng.*, vol. 53, no. 4, pp. 1953–1971, 2020, doi: 10.1007/s00603-019-02025-x.

[47] B. Q. Li, B. G. da Silva, and H. Einstein, “Laboratory hydraulic fracturing of granite: Acoustic emission observations and interpretation,” *Eng. Fract. Mech.*, vol. 209, pp. 200–220, 2019.

[48] A. Tarokh, R. Y. Makhnenko, A. Fakhimi, and J. F. Labuz, “Scaling of the fracture process zone in rock,” *Int. J. Fract.*, vol. 204, no. 2, pp. 191–204, 2017, doi: 10.1007/s10704-016-0172-0.

[49] C. Janssen, F. C. Wagner, A. Zang, and G. Dresen, “Fracture process zone in granite: A microstructural analysis,” *Int. J. Earth Sci.*, vol. 90, no. 1, pp. 46–59, 2001, doi: 10.1007/s005310000157.

[50] A. Zang, F. C. Wagner, S. Stanchits, C. Janssen, and G. Dresen, “Fracture process zone in granite,” *J. Geophys. Res. Solid Earth*, vol. 105, no. B10, pp. 23651–23661, Oct. 2000, doi: 10.1029/2000JB900239.

[51] Y. Niu, X. P. Zhou, and F. Berto, “Evaluation of fracture mode classification in flawed red sandstone under uniaxial compression,” *Theor. Appl. Fract. Mech.*, vol. 107, p. 102528, Jun. 2020, doi: 10.1016/J.TAFMEC.2020.102528.

[52] R. Lei, Z. Zhang, F. Berto, P. G. Ranjith, and L. Liu, “Cracking process and acoustic

emission characteristics of sandstone with two parallel filled-flaws under biaxial compression," *Eng. Fract. Mech.*, vol. 237, p. 107253, 2020, doi: https://doi.org/10.1016/j.engfracmech.2020.107253.

[53] L. N. Y. Wong and H. H. Einstein, "Crack coalescence in molded gypsum and carrara marble: Part 2 - Microscopic observations and interpretation," *Rock Mech. Rock Eng.*, vol. 42, no. 3, pp. 513–545, 2009, doi: 10.1007/s00603-008-0003-3.

[54] Y. Zhao, J. Huang, and R. Wang, "Real-time SEM observations of the microfracturing process in rock during a compression test," *Int. J. Rock Mech. Min. Sci.*, vol. 30, no. 6, pp. 643–652, 1993, doi: 10.1016/0148-9062(93)91224-7.

[55] E. Eberhardt, D. Stead, B. Stimpson, and R. S. Read, "Changes in acoustic event properties with progressive fracture damage," *Int. J. Rock Mech. Min. Sci.*, vol. 34, no. 3–4, pp. 71-e1, 1997, doi: 10.1016/s0148-9062(97)00284-2.

[56] P. F. Yin and S. Q. Yang, "Experimental investigation of the strength and failure behavior of layered sandstone under uniaxial compression and Brazilian testing," *Acta Geophys.*, vol. 66, no. 4, pp. 585–605, 2018, doi: 10.1007/s11600-018-0152-z.

[57] H. Munoz, A. Taheri, and E. K. Chanda, "Pre-Peak and Post-Peak Rock Strain Characteristics During Uniaxial Compression by 3D Digital Image Correlation," *Rock Mech. Rock Eng.*, vol. 49, no. 7, pp. 2541–2554, 2016, doi: 10.1007/s00603-016-0935-y.

[58] Z. A. Moradian, G. Ballivy, P. Rivard, C. Gravel, and B. Rousseau, "Evaluating damage during shear tests of rock joints using acoustic emissions," *Int. J. Rock Mech. Min. Sci.*, vol. 47, no. 4, pp. 590–598, 2010, doi: 10.1016/j.ijrmms.2010.01.004.

[59] K. Du, X. Li, M. Tao, and S. Wang, "Experimental study on acoustic emission (AE) characteristics and crack classification during rock fracture in several basic lab tests," *Int. J. Rock Mech. Min. Sci.*, vol. 133, no. August 2019, p. 104411, 2020, doi: 10.1016/j.ijrmms.2020.104411.

[60] Y. Nie, G. Zhang, J. Wen, S. Li, and D. Zhou, "Cyclic injection to reduce hydraulic fracture surface roughness in glutenite reservoirs," *Int. J. Rock Mech. Min. Sci.*, vol. 142, p. 104740, 2021.

[61] H. Alehossein and J. N. Boland, "Strength, toughness, damage and fatigue of rock," *Struct. Integr. Fract.*, 2004.

[62] P. P. Cacciari and M. M. Futai, "Assessing the tensile strength of rocks and geological discontinuities via pull-off tests," *Int. J. Rock Mech. Min. Sci.*, vol. 105, no. 380, pp. 44–52, 2018, doi: 10.1016/j.ijrmms.2018.03.011.

[63] M. Mellor and I. Hawkes, "Measurement of tensile strength by diametral compression of discs and annuli," *Eng. Geol.*, vol. 5, no. 3, pp. 173–225, 1971, doi: 10.1016/0013-7952(71)90001-9.

[64] S. Qi, H. Lan, D. Martin, and X. Huang, "Factors Controlling the Difference in Brazilian and Direct Tensile Strengths of the Lac du Bonnet Granite," *Rock Mech.*

Rock Eng., no. 0123456789, 2019, doi: 10.1007/s00603-019-01946-x.

[65] Y. V Ramana and L. P. Sarma, "Split-collar, tensile test grips for short rock cores," *Eng. Geol.*, vol. 23, no. 3–4, pp. 255–261, 1987.

[66] D. Li and L. N. Y. Wong, "The brazilian disc test for rock mechanics applications: Review and new insights," *Rock Mech. Rock Eng.*, vol. 46, no. 2, pp. 269–287, 2013, doi: 10.1007/s00603-012-0257-7.

[67] N. Erarslan and D. J. Williams, "Experimental, numerical and analytical studies on tensile strength of rocks," *Int. J. Rock Mech. Min. Sci.*, vol. 49, pp. 21–30, 2012, doi: 10.1016/j.ijrmms.2011.11.007.

[68] C. K. M. Jawalkar, "Interface cracks: fracture mechanics studies leading towards safety assessment of dams," University of Colorado at Boulder, 1996.

[69] Electric Power Research Institute (EPRI), "Uplift pressures, shear strengths and tensile strengths for stability analysis of concrete gravity dams," 1992.

[70] J. Zhu, W. Bao, Q. Peng, and X. Deng, "Influence of substrate properties and interfacial roughness on static and dynamic tensile behaviour of rock-shotcrete interface from macro and micro views," *Int. J. Rock Mech. Min. Sci.*, vol. 132, p. 104350, Aug. 2020, doi: 10.1016/j.ijrmms.2020.104350.

[71] X. Chang, J. Lu, S. Wang, and S. Wang, "Mechanical performances of rock-concrete bi-material disks under diametrical compression," *Int. J. Rock Mech. Min. Sci.*, vol. 104, no. November 2017, pp. 71–77, 2018, doi: 10.1016/j.ijrmms.2018.02.008.

[72] M. Son, "Adhesion strength at the shotcrete-rock contact in rock tunneling," *Rock Mech. Rock Eng.*, vol. 46, no. 5, pp. 1237–1246, 2013, doi: 10.1007/s00603-013-0380-0.

[73] S. V. L. Barrett and D. R. McCreath, "Shortcrete support design in blocky ground: Towards a deterministic approach," *Tunn. Undergr. Sp. Technol. Inc. Trenchless*, vol. 10, no. 1, pp. 79–89, Jan. 1995, doi: 10.1016/0886-7798(94)00067-U.

[74] M. Torsæter, J. Todorovic, and A. Lavrov, "Structure and debonding at cement-steel and cement-rock interfaces: Effect of geometry and materials," *Constr. Build. Mater.*, vol. 96, pp. 164–171, Aug. 2015, doi: 10.1016/j.conbuildmat.2015.08.005.

[75] A. M. Stroisz, K. Gawel, R. Bjørge, and P. R. Cerasi, "Tensile Strength of the Interface Between Cement and Shale Caprock and the Mechanism of Strength Development." OnePetro, 23-Jun-2019.

[76] L. Selçuk and D. Aşma, "Experimental investigation of the Rock–Concrete bi materials influence of inclined interface on strength and failure behavior," *Int. J. Rock Mech. Min. Sci.*, vol. 123, no. June, 2019, doi: 10.1016/j.ijrmms.2019.104119.

[77] D. Saiang, L. Malmgren, and E. Nordlund, "Laboratory tests on shotcrete-rock joints in direct shear, tension and compression," *Rock Mech. Rock Eng.*, vol. 38, no. 4, pp. 275–297, 2005, doi: 10.1007/s00603-005-0055-6.

[78] J. G. Gutiérrez-Ch, S. Senent, S. Melentijevic, and R. Jimenez, "Distinct element method simulations of rock-concrete interfaces under different boundary conditions," *Eng. Geol.*, vol. 240, no. November 2017, pp. 123–139, Jun. 2018, doi: 10.1016/j.enggeo.2018.04.017.

[79] V. Andjelkovic, N. Pavlovic, Z. Lazarevic, and V. Nedovic, "Modelling of shear characteristics at the concrete-rock mass interface," *Int. J. Rock Mech. Min. Sci.*, vol. 76, pp. 222–236, 2015, doi: 10.1016/j.ijrmms.2015.03.024.

[80] H. Mouzannar, M. Bost, M. Leroux, and D. Virely, "Experimental Study of the Shear Strength of Bonded Concrete–Rock Interfaces: Surface Morphology and Scale Effect," *Rock Mech. Rock Eng.*, vol. 50, no. 10, pp. 2601–2625, 2017, doi: 10.1007/s00603-017-1259-2.

[81] H. M. Tian, W. Z. Chen, D. S. Yang, and J. P. Yang, "Experimental and Numerical Analysis of the Shear Behaviour of Cemented Concrete–Rock Joints," *Rock Mech. Rock Eng.*, vol. 48, no. 1, pp. 213–222, 2014, doi: 10.1007/s00603-014-0560-6.

[82] J. K. Kodikara and I. W. Johnston, "Shear behaviour of irregular triangular rock-concrete joints," *Int. J. Rock Mech. Min. Sci.*, vol. 31, no. 4, pp. 313–322, 1994, doi: 10.1016/0148-9062(94)90900-8.

[83] L. Luo, X. Li, M. Tao, and L. Dong, "Mechanical behavior of rock-shotcrete interface under static and dynamic tensile loads," *Tunn. Undergr. Sp. Technol.*, vol. 65, pp. 215–224, 2017, doi: 10.1016/j.tust.2017.03.005.

[84] Z. Zhou, J. Lu, and X. Cai, "Static and dynamic tensile behavior of rock-concrete bi-material disc with different interface inclinations," *Constr. Build. Mater.*, vol. 256, p. 119424, 2020, doi: 10.1016/j.conbuildmat.2020.119424.

[85] H. Qiu, Z. Zhu, M. Wang, F. Wang, C. Luo, and D. Wan, "Study of the failure properties and tensile strength of rock-mortar interface transition zone using bi-material Brazilian discs," *Constr. Build. Mater.*, vol. 236, p. 117551, 2020, doi: 10.1016/j.conbuildmat.2019.117551.

[86] S. Bauret and P. Rivard, "Experimental assessment of the tensile bond strength of mortar-mortar interfaces: Effects of interface roughness and mortar strength," *Geotech. Test. J.*, vol. 41, no. 6, pp. 1139–1146, 2018, doi: 10.1520/GTJ20170173.

[87] M. Flansbjer and J. Magnusson, "Mechanical properties of rock-concrete interface," 2014.

[88] S.-J. Choi, K.-H. Yang, J.-I. Sim, and B.-J. Choi, "Direct tensile strength of lightweight concrete with different specimen depths and aggregate sizes," *Constr. Build. Mater.*, vol. 63, pp. 132–141, Jul. 2014, doi: 10.1016/J.CONBUILDMAT.2014.04.055.

[89] S. Swaddiwudhipong, H.-R. Lu, and T.-H. Wee, "Direct tension test and tensile strain capacity of concrete at early age," *Cem. Concr. Res.*, vol. 33, no. 12, pp. 2077–2084, Dec. 2003, doi: 10.1016/S0008-8846(03)00231-X.

[90] E. Hoek, "Fracture of anisotropic rock," *J. South African Inst. Min. Metall.*, vol. 64,

no. 10, pp. 501–523, 1964.

[91] J. Shang, S. R. Hencher, and L. J. West, “Tensile Strength of Geological Discontinuities Including Incipient Bedding, Rock Joints and Mineral Veins,” *Rock Mech. Rock Eng.*, vol. 49, no. 11, pp. 4213–4225, 2016, doi: 10.1007/s00603-016-1041-x.

[92] Z. T. Bieniawski and I. Hawkes, “Suggested Methods for Determining Tensile Strength of Rock Materials,” *Int. J. Rock Mech. Min. Sci.*, vol. 15, no. 3, pp. 99–103, 1978, doi: 10.1016/0148-9062(78)91494-8.

[93] B. P. Gorski, “Tensile testing apparatus.” Google Patents, 16-Mar-1993.

[94] J. Shang, “Persistence and tensile strength of incipient rock discontinuities,” 2016.

[95] Z. Briševac, T. Kujundžić, and S. Čajić, “Current Cognition of Rock Tensile Strength Testing By Brazilian Test,” *Rud. Geol. Naft. Zb.*, vol. 30, no. 2, pp. 101–114, 2015, doi: 10.17794/rgn.2015.2.2.

[96] C. S. Chen and S. C. Hsu, “Measurement of indirect tensile strength of anisotropic rocks by the ring test,” *Rock Mech. Rock Eng.*, vol. 34, no. 4, pp. 293–321, 2001, doi: 10.1007/s006030170003.

[97] E. Komurlu and A. Kesimal, “Evaluation of Indirect Tensile Strength of Rocks Using Different Types of Jaws,” *Rock Mech. Rock Eng.*, vol. 48, no. 4, pp. 1723–1730, 2015, doi: 10.1007/s00603-014-0644-3.

[98] F. Carneiro, “A new method to determine the tensile strength of concrete,” in *Proceedings of the 5th meeting of the Brazilian Association for Technical Rules*, 1943, vol. 3, no. 16, pp. 126–129.

[99] T. Akazawa, “New test method for evaluating internal stress due to compression of concrete (the splitting tension test)(part 1),” *J Jpn Soc Civ Eng*, vol. 29, pp. 777–787, 1943.

[100] S. C. C. Bandis, A. C. C. Lumsden, and N. R. R. Barton, “Fundamentals of rock joint deformation,” in *International Journal of Rock Mechanics and Mining Sciences & Geomechanics Abstracts*, 1983, vol. 20, no. 6, pp. 249–268, doi: 10.1016/0148-9062(83)90595-8.

[101] R. Berenbaum and I. Brodie, “Measurement of the tensile strength of brittle materials,” *Br. J. Appl. Phys.*, vol. 10, no. 6, pp. 281–287, 1959, doi: 10.1088/0508-3443/10/6/307.

[102] C. Rocco, G. V. Guinea, J. Planas, and M. Elices, “Experimental analysis of rupture mechanisms in the brazilian test,” *Fract. Mech. Concr. Struct.*, vol. 1, pp. 121–130, 1998.

[103] M. Mousavi Nezhad, Q. J. Fisher, E. Gironacci, and M. Rezania, “Experimental Study and Numerical Modeling of Fracture Propagation in Shale Rocks During Brazilian Disk Test,” *Rock Mech. Rock Eng.*, vol. 51, no. 6, pp. 1755–1775, 2018, doi: 10.1007/s00603-018-1429-x.

[104] C. Rocco, G. V. Guinea, J. Planas, and M. Elices, "Size effect and boundary conditions in the Brazilian test: Experimental verification," *Mater. Struct. Constr.*, vol. 32, no. 217, pp. 210–217, 1999, doi: 10.1007/bf02481517.

[105] Y. Ma and H. Huang, "DEM analysis of failure mechanisms in the intact Brazilian test," *Int. J. Rock Mech. Min. Sci.*, vol. 102, no. August 2017, pp. 109–119, 2018, doi: 10.1016/j.ijrmms.2017.11.010.

[106] F. Lanaro, T. Sato, and O. Stephansson, "Microcrack modelling of Brazilian tensile tests with the boundary element method," *Int. J. Rock Mech. Min. Sci.*, vol. 46, no. 3, pp. 450–461, 2009, doi: 10.1016/j.ijrmms.2008.11.007.

[107] L. Biolzi, S. Cattaneo, and G. Rosati, "Flexural/tensile strength ratio in rock-like materials," *Rock Mech. Rock Eng.*, vol. 34, no. 3, pp. 217–233, 2001, doi: 10.1007/s006030170010.

[108] V. J. García, C. O. Márquez, A. R. Zúñiga-Suárez, B. C. Zuñiga-Torres, and L. J. Villalta-Granda, "Brazilian Test of Concrete Specimens Subjected to Different Loading Geometries: Review and New Insights," *Int. J. Concr. Struct. Mater.*, vol. 11, no. 2, pp. 343–363, 2017, doi: 10.1007/s40069-017-0194-7.

[109] R. K. Verma, G. D. Nguyen, M. Karakus, A. Taheri, and H. H. Bui, "Numerical Analysis of Fracture Propagation in Brazilian Disc Test," *Aust. Conf. Comput. Mech.*, no. 3, 2018.

[110] S. Patel and C. D. Martin, "Evaluation of Tensile Young's Modulus and Poisson's Ratio of a Bi-modular Rock from the Displacement Measurements in a Brazilian Test," *Rock Mech. Rock Eng.*, vol. 51, no. 2, pp. 361–373, 2018, doi: 10.1007/s00603-017-1345-5.

[111] W. C. Zhu and C. A. Tang, "Numerical simulation of Brazilian disk rock failure under static and dynamic loading," *Int. J. Rock Mech. Min. Sci.*, vol. 43, no. 2, pp. 236–252, Feb. 2006, doi: 10.1016/j.ijrmms.2005.06.008.

[112] M. Cai and P. K. Kaiser, "Numerical simulation of the Brazilian test and the tensile strength of anisotropic rocks and rocks with pre-existing cracks," *Int. J. Rock Mech. Min. Sci.*, vol. 41, no. SUPPL. 1, pp. 1–6, 2004, doi: 10.1016/j.ijrmms.2004.03.086.

[113] R. Gutiérrez-Moizant, M. Ramírez-Berasategui, S. Santos-Cuadros, and C. C. García-Fernández, "A Novel Analytical Solution for the Brazilian Test with Loading Arcs," *Math. Probl. Eng.*, vol. 2020, no. c, 2020, doi: 10.1155/2020/2935812.

[114] C. C. Garcia-Fernandez, C. Gonzalez-Nicieza, M. I. Alvarez-Fernandez, and R. A. Gutierrez-Moizant, "Analytical and experimental study of failure onset during a Brazilian test," *Int. J. Rock Mech. Min. Sci.*, vol. 103, no. December 2017, pp. 254–265, 2018, doi: 10.1016/j.ijrmms.2018.01.045.

[115] S. K. Kourkoulis, C. F. Markides, and P. E. Chatzistergos, "The standardized Brazilian disc test as a contact problem," *Int. J. Rock Mech. Min. Sci.*, vol. 57, pp. 132–141, 2013, doi: 10.1016/j.ijrmms.2012.07.016.

[116] ASTM, *D3967-16 Standard test method for splitting tensile strength of intact rock core specimens*. ASTM International, West Conshohocken, USA., 2016.

[117] J. A. Hudson, E. T. Brown, and F. Rummel, "The controlled failure of rock discs and rings loaded in diametral compression," *Int. J. Rock Mech. Min. Sci.*, vol. 9, no. 2, pp. 241–248, 1972, doi: 10.1016/0148-9062(72)90025-3.

[118] C. F. Markides and S. K. Kourkoulis, "The influence of jaw's curvature on the results of the Brazilian disc test," *J. Rock Mech. Geotech. Eng.*, vol. 8, no. 2, pp. 127–146, 2016, doi: 10.1016/j.jrmge.2015.09.008.

[119] R. Yuan and B. Shen, "Numerical modelling of the contact condition of a Brazilian disk test and its influence on the tensile strength of rock," *Int. J. Rock Mech. Min. Sci.*, vol. 93, no. January, pp. 54–65, 2017, doi: 10.1016/j.ijrmms.2017.01.010.

[120] Q. Z. Wang, X. M. Jia, S. Q. Kou, Z. X. Zhang, and P. A. Lindqvist, "The flattened Brazilian disc specimen used for testing elastic modulus, tensile strength and fracture toughness of brittle rocks: Analytical and numerical results," *Int. J. Rock Mech. Min. Sci.*, vol. 41, no. 2, pp. 245–253, 2004, doi: 10.1016/S1365-1609(03)00093-5.

[121] M. I. Alvarez-Fernandez, C. C. Garcia-Fernandez, C. Gonzalez-Nicieza, and D. J. Guerrero-Miguel, "Effect of the Contact Angle in the Failure Pattern in Slate Under Diametral Compression," *Rock Mech. Rock Eng.*, no. 2, 2020, doi: 10.1007/s00603-020-02044-z.

[122] S. Q. Yang, P. F. Yin, and Y. H. Huang, "Experiment and Discrete Element Modelling on Strength, Deformation and Failure Behaviour of Shale Under Brazilian Compression," *Rock Mech. Rock Eng.*, vol. 52, no. 11, pp. 4339–4359, 2019, doi: 10.1007/s00603-019-01847-z.

[123] C. F. Markides, D. N. Pazis, and S. K. Kourkoulis, "Closed full-field solutions for stresses and displacements in the Brazilian disk under distributed radial load," *Int. J. Rock Mech. Min. Sci.*, vol. 47, no. 2, pp. 227–237, 2010, doi: 10.1016/j.ijrmms.2009.11.006.

[124] A. Tavallali and A. Vervoort, "Effect of layer orientation on the failure of layered sandstone under Brazilian test conditions," *Int. J. rock Mech. Min. Sci.*, vol. 47, no. 2, pp. 313–322, 2010, doi: 10.1016/j.jrmge.2013.01.004.

[125] A. Elghazel, R. Taktak, and J. Bouaziz, "Determination of elastic modulus, tensile strength and fracture toughness of bioceramics using the flattened Brazilian disc specimen: analytical and numerical results," *Ceram. Int.*, vol. 41, no. 9, pp. 12340–12348, 2015, doi: 10.1016/j.ceramint.2015.06.063.

[126] C. Fairhurst, "On the validity of the 'Brazilian' test for brittle materials," *Int. J. Rock Mech. Min. Sci.*, vol. 1, no. 4, pp. 535–546, 1964, doi: 10.1016/0148-9062(64)90060-9.

[127] G. Hondros, "The evaluation of Poisson's ratio and the modulus of materials of low tensile resistance by the Brazilian (indirect tensile) test with particular reference to

concrete," *Aust. J. Appl. Sci.*, vol. 10, no. 3, pp. 243–268, 1959.

[128] P. S. B. Colback, "An analysis of brittle fracture initiation and propagation in the Brazilian test," in *1st ISRM Congress*, 1966.

[129] Z. T. Bieniawski and M. J. Bernede, "Suggested methods for determining the uniaxial compressive strength and deformability of rock materials," in *International journal of rock mechanics and mining sciences & geomechanics abstracts*, 1979, vol. 16, no. 2, pp. 138–140.

[130] T. Jayakumar and C. K. Mukhopadhyay, "NDT Techniques: Acoustic Emission," *Ref. Modul. Mater. Sci. Mater. Eng.*, vol. 1, no. March 2015, pp. 1–7, 2016, doi: 10.1016/b978-0-12-803581-8.02682-5.

[131] M. Meo, *Acoustic emission sensors for assessing and monitoring civil infrastructures*, vol. 1. Woodhead Publishing Limited, 2014.

[132] A. E. Lord, "6 - Acoustic Emission," in *Physical Acoustics*, vol. 11, no. C, W. P. MASON and R. N. B. T.-P. A. THURSTON, Eds. Academic Press, 1975, pp. 289–353.

[133] Y. Dong and F. Ansari, "Non-destructive testing and evaluation (NDT/NDE) of civil structures rehabilitated using fiber reinforced polymer (FRP) composites," *Serv. Life Estim. Ext. Civ. Eng. Struct.*, pp. 193–222, 2011, doi: 10.1533/9780857090928.2.193.

[134] K. Ohno and M. Ohtsu, "Crack classification in concrete based on acoustic emission," *Constr. Build. Mater.*, vol. 24, no. 12, pp. 2339–2346, 2010, doi: 10.1016/j.conbuildmat.2010.05.004.

[135] Z. H. Zhang, J. H. Deng, J. B. Zhu, and L. R. Li, "An Experimental Investigation of the Failure Mechanisms of Jointed and Intact Marble under Compression Based on Quantitative Analysis of Acoustic Emission Waveforms," *Rock Mech. Rock Eng.*, vol. 51, no. 7, pp. 2299–2307, 2018, doi: 10.1007/s00603-018-1484-3.

[136] D. Lockner, "The role of acoustic emission in the study of rock fracture," *Int. J. Rock Mech. Min. Sci.*, vol. 30, no. 7, pp. 883–899, 1993, doi: 10.1016/0148-9062(93)90041-B.

[137] C. K. Mukhopadhyay, T. K. Haneef, T. Jayakumar, G. K. Sharma, and B. P. C. Rao, "Structural integrity assessment of H2S storage tanks using acoustic emission and ultrasonic techniques," *Int. J. Struct. Integr.*, 2015.

[138] C. Barile, C. Casavola, G. Pappalettera, and P. K. Vimalathithan, "Damage characterization in composite materials using acoustic emission signal-based and parameter-based data," *Compos. Part B Eng.*, vol. 178, p. 107469, 2019.

[139] B.-A. Behrens, S. Hübner, and K. Wölki, "Acoustic emission—A promising and challenging technique for process monitoring in sheet metal forming," *J. Manuf. Process.*, vol. 29, pp. 281–288, 2017.

[140] P. Zhao, Y. Sun, J. Jiao, and G. Fang, "Correlation between acoustic emission

detection and microstructural characterization for damage evolution," *Eng. Fract. Mech.*, vol. 230, p. 106967, 2020, doi: https://doi.org/10.1016/j.engfracmech.2020.106967.

[141] C. Ennaceur, A. Laksimi, C. Herve, and M. Cherfaoui, "Monitoring crack growth in pressure vessel steels by the acoustic emission technique and the method of potential difference," *Int. J. Press. Vessel. Pip.*, vol. 83, no. 3, pp. 197–204, 2006.

[142] J. D. Butterfield, A. Krynkin, R. P. Collins, and S. B. M. Beck, "Experimental investigation into vibro-acoustic emission signal processing techniques to quantify leak flow rate in plastic water distribution pipes," *Appl. Acoust.*, vol. 119, pp. 146–155, 2017.

[143] H. R. Hardy, "Application of acoustic emission techniques to rock mechanics research," in *Acoustic Emission*, ASTM International, 1972.

[144] E. A. Hodgson, "Velocity of elastic waves and structure of the crust in the vicinity of Ottawa, Canada," *Bull. Seismol. Soc. Am.*, vol. 32, no. 4, pp. 249–255, 1942.

[145] H. R. Hardy Jr, R. Y. Kim, R. Stefanko, and Y. J. Wang, "Creep and microseismic activity in geologic materials," in *The 11th US Symposium on Rock Mechanics (USRMS)*, 1969.

[146] S. Q. Yang, H. W. Jing, and S. Y. Wang, "Experimental investigation on the strength, deformability, failure behavior and acoustic emission locations of red sandstone under triaxial compression," *Rock Mech. Rock Eng.*, vol. 45, no. 4, pp. 583–606, 2012, doi: 10.1007/s00603-011-0208-8.

[147] S. Wu, H. Ge, X. Wang, and F. Meng, "Shale failure processes and spatial distribution of fractures obtained by AE monitoring," *J. Nat. Gas Sci. Eng.*, vol. 41, pp. 82–92, 2017, doi: 10.1016/j.jngse.2017.02.015.

[148] D. Lockner, J. D. Byerlee, V. Kuksenko, A. Ponomarev, and A. Sidorin, "Quasi-static fault growth and shear fracture energy in granite," *Nature*, vol. 350, no. 6313, pp. 39–42, 1991.

[149] M. H. B. Nasseri, S. D. Goodfellow, L. Lombos, and R. P. Young, "3-D transport and acoustic properties of Fontainebleau sandstone during true-triaxial deformation experiments," *Int. J. Rock Mech. Min. Sci.*, vol. 69, pp. 1–18, 2014, doi: 10.1016/j.ijrmms.2014.02.014.

[150] Z. A. Moradian, G. Ballivy, and P. Rivard, "Correlating acoustic emission sources with damaged zones during direct shear test of rock joints," *Can. Geotech. J.*, vol. 49, no. 6, pp. 710–718, 2012.

[151] J. H. Kurz, C. U. Grosse, and H. W. Reinhardt, "Strategies for reliable automatic onset time picking of acoustic emissions and of ultrasound signals in concrete," *Ultrasonics*, vol. 43, no. 7, pp. 538–546, 2005, doi: 10.1016/j.ultras.2004.12.005.

[152] M. Ohtsu, "Simplified moment tensor analysis and unified decomposition of acoustic emission source: application to in situ hydrofracturing test," *J. Geophys. Res. Solid Earth*, vol. 96, no. B4, pp. 6211–6221, 1991.

[153] T. O. Masayasu Ohtsu and Shigenori Yuyama, "Moment Tensor Analysis of Acoustic Emission for Cracking Mechanisms in Concrete," *ACI Struct. J.*, vol. 95, no. 2, doi: 10.14359/529.

[154] M. Ohtsu, "Acoustic emission theory for moment tensor analysis," *Res. Nondestruct. Eval.*, vol. 6, no. 3, pp. 169–184, 1995.

[155] J. Davidsen, T. Goebel, G. Kwiatek, S. Stanchits, J. Baró, and G. Dresen, "What Controls the Presence and Characteristics of Aftershocks in Rock Fracture in the Lab?," *J. Geophys. Res. Solid Earth*, vol. 126, no. 10, pp. 1–25, 2021, doi: 10.1029/2021JB022539.

[156] H. Z. Xing, Q. B. Zhang, C. H. Braithwaite, B. Pan, and J. Zhao, *High-Speed Photography and Digital Optical Measurement Techniques for Geomaterials: Fundamentals and Applications*, vol. 50, no. 6. Springer Vienna, 2017.

[157] M. A. Sutton, J. J. Orteu, and H. Schreier, *Image correlation for shape, motion and deformation measurements: basic concepts, theory and applications*. Springer Science & Business Media, 2009.

[158] N. McCormick and J. Lord, "Digital image correlation," *Mater. Today*, vol. 13, no. 12, pp. 52–54, 2010, doi: 10.1016/S1369-7021(10)70235-2.

[159] R. A. Stirling, D. J. Simpson, and C. T. Davie, "The application of digital image correlation to Brazilian testing of sandstone," *Int. J. Rock Mech. Min. Sci.*, vol. 60, pp. 1–11, 2013, doi: 10.1016/j.ijrmms.2012.12.026.

[160] Z. Aliabadian, G. F. Zhao, and A. R. Russell, "Failure, crack initiation and the tensile strength of transversely isotropic rock using the Brazilian test," *Int. J. Rock Mech. Min. Sci.*, vol. 122, no. July, p. 104073, 2019, doi: 10.1016/j.ijrmms.2019.104073.

[161] W. H. Peters and W. F. Ranson, "Digital imaging techniques in experimental stress analysis," *Opt. Eng.*, vol. 21, no. 3, p. 213427, 1982.

[162] T. C. Chu, W. F. Ranson, and M. A. Sutton, "Applications of digital-image-correlation techniques to experimental mechanics," *Exp. Mech.*, vol. 25, no. 3, pp. 232–244, 1985, doi: 10.1007/BF02325092.

[163] M. Bornert, F. Vales, H. Gharbi, and D. Nguyen Minh, "Multiscale full-field strain measurements for micromechanical investigations of the hydromechanical behaviour of clayey rocks," *Strain*, vol. 46, no. 1, pp. 33–46, 2010.

[164] T. L. Nguyen, S. A. Hall, P. Vacher, and G. Viggiani, "Fracture mechanisms in soft rock: Identification and quantification of evolving displacement discontinuities by extended digital image correlation," *Tectonophysics*, vol. 503, no. 1, pp. 117–128, 2011, doi: https://doi.org/10.1016/j.tecto.2010.09.024.

[165] W. He, K. Chen, A. Hayatdavoudi, P. Huang, K. Sawant, and C. Zhang, "Incorporating the effects of elemental concentrations on rock tensile failure," *Int. J. Rock Mech. Min. Sci.*, vol. 123, no. September, p. 104062, 2019, doi: 10.1016/j.ijrmms.2019.104062.

[166] L. Y. Chi, Z. X. Zhang, A. Aalberg, J. Yang, and C. C. Li, "Fracture Processes in Granite Blocks Under Blast Loading," *Rock Mech. Rock Eng.*, vol. 52, no. 3, pp. 853–868, 2019, doi: 10.1007/s00603-018-1620-0.

[167] Q. B. Zhang and J. Zhao, "Determination of mechanical properties and full-field strain measurements of rock material under dynamic loads," *Int. J. Rock Mech. Min. Sci.*, vol. 60, pp. 423–439, 2013.

[168] G. Gao, S. Huang, K. Xia, and Z. Li, "Application of Digital Image Correlation (DIC) in Dynamic Notched Semi-Circular Bend (NSCB) Tests," *Exp. Mech.*, vol. 55, no. 1, pp. 95–104, 2015, doi: 10.1007/s11340-014-9863-5.

[169] Z. Aliabadian, G. F. Zhao, and A. R. Russell, "Crack development in transversely isotropic sandstone discs subjected to Brazilian tests observed using digital image correlation," *Int. J. Rock Mech. Min. Sci.*, vol. 119, no. May, pp. 211–221, 2019, doi: 10.1016/j.ijrmms.2019.04.004.

[170] N. Lenoir, M. Bornert, J. Desrues, P. Bésuelle, and G. Viggiani, "Volumetric digital image correlation applied to X-ray microtomography images from triaxial compression tests on argillaceous rock," *Strain*, vol. 43, no. 3, pp. 193–205, 2007.

[171] Y. Lu *et al.*, "Fracture evolution in mudstone specimens containing a pre-existing flaw under true triaxial compression," *Int. J. Rock Mech. Min. Sci.*, vol. 138, p. 104594, 2021, doi: https://doi.org/10.1016/j.ijrmms.2020.104594.

[172] G. Yang, Z. Cai, X. Zhang, and D. Fu, "An experimental investigation on the damage of granite under uniaxial tension by using a digital image correlation method," *Opt. Lasers Eng.*, vol. 73, pp. 46–52, 2015, doi: https://doi.org/10.1016/j.optlaseng.2015.04.004.

[173] Y. Tang, S. Okubo, J. Xu, and S. Peng, "Experimental Study on Damage Behavior of Rock in Compression–Tension Cycle Test Using 3D Digital Image Correlation," *Rock Mech. Rock Eng.*, vol. 52, no. 5, pp. 1387–1394, 2019, doi: 10.1007/s00603-018-1685-9.

[174] T. M. Fayyad and J. M. Lees, "Application of digital image correlation to reinforced concrete fracture," *Procedia Mater. Sci.*, vol. 3, pp. 1585–1590, 2014.

[175] S. Y. Alam, J. Saliba, and A. Loukili, "Fracture examination in concrete through combined digital image correlation and acoustic emission techniques," *Constr. Build. Mater.*, vol. 69, pp. 232–242, 2014, doi: 10.1016/j.conbuildmat.2014.07.044.

[176] G. Lacidogna, G. Piana, F. Accornero, and A. Carpinteri, "Multi-technique damage monitoring of concrete beams: Acoustic Emission, Digital Image Correlation, Dynamic Identification," *Constr. Build. Mater.*, vol. 242, p. 118114, 2020, doi: https://doi.org/10.1016/j.conbuildmat.2020.118114.

[177] B. Pan, K. Qian, H. Xie, and A. Asundi, "Two-dimensional digital image correlation for in-plane displacement and strain measurement: a review," *Meas. Sci. Technol.*, vol. 20, no. 6, p. 62001, 2009.

[178] CorelatedSolutions, "Vic-2D 2020 Reference Manual. Colum- bia, SC, USA,"

2020. [Online]. Available: www.CorrelatedSolutions.com. [Accessed: 02-Jun-2021].

[179] M. Ghamgosar and N. Erarslan, "Experimental and Numerical Studies on Development of Fracture Process Zone (FPZ) in Rocks under Cyclic and Static Loadings," *Rock Mech. Rock Eng.*, vol. 49, no. 3, pp. 893–908, 2016, doi: 10.1007/s00603-015-0793-z.

[180] A. K. Maji and J. L. Wang, "Experimental study of fracture processes in rock," *Rock Mech. Rock Eng.*, vol. 25, no. 1, pp. 25–47, 1992, doi: 10.1007/BF01041874.

[181] M. Haggerty, Q. Lin, and J. F. Labuz, "Observing Deformation and Fracture of Rock with Speckle Patterns," *Rock Mech. Rock Eng.*, vol. 43, no. 4, pp. 417–426, 2010, doi: 10.1007/s00603-009-0055-z.

[182] N. Y. Wong, "Crack coalescence in molded gypsum and Carrara marble." Massachusetts Institute of Technology, 2008.

[183] J. F. Labuz, S. Cattaneo, and L.-H. Chen, "Acoustic emission at failure in quasi-brittle materials," *Constr. Build. Mater.*, vol. 15, no. 5, pp. 225–233, 2001, doi: https://doi.org/10.1016/S0950-0618(00)00072-6.

[184] T. Backers, S. Stanchits, and G. Dresen, "Tensile fracture propagation and acoustic emission activity in sandstone: The effect of loading rate," *Int. J. Rock Mech. Min. Sci.*, vol. 42, no. 7, pp. 1094–1101, 2005, doi: https://doi.org/10.1016/j.ijrmms.2005.05.011.

[185] S. Stanchits, J. Burghardt, and A. Surdi, "Hydraulic Fracturing of Heterogeneous Rock Monitored by Acoustic Emission," *Rock Mech. Rock Eng.*, vol. 48, no. 6, pp. 2513–2527, 2015, doi: 10.1007/s00603-015-0848-1.

[186] B. Q. Li and H. H. Einstein, "Comparison of Visual and Acoustic Emission Observations in a Four Point Bending Experiment on Barre Granite," *Rock Mech. Rock Eng.*, vol. 50, no. 9, pp. 2277–2296, 2017, doi: 10.1007/s00603-017-1233-z.

[187] Z. Moradian, H. H. Einstein, and G. Ballivy, "Detection of Cracking Levels in Brittle Rocks by Parametric Analysis of the Acoustic Emission Signals," *Rock Mech. Rock Eng.*, vol. 49, no. 3, pp. 785–800, Mar. 2016, doi: 10.1007/S00603-015-0775-1/FIGURES/17.

[188] F. Dai and K. Xia, "Loading Rate Dependence of Tensile Strength Anisotropy of Barre Granite," *Pure Appl. Geophys.*, vol. 167, no. 11, pp. 1419–1432, 2010, doi: 10.1007/s00024-010-0103-3.

[189] C. Chen, X. Fan, and X. Chen, "Experimental investigation of concrete fracture behavior with different loading rates based on acoustic emission," *Constr. Build. Mater.*, vol. 237, p. 117472, Mar. 2020, doi: 10.1016/J.CONBUILDMAT.2019.117472.

[190] X. Wang, E. Wang, X. Liu, and X. Zhou, "Failure mechanism of fractured rock and associated acoustic behaviors under different loading rates," *Eng. Fract. Mech.*, vol. 247, no. November 2020, pp. 1–15, 2021, doi: 10.1016/j.engfracmech.2021.107674.

[191] S. Li, X. Fan, X. Chen, S. Liu, and Y. Guo, "Development of fracture process zone in full-graded dam concrete under three-point bending by DIC and acoustic emission," *Eng. Fract. Mech.*, vol. 230, p. 106972, May 2020, doi: 10.1016/J.ENGFRACMECH.2020.106972.

[192] P. Wang, M. Cai, F. Ren, C. Li, and T. Yang, "Theoretical investigation of deformation characteristics of stratified rocks considering geometric and mechanical variability," *Geosci. J.*, vol. 21, no. 2, pp. 213–222, 2017.

[193] M. J. Iqbal and B. Mohanty, "Experimental calibration of stress intensity factors of the ISRM suggested cracked chevron-notched Brazilian disc specimen used for determination of mode-I fracture toughness," *Int. J. Rock Mech. Min. Sci.*, vol. 43, no. 8, pp. 1270–1276, 2006, doi: 10.1016/j.ijrmms.2006.04.014.

[194] A. Lu, S. Wang, and H. Cai, "Closed-Form Solution for the Stresses in Brazilian Disc Tests Under Vertical Uniform Loads," *Rock Mech. Rock Eng.*, vol. 51, no. 11, pp. 3489–3503, 2018, doi: 10.1007/s00603-018-1511-4.

[195] C. U. Grosse, M. Ohtsu, D. G. Aggelis, and T. Shiotani, *Acoustic Emission Testing: Basics for Research-Applications in Engineering*. Springer Nature, 2021.

[196] Z. Moradian and B. Q. Li, "Hit-based acoustic emission monitoring of rock fractures: Challenges and solutions," *Springer Proc. Phys.*, vol. 179, no. November 2015, pp. 357–370, 2017, doi: 10.1007/978-3-319-29052-2_31.

[197] A. Fathi, Z. Moradian, P. Rivard, and G. Ballivy, "Shear mechanism of rock joints under pre-peak cyclic loading condition," *Int. J. Rock Mech. Min. Sci.*, vol. 83, pp. 197–210, 2016, doi: 10.1016/j.ijrmms.2016.01.009.

[198] S. Renaud, T. Saichi, N. Bouaanani, B. Miquel, M. Quirion, and P. Rivard, "Roughness Effects on the Shear Strength of Concrete and Rock Joints in Dams Based on Experimental Data," *Rock Mech. Rock Eng.*, vol. 52, no. 10, pp. 3867–3888, 2019, doi: 10.1007/s00603-019-01803-x.

[199] N. O. Myers, "Characterization of surface roughness," *Wear*, vol. 5, no. 3, pp. 182–189, 1962.

[200] R. Tse and D. M. Cruden, "Estimating joint roughness coefficients," *Int. J. Rock Mech. Min. Sci.*, vol. 16, no. 5, pp. 303–307, 1979, doi: 10.1016/0148-9062(79)90241-9.

[201] B. S. A. A. Tatone and G. Grasselli, "A new 2D discontinuity roughness parameter and its correlation with JRC," *Int. J. Rock Mech. Min. Sci.*, vol. 47, no. 8, pp. 1391–1400, 2010, doi: 10.1016/j.ijrmms.2010.06.006.

[202] G. Zhang, M. Karakus, H. Tang, Y. Ge, and L. Zhang, "A new method estimating the 2D Joint Roughness Coefficient for discontinuity surfaces in rock masses," *Int. J. Rock Mech. Min. Sci.*, vol. 72, pp. 191–198, 2014, doi: 10.1016/j.ijrmms.2014.09.009.

[203] T. Belem, F. Homand-Etienne, and M. Souley, "Fractal analysis of shear joint roughness," *Int. J. Rock Mech. Min. Sci.*, vol. 34, no. 3–4, pp. 130.e1-130.e16, 1997,

doi: 10.1016/s1365-1609(97)80001-9.

[204] N. Fardin, O. Stephansson, and L. Jing, "The scale dependence of rock joint surface roughness," *Int. J. Rock Mech. Min. Sci.*, vol. 38, no. 5, pp. 659–669, 2001, doi: 10.1016/S1365-1609(01)00028-4.

[205] B. S. A. Tatone and G. Grasselli, "A method to evaluate the three-dimensional roughness of fracture surfaces in brittle geomaterials," *Rev. Sci. Instrum.*, vol. 80, no. 12, p. 125110, Dec. 2009, doi: 10.1063/1.3266964.

[206] T. Belem, F. Homand-Etienne, and M. Souley, "Quantitative parameters for rock joint surface roughness," *Rock Mech. Rock Eng.*, vol. 33, no. 4, pp. 217–242, 2000, doi: 10.1007/s006030070001.

[207] P. Kulatilake, P. Balasingam, J. Park, and R. Morgan, "Natural rock joint roughness quantification through fractal techniques," *Geotech. Geol. Eng.*, vol. 24, no. 5, pp. 1181–1202, 2006, doi: 10.1007/s10706-005-1219-6.

[208] Z. X. Zhang, S. Q. Kou, J. Yu, Y. Yu, L. G. Jiang, and P.-A. Lindqvist, "Effects of loading rate on rock fracture," *Int. J. Rock Mech. Min. Sci.*, vol. 36, no. 5, pp. 597–611, 1999.

[209] K. Hashiba and K. Fukui, "Index of Loading-Rate Dependency of Rock Strength," *Rock Mech. Rock Eng.*, vol. 48, no. 2, pp. 859–865, 2015, doi: 10.1007/s00603-014-0597-6.

[210] A. Zang, F. C. Wagner, S. Stanchits, G. Dresen, R. Andresen, and M. A. Haidekker, "Source analysis of acoustic emissions in Aue granite cores under symmetric and asymmetric compressive loads," *Geophys. J. Int.*, vol. 135, no. 3, pp. 1113–1130, 1998, doi: 10.1046/j.1365-246X.1998.00706.x.

[211] V. Vavryčuk, "Moment tensor decompositions revisited," *J. Seismol.*, vol. 19, no. 1, pp. 231–252, 2015, doi: 10.1007/s10950-014-9463-y.

[212] T. Candela, F. Renard, Y. Klinger, K. Mair, J. Schmittbuhl, and E. E. Brodsky, "Roughness of fault surfaces over nine decades of length scales," *J. Geophys. Res. Solid Earth*, vol. 117, no. 8, pp. 1–30, 2012, doi: 10.1029/2011JB009041.

[213] T. Candela, F. Renard, J. Schmittbuhl, M. Bouchon, and E. E. Brodsky, "Fault slip distribution and fault roughness," *Geophys. J. Int.*, vol. 187, no. 2, pp. 959–968, 2011, doi: 10.1111/j.1365-246X.2011.05189.x.

[214] T. H. W. Goebel, T. Candela, C. G. Sammis, T. W. Becker, G. Dresen, and D. Schorlemmer, "Seismic event distributions and off-fault damage during frictional sliding of saw-cut surfaces with pre-defined roughness," *Geophys. J. Int.*, vol. 196, no. 1, pp. 612–625, Jan. 2014, doi: 10.1093/GJI/GGT401.

[215] L. Dong and X. Li, "A Microseismic/Acoustic Emission Source Location Method Using Arrival Times of PS Waves for Unknown Velocity System:," *http://dx.doi.org/10.1155/2013/307489*, vol. 2013, Oct. 2013, doi: 10.1155/2013/307489.

[216] C. Saroglou and V. Kallimogiannis, “Fracturing process and effect of fracturing degree on wave velocity of a crystalline rock,” *J. Rock Mech. Geotech. Eng.*, vol. 9, no. 5, pp. 797–806, Oct. 2017, doi: 10.1016/J.JRMGE.2017.03.012.

[217] Z. T. Bieniawski, “Time-dependent behaviour of fractured rock,” *Rock Mech. 1970 23*, vol. 2, no. 3, pp. 123–137, Sep. 1970, doi: 10.1007/BF01239744.

[218] L. N. Y. Wong and T. Y. Guo, “Microcracking behavior of two semi-circular bend specimens in mode I fracture toughness test of granite,” *Eng. Fract. Mech.*, vol. 221, no. July, p. 106565, 2019, doi: 10.1016/j.engfracmech.2019.106565.

[219] Q. Lin, B. Wan, Y. Wang, Y. Lu, and J. F. Labuz, “Unifying acoustic emission and digital imaging observations of quasi-brittle fracture,” *Theor. Appl. Fract. Mech.*, vol. 103, no. July, p. 102301, 2019, doi: 10.1016/j.tafmec.2019.102301.

[220] H. Zhang *et al.*, “Damage and Fracture Investigation of Three-Point Bending Notched Sandstone Beams by DIC and AE Techniques,” *Rock Mech. Rock Eng.*, vol. 48, no. 3, pp. 1297–1303, May 2015, doi: 10.1007/S00603-014-0635-4/FIGURES/6.

[221] Y. Cheng and L. N. Y. Wong, “Microscopic Characterization of Tensile and Shear Fracturing in Progressive Failure in Marble,” *J. Geophys. Res. Solid Earth*, vol. 123, no. 1, pp. 204–225, 2018, doi: 10.1002/2017JB014581.

[222] A. Khosravi, R. Simon, and P. Rivard, “The shape effect on the morphology of the fracture surface induced by the Brazilian test,” *Int. J. Rock Mech. Min. Sci.*, vol. 93, no. February 2016, pp. 201–209, 2017, doi: 10.1016/j.ijrmms.2017.01.007.

[223] A. Bobet and H. H. Einstein, “Fracture coalescence in rock-type materials under uniaxial and biaxial compression,” *Int. J. Rock Mech. Min. Sci.*, vol. 35, no. 7, pp. 863–888, 1998, doi: 10.1016/S0148-9062(98)00005-9.

[224] B. Q. Li and H. H. Einstein, “Direct and Microseismic Observations of Hydraulic Fracturing in Barre Granite and Opalinus Clayshale,” *J. Geophys. Res. Solid Earth*, vol. 124, no. 11, pp. 11900–11916, Nov. 2019, doi: 10.1029/2019JB018376.

[225] L. Liu, H. Li, X. Li, D. Wu, and G. Zhang, “Underlying Mechanisms of Crack Initiation for Granitic Rocks Containing a Single Pre-existing Flaw: Insights From Digital Image Correlation (DIC) Analysis,” *Rock Mech. Rock Eng.*, vol. 54, no. 2, pp. 857–873, 2021, doi: 10.1007/s00603-020-02286-x.

[226] T. Y. Guo and Q. Zhao, “Acoustic Emission Characteristics During the Microcracking Processes of Granite, Marble and Sandstone Under Mode I Loading,” *Rock Mech. Rock Eng.*, vol. 55, no. 9, pp. 5467–5489, 2022.

[227] J. F. Labuz, S. P. Shah, and C. H. Dowding, “The fracture process zone in granite: evidence and effect,” *Int. J. Rock Mech. Min. Sci. Geomech. Abstr.*, vol. 24, no. 4, pp. 235–246, Aug. 1987, doi: 10.1016/0148-9062(87)90178-1.

[228] J. F. Labuz, S. P. Shah, and C. H. Dowding, “Experimental analysis of crack propagation in granite,” *Int. J. Rock Mech. Min. Sci.*, vol. 22, no. 2, pp. 85–98, 1985, doi: 10.1016/0148-9062(85)92330-7.

[229] F. Ouchterlony, “Review of fracture toughness testing of rock,” *SM Arch.*, vol. 7, pp. 131–211, 1982.

[230] W. K. Zietlow and J. F. Labuz, “Measurement of the intrinsic process zone in rock using acoustic emission,” *Int. J. rock Mech. Min. Sci.*, vol. 35, no. 3, pp. 291–299, 1998.

[231] X. Lei, K. Kusunose, T. Satoh, and O. Nishizawa, “Fractal Structure of the Hypoceeter Distributions and Focal Mechanism Solutions of Acoustic Emission in Two Granites of Different Grain Sizes,” *J. Phys. Earth*, vol. 40, no. 6, pp. 617–634, 1992, doi: 10.4294/jpe1952.40.617.

[232] S. C. Maxwell and C. Cipolla, “What Does Microseismicity Tell Us About Hydraulic Fracturing?,” *Proc. - SPE Annu. Tech. Conf. Exhib.*, vol. 4, pp. 3033–3046, Oct. 2011, doi: 10.2118/146932-MS.

[233] ASTM, “D2936-08 Standard Test Method for Direct Tensile Strength of Intact Rock Core Specimens,” *ASTM Int.*, pp. 9–11, 2008, doi: 10.1520/D2936-20.2.

[234] C. U. Grosse and M. Ochtsu, *Acoustic Emission Testing. Basic for Research-Applications in Civil Engineering*, vol. 53, no. 9. Springer, 2008.

[235] ASTM, “E976 − 15 Standard guide for determining the reproducibility of acoustic emission sensor response,” ASTM International, West Conshohocken, USA., 2015.

[236] H. Akaike, “Information theory and an extension of the maximum likelihood principle,” in *Selected papers of hirotugu akaike*, Springer, 1998, pp. 199–213.

[237] H. Akaike, “A new look at the statistical model identification,” *IEEE Trans. Automat. Contr.*, vol. 19, no. 6, pp. 716–723, 1974.

[238] Y. Sakamoto, M. Ishiguro, and G. Kitagawa, “Akaike information criterion statistics,” *Dordrecht, Netherlands D. Reidel*, vol. 81, no. 10.5555, p. 26853, 1986.

[239] J. A. Nelder and R. Mead, “A simplex method for function minimization,” *Comput. J.*, vol. 7, no. 4, pp. 308–313, 1965.

[240] M. A. Sutton, J. H. Yan, V. Tiwari, H. W. Schreier, and J. J. Orteu, “The effect of out-of-plane motion on 2D and 3D digital image correlation measurements,” *Opt. Lasers Eng.*, vol. 46, no. 10, pp. 746–757, 2008, doi: 10.1016/j.optlaseng.2008.05.005.

[241] G. Shams, P. Rivard, and O. Moradian, “Observation of fracture process zone and produced fracture surface roughness in granite under Brazilian splitting tests,” *Theor. Appl. Fract. Mech.*, no. June, p. 103680, 2022, doi: 10.1016/j.tafmec.2022.103680.

[242] D. E. Moore and D. A. Lockner, “The role of microcracking in shear-fracture propagation in granite,” *J. Struct. Geol.*, vol. 17, no. 1, 1995, doi: 10.1016/0191-8141(94)E0018-T.

[243] M. Nicksiar and C. D. Martin, “Factors affecting crack initiation in low porosity

crystalline rocks," *Rock Mech. Rock Eng.*, vol. 47, no. 4, pp. 1165–1181, 2014, doi: 10.1007/s00603-013-0451-2.

[244] K. K. Kabeya and T. F. H. Legge, "Relationship between grain size and some surface roughness parameters of rock joints," *Int. J. rock Mech. Min. Sci. Geomech. Abstr.*, vol. 34, no. 3–4, p. 528, Apr. 1997, doi: 10.1016/S1365-1609(97)00186-X.

[245] P. Zhao, D. Kühn, V. Oye, and S. Cesca, "Evidence for tensile faulting deduced from full waveform moment tensor inversion during the stimulation of the Basel enhanced geothermal system," *Geothermics*, vol. 52, no. December 2006, pp. 74–83, 2014, doi: 10.1016/j.geothermics.2014.01.003.

[246] O. S. Boyd, D. S. Dreger, V. H. Lai, and R. Gritto, "A systematic analysis of seismic moment tensor at The Geysers geothermal field, California," *Bull. Seismol. Soc. Am.*, vol. 105, no. 6, pp. 2969–2986, 2015.

[247] V. S. Gischig and G. Preisig, "Hydro-fracturing versus hydro-shearing: a critical assessment of two distinct reservoir stimulation mechanisms," in *13th ISRM International Congress of Rock Mechanics*, 2015.

[248] Y. A. Fishman, "Stability of concrete retaining structures and their interface with rock foundations," *Int. J. Rock Mech. Min. Sci.*, vol. 46, no. 6, pp. 957–966, 2009, doi: 10.1016/j.ijrmms.2009.05.006.

[249] H. Zhong, E. T. Ooi, C. Song, T. Ding, G. Lin, and H. Li, "Experimental and numerical study of the dependency of interface fracture in concrete-rock specimens on mode mixity," *Eng. Fract. Mech.*, vol. 124–125, pp. 287–309, 2014, doi: 10.1016/j.engfracmech.2014.04.030.

[250] W. Dong, S. Song, B. Zhang, and D. Yang, "SIF-based fracture criterion of rock-concrete interface and its application to the prediction of cracking paths in gravity dam," *Eng. Fract. Mech.*, vol. 221, no. March, p. 106686, 2019, doi: 10.1016/j.engfracmech.2019.106686.

[251] G. Shams, P. Rivard, and O. Moradian, "Effects of roughness on the strength and fracturing processes in Mortar-Granite interface under tensile loading," in *The 75th Canadian geotechnical conference. Canadian Geotechnical Society (CGS)*, 2022.

[252] K. Fuenkajorn and S. Klanphumeesri, "Laboratory determination of direct tensile strength and deformability of intact rocks," *Geotech. Test. J.*, vol. 34, no. 1, pp. 97–102, 2011, doi: 10.1520/GTJ103134.

[253] ISRM, "ISRM Commission on Testing Methods: Basic Rock Sample Preparation," 2016. [Online]. Available: https://isrm.net/page/show/1233?tab=1272.

[254] D. Shirole, A. Hedayat, and G. Walton, "Illumination of Damage in Intact Rocks by Ultrasonic Transmission-Reflection and Digital Image Correlation," *J. Geophys. Res. Solid Earth*, vol. 125, no. 7, pp. 1–34, 2020, doi: 10.1029/2020JB019526.

[255] M. S. Diederichs, "Manuel Rocha Medal Recipient Rock Fracture and Collapse Under Low Confinement Conditions," *Rock Mech. Rock Eng.*, vol. 36, no. 5, pp. 339–381, 2003, doi: 10.1007/s00603-003-0015-y.

[256] F. Gao, D. Stead, and D. Elmo, “Numerical simulation of microstructure of brittle rock using a grain-breakable distinct element grain-based model,” *Comput. Geotech.*, vol. 78, 2016, doi: 10.1016/j.compgeo.2016.05.019.

[257] D. Vogler, S. D. C. Walsh, P. Bayer, and F. Amann, “Comparison of Surface Properties in Natural and Artificially Generated Fractures in a Crystalline Rock,” *Rock Mech. Rock Eng.*, vol. 50, no. 11, pp. 2891–2909, 2017, doi: 10.1007/s00603-017-1281-4.

[258] G. Shams, P. Rivard, and O. Moraidan, “Micro-scale Fracturing Mechanisms in Rocks During Tensile Failure,” *Rock Mech. Rock Eng.*, 2023.

[259] J. J. Liao, M.-T. Yang, and H.-Y. Hsieh, “Direct tensile behavior of a transversely isotropic rock,” *Int. J. Rock Mech. Min. Sci.*, vol. 34, no. 5, pp. 837–849, 1997.

[260] F. Dai, M. D. Wei, N. W. Xu, Y. Ma, and D. S. Yang, “Numerical Assessment of the Progressive Rock Fracture Mechanism of Cracked Chevron Notched Brazilian Disc Specimens,” *Rock Mech. Rock Eng.*, vol. 48, no. 2, pp. 463–479, 2015, doi: 10.1007/s00603-014-0587-8.

[261] M. Wei, F. Dai, Y. Liu, and R. Jiang, “A fracture model for assessing tensile mode crack growth resistance of rocks,” *J. Rock Mech. Geotech. Eng.*, no. xxxx, pp. 1–17, 2022, doi: 10.1016/j.jrmge.2022.03.001.

[262] M. Wei, F. Dai, Y. Liu, A. Li, and Z. Yan, “Influences of Loading Method and Notch Type on Rock Fracture Toughness Measurements: From the Perspectives of T-Stress and Fracture Process Zone,” *Rock Mech. Rock Eng.*, vol. 54, no. 9, pp. 4965–4986, 2021, doi: 10.1007/s00603-021-02541-9.

[263] H. S. Jang, S. S. Kang, and B. A. Jang, “Determination of Joint Roughness Coefficients Using Roughness Parameters,” *Rock Mech. Rock Eng.*, vol. 47, no. 6, pp. 2061–2073, 2014, doi: 10.1007/s00603-013-0535-z.

[264] Y. Li and Y. Zhang, “Quantitative estimation of joint roughness coefficient using statistical parameters,” *Int. J. Rock Mech. Min. Sci.*, vol. 77, pp. 27–35, 2015, doi: 10.1016/j.ijrmms.2015.03.016.

[265] X. Yu and B. Vayssade, “Joint profiles and their roughness parameters,” *Int. J. Rock Mech. Min. Sci.*, vol. 28, no. 4, pp. 333–336, 1991, doi: 10.1016/0148-9062(91)90598-G.

[266] B. S. A. Tatone and G. Grasselli, “An investigation of discontinuity roughness scale dependency using high-resolution surface measurements,” *Rock Mech. Rock Eng.*, vol. 46, no. 4, pp. 657–681, 2013, doi: 10.1007/s00603-012-0294-2.